ISBN 978-82-326-2784-4 (printed version)
ISBN 978-82-326-2785-1 (electronic version)
ISSN 1503-8181

Doctoral theses at NTNU, 2017:357

Patrícia Moura Rosa

IMMUNITY-ON-A-CHIP

Microfluidic Devices for Immunoengineering

Doctoral Thesis

Patrícia Moura Rosa

Doctoral theses at NTNU, 2017:357

NTNU
Norwegian University of
Science and Technology
Faculty of Medicine and Health Sciences
Department of Cancer Researchand Molecular Medicine

NTNU
Norwegian University of
Science and Technology

NTNU
Norwegian University of
Science and Technology

NTNU

Patrícia Moura Rosa

IMMUNITY-ON-A-CHIP

Microfluidic Devices for Immunoengineering

Thesis for the degree of Philosophiae Doctor

Trondheim, November 2017

Norwegian University of Science and Technology
Faculty of Medicine and Health Sciences
Department of Cancer Researchand Molecular Medicine

NTNU
Norwegian University of
Science and Technology

NTNU
Norwegian University of Science and Technology

Thesis for the degree of Philosophiae Doctor

Faculty of Medicine and Health Sciences
Department of Cancer Researchand Molecular Medicine

ISBN 978-82-326-2784-4 (printed version)
ISBN 978-82-326-2785-1 (electronic version)
ISSN 1503-8181

Doctoral theses at NTNU, 2017:357

Printed by Skipnes Kommunikasjon as

Immunitet-på-mikrobrikke
Mikrofluidiske innretninger for immunologisk forskning og utvikling

Sammendrag:

Det siste tiåret har mikrofluidteknologi, dvs væskestrømmer i mikroskala basert på prosesser fra halvlederindustrien, gitt et betydelig løfte om forbedringer innen diagnostikk, biomedisinsk forskning og individ-tilpasset medisin. Det er også i ferd med å bli et bærekraftig alternativt verktøy for dyremodeller og dagens *in vitro*-modeller for sykdom og helse for utprøving av nye medikamenter

I dette prosjektet ble mikrofluidiske innretninger utviklet med det formål å gjenskape og etterligne komplekse immunologiske og inflammatoriske celle-prosesser som naturlig skjer i kroppene våre. Spesielt var vi interessert i de to sentrale immunologiske prosessene cellemigrasjon, hvordan celler finner veien mot ønskede mål, og celle:celle interaksjon, hvordan cellene snakker sammen gjennom direkte kontakt.

Produksjonen av disse biochipene ble gjort på renrommet ved NTNU NanoLab mens celleforsøkene ble utført ved Institutt for Klinisk og Molekylær Medisin ved Fakultet for Medisin og Helsevitenskap.

Resultatene viser at vi kan gjenskape fysiologiske hendelser inne i våre kunstige immunologiske mikromiljøer. Dette åpner for helt nye tilnærminsgmåter og helt nye muligheter for immunterapi mot kreft og andre sykdommer med immunologisk komponenter, og kan bli et helt nytt verktøy for uttesting av vaksiner og medikamentelle terapier.

Navn kandidat: Patricia Moura Rosa
Institutt: Institutt for klinisk og molekylær medisin, Fakultet for medisin og helsevitenskap
Veileder(e):Øyvind Halaas

Finansieringskilde: *Dette arbeidet har blitt finansiert av det strategiske satsningsområdet NTNU nanoteknologi med støtte fra NorFab (prosjektnummer 245963/F50, Norges forskningsråd anerkjennes for støtte til norsk mikro- og nanofabrikasjon NorFab), og Institutt for Klinisk og Molekylær Medisin, Fakultet for Medisin og Helsevitenskap ved NTNU. Mikrofabrikasjonsprosessen ble utført på NTNU NanoLab renrom. Mikroskopi ble utført ved Cellular and Molecular Imaging Core Facility (CMIC), NTNU. CMIC er finansiert av Det medisinske fakultet ved NTNU og Helse Midt-Norge.*

Ovennevnte avhandling er funnet verdig til å forsvares offentlig
for graden PhD i Medisinsk Teknologi,
Disputas finner sted i Auditoriet, MTA, Medical Technical Research Centre
(Norsk hjernesenter),
29 November, 2017.

Abstract

The immune system plays an important role on the defense and regulation of the human body. To study human immunity and diseases, animal models and traditional cell cultures have been used for many years, and contributed significantly on the development of powerful new therapies. However, animal studies have evidenced limitations considering the differences with the human metabolism and disease. Additionally, traditional *in vitro* models have failed to mimic the normal microarchitecture environment of cells in tissues because of the absence of biochemicomechanical features (e.g., scaffold stiffness; controlled flow for the delivery of nutrients and gases; shear stress; haptotatic gradients). In this context, in the past decade microfluidic technology has emerged as an important alternative tool for translational immunology. Microfluidics offer the possibility to recreate *in vivo* compartmentalization of microphysiological models on *in vitro* platforms, allowing precise control of cellular biophysical and biochemical stimuli. These platforms capabilities further increase by coupling on-chip technologies for detection, sorting and 3D scaffold growth, or other needs/requirements to be explored in the future (e.g., the development of a recirculation system through a vascular network for a multi-organ-on-a-chip).

Thus, this technology has a remarkable potential for medical applications, and with industrial scale up, especially as a diagnostic and research tool for point-of-care testing, drug screening tests and translational cancer and immunology. Microfluidic technology also allows the development of clinical tool towards *in vitro* immunization, personalized cancer vaccination, immunotherapeutic approaches for cancer and autoimmune diseases etc.

In this context, the scope of this project was focused on the conception of microfluidic platforms, which allowed to mimic and to explore *in vitro* microphysiological models for translational immunology. These platforms allowed to study in real time on-a-chip several physiological events that occur during the initial stage of inflammation and adaptive immune response, such as the encounters and interactions between T cells with dendritic cells supported by a natural 3D fibroblast reticular scaffold, the immunological synapse formation and its cleavage, the immune cell migration and decision-making processes under inflammatory conditions.

In this work, the fabrication of the microfluidic devices was performed at NTNU NanoLab cleanroom. Cell preparations and experiments were done at the Department of Clinical and Molecular Medicine, Faculty of Medicine NTNU (Trondheim, Norway).

The microfabrication methodology consisted initially on the creation of designs and Multiphysics simulations to predict hemodynamic velocity and shear stress inside microchannels or microchambers. By using standard semiconductor photolithography and well-suited soft lithography for biomedical applications, to produce polydimethylsiloxane (PDMS)-based microfluidic devices.

During this project, in order to mimic the immune environment conditions several cell types were used such as mouse lymph node fibroblast reticular cells (FRCs), primary bone marrow-derived dendritic cells (BMDC), enhanced green fluorescent protein (eGFP)+murine dendritic cell line "MutuDC 1940", and non-adherent $CD4^+$ and $CD8^+$ T cells.

In this context, narrowing the focus to more specific sub-goals, during this PhD project three classes of microfluidic devices were developed: (i) Paper I, a microfluidic channel to promote the cognate physical interactions between T cells:APCs under varying shear stress, in order to study and to establish basic operational procedures associated with the immunological synapse formation; (ii) Paper II, a single-step and user friendly diffusion flow-free device to study the immune cell migration and decision-making process under inflammatory conditions; and (iii) Paper III, a microfluidic chamber that mimicked the microarchitecture of immune environment and cell behavior in the T cell zone of a lymph node (LN), being considered as a LN-T cell zone-on-the-chip. In this paper, the

mechanisms and dynamics of the growth of FRC scaffold by induction of continuous flow was explored. Basic cell behavior were further performed namely, attachment and detachment of antigen-specific and unspecific T cells to active antigen-presenting or non-activated dendritic cells supported on FRC meshwork at different shear stresses. The studied immune platforms demonstrated microphysiological events very similar to the ones reported *in vivo*.

As main results, in Paper I we observed random migration of antigen-specific T cells onto the antigen-presenting DC monolayer with a mean T cell:DC dwell time of 12.8min and a mean velocity of 6μm min^{-1} at a shear stress of 0.01Dyn cm^{-2}. In this study, we further identified that the range of mechanical force associated with the immunological synapse formation was ~0.25-4.8nN. Through the Paper II, the developed platform allowed us to identify the directional migration of T cells and DCs towards the inflammation foci (with a mean speed 9μm min^{-1}). In Paper III, we developed a microfluidic chamber that allowed the growth of FRC scaffold through the application of perfusion flow, which induces both chemical and mechanical stimuli. This was attained upon continuous perfusion during 48h at 100nl min^{-1} with a corresponding shear stress 0.001 to 0.004Dyn cm^{-2}. By using this FRC scaffold, a second stage of cell attachment/detachment tests were performed with 2 types of cell interactions: DCs:FRC scaffold and T cells:FRC scaffold. From these tests, high cell motility was observed on DCs and T cells, both with a mean velocity of ~10μm min^{-1}. At a third stage of attachment/detachment tests, 3 types of cells and interactions T cell:DC:FRC scaffold were analyzed: without cognate interactions, T cells and DCs presented a mean velocity of ~5μm min^{-1}, random movements and "stop and go" interactions during 3min. With cognate interactions, it was visible a significant decrease of DC and T cell velocity to ~2.5μm min^{-1}, where T cells moved in characteristic looping patterns making serial contacts with the same or with neighboring DCs, with interval of interactions around ~7min.

In this sense, we believe that these microfluidic platforms can open new horizons for the investigation of intercellular signaling of immune synapses and therapeutic targets for immunotherapies.

Acknowledgements

This work was carried out at the Department of Clinical and Molecular Medicine, Faculty of Medicine, St. Olavs University Hospital at the Norwegian University of Science and Technology (NTNU), Trondheim during 2013-2017.

This work has been supported by the Faculty of Medicine at NTNU and Central Norway Regional Health Authority. Microfabrication process was performed at the NTNU NanoLab (NorFab), NTNU. The Research Council of Norway is acknowledged for the support to the Norwegian Micro- and Nano-Fabrication Facility, NorFab, project number 245963/F50. Cell experiments were performed at the Cellular and Molecular Imaging Core Facility (CMIC), NTNU. CMIC is funded by the Faculty of Medicine at NTNU and Central Norway Regional Health Authority.

I am very grateful for the opportunity to work in this project with high level of pluri- and interdisciplinary from the microfabrication of devices in NTNU NanoLab cleanroom facilities to the cell tests at St. Olav Hospital, and the opportunity to have had excellent international experiences with courses and conferences.

Firstly, I would like to thank my main supervisor Øyvind Halaas. Thank you for being patient and for your open-door policy for my doubts/questions/ideas. Foremost, thank you for being a big enthusiastic of science and technology! Working with you was a rewarding experience in my life, and I will cherish it forever.

I would like to thank my co-supervisor, Nimi Gopalakrishnan for her support and constructive advices, and constant motivation.

It has also been a pleasure to work with all co-authors and contributors to this project, including Markus Haug and Hany Ibrahim from the Department of Clinical and Molecular Medicine.

A special thanks to Cecilie Lund, Rosanne van de Wijdeven, Kaung Myat, Lisa Gregusson Svartdal, Adriana Kyvik Ruiz, Vilde Michaelsen Sørdal, Ryan Hannam and Giovanna Perinetti Casoni for your important and special participation and for your contribution on the development of this project. Thank you for all your dedication, effort and motivation, and your new doubts, ideas and solutions!

I would like to thank all people with whom I have daily interacted at the Department of Clinical and Molecular Medicine, Faculty of Medicine, St. Olavs Hospital, and to the NTNU NanoLab staff. A special thanks to Ingrid Kathrin Hals, Anne Eleanor Kristensen, Kai Beckwith, Bjørnar Sporsheim, Terje Espevik, Alexandre Gidon, Peter Köllensperger, Birgitte Hjelmeland McDonagh, Trine Østlyng Hjertås, Mathilde Barriet, Ken Roger Ervik, Svenn Ove Linde, Mark Chiappa, Ida Noddeland, Hanna Gautun, Kay Gastinger.

Finally, I would like to express my deepest gratitude to all people around me, especially my parents and my boyfriend, who have always given me the strength and wisdom, for their immense love and affection.

List of Papers

The following publications are included in this thesis:

I. **The intercell dynamics of T cells and dendritic cells in a lymph node-on-a-chip flow device**

Moura Rosa, P., Gopalakrishnan, N., Ibrahim, H., Haug, M. and Halaas, Ø.

Lab Chip, 2016, **16** (19), 3728-3740. DOI: 10.1039/c6lc00702c.

II. **Immune cells moving in a microchannel network in search of targets**

Moura Rosa, P., Gopalakrishnan, N., Perinetti Casoni, G., van de Wijdeven, R., Haug, M. and Halaas, Ø.

Submitted to: *Lab Chip*

III. **Lymph node-on-a-chip: mimicking the microphysiology of the T cell zone**

Moura Rosa, P., Lund, C., Haug, M. and Halaas, Ø.

Manuscript

Related paper not included in the thesis:

I. **High-throughput study of alpha-synuclein expression in yeast using microfluidics for control of local cellular microenvironment**

Moura Rosa, P., Tenreiro, S., Chu, V., Outeiro, T. F. and Conde J.P.

Biomicrofluidics, 2012, **6** (1), 014109 – 014109-9. DOI: 10.1063/1.3683161

List of Abbreviations

APC	Antigen-presenting cell
BCR	B cell receptor
cSMAC	Central region of the supra-molecular activation complex
CMP	Common myeloid-erythroid progenitor
CLP	Common lymphoid progenitor
Col	Collagen
dSMAC	Distal region of the supra-molecular activation complex
DCs	Dendritic cells
DF	Dark field
ECM	Extracellular matrix
FN	Fibronectin
FRC	Fibroblast reticular cell
HEV	High endothelial venules
HSC	Hematopoietic stem cell
HuALN	Human artificial lymph node
IS	Immunological synapse
LFA1	Leukocytes function-associated antigen 1
LF	Light field
LNs	Lymph nodes
LoC	Lab-on-a-chip
LSCM	Laser scanning confocal microscope
LT- α	Lymphotoxin α
LTi	Lymphoid tissue inducer cells
mTAS	Miniaturized total analysis systems
MALT	Mucosa-associated lymphoid tissue
MEMS	Microelectromechanical systems
MHC	Major histocompatibility complex

MC	Microcluster
pSMAC	Peripheral region of the supra-molecular activation complex
PAC	Photoactive compound
PC	Polycarbonate
PD	Polydopamine
PDMS	Poly-dimethylsiloxane
PDPN	Podoplanin
Pe	Péclet number
PEB	Post-exposure bake
PET	Polyester poly(ethyleneterephthalate)
PKC- Θ	Protein kinase C-Θ
PMMA	Polymethylmethacrylate
PTFE	Polytetrafluoroethylene
Sh	Sherwood number
Si	Silicon
SLO	Secondary lymphoid organs
SMAC	Supra-molecular activation complex
R&D	Research and development
TEER	Transendothelial electrical resistance
TCR	T cells receptor
UV	Ultraviolet light
2PM	Two-photon microscopy
3D	Three-dimensional

Contents

1. INTRODUCTION

1.1. From The Cell-Cell Communication to The Immunoengineering

Cardiovascular disease, cancer and neurological disorders are the most common diseases afflicting millions of people around the globe annually, being the main causes of morbility and mortality (1-4). Despite recent advances in diagnosis and therapies, and coupled with the dramatic increase in average life expectancy during the 20th century, cancer is still the most terminal disease worldwide representing 11.5 million deaths being in 2030 (1).

Cancer is a heterogeneous group of diseases characterized by a multi-step process, as a result of uncontrolled tumor cell proliferation, invasion and metastasis. Tumor cells are especially skilled by their capability to evade cell death and to escape immune system surveillance. Currently, there are several strategies for cancer treatment including chemotherapy, radiotherapy, immunotherapy and surgery. However, more effective, more specific, less invasive and less painful treatment alternatives are still needed (1).

Recent studies reveal that inflammation and immune responses are implicated in the pathogenesis of these diseases (5-7), creating an urgent clinical need to develop new therapeutic approaches based on the understanding and recodification of immune cell-cell communication (1-4).

Cell-cell communication is involved in the transfer of information that generate a proper response, and is fundamental in directing cellular processes crucial to their survival in function of their microenvironment (8). These numerous processes include cell growth and development, cell proliferation, apoptosis, differentiation, metabolism, immune responses, and disease/injury management and repair. Further, mismatch and dysfunctional cell signaling can also occur, being implicit later in numerous diseases and pathological conditions such as cancer, autoimmune disorders, and diabetes (2, 8). In this context, revealing the subjacent mechanisms of intercellular communication is crucial for understanding and treatment of such diseases, leading to the creation of novel biomedical approaches and technologies as immunotherapy, drug delivery vehicles, stem cell regenerative therapy, tissue engineering, cancer diagnosis, neural prosthetics and robotics, and nanotechnology/nanomaterials/nanomedicine (2, 4).

There are several types of intercellular signaling: gap junction signalling, juxtacrine signalling, autocrine signalling, paracrine signalling, endocrine signalling and synaptic signalling (8). Commonly cell-cell communication are categorized in function of its type of physiological intercellular signals and in function of its distance over which occurs in one system. The two fundamental types of physiological intercellular signals can be stablished: chemical and electrical. The most abundant and varied signal is chemical, and their dimension ranges from small inorganic ions to big proteins (8).

Given the complexity and diversity of cell signaling mechanisms, the success of these mechanisms are dependent on the *specificity criteria* of cells, despite being exposed to high expression of signal molecules, cells are prepared to only respond to the target cell, which contains only receptors that specifically detect the signals they are concerned with, integrating the *receptor binding affinity criteria*. And finally the *transmission capacity criteria*, where the specific signal molecule and in specific combinations, receptors, intracellular mediators, machinery involved and microenvironment factors, all influence the final outcome, generating in this way distinct responses in differing types of cells (8).

However, due to the complexity of intercellular communication networks in multicellular systems and several limitations found on conventional tools and techniques used to study cell communication, the exact underlying mechanisms of cell communication still continue poorly understood (2, 4, 8, 9).

Although conventional methods used have been valuable tools in providing information about these mechanisms, they present various limitations including the lack of precision available for spatial and temporal control of cells and stimuli, flow pathways that guide the transport and distributions of chemokines and cytokines, restricted to static conditions, and lack the ability to manipulate and isolate cells as well as the ability to track and image cells (2, 4, 8).

Several conventional *in vivo*, *ex vivo* and *in vitro* techniques have been used to explore the intercellular communication. As direct *in vivo* and *ex vivo* studies, such as dissection, confocal microscopy and intravital multiphoton microscopy have been used in the analysis in zebrafish, mice, rat, sheep and humans (10-14). These techniques possess the power to maintain the native microenvironment during investigations, albeit with severe limitations in expense and complexity of imaging systems, being extremely difficult to precisely distinguish signals of interest from background noise (10-13), and time limitation due to the tissue degradation. Particularly *in vivo* animal studies, ethical issues are elevated and in some cases, when immune-suppressed mouse models are used to introduce human cancer cells in order to reduce rejection by the host immune system, these methods can exhibit limitations if some key players are absent (14).

As an important complementary approach for investigation of cell communication, the *in vitro* platforms can provide simplified experimental conditions and data analysis, but are insufficient for the acquisition of higher spatial and temporal resolutions (2).

One of the oldest, simple and robust technologies for culture used today is the Boyden chamber' or 'Transwell' systems, created by Boyden in 1962 (15). This system is characterized by two compartments separated by several types of membrane surfaces (as polycarbonate (PC), polyester (PET), and collagen-coated polytetrafluoroethylene (PTFE)) for cell culture, promoting studies of secretion, differentiation and migration (4). Transwell chamber and Zigmond chambers, and subsequent design improvements of Dunn chamber and Insall chamber have been used for chemotaxis studies over five decades, creating gradients with no liquid flow through the cell culture (15-18) (**Figure 1.1.1**). All these chambers measure the average direction of migration of cells in response to chemical or biological concentrations gradients via generation molecular diffusion (15-18).

However, these techniques are limited in the investigation of their concentration gradient profiles, once they cannot be maintained for long periods of time (<1-2h); cell migration is not polarised and the migratory bias is not controlled, lacking the internal controls (19-21). Moreover, conventional devices are generic and are not customized for the specific purposes: in bacterial infections studies, the lack of compartmentalizations leads to bacterial spread in the entire system, making any long term conclusion infeasible (20).

For the image acquisition, with this technique, it is difficult to observe the cell migration path and cell morphology (21). Furthermore, as drawbacks, this system lacks in some microphysiological factors - including suitable promoters for posterior signaling, migration, proliferation, and differentiation - because of the absence of an extracellular matrix (ECM) (3, 22, 23), haptotactic gradients (24), shear stress and other hemodynamic forces (3, 25) are important for successful cell-cell interaction and chemotaxis assays (21).

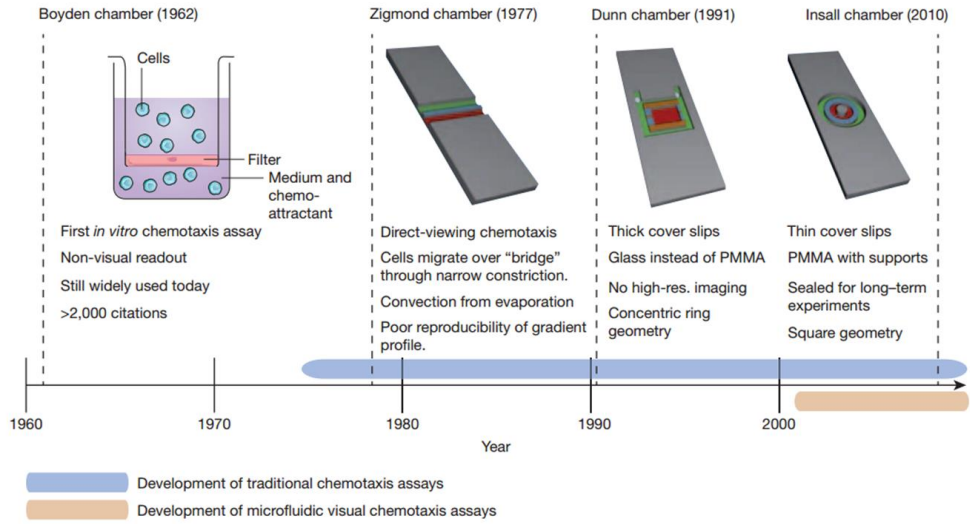

Figure 1.1.1 Illustration of the evolution on development of chemotaxis assay over time. It is worth mentioning, the relative short time, condensed in 10 years, of the development and application of microfluidic visual chemotaxis assays, in comparison to the traditional chemotaxis assays (21). Adapted from Macmillan Publishers Ltd.: Nature Review. Copyright 2014.

As other co-culture systems to be used, we can include heterogeneous culture on Petri dishes, microcontact printing, culture in gels, or bioreactors. Although these techniques are better than traditional Petri dishes, their weaknesses include the lack of ability to be customized and versatile for multiples scenarios, as playing with different gradients, different cell sizes and spatiotemporal control (4).

To overcome these limitations and to find important clues to better understand the process of intercellular communication, in the recent years, attention has been focused on the emerging microfluidic technology (21).

Microfluidic is the science and technology of manipulating and controlling of fluids in channels and chambers at micron-size level, using a microscale devices built with technologies first established by the semiconductor industry and thereafter expanded by the micro-electromechanical systems (MEMS) (21, 26). These microdevices, commonly referred to as miniaturized total analysis systems (μTASs) (27, 28) or lab-on-a-chip (LoC) technology, have been recognized in academic and industrial sectors as a strategic tool for improvement of the life sciences, clinical research and diagnostic (21). Also known as "lego"-devices, the integration on the chip with several outer or inner technologies and methods - the incorporation of pumps, valves, splitters, mixers, analytical capabilities, sensors and transducers*, etc.* - brings benefits for a separate and sustainable research and development (R&D) stage, and for the *revenues* with the later combinations of different parts in a final platform. Thus, using rapid prototyping techniques and several materials as poly-dimethylsiloxane (PDMS), polymethylmethacrylate (PMMA), paper, hydrogels, and thermoplastics, *etc.*, researchers can design multiple customized devices in function of the specific application (4, 21, 29).

In this context, microfluidics offer reduced costs with reduced sample and reagent requirements, and coupled with a capacity for multiplexing and automation, provide rapid analysis and portability, and enhance sensitivity and efficiency (21).

The impact of microfluidics on biomedical research makes it well suited to the cell-cell communication. Microfluidics provide the researcher with precise and dynamic control over a specific environment, including spatial and temporal control over *stimuli* (chemical, physical and mechanical *stimuli*) and cells (single or clusters), and allowing cell signaling trials to be manipulated, characterized and quantified with high-throughput and resolution (4, 8, 21, 29). Furthermore, by simulating the *in vitro* environment and mimicking the *in vivo* natural microphysiology (e.g. tissues-on-a-chip and organ-on-a-chip), microfluidics makes a bridge between *in vitro* and *in vivo* studies (8, 14, 21).

In this context, learning how cell can communicate at a single cell or in special subpopulations of cells by cellular and molecular level using microfluidic platforms will help us to understand better the cell communication pathways, which will have direct implications and impacts in studying circulating tumor cells, immune cell education, drug development and immunotherapy (1, 3, 4, 14, 21). It is worth noting that microfluidic models have not only the potential to help us to characterize novel therapeutic target in immune cell interactions, as well as to help us in testing the efficacy of novel immunotherapies (14).

In this context, immunoengineering is an emerging field and as a consequence of the evolution and integration of different areas - biology, pharmaceutics, biomedicine and biophysics with engineering - seeks to design new approaches to problems in translational immunology. When immunology meets engineering, several areas appear and define their strategies to approach their problem such as the development of nanomaterials in vaccines (e.g., delivering antigen to anatomical and subcellular locations, delivering adjuvants, targeting suppressors of vaccines responses); scaffolds in vaccines; molecular engineering approaches in tolerance (e.g., modeling the education of immune cells); cell surface engineering and systems analysis of immunity; and engineering immune microenvironments.

In this thesis, we will mainly highlight the technology behind the encounter of immunology with microfluidics, especially in the conception and performing of engineering immune microenvironments in platforms, mimicking *in vivo* lymphoid tissue in *in vitro* models of engineering for cell-cell communication studies.

Nowadays, there are two active areas of immune tissue engineering: (i) the *in vivo* lymphoid tissue engineering for therapeutic translation, and (ii) the *in vitro* models that recreate features of microenvironments important for immune cell activation and functioning, for therapeutic use or to study, modulate and screen immunomodulatory effects in human cells (3, 30-32).

As *in vivo* models, several clinical strategies for immune cell activation such as from transplantable tissue-organoid construction to vaccination, by using mice lines, have been developed in order to mount and manipulate human humoral and cellular immune responses (mainly as strategies for antitumor therapy) (3, 33).

For example, Suematsu and Watanable (33) have demonstrated the important role of stromal cells in the formation of normal organized microarchitecture of secondary lymphoid organs, by transplantation of a tissue-engineered, lymphoid tissue–like organoid that had evidenced an organized tissue structure similar to secondary lymphoid organs. This study showed that lymphoid tissues could develop in a mice with only thymic stromal cells, transfected to express lymphotoxin α (LT- α), and activated dendritic cells (DCs) embedded in collagen scaffolds into the renal subcapsular space in mice (33, 34). LT- α, which is important in lymphoid neogenesis was crucial during these studies attracting lymphoid tissue inducer (LTi) cells to construct and organize tissue structure similar to lymph nodes. These artificial lymph nodes were characterized with compartmentalized B-cell and T-cell clusters, high

endothelial venule-like vessels, germinal centers and follicular dendritic cell networks, allowing to analyze cell-cell interactions on secondary lymphoid organs and to induce humoral and cellular immune responses to vaccination (3, 33).

Another therapeutic strategy in oncology is to improve antitumor immunity by mimicking lymph node functions in the tumor itself. This method consists on the releasing of lymphoid chemokines such as CCL21 or CCL19 (both CCR7 ligands), which attract LTi cells and other CCR7-expressing cells, as DCs and naïve T cells, to the tumor, promoting lymphoid neogenesis around the tumor and consequently, to stimulate the *in situ* education of antitumor cytotoxic T cells (3, 35, 36).

However, some studies have demonstrated that CCR7 ligands can perform several roles depending on the complex inflammatory environment, for example they can promote the attraction of different lymphocyte subsets such as T_{reg} cells, inhibition of T cell proliferation or promotion of the death of activated T cells (3, 37). Additionally, some studies evidenced that some aggressive tumors express CCL21 endogenously, at the same physiological levels to those expressed by latent lymph nodes, inducing in this way the immune tolerance by stimulating T cell education in the high immune regulatory tumor microenvironment (for instance, by suppressive macrophage and monocyte subsets, and in cytokine enrichment involved in transforming growth factor-β and IL-10) (3, 38).

Another relevant issue to be recognized for strategies to engineer lymphoid tissues, is the duality of lymphoid stromal functions in promoting adaptive cellular immunity and maintaining peripheral tolerance to self-antigens (3, 37, 39, 40).

In this context and complexity level, a deeper understanding of systematic studies of how dose, location, and microenvironment affect the host immune response to chemokines, cells and matrix is needed, in order to help effectively on the instruct design criteria for future therapies of immuno-engineering (3, 36).

As a complementary alternative, *in vitro* models can also be used to study and screen immuno-modulatory effects in human cells. Clark *et al*. demonstrated that co-cultures of human dermal fibroblasts and keratinocytes in a synthetic three-dimensional (3D) matrix can induce the development of functional T cells with a variable receptor repertoire, from hematopoietic precursor cells. This technique suggests a new therapeutic approach for the new generation of functional T cells *ex vivo* from skin biopsies (41).

Another important approach developed by Randolph *et al.* consisted on the modulation of the initial steps in adaptive immunity *in vitro*, and demonstrated that human peripherial blood mononuclear cells (PBMCs) when co-cultured with human endothelial cells on a 3D matrix, could be quickly differentiated into functional DCs. And in absence of endothelial cells, PBMCs needed specific culture in GM-CSF and IL-4 for 7-10 days to differentiate into DCs (3, 42).

Other example of lymphoid tissue engineering include the recreation of a model the lymph node paracortex, containing T cell zone fibroblastic reticular cells (FRC) inside a macroporous polyurethane scaffold (collagen and matrigel), and with application of slow interstitial fluid flow in order to analyze the expression of CCL21 secretion. This study proved that the 3D environment and the presence of shear stress induced by interstitial flow are important parameters for the T zone fibroblastic reticular cells (TRCs) morphology, organization, and CCL21 secretion (3, 43). As direct application of such *in vitro* immune models, may be suitable for the study and redesign as the therapeutic criteria as referred above; however as transplantable platform for immune responses, it is a still distant reality,

considering our limited understanding about all the complexity of immunity and lymphoid tissues (3, 43).

As previously mentioned, a large number of analysis methods in immuno-engineering have been emerging in recent years, integrating new advancements in smart biomaterials (i.e. nanomaterials and scaffolds in vaccines), tissue engineering, 3D cell culture, microfabrication and microfluidic technology.

In this context, microfluidics represent a relevant compromise between the *in vivo* compartmentalization of microphysiology in *in vitro* platforms allowing precise control of the cellular, biophysical and biochemical stimuli coupling with *on-chip* technologies for detection, separation, characterization and 3D cell propagation, resulting in platforms with a remarkable potential for point-of-care testing, drug screening tests, and fundamental and translational cancer and autoimmune research.

In the scope of this work and considering the objective of the research in this thesis, this chapter will review and integrate microphysiological concepts of the immune system and lymph nodes, evolution and criteria of microfluidic platforms for cell-cell interaction, and direct applications in immuno-enginnering.

1.2. Anatomy and Histology of the Lymphatic and Immune System

The lymphatic system is intrinsically interconnected with immune system, considering that the lymphatic system is a network of vessels, cells and organs, which drain excess fluids to the bloodstream and filter pathogens from the blood. In complementary mode, the immune system is responsible by the destruction or neutralization of pathogens through a complex collection of cells and organs (10, 24, 44-46).

1.2.1. Functions and Structure of Lymphatic System

The immune cells are characterized by high mobility in the human body and use two different circulatory systems to traffic through tissues: the cardiovascular system, which distributes blood, and the lymphatic vascular system, which circulates lymph (10, 24, 44-46).

The cardiovascular system is characterized by unidirectional flow pumping from the heart via active pumping networks (arteries), and back to the heart via passive valve-based systems (veins). The blood virtually accesses every organ and tissue, but is delineated by endothelial cells which are very responsive to inflammatory signals (10, 24, 44-46) .

The lymphatic system parallels the cardiovascular system, once the lymphatic vessels are found in close association to the vascular system, being characterized to drain excess of body fluids and return them to the bloodstream. As general functions, the lymphatic system ensures important roles as the steady-state levels of fluid within the circulatory systems - once lymphatic system absorbs fluid from the interstitial tissues which is called by **lymph**, and it return into the blood. More specifically, the lymphatic system consists in a network of thin walled vessels that play a main part of immune cell trafficking, since the travel of antigen and antigen-presenting cells to secondary lymphoid organs, and the exit of lymphocytes from lymph nodes (10, 24, 44-46).

This system is characterized by unidirectional flow, but there is no pump and lymphatic pressure is very low. The low-pressure flow of lymph can be propelled by skeletal muscle action, changes in thoracic pressure, pulsation of nearby arteries and a series of one-way valves along the lymphatic vessels (10, 24, 44-46).

It is important to realize that in an adult, 20 liters per day of plasma are drained into the interstitial space of the tissues by capillary filtration. This fluid being out of the bloodstream and in the tissue and cells spaces, is called **interstitial fluid**. From these, 17 liters are reabsorbed to the blood directly through the walls of venules. And the remainder 3 liters of interstitial fluid enter the network of primary lymphatic vessels, and is now called lymph. The porous architecture of these vessels allows the passage of fluid and cells to the lymphatic network. Within these vessels, the lymph flows into a series of progressively larger collecting vessels defined as **lymphatic vessels**. Within these vessels, the lymph flows back into the bloodstream via a series of **vessels**, **trunks**, and **ducts** (10, 24, 44-46).

When a foreign antigen attacks the tissues, it is picked up by the lymphatic system and is carried to various organized lymphoid tissues, for example lymph nodes, which trap the invaders. In this context, immune cells use lymphatic system not only as a way to traffic from interstitial spaces back into the circulation, but also to use lymph nodes as key staging organs to develop critical immune response (10, 24, 44-46).

The driving force and guide of immune cells through tissues, blood and lymph are the chemokines. These influential proteins are released by stromal cells, antigen-presenting cells and lymphocytes and can establish gradients that guide for other immune cells, which display a diverse set of receptors for these chemokines, allowing in this way the extremely refined organization of immune responses (10, 24, 44-46).

During the last two decades, lymphatic vascular has gained notoriety through the discovery of lymphangiogenic factors, identification of lymphatic vascular markers (that allow identifying blood and lymphatic vessels), isolation and culture of lymphatic endothelial cells and lymphangiogenesis.

Several recent studies have questioned the importance of the mechanical properties of the stresses imposed by fluid pressure gradients on interstitial flow and during lymph formation, which can be dramatically altered during a inflammation and cancer, defining critic consequences for a variety of cell functions. Recent advances elucidate that pathological changes in these properties often drive tissue remodeling, cell migration, stem cell differentiation, and malignant transformation (10, 24, 44-46). Hydraulic conductivity, as another interstitial mechanical property and defined by the interstitial fluid flow for given pressure gradients, has gained evidence by its importance in matrix remodeling, cell migration and regulation of immune responses through novel in vitro approaches, which allow passage of slow interstitial flow through 3D cell culture by outer control. It is important to note that exchange and formation of interstitial fluid may be determined by structural properties of the capillary wall, transcapillary pressure differences and protein concentrations (10, 24, 44-46).

Recent advances include elucidating that the lymph formation is facilitated by cyclically variable hydraulic pressure gradients between the interstitium and initial lymphatics and by vesicular transport. However, additional studies are yet required to determine the relevance of active transport mechanism in lymph formation (10, 24, 44-46).

Several recent studies have proven that interstitial flow and lymph flow influence immunity and peripheral tolerance. One example of the many and diverse biological effects of interstitial fluid flow is within a tumor itself, the variation of interstitial flow may induce lymphoid-like features to develop

in the stroma, mimicking in this way the lymph node T-cell zone, which is relevant for the recruitment and education of T cells (10, 24, 44-46).

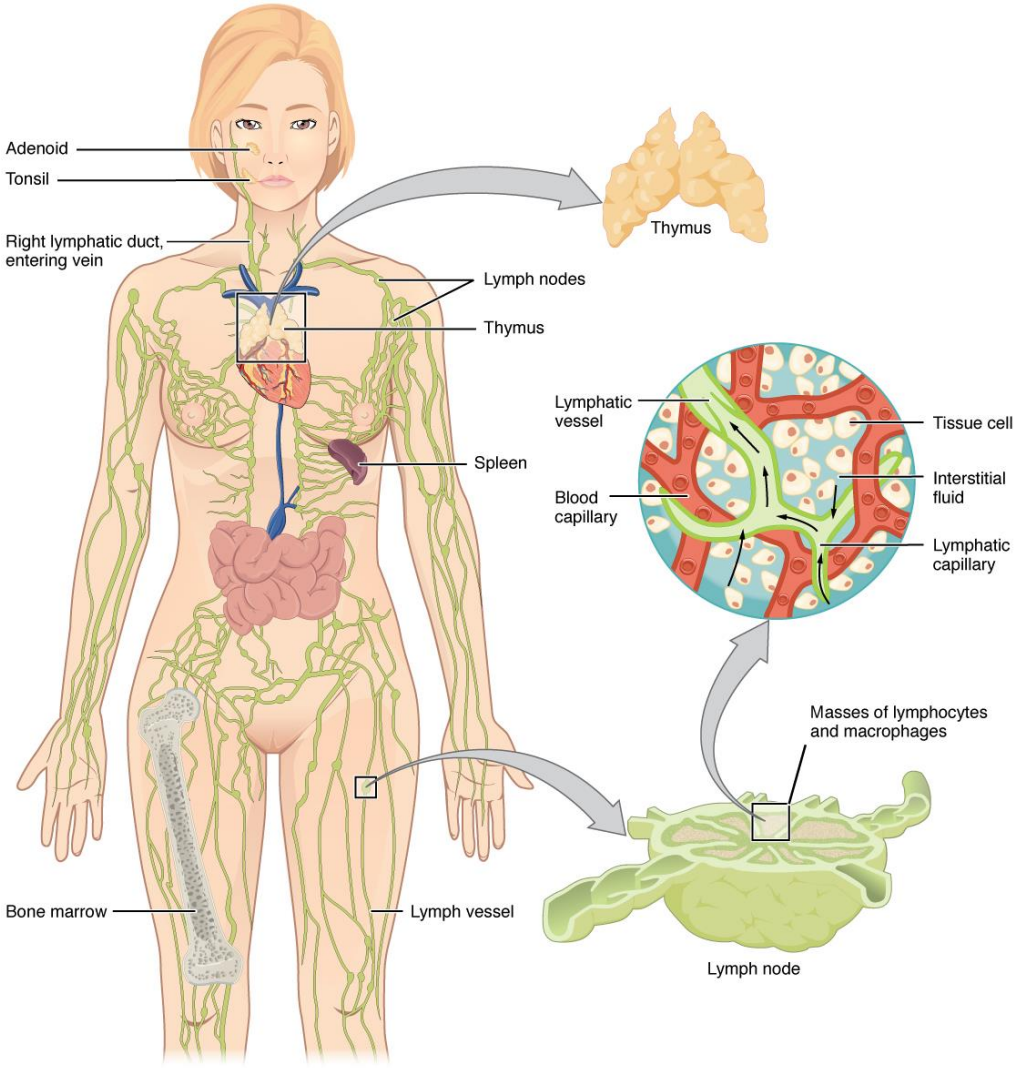

Figure 1.2.1.1 Anatomy of the lymphatic system: lymphoid organs and tissues are interlaced by blood vessels and lymphatic vessels. Adapted from (47).

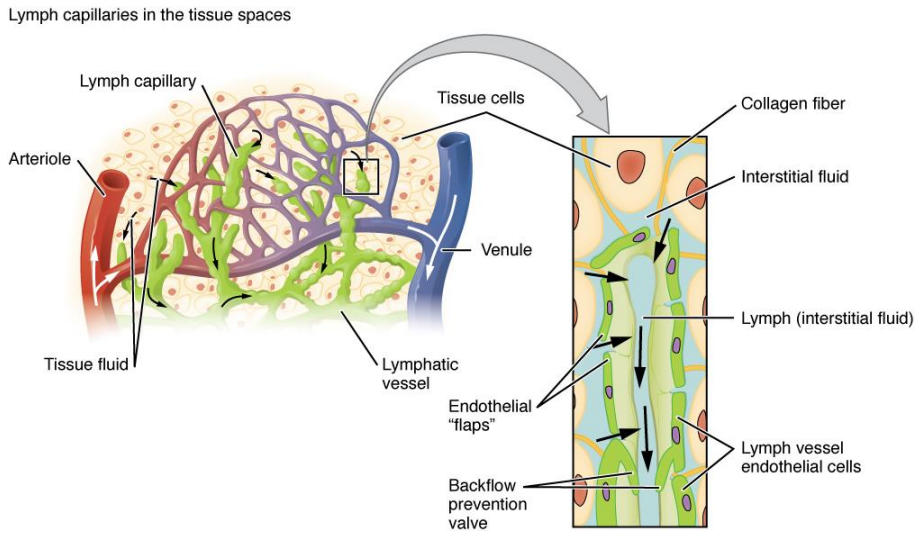

Figure 1.2.1.2 Lymphatic capillaries in more detail and the relationship between blood and lymphatic capillaries in tissue. Adapted from (47).

1.2.2. The Organization of Immune Response

A successful immune response to a pathogen or substances (antigens) results from the coordinated activities of many types of cells, organs, and microenvironments dispersed throughout the body and organized steps in time and space (10, 44, 45).

The vertebrate immune response is composed of two complementary and cooperative processes: **the innate** and **the adaptive immune response**. The innate response is considered as the first line of body defense by using germline-encoded recognition molecules and phagocytic cells, proliferating signals that stimulate adaptive immune response. The innate pathway is faster and less specific than adaptive response, which develops in several days and is highly antigen specific. The specificity of adaptive immunity response is characterized by relying upon surfaces receptors - B cell receptor (BCR) and T cells receptor (TCR) - which are randomly generated during the development of B and T lymphocytes by DNA rearrangements (10, 44, 45).

It is worth nothing that the encounter of a T cell and a dendritic cell is a key event in adaptive immune response, providing the opportunity for antigen recognition, which occurs through TCR interactions with major histocompatibility complex (MHC)-bound peptide antigens that are present at the DC surface. Successful activation of naïve T cells by DCs results in clonal expansion and differentiation into effector population of antigen-reactive cells and a residual population of memory cells for a subsequent secondary response (10, 44, 45).

In this context, the immune response depends on finely arranged interactions among diverse cell types: (i) innate immune cells mount the first line of defense against pathogen; (ii) in response to inflammatory signals, tissue-resident DCs acquire local antigens and migrate to lymph nodes to present MHC-bound peptide antigens to B and T lymphocytes recruited from blood. (iii) The adaptive immune response is then initiated by the cognate physical interactions between naïve lymphocytes and antigen-presenting cells (APCs). (iv) Afterwards, a coordinated adaptive response with primed/activated effector and memory lymphocytes, which prevent future infections, enter the lymph

and blood and are recruited to inflammation sites where new T cell : target cell interactions take place (**Figure 1.2.2.1**).

Primary lymphoid organs regulate the development of immune cells from immature precursors, including the bone marrow and the thymus. **Secondary lymphoid organs** are responsible to coordinate the encounter of antigen with antigen-specific lymphocytes and their development into effector and memory cells, including the spleen, lymph node, and specialized sites in the gut and other mucosal tissues. Blood vessels and lymphatic systems establish the connection with these organs, uniting them into a functional whole (44, 45) (**Figure 1.2.1.1**).

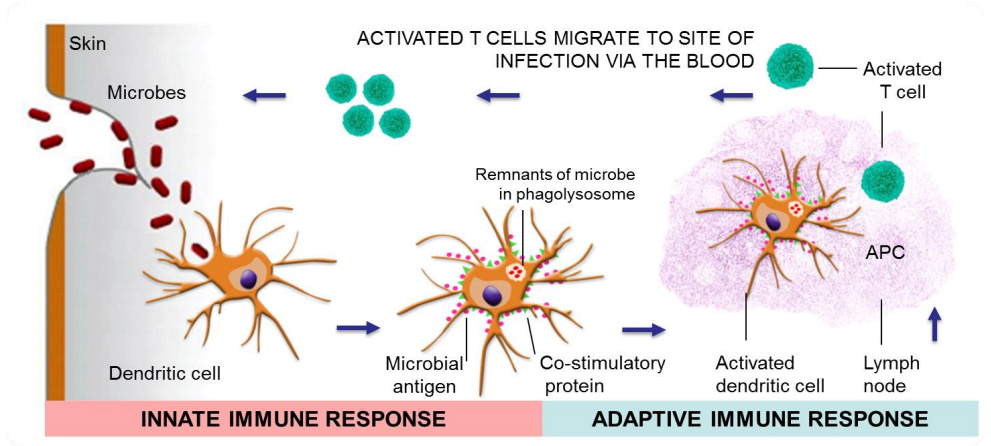

Figure 1.2.2.1 Features of the lymph node, host response to pathogen infection: Schematic illustration of the development of the immune responses. Dendritic cells (DCs) move from periphery into lymph node; T cell are pushed through lymph node being forced to interact with DCs along the way. Image from our work (48).

All specialized mature blood cells, including red blood cells, granulocytes, macrophages, dendritic cells and lymphocytes have origin from a single cell type, the **hematopoietic stem cell** (HSC), through the process of **hematopoiesis** (45). The development of stem cells into mature immune cells occurs in two primary lymphoid organs: in bone marrow, where HSCs are located and can replenish all blood cell types (i.e., are multipotent) and self-renew; and the thymus, where T cells conclude their maturation (45).

In the scope of this thesis, we will begin by describing the cell types of immune system, the secondary lymphoid organs and the specialized immune microenvironment involved where the immune response is initiated.

1.2.2.1. Cells of the Immune System

As referred above, **hematopoiesis** is the process by which HSCs develop into matured blood cells, losing its self-renewal capacity and giving rise to both myeloid and lymphoid lineages of blood cells. It can generate a **common myeloid-erythroid progenitor** (CMP), including all red blood cells (the erythroid lineage), granulocytes, monocytes and macrophages (the myeloid lineage). Or it can generate a **common lymphoid progenitor** (CLP), including T lymphocytes, B lymphocytes, and natural killer (NK) cells. Myeloid cells and NK cells are involved in the innate immune response, being the first cell line to respond to infection. Lymphocytes are participants of the adaptive immune response, generating an effector and memory refined antigen immune response. Dendritic cells are generated by

both myeloid and lymphoid lineages, as antigen-presenting cells (APC) with variable features and functions involved in initiating adaptive immune response (**Figure 1.2.2.1.1**). **Table 1.2.2.1.1** represents the distribution of concentration and percentage of immune cells in blood (45).

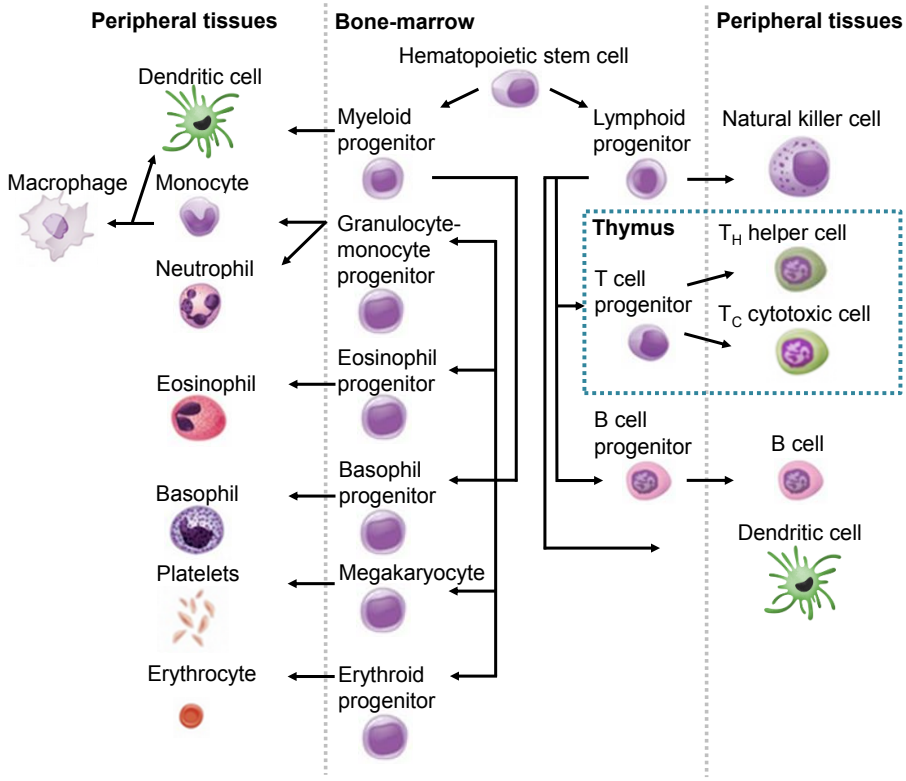

Figure 1.2.2.1.1 Hematopoiesis. Hematopoietic stem cells can generate in myeloid and lymphoid progenitor. Adapted from (47).

Table 1.2.2.1.1 Distribution of concentration and percentage of cells in human blood. Adapted from (45).

Concentration and percentage of cells in human blood			
Cell Type	Cells/µL	Cells (%)	Leukocytes (%)
	$5.3x10^6$	100	
Red blood cells	$5.0x10^6$	95.0	
Platelets	$2.5x10^5$	4.8	
Leukocytes	$7.3x10^3$	0.2	100
Neutrophil	$(3.7\text{-}5.1)x10^3$	(0.070-0.097)	(50.7-70.0)
Lymphocyte	$(1.5\text{-}3.0)x10^3$	(0.028-0.057)	(20.5-41.1)
Monocyte	$(1\text{-}4.4)x10^2$	(0.002-0.008)	(1.4-6.0)
Eosinophil	$(1\text{-}2.2)x10^2$	(0.002-0.004)	(1.4-3.0)
Basophil	$<1.3x10^2$	<0.002	<1.0

In the scope of this thesis in order to study the dynamic cell-cell interaction of DCs as APC for T cell activation involved in adaptive immune response, we will approach only these two principal cell players of adaptive response: myeloid -derived dendritic cells, and lymphoid-derived T cells.

Dendritic cells

Dendritic cells play an important role for the initiation on immune response, and are characterized with long membranous protuberances that extend and retract dynamically, changing their surface area accessible for sampling the environment and browsing lymphocytes (**Figure 1.2.2.1.2**) (10, 45).

These cells are emerged from both the myeloid and lymphoid lineages, and are characterized as a diverse cell population with distinct dynamic and flexible functions, such as sentinels when the antigen is captured in the tissue peripheries, or as antigen presentation inside the lymph nodes. As referred above, the innate immune response is initiated when tissue-resident immature dendritic cells phagocyte the pathogens in the infected tissue, monitoring the body in space and time by signs of invasion of foreign pathogens (10, 45).

During this maturation process of DCs, their antigen-capturing phenotype is changed to one which is specialized for presentation of antigen to T cells, and consequently their phagocyte capacity is lost and their ability to present antigen and the expression of co-stimulatory molecules for the activation of naïve T cells is increased significantly. After their maturation, DCs leave the peripheral tissue, entering the blood or lymphatic circulation, and migrate to lymph nodes where they interact with recirculating naïve T cells, beginning the adaptive immune response (10, 45). Several studies have indicated that the Ag-DC complex has a relatively short-life time (from a couple of seconds to hours), presumably once they enter the LN (paracortex), they will remain there until they die. DCs are characterized to sample a large volume using their dendrites, which can extend up to twice their body length (13, 49).

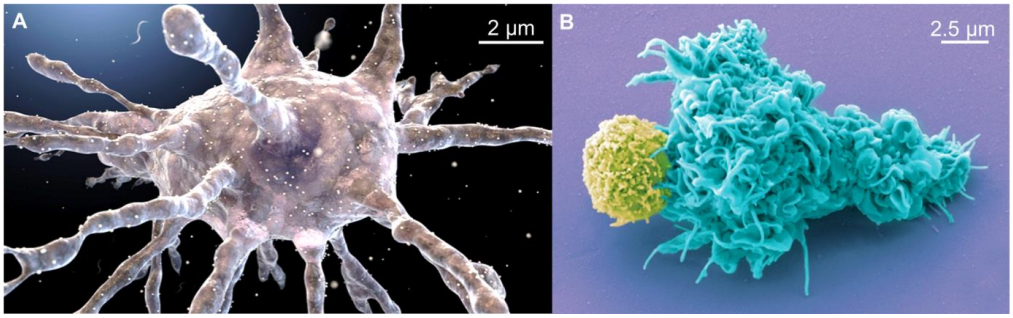

Figure 1.2.2.1.2 Example of dendritic cell in 3D: A) Adapted with permission from (50); B) Dendritic cell (blue) and lymphocyte (yellow), SEM. Adapted from (45).

T Lymphocytes

Lymphocytes are the central players in the adaptive immune response, representing around (20 - 40) % of circulating white blood cells and 99% of cells in the lymph (**Figure 1.2.2.1.2.B**) (10, 44).

Considering their phenotypic and functional differences, lymphocytes can be divided in three subgroups of populations: B lymphocytes (or B cells), T lymphocytes (or T cells) and natural killer (NK) cells. It is worth nothing that each lymphocyte expresses a unique antigen-binding specific

receptor on its surface – the T cell receptor (TCR) or the B cell receptor (BCR). And even though the populations of T cells and B cells express a variable myriad of antigen receptors (more than a billion!), all receptors on an individual cell's surface are characterized by similar structures and specificities for antigens (44). Though, unlike of membrane-bound antibodies on B cells that identify immediately soluble antigen, T cells receptors are a demanding process that only recognizes "digested" peptides of antigen coupled to cell membrane proteins – major histocompatibility complex (MHC) - and requires time from the time of infection to the mounting of a protective response (10, 44, 45).

TCR

The structure of the T cell receptor complex is a transmembrane heterodimer made up of two covalently disulfide-linked polypeptide chains. The vast majority of T lymphocyte expresses predominant antigen-binding chains, alpha (α) and beta (β), on their surfaces. Both transmembrane peptides display a variable (antigen recognition) domain and a constant external domain connected by a disulfide bond. CD3 complex is always associated with TCR expression once presented antigen is encountered, required for signal transduction (10, 44, 45). Recent studies have estimated αβ TCR repertoire diversity varying from more than $2x10^7$ in humans to approximately $2x10^6$ in mice (13).

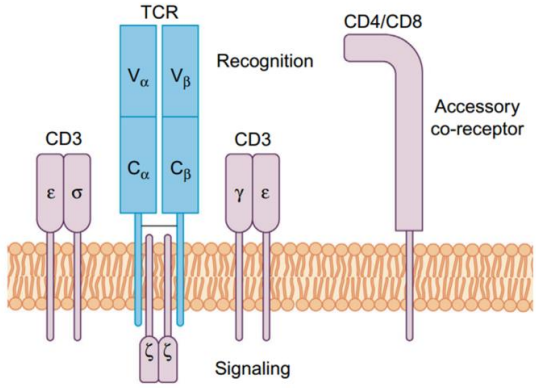

Figure 1.2.2.1.3 Structure of the TCR complex. Adapted from (44).

Antigen recognition by T cells: requirement of major histocompatibility molecules

MHC molecules are not only involved with interactions of lymphocytes, but also play a role on the compatibility of donors for organ transplant and on the susceptibility to an autoimmune disease via cross-reacting immunization (10, 44, 45).

MHC molecules are diverse glycoproteins of the host's own phenotype that are continually synthesized and degraded, being exposed to browsing T cells. Each MHC molecule displays a molecular fraction of a protein called epitope. Currently, MHC family can be segmented in two subgroups: class I MHC and class II MHC molecules.

Class I MHC molecules are expressed by all nucleated cells of vertebrate species, and have β2 subunits. Class II MHC molecules are produced by "professional" antigen-presenting cells (APCs; B cells, dendritic cells (DCs), and macrophages), and have β1 and β2 subunits (44).

T lymphocytes can be segmented into two major cell groups: T Helper (T_H) cells which are characterized with CD4 co-receptors membrane glycoproteins on their surfaces, and T cytotoxic (T_C) cells with CD8 co-receptors membrane glycoproteins on their surfaces.

In this context, and since different lymphocytes express different TCR co-receptors, MHC molecules chaperone for which type of lymphocytes can bind to the specified antigen with high affinity: when T cell displays CD4 co-receptors, generally works as T_H cells and recognizes antigen complex with β1 and β2 subunits of Class II MHC; and thus when T cell displays CD8, works as T_C cells and recognizes antigen complex with β2 subunits of Class I MHC. The proportion of $CD4^+$ or $CD8^+$ cells in human peripheral and normal mouse is approximately 2:1 (10, 44, 45).

$CD4^+$ T cells

When naïve $CD4^+$ T cells browse the surfaces of antigen presenting cells with their co-receptors, and if they match the complex of Class II MHC, they become activated and start the proliferation and differentiation into one of a variety of effector T cell subsets.

The effector T_H cells can be segmented in four subpopulations: (i) **T helper type 1 (T_H1) cells**, which regulate the immune response to intracellular pathogens; (ii) **T helper type 2 (T_H2) cells**, which regulate the response to many extracellular pathogens; (iii) T helper type 17 **(T_H17) cells,** which secret IL-17 and regulate cell-mediated immunity and the immune response against fungi; (iv) **regulatory T (T_{REG}) cells**, which has the unique capacity to inhibit an immune response, for instance playing a role in limiting the normal T cell response to a pathogen (10, 44, 45).

$CD8^+$ T cells

When naïve $CD8^+$ T cells browse the surfaces of APC with their co-receptors, and if they match the complex Class I MHC, they start their activation, proliferation and differentiation into an effector cell called a **cytotoxic T lymphocytes (CTL)**. The CTL regulate a vital function in monitoring the cells of the body and removing any cells which present foreign antigen complex of Class I MHC (e.g., virus-infected cells, tumor cells, or cells of a tissue implant). However, for their optimal proliferation and differentiation, naïve $CD8^+$ T cells are dependent from mature $CD4^+$ T cells (10, 44, 45).

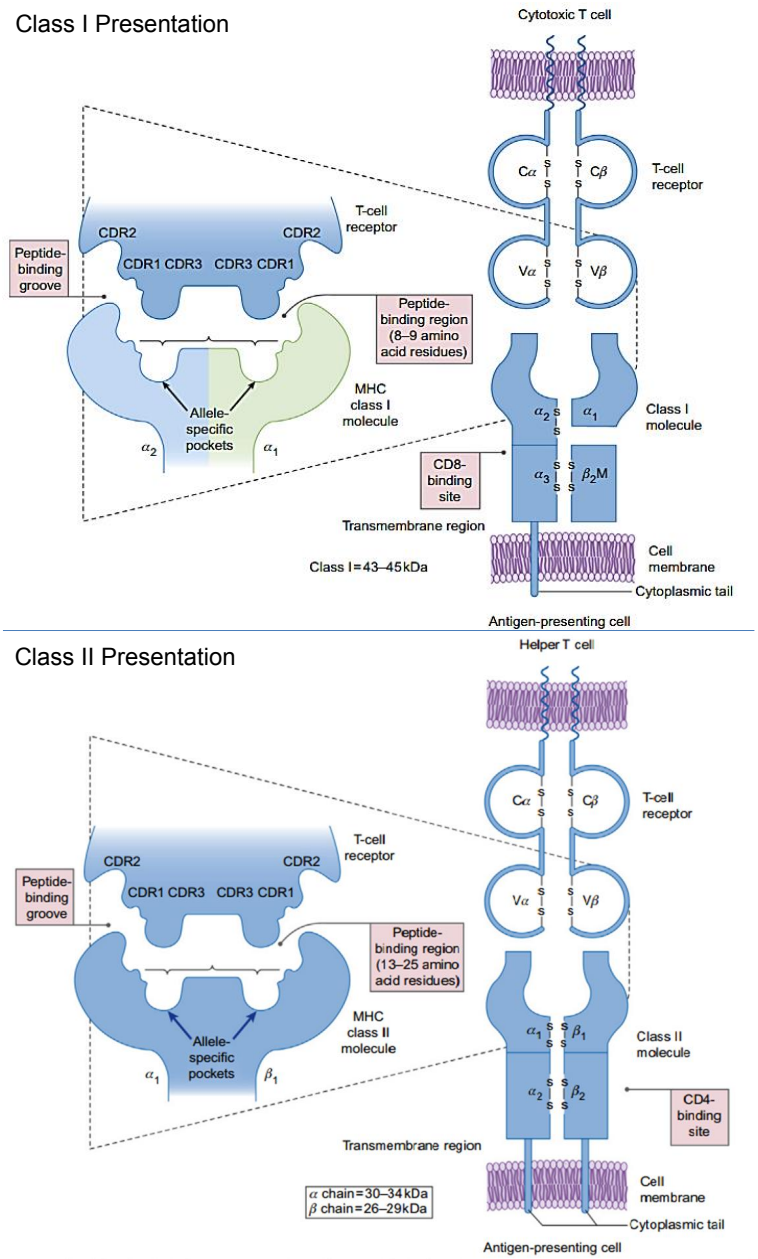

Figure 1.2.2.1.4 Antigen recognition by T cells: Class I MHC and Class II MHC presentation to CD8$^+$ and CD4$^+$ T cell. (a) The MHC class I transmembrane molecule is connected with the invariant β2-microglobulin β2M, promoting the structure to the extracellular domain for presentation of processed antigen to CTLs. The molecular rearrangement consists on short peptide fragments (i.e., 8-10 amino acids in length) non-covalently connected to the domains on the class I molecule and complementarity determining regions (CDRs) on the TCR, and the interactions with the TCR are stabilized by CD8 recognition. (b) The processed antigens for presentation to CD4+T cells via MHC class II-regulated mechanisms is established through the processed antigenic fragments (13-25 amino acids in length) cooperate with domains on the class II molecule within the peptide-binding groove, promoting presentation to CD4+ T-helper cells. The interactions are stabilized by CD4 recognition of conserved regions on the class II molecule. Adapted from (44).

1.2.2.2. Secondary Lymphoid Organs: where the immune response is initiated

Lymphocytes and myeloid cells develop their maturity in the primary lymphoid organs: T lymphocytes in the thymus, and B cells, dendritic cells, monocytes and granulocytes in the bone marrow. The immune responses and tolerance is further generated when naïve lymphocytes encounter antigen in the micro-environments of secondary lymphoid organs (SLO) (24, 34, 44-46, 51).

SLO are specialized sites where lymphocytes encounter antigen, become activated, and undergo clonal expansion and differentiation into effector cells. Anatomically they include the lymph nodes (LNs), spleen, Peyer's patches and mucosal tissues- the nasal associated lymphoid tissue, adenoids, and tonsils (34). A discrete amount of reduced structures defined cellular accumulations include the bronchus associated lymphoid tissue, cryptopatches, and isolated lymphoid follicles (34). Lymph nodes and the spleen are characterized by fibrous capsule, compartmentalizing thus them from the rest of the body. Although SLO vary in their location and level of organization, they have many key features in common: (i) the presence of lymphoid follicles with specific compartmentalization into T cell-rich areas and B cell-rich areas; (ii) an internal structure constituted by reticular fibers associated with fixed macrophages; (iii) specialized post-capillary vessels named as high endothelial venules (HEV), as specialized sites (with small veins that join capillaries to larger veins, and which are lined by endothelial cells) of a large-scale migration of lymphocyte entry from the blood; with the exception of the spleen; (iv) and germinal centers, as sites of rapidly dividing B lymphocytes and plasma cells, except the spleen (24, 34, 44-46, 51).

1.2.2.3. Architecture of Lymph Node

In humans and primates, lymph nodes (LN) vary from a few millimeters to a few centimeters (13). Lymph nodes are the most specialized SLO and are found throughout the body, concentrating antigens from a network of lymphatic vessels and providing ideal microenvironments for interactions between antigen and lymphocytes in order to organize cellular and humoral immune responses (51-54). Soluble antigens with size between 20 and 50 nm or molecular weights ~70 kDa diffusively pass along the lymphatic vessels, while antigens or pathogens with larger dimensions or size are processed by phagocytosis and convectively transported to these LNs by APC such as DCs (13, 24, 52, 55).

As mentioned above, APCs constantly monitor tissue and blood for inflammatory signals, and when upon detection, they phagocyte and switch their expression of homing receptors, allowing antigen-experienced APCs to migrate to LNs. Once inside the LNs, APCs with processed antigens interact with naïve T and B cells for generation of effector cells. Upon activation and expansion, T cells and B cells exit the LNs and move to the periphery to destroy the pathogens (13, 51-54).

Anatomically, LNs are surrounded by a collagen-rich fibrous capsule with bean-shaped and divided into three concentric regions: (i) the cortex, (ii) the paracortex and (iii) the medulla, each of which supports a distinct microenvironment domain (13, 51, 52).

Beneath the lymph node capsule is the subcapsular sinus (SCS), in which *afferent lymphatic vessels* drain lymph, antigens in soluble form or phagocytosed by APCs, lymphocytes from upstream lymphatic vessels. This fluid is completely dispersed throughout the SCS (as a region with macrophage line to capture incoming antigen or particles) and by supportive reticular network (51, 52).

The immune-architecture of this reticular network of the LN is composed of reticular fibers (RFs), fibrous extracellular matrix (ECM) bundles, and fibroblastic reticular cells (FRCs). It is worth noting that FRCs in the LN are sheathed by thin parts of ECM, allowing the continuous contact with immune cells (in contrast with connective tissues, where fibroblasts are completely embedded in the ECM) (52, 56-59). In recent studies, T cells have been observed crawling along the surface of the FRC network (13, 49, 51, 60). This typical FRC network configuration promotes in this manner the optimal mechanical strength to the tissue and serves as a track for T cell movement (13). However, how FRCs project this network and remodel it in response to lymphocyte activation have not yet been elucidated (59). Shaw et al. have discovered the existence of "paracortical cord" or "conduit" as a part of FRC/RN network and function, ensuring that small soluble antigens can efficiently penetrate deeply into LNs for immune synchronism response (13, 51, 52, 56-59).

Structurally, the cortex as outermost layer contains lymphocytes (mostly B cells), macrophages, and follicular dendritic cells reorganized in follicles. Under the cortex the paracortex is situated, populated largely by T lymphocytes and also DCs. And as the innermost layer, the medulla is the place where lymphocytes exit the lymph node by the *efferent lymphatics vessels* and is sparsely populated with lymphoid lineage cells, including plasma actively secreting antibody molecules.

B cells and specialized follicular dendritic cells (FDCs) form a surrounding cortex named the "B cell zone". DCs and T cells compose an interior region of LNs, named by paracortex ("T cell zone") (51-54). High endothelial venules (HEVs) are rearranged in regions between the B and T cell zones, called cortical ridges. HEVs are specialized portals that allow continuous exchange of lymphocytes with blood, as a result of the adhesion molecules and chemokines expression at their luminal surface (51).

T cells expressing CCR7 are attracted to paracortex by CCL19 and CCL21 chemokines, while B cells expressing CXCR5 are attracted to the follicles of the cortex by CXCL13 (52-54). But fascinatingly, this balance is completely inverted during the generation of adaptive immunity: T cells upregulate CXCR5 receptors for CXCL13 chemokines, while B cells upregulate the expression of CCR7 receptors for CCL19 and CCL21 (13, 52-54, 59).

This purpose increase and promote the level of interactions between APCs, T cells, and B cells at the interface of the T and B cell zones, generating effectively effector cells and secreted antibodies specifically for a particular antigen. Upon activation and expansion, T cells and B cells are collected to the medulla efferent lymphatic vessels, leaving the LN (13, 52-54). Table 2 summarizes the key cells and structures of the LN (52).

In this context, it makes sense to use LNs as a key platform for vaccines and immunotherapies in order to generate antigen-specific responses to kill or immobilize pathogens and diseased tissue (3, 13, 52-54).

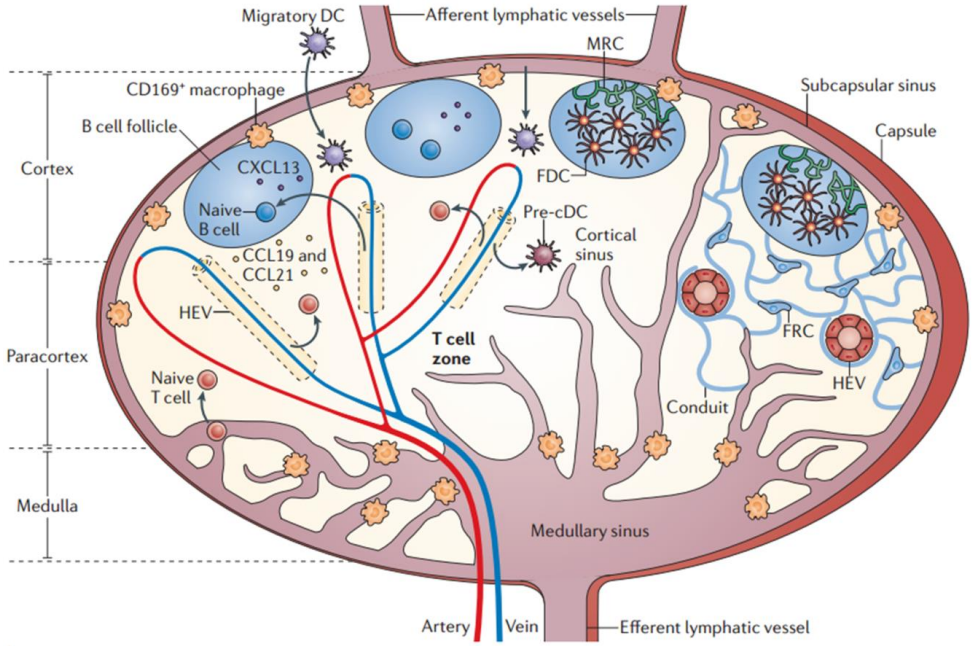

Figure 1.2.2.3.1 Structure of a lymph node (24). Adapted from Macmillan Publishers Ltd.: Nature Reviews Immunology (24). Copyright 2012.

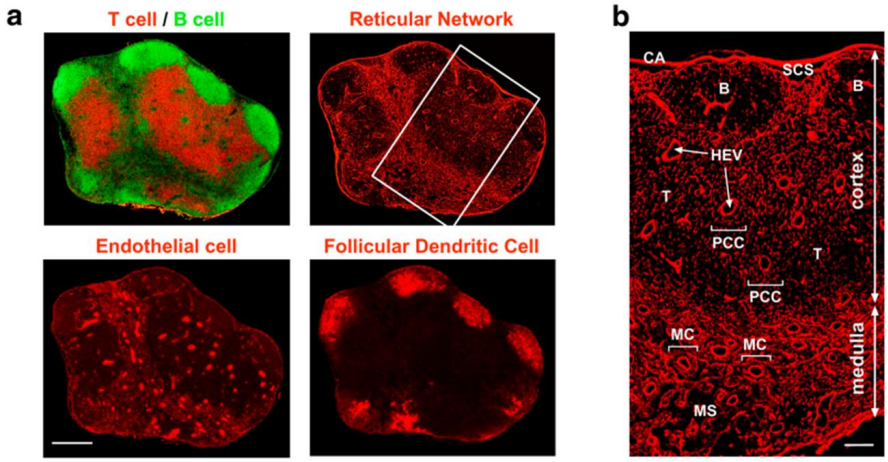

Figure 1.2.2.3.2 Immunoarchitecture of a mouse LN (59) a) The images shown are composites of multiple high-magnification images at distinct positions of an LN assembled: T cells/ B cells; reticular fibroblasts; endothelial cells; and follicular dendritic cells. Scale bar, 400 µm. b) Higher magnification detailed view of RW (white panel) evidences subreticular structures or compartments: B, B zone [follicle]; CA, capsule; HEV, high endothelial venule; MC, medullary cord; MS, medullary sinus; PCC, paracortical cord; SCS, subcapsular sinus; T, T zone. Scale bar, 100 µm. Adapted from Katakai T. et al., 2004. Originally published in *The Journal of Experimental Medicine* doi: 10.1084/jem.20040254. Copyright 2004.

Table 1.2.2.3.1 Cells and structures of Lymph Nodes. Adapted from Andorko, J.I., Hess, K.L. & Jewell, C.M. AAPS J (2015) 17: 323. https://doi.org/10.1208/s12248-014-9708-2 (52). Copyright 2015.

Cell or tissue	Acronym	Key function
Profession antigen presenting cell	APC	Cells exhibiting a primary function of processing and presenting antigen. Key populations include DCs, B cells, and macrophages
Dendritic cell	DC	APCs surveying peripheral tissue for antigen. DCs take up antigen, migrate to LNs, then present antigen to T and B cells to generate antigen-specific immunity.
T lymphocyte	T cell	Cells involved in direct cell killing of infected host cells ($CD8^+$ cytotoxic T cell population) and helper functions that support antibody production ($CD4^+$ helper T cells).
B lymphocyte	B cell	Cells that differentiate to plasma cells that are able to secrete antibody molecules that bind antigens. Binding leads to neutralization or destruction of these targets.
Fibroblastic reticular cell	FRC	Stromal cells that support trafficking of soluble signals and antigen throughout LNs. These cells also organize LN structure by secreting extracellular matrix components.
Follicular dendritic cell	FDC	Specialized dendritic cells able to capture and present antigen to B cells in GCs to promote high-affinity antibodies.
Capsule		Dense layer of connective tissue that surrounds the internal structure of LNs.
Afferent lymphatics		Entry of antigen and immune cells from lymphatics.
Efferent lymphatics		Exit of immune cells from LNs to lymphatics.
Subcapsular sinus	SCS	Drains and distributes lymph throughout LNs.
Medulla		Drains activated lymphocytes in LNs to efferent lymphatics for return to tissue and blood.
High endothelial venule	HEV	Portal allowing exchange of lymphocytes with blood.
T lymphocyte zone (paracortex)		Interior domain rich in T cells and DCs.
B lymphocyte zone (cortex)		Follicular region located at the peripheries of the paracortex that is rich in B cells and FDCs.
Germinal center	GC	Structures that form to co-mingle specialized DCs, helper T cells, and B cells during induction of high-affinity antibodies.

1.2.3. The Immune Response in Space and Time

There are many challenges to be assimilated and understood in order to recreate *in vitro* the T cell-DC interaction as close as possible to reality and with same level of complexity in LNs. In this context, tremendous efforts and studies have been developed to analyze the detailed structure of the LN, and how the environment and cell-cell interactions can affect the immune cell response. Until recently, LNs have been considered, in a large part, as a “black box” by the role in initiating and regulating immunity (11-13, 49, 61).

During the last years, numerous *in vivo* and *in vitro* studies have been developed to describe the molecules and responses involved in T cell-DC interactions. However, a comprehensive understanding of the lymph node immune physiology and dynamics considering physical parameters (i.e. influence of shear stress, the duration and stability of the interaction, the magnitude of force sustained at the T cell–APC interface, the relative motions between the two plasma membranes at the T cell–DC interface, the number of sequential T cell : DC interactions, recirculation requirements) underlying molecular mechanisms to achieve priming, activation and proliferation is still lacking (3, 11, 24, 62).

Conventional techniques involved in the study of cell interaction dynamics and their behaviour inside lymph nodes, such as dissection, confocal microscopy and intravital multiphoton microscopy, have been used in the analysis of LNs in mice, rat, sheep and humans (10, 11, 13).

During the last 15 years, significant advances have been achieved with two-photon microscopy (2PM), that has allowed to bring a ray of light into this "black box", being used extensively for the quantitative analysis of cell motility and behavior in LN in vivo studies (11-13, 49).

For instance, Miller at el. has studied in mouse LNs using 2PM, the specific T cell motility patterns in the absence of infection. Cells are characterized to move in straight lines, on average for several minutes at a time, and to cross a *mean free path* of 20-30 μm. The analysis in 3D measurements for CD4 and CD8 T cell speeds in vivo are approximately in agreement with the initial 2D measurements (since motion in z plane is not considered), resulting values of ~ 9-12 μm/min for CD4 T cells and CD8 T cells (11-13, 49).

In this sequence, several models of the T cell priming dynamics in LN have been proposed based on results obtained by 2PM imaging. **Figure 1.2.3.1** presents a consensual overview of current thought about the activity of T cell priming by Ag-DCs in the T cell zone of a LN during an immune response. Summarizing, we can identify that CD4+ T cells and CD8+ T cells priming behaviors could be aggregated into four distinct stages.

In response to inflammation, T cell zones of LNs serve as meeting grounds for DCs and T cells. In the stage 1, DCs enter through afferent lymphatic vessels while T cells enter through HEVs, and motile T cells exhibit *short-term persistence* and maintain a longer-term random walk for scanning DCs for cognate antigen (*repertoire scanning*), characterizing with free path lengths, speed distributions and motility coefficients (T cells velocity ~9 μm/min). It is important realized that the browsing of T cells on DCs, and posterior specific binding of the TCR to pMHC sets, is also supported by a LN environment which contains a dense FRC network and a complex cytokine and chemokine signaling.

If the cognate antigen is located, T cells process an intracellular signaling cascade through a multiple-phase activation process to the stage 2, decreasing significantly the T cell speed with transient interactions and increasing turning behavior (time (1-3)h; T cells velocity ~5 μm/min; motility coefficient ~10 μm^2/min), and posteriorly to the stage 3, with more prolonged and stable contacts with DC along time including T cell clusters and swarms (time (3-24)h; T cells velocity ~3 μm/min; motility coefficient ~5 μm^2/min), as defined by 2PM imaging (11, 63).

The stage 4 is characterized by a resumption of motility and brief interaction with DCs that is combined with periods of cell arrest and cytokines (time (>24)h; T cells velocity ~9 μm/min). After several rounds of proliferation, differentiated T cells are collected and enter to the circulation via efferent lymphatic vessels, leaving the LN and migrating to the site of infection. More details of other models for the initial activation in the lymph node can be found in (11, 63-69).

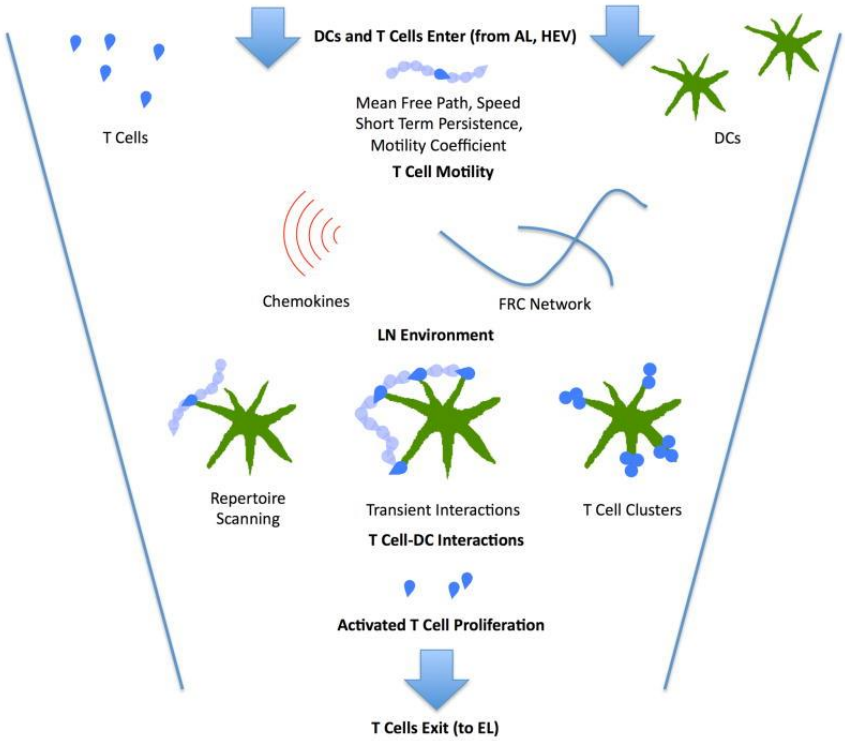

Figure 1.2.3.1 Overview of principal dynamics leading to T cell priming by Ag-DCs in the T cell zone of a LN during an immune response. From (13) reprinted from Elsevier.

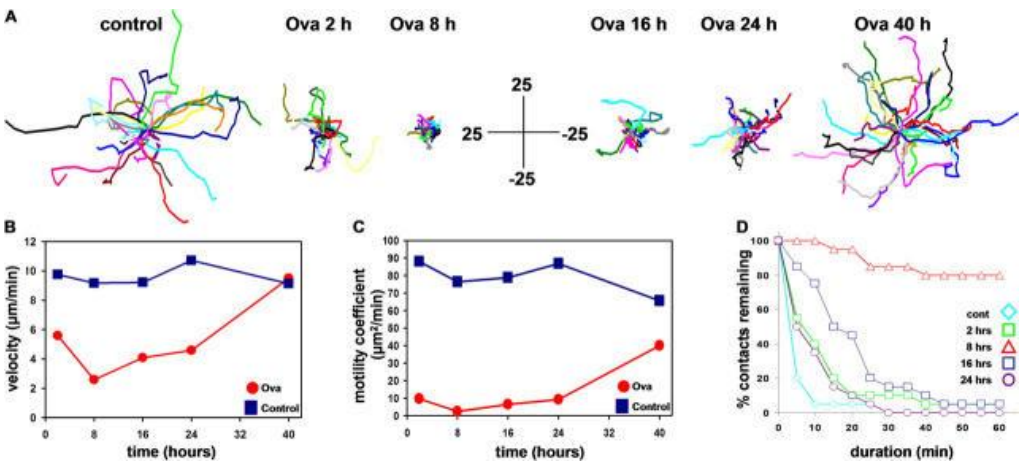

Figure 1.2.3.2 Detailed example of a model of T cell priming dynamics in LN that have been proposed based on 2PM imaging - Miller et al. proposed a model whereby CD4+ T cells pass through five sequential stages during initial activation in the lymph node (11): Stage I: *Stochastic Scanning*; Stage II: *Serial Interactions;* Stage III: *Dynamic Clusters*; Stage IV: *T Cell Swarms*; Stage V: *Proliferation.* **A)** Tracks of individual T cells (different colors, normalized to their starting coordinates) evidencing representative motility of cells in control experiments (without peptide antigen, OVA) and at various times as indicated in OVA-challenged mice. **B)** Evolution of average instantaneous velocities of T cells in function of time: in OVA-immunized mice (red) and control mice (blue). **C)** Evolution of correspondent measurements of motility coefficients in function of time, derived from

plots of mean displacement against square root of time. **D)** T cell-DC interactions in OVA-immunized after adoptive transfer and control mice at various times: cumulative plots showing the percentage of T cells that remained in contact for any given interval of time (11). Adapted from Miller M. et al., 2004. Originally published in *The Journal of Experimental Medicine* DOI: 10.1084/jem.20041236. Copyright 2004.

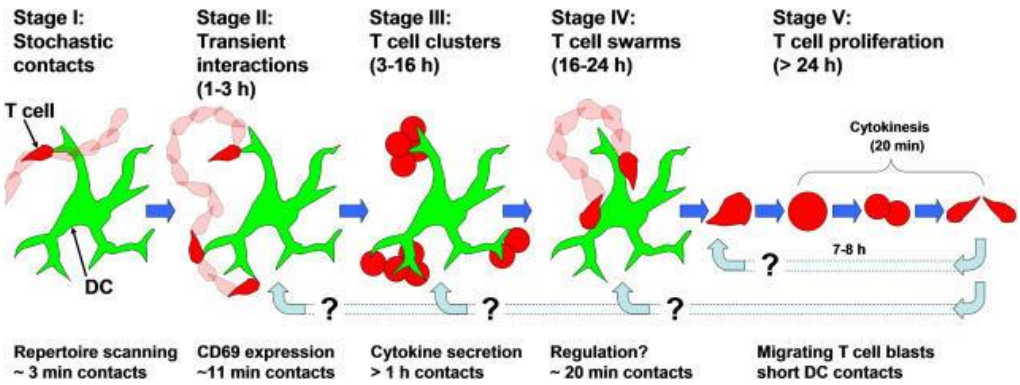

Figure 1.2.3.3 Overview proposed by Miller et al. about the principal sequences stages of antigen recognition and CD4+ T cell activation (11). Adapted from Miller M. et al., 2004. Originally published in *The Journal of Experimental Medicine* DOI: 10.1084/jem.20041236. Copyright 2004.

1.2.3.1. The immunological synapse

The immunological synapse (IS) describes the molecular interaction underlying activation and regulation of the immune response and occurs in a nanoscale gap between the T cell:APC interaction (70).

In recent years, with new technologies approaches, a lot of effort has been applied to visualize the recruitment and activation of signaling molecules *in vivo* and *in vitro* within individual interface between the T cell and the APC. Although some progresses associated with the molecular steps involved in T cell signaling and activation have been defined, it has remained less clear how a T cell can scan a large number of other cells, find one with the appropriate antigen and carry out a complex activation process during hours. It is also unknown how antigen recognition, adhesion and co-stimulation receptors can be orchestrated simultaneously during the immunological synapse (70-72).

Essentially, two main approaches have been dominating the efforts for molecular analysis of T cell-APC pairs: (i) as a top down approach using immunofluorescence; and, (ii) as a bottom up approach by applying purified molecules to substrates and recombine them with the method based on fluid supported lipid bilayers (SLB), where the purified molecules are combined in a laterally mobile form, recreating the organization of the immune synapse formed with living T cells (70, 73, 74).

In 1998, Kupfer and co-workers visualized and identified the canonical organization of the immune synapses through “optical sectioning“ of T cell:APC in 3D (74) (**Figure 1.2.3.1.1**).

This landmark study clarified that key molecules such as the TCR and the adhesion integrin leukocytes function-associated antigen 1 (LFA1) were not only capped at the interface, but also organized in distinct areas within the immune synapse (74). Essentially, the canonical organization of the immune synapse consists in a bull’s eye structure with the main TCR-MHC interaction cluster

surrounded by a ring of LFA-1-ICAM-1 adhesion, and a distal ring which includes the transmembrane tyrosine phosphate CD45 (70).

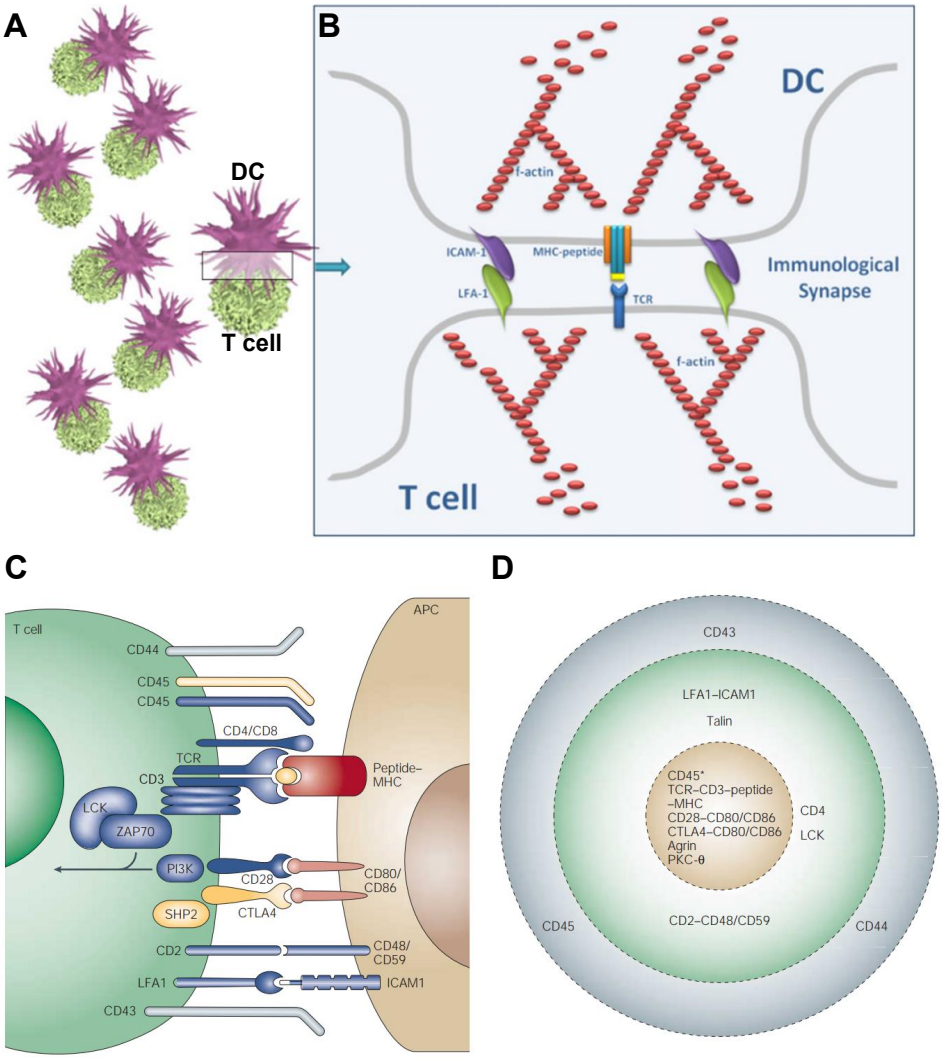

Figure 1.2.3.1.1 Overview of a immunological synapse. A) DC and T cell pairs, involved in an immune synapse. B) A profile view of DC and T cell immunological synapse formation, characterized by MHC:TRC engagement, recruitment of adhesion molecules (LFA-1, ICAM) and structural assembly of the cell membrane via the polymerization of f-actin. (A and B, from (75) reprinted from Elsevier). C) A profile showing the model immunological synapse of Kupfer'a SMAC. In this illustration it is possible to identify a selection of the key ligand pairs and signaling molecules that are involved in T cell recognition (the arrow indicates converging signals that promote the T cell activation). In this illustration the stimulatory peptide-MHC molecule is represented in red, activating/co-stimulatory molecules in blue, inhibitory molecules in yellow, and molecules without contribution to signaling in grey. D) Elevated and front view of model for synapse focusing on interface with the characteristic "bulls-eye" zone pattern, including the central region of the supra-molecular activation complex (cSMAC, yellow), the peripheral ring surrounding the cSMAC (pSMAC; green) and the region distal to the synapse outside the pSMAC (dSMAC, grey) (72). (C and D, Adapted from Macmillan Publishers Ltd.: Nature Reviews Immunology (72). Copyright 2003).

Kupfer referred these radially symmetric areas as supra-molecular activation complexes (SMACs) (**Figure 1.2.3.1.1**). The central region of the SMAC (cSMAC) is composed by TCRs and one of its downstream signaling effectors, protein kinase C-Θ (PKC- Θ) (72, 74). The peripheral ring that surrounds the cSMAC (pSMAC) is related with cell adhesion, showing a high surface density of LFA1 and the cytoskeletal linker talin. The distal region to the synapse outside the pSMAC is referred as dSMAC and is characterized with large and bulky molecules as CD43 and CD45 (74).

From this study, the segregation of TCR-MHC interactions from LFA-1-ICAM-1 interactions was proved. Furthermore, the model developed by Springer in 1990 (76), based on the hypothesis that TRC-MHC interactions would need to segregate laterally from the LFA-1-ICAM-1 interactions, as a stereotypical response of helper, cytotoxic and regulatory T cells was confirmed. The current understanding of this picture of a compartmentalized IS of the T cell-planar bilayer model forecasts the presence of a dynamic T cell-APC IS, where signaling is hold by formation of TCR microclusters (MCs), and the SMACs with a stable synapse is related to polarized compartments in a kinase. It is also worth noting that three categories of receptors - T cell antigen receptors, adhesion receptors and costimulary/checkpoint receptors - are highly interdependent to recreate into a functional synapse (70).

Recent studies with higher resolution has confirmed Kupfer's SMAC definition, where the active TRC-MHC interactions that induce to signaling in the immunological synapse, are concentrated in small MCs, which are formed in the dSMAC and move centripetally through the pSMAC to the cSMAC (70). This process of attachment starts within seconds after conjugation and reaches a maximum strength at around 30 min before cell activity cause changes in adhesion and subsequent release (77).

Others studies have stablished that mechanical forces are involved in discriminating endogenous from foreign pMHC and in the activation of TCR triggering, described in studies via traction force microcopy (TFM), atomic force microscopy (AFM), optical tweezers (OT) and biomembrane force probe (62, 77-80).

In summary, several studies have shown that the formation of SMAC is dependent on the mechanical force, cell-cell contact area and time, shear stress induced between T cells and APC, expression of surfaces molecules (such as TCR and LFA-1), cytoskeleton dynamics, antigen affinities and cell phenotype. For more details about the immunological synapse process, readers may refer to (81-84).

In this context, our objective with Paper I and Paper III was to establish basic principles and approaches in a system that allows further exploration of the mechanism, dynamics and basic cell behavior of attachment and detachment of unspecific and antigen-specific T cells to activated antigen-presenting or non-activated DCs during flow at different shear stresses. It is worth noting that in our work, we use effector T cells and not naïve T cells.

1.3. Microfluidic technology for Immunoengineering

1.3.1. Microfluidic Technology

As referred in section **1.1**, the microfluidic field is characterized to manipulate and control fluids in channels and chambers at micron-level size, using miniaturized total analysis systems (mTASs), lab-on-a-chip (LoC) or micro total analysis systems (μTAS) built with micro-electromechanical systems (MEMS) microfabrication technologies (21, 26, 85, 86). More precisely, a microfluidic platform

provides a set of fluidic unit operations, which are designed for an easier combination with a well-defined fabrication technology, in order to comprehend a consistent way for miniaturization, integration, automation and parallelization of (bio-)chemical processes (85, 86). This technology allows the manipulation of micro- (10^{-6}) to atto- (10^{-18}) liter volume of fluid. As a consequence, this control offers several opportunities from both analytical and economic perspectives: portability, higher sensitivity, lower cost per test, shorter time-to-result and less laboratory space consumption (85, 86).

In the past several years, these µTAS technologies have been recognized by academic and industrial sectors, to figure out relevant solutions that have not yet been addressed by macroscale approaches, for example in life sciences, clinical research and diagnostic (21, 85). In this sense, the scaling effects lead to new phenomena and allow new applications that are not accessible to classical liquid handling platforms, such as (85, 86):

- low Reynolds number, laminar flow reduce sample dispersion;
- Predictable and controllable diffusion, allowing defined concentration gradients on the length and time scales;
- Surface forces dominate over gravitational forces: the relative effect of force produced by gravity at microscale dimensions is significantly reduced; surface tension and capillary forces are more dominant at the micro domain;
- Faster separations, higher Electrical fields result in faster sample migration;
- Liquid compartmentalization;
- High speed serial processing and degree of parallelization.

The fluid phenomena of liquids at microscale are measurably different from those that dominate liquids at the macroscale, making micro-technology as a particular field of interest. Inside a lab on a chip system, the fundamental laws of Nature in mechanics, fluid dynamics, electromagnetism, thermodynamics and physical chemistry underlying our understanding of the operation systems are all known. However, the new perspective in the microscale compared to the macroscale is the interplay between many different forces and the change of the relative importance of these forces (85-88). What follows is a short introduction to the physics of microscale and their implications on cell transport and cell culture in microfluidic devices.

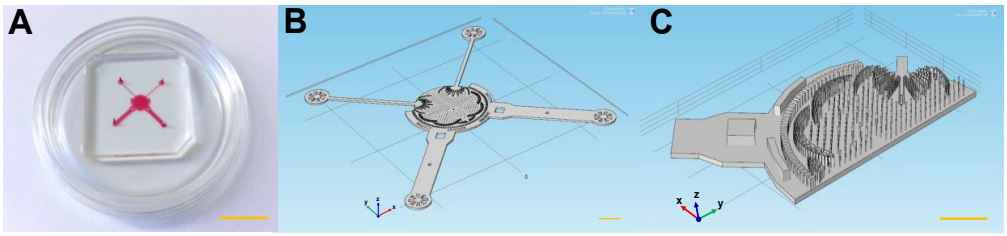

Figure 1.3.1.1 Example of a microfluidic device (Paper III/Manuscript). A) Photograph of the biochip. Scale bar: 1cm. B) Top view of the 3D cell microchamber of the biochip. Scale bar: 1mm. C) 3D cross section of the biochip with the same thickness in all pillars and filters, 100µm. Scale bar: 1mm.

1.3.2. Microfluidic Fundamentals

Many biotechnological applications deal with the micro-manipulation of biological target, and its micro-manipulation can be achieved with temporal and spatial control by using microfluidics. This revolutionary area defines as its ultimate goal, the manipulation and control from a multiple target as cell-tissue population to the single target as single-cell or a single DNA strand (86). For this versatile level of actuation in microfluidics, a significant effort has been applied for 30 years in order to achieve more and more precise and selective manipulation. **Figure 1.3.2.1** summarizes the different methods that can be used as a function of their low to high order of selective manipulation (86). Analyzing this figure, we can assume as a primary carrier of selectivity and precision of biological targets: the behavior of the buffer liquid as a carrier fluid, with or without drops (known as transport only by convection); the transport only by diffusion of the molecules; and the transport by diffusion and convection by the buffer fluid.

In practical cases, the use of a carrier fluid to transport biological objects lacks specificity – sometimes, it is not possible to bring by microfluidic transport a biological target to a specific spot inside the biochip. Then as a second complementary carrier, we can assume with high selectivity on the transport, magnetic beads or electric field, and as the highest level by manipulation of optical or magnetic tweezers (86).

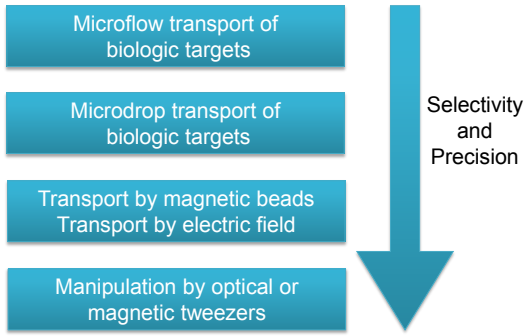

Figure 1.3.2.1 Schematic approach about the level of selectivity and precision on micromanipulation of biologic targets. Adapted from (86).

In this sense, the first step is to understand the transport by microfluidics and its transport mechanisms, and the second step is to analyze, in function of type of particulates and its application, the level of selectivity that can be used for our objective.

From this point of view and considering the scope of this work, in this chapter, the principles of microfluidic transport of macromolecules or microparticles will be firstly discussed, presenting the topics of the microflows (associated with Paper I and Paper III) and diffusion in microfluidics (associated with Paper II), and second, to show how these principles are used to displace and manipulate these objects inside microsystems, presenting a general approach of cell transport in microchannels and the forces present on particle/cell transport.

1.3.2.1. Microflows

1.3.2.1.1. The Continuum approximation

In fluid mechanics, although the fact that properties such as velocity and density oscillate at the molecular scale, fluidics are usually accounted as *continuous* and fluid properties are considered as an

average rather than the properties of each molecule. For the volumes used in the large lab-on-a-chip applications, the *continuum approximation* remains sufficiently valid: a 1 picoliter (10^3 μm^3) volume of fluid still contains $3x10^{13}$ water molecules, which is sufficient to consider their average behavior. Normally, for the major properties of the *continuum approximation* does not break until it considers length scale on the order of several diameters (85, 86).

In this sense, the validity of the *continuum hypothesis* should be considered, because it assumes that macroscopic properties of a fluid are the same if the fluid was perfectly continuous in structures instead of, as in reality, consisting of molecules. Essentially, it is possible to assume that physical quantities like the mass, momentum, and energy implicated in a small volume of fluid containing a sufficiently large number of molecules are to be defined as a result of the sum of the corresponding quantities for the molecule in the volume (85, 86).

1.3.2.1.2. Newtonian and Non-Newtonian fluids

In the fluid mechanics, as the study of the physics of continuous materials which deform when subjected to a force, two categories of fluids can be identified: Newtonian versus non-Newtonian fluids.

When a shear stress is applied to a fluid, the fluid particles move in relation to each other and viscous stresses (τ) develops between them. Due to these viscous stresses (τ), the fluid resists deformation. In this way, when the viscous stress tensor (τ) and the velocity gradient in the direction perpendicular to the plane of shear (i.e., the applied shear stresses) $\left(\frac{dv}{dy}\right)$ varies linearly, the fluid is Newtonian. The constant of proportionality between the viscous stress tensor and the velocity gradient is the viscosity of the Newtonian fluid. The viscosity of a Newtonian fluid depends on temperature and pressure (but, not on the forces acting upon it!).

$$\tau = -\mu \frac{dv}{dy} \tag{1.1}$$

When the relation between shear stress exerted by the fluid and the velocity gradient in the direction perpendicular to the plane of shear is non-linear, the fluid is Non-Newtonian.

In the scope of this thesis, the fluids applied during our hemodynamic analysis of fluid flow phenomena (i.e., to study the shear stresses and the reattachment length as a function of the fluid velocity) will be assumed as high diluted cell suspensions, as the first approximation of Newtonian fluid behavior.

1.3.2.1.3. Laminarity of Microflows

The Reynolds number (Re) is a dimensionless number used to define the transition from laminar to turbulent regime: Re<2100 is stablished laminar flow for cylindrical channels. This parameter determines the ratio between inertia (convective forces) and viscous forces,

$$Re = \frac{L\, V_{avg} \rho}{\eta} \tag{1.2}$$

Where L (m) is the most relevant length scale, V_{avg} (m/s) is the average velocity of the flow, ρ (kg/m3) is the fluid density and η (Pa.s) is the viscosity. For many microchannels, L is equal to $4A/P$, where A

(m^2) is the cross sectional area of the channel and *P* (m) is the wetted perimeter of the channel (87, 88). According to relation *Re,* the small dimension of microfluids channel confer very low Reynolds numbers, occurring laminar flow – the range of values estimated inside the microdevices used along in this work were 0.0023 < Re < 2.6. Considering that the flow rates are limited by physical dimensions and material properties and the viscosity and density of fluids are properties dependent on temperature, the micro-scaling of systems define the fluid into the low Re regime. Consequently, the laminarity of the flow is high, meaning that the streamlines are locally parallel and that even obstacles in the flow are not going to induce any turbulent flow – the flow is totally predictable, enabling greater spatiotemporal control (85). It is worth noting that from the (1.2) equation and when Re<1 (i.e., named by *creeping flow* or *Stokes flow*), the viscous forces dominate, the mass transport is dominated by viscous dissipation, and the inertial effects are neglected (85, 87, 88).

1.3.2.1.4. Continuity equation – Incompressible Fluids

The continuity equation consists on the first fundamental equation of fluid mechanics and expresses the conservation of mass in classical mechanics (87). Considering a mass balance over a volume element $\Delta x \Delta y \Delta z$ fixed in space, and arranging the expression in order to obtain one concisely equation that expresses the equation of continuity, results (1.3),

$$\partial_t \rho = -(\nabla . \rho v) \tag{1.3}$$

The vector ρv is the mass flux, and its divergence has a meaning, it is the net rate of mass efflux per unit volume. In microfluidic field, where the flow velocities are much smaller that the sound velocity in the liquid, the fluid can be assumed as being *incompressible* (87). Meaning that ρ is constant in space and time, and the continuity equation (1.3) is simplified,

$$\nabla v = 0 \tag{1.4}$$

1.3.2.1.5. The Navier-Stokes equation- Incompressible Fluids

In the field of fluid mechanics, there are equations that explain what occurs to particles of the fluid in the system where they are. One of these is Navier-Stokes equation, which describes the motion of fluids, liquids and gases. These equations consider that changes in momentum in infinitesimal volumes of fluid are simply the sum of dissipative viscous forces (friction), the differences in pressure, gravity and other forces acting inside the fluid, which is an incompressible fluid under laminar flow conditions with low Reynolds number, equation (1.5).

$$\rho(\partial_t v + (v\nabla)v) = -\nabla \mathrm{p} + \eta \nabla^2 v + f \tag{1.5}$$

It is possible to identify in this equation that the term on the left side of the equation is related to inertia, more precisely the first term is associated with the unstable acceleration and the second, the convective acceleration, and the terms on the right side correspond to the pressure gradient, viscosity and other forces, respectively. The solution of the Navier-Stokes equation is called the velocity field or flow describing the fluid velocity at a given point in space and time. Obtained this solution, other parameters related to the behavior of fluid can be obtained as the position of the particles that constitute it (87). Note that these equations are adapted to applications of microscale phenomena without major discrepancies.

1.3.2.1.5.1. Stokes Equation

It is worth noting that the Navier-Stokes equation is particularly complex to solve analytically, once it is a nonlinear differential equation. However, it is possible to find analytical solutions for a few important cases.

Navier-Stokes solutions for microfluidics, two important assumptions need to be considered: (i) the flow is unidirectional and (ii) the channel is infinitely long (88). The first assumption is valid in most microfluidic devices, where the fluid flows from an inlet to an outlet as a closed system. The second condition can be assumed as "valid" when the flow is fully developed; a laminar flow is fully developed when the distance from the inlet l in a narrow circular pipe of radius R satisfies the relation $l/R \gg Re$ and $l/R \gg 1$ (88).

Given these assumptions, the Stokes equation (1.6) can be obtained from equation (1.5) assuming that the fluid velocity (v) and fluid gradient $(v\nabla)$ are assumed to be orthogonal, and the flow is in a steady-state:

$$\nabla \mathrm{p} = \eta \nabla^2 v \tag{1.6}$$

In this context, the Stokes equation (1.6) can be addressed for several cases with specific geometrical constraints: Poiseuille flow (pressure induced steady-state fluid flow in infinitely long, translation-invariant channels); liquid film on inclined plane; Couette flow (fluid flow between two parallel plates). More details about the specificity of each case can be found in (88).

1.3.2.1.5.2. Hagen-Poiseuille Flow

Before analyzing the particular Poiseuille problem, it is important to refer that there is no analytical solution for Poiseuille flow problem in a rectangular cross-section channel, but despite of high symmetry of the boundary, the best analytical approximation is to find a Fourier sum representing the solution. More details can be found in (87).

However, it is important to note during the evolution of this work and for practical cases, the systems were simulated um COMSOL Multiphysics software using Finite Element Mode. Although there are several methods for spatially discretizing differential equations over a solution domain, such as the finite difference and the finite volume methods, the most common method for solving fluidics problems to be used is the Finite Element Methods. For more details about the Finite Element Methods, readers may refer (87).

In the following example, we will present the simple case of Poiseuille flow (v_x) in a circular pipe with radius R symmetric around the x-axis (**Figure 1.3.2.1.5.1**). In this case from the Stokes equation (1.6), if the pressure is a linear function of x, the equation reduces to,

$$\frac{\partial p}{\partial x} = \eta \frac{1}{r} \frac{\partial}{\partial r} r \frac{\partial v_x}{\partial r} \tag{1.7}$$

To solve the linear differential equation, this demands two boundary conditions: (i) the velocity at the wall is zero (no-slip): $v_x(r = R) = 0$; and (ii) the velocity is finite in the center of the channel ($r = 0$). Integrating the (1.7) equation in r and using the boundary conditions, obtaining:

$$v_x = -\frac{1}{4\eta}\frac{\partial p}{\partial x}(R^2 - r^2) \tag{1.8}$$

This equation evidences that the pressure driven flows have a parabolic profile, characterizing in the center of the channel ($r = 0$) with a max velocity (v_{max}),

$$\frac{\partial v_x}{\partial r} = 0 \implies v_{max}(r = 0) = -\frac{R^2}{4\eta}\frac{\partial p}{\partial x} \tag{1.9}$$

Integrating the velocity over the cross-section, we obtain the average velocity (v_{avg}) in the channel by the expression (87),

$$v_{avg} = \frac{1}{\pi R^2}\int_0^R v_x . 2\pi r dr = -\frac{R^2}{8\eta}\frac{\partial p}{\partial x} = \frac{1}{2}v_{max} \tag{1.10}$$

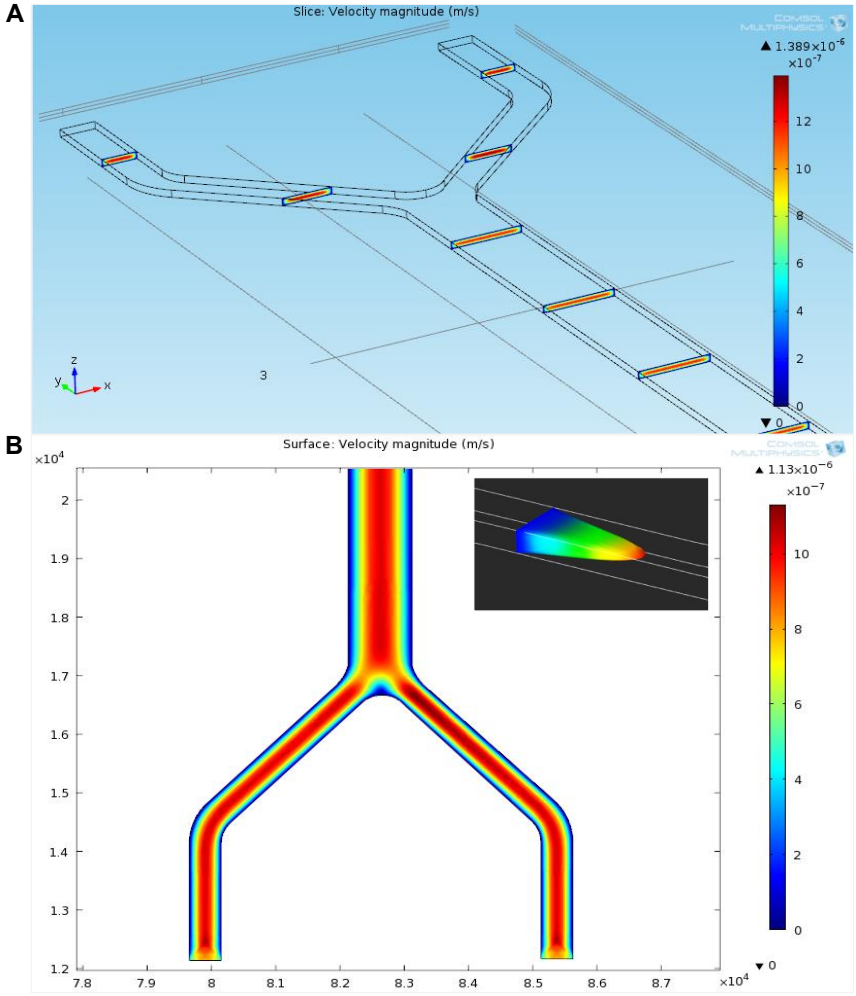

Figure 1.3.2.1.5.1 Poiseuille flow from COMSOL Multiphysics simulations. Initial studies of velocity profile for the microchannel of Paper I. A) 3D representation of cross-sectional velocity profile inside a rectangular microchannel (w=100µm, h=1000µm). B) Surface representation of velocity profile inside a rectangular microchannel.

1.3.2.1.5.3. Shear Stress

Shear stress in fluids is defined as the component of stress coplanar with a material cross section, in this case when a real fluid moves along a solid boundary, it will incur shear stress on that boundary. The simplest way to introduce the physical meaning of shear stress is to consider the relative motion of two planar surfaces a distance it apart, named as the boundary layer (87, 89). At the layer boundary, the no-slip condition dictates that the speed of the fluid at the boundary (relative to the boundary) is zero. At some height (H) from the boundary, the flow speed must equal with the fluid speed. In this case, for Newtonian fluids in laminar flow, the velocity profile is expected to vary linearly between the two surfaces, and consequently the wall shear stress (WSS) values for this type of flow can be determined by the relation between fluid viscosity coefficient (μ) and the flow rate (v),

$$\tau = \mu \left[\frac{\partial v(y)}{\partial y}\right]_{y=0,h} \tag{1.11}$$

By modeling microfluidic flow in the center of a channel and assuming flow between flat plates, the wall shear equation can also be expressed by (1.12), where h is the channel height.

$$\tau_w = \tau_{xy} = \frac{[2\mu v_{max}]}{h} \tag{1.12}$$

1.3.2.2. Diffusion

Diffusional transport is the process by which a concentrated group of particles in a volume will spread out over time by Brownian motion, so that the average concentration of particles throughout the volume is constant (86, 87).

In most microfluidic systems, it is possible to detect diffusive transport with convective flow of the bulk fluid. The Sherwood number (Sh) is a dimensionless number that represents the ratio of convective mass transfer to diffusive mass transfer in a system, in order to compare the relative importance to each effect (1.11),

$$Sh = \frac{kd}{D_\alpha} \tag{1.11}$$

Where k (m/s) is the mass transfer coefficient, d (m) is the characteristic length of the system (e.g., channel diameter), and D_α (m^2/s) is the diffusion coefficient of solute α in the solvent (86, 87). In this sense, for microfluidic systems, the Sherwood number is much lower due to the low characteristics length scale in the numerator. Consequently, diffusion is much more relevant in microfluidic systems (86, 87). On the other hand, in macroscale systems, Sh is large leading to convective transport being dominant over diffusive transport.

Refer that the diffusion coefficient for any particle can be determined approximately by the Stokes-Einstein relation (1.12),

$$D_\alpha = \frac{k_B T}{6\pi\eta a} \tag{1.12}$$

which depends on the effective size of a particle a, the viscosity of the fluid the particle is in, η, and the absolute temperature T (K), considering k_B as Boltzmann's constant. In this sense, the linear size, a, of a molecule generally varies in function of the cube root of the molecular weight (($a \sim (MW)^{1/3}$),

so the diffusion coefficient for a large protein is only about 10 times smaller than for a water molecule (86, 87).

To describe the diffusive transport without flow some equations can be applied. Fick's first law is a mathematical description of diffusion in steady state to binary ideals solutions, that should also be diluted and of constant density (1.13),

$$J_{\alpha}^{diff} = -D_{\alpha}\frac{\partial C}{\partial x} \tag{1.13}$$

Where D_{α} is the diffusion coefficient and $C(mol/m^3)$ is a concentration of particles. This law defines for low flows, a linear variation of the diffusive flux, J_{α}^{diff} $(kg/m^2 s)$ with the concentration gradient $\partial C/\partial x\,(mol/m^4)$, through constant proportionality, that is diffusion coefficient. From the simplified mass transfer equation, an equation in transient state can be obtained. This equation was defined by Fick's second law (1.14), which at one dimension is,

$$\frac{\partial C}{\partial t} = D_{\alpha}\frac{\partial^2 C}{\partial x^2} \tag{1.14}$$

The variation of the concentration with time (s) and distance(m), implied in the definition of Fick's second law, can be obtained for specific situations associating boundary conditions and initial condition, leading to integrate the equation (86, 87).

Diffusion distance of a particle at one dimension over time (1.15) is,

$$x_{D_{\alpha}=\sqrt{2D_{\alpha}t}} \tag{1.15}$$

And the characteristic time required for diffusion over a given distance (1.16) is,

$$t_{diff} = \frac{x^2}{2\,D_{\alpha}} \tag{1.16}$$

In contrast with this scaling, the characteristic time of convective motion fluid, solutes, cells, is (1.17),

$$t_{con} = \frac{l}{v} \tag{1.17}$$

where l is a characteristic length scale and v, the characteristic velocity (86, 87).

The ratio of these two transport timescales defines the mass transfer Péclet number (Pe), as a parameter to characterize the dominant mode of transport (86, 87) (1.18),

$$Pe \equiv \frac{t_{diff}}{t_{con}} = \frac{Ul}{D} \tag{1.18}$$

By preceding analysis of a microdevice regime, the Péclet number is characterized to be very large and the Reynolds and Stokes numbers are very small.

Table 1.3.2.2.1 evidences the relation between the diffusivities, as calculated by the Stokes-Einstein relation (1.12), and Pe, at specific conditions (assuming 100 μm wide channel and 100 μm/s mean velocity), of dilute analytes in water at 25 °C (90). As we can identify, and considering the scope of this work, the diffusivity of erythrocyte is very small, and the Pe is large for cells in any microfluidic flow, concluding that mammalian cells neither advect nor diffuse away from streamlines, except if there is external forcing and being the particle trajectories mainly defined by fluid streamlines (90).

Table 1.3.2.2.1 Diffusivities and representative Péclet number for dilute analytes in water at 25 °C. Diffusivities were determined by Stokes-Einstein relation (1.12), and for Péclet number, it was assumed a wide channel 100 µm and mean velocity 100 µm/s. Adapted from Ref. (90).

Analyte	Diameter (d_h)	Diffusion constant (D) [$m^2 s^{-1}$]	Péclet number (*Pe*)
Na^+	100 pm	10^{-9}	10
BSA	100 Å	10^{-11}	10^3
Viron	100 nm	10^{-12}	10^4
Bacterial cell	1 µm	10^{-13}	10^5
Erythrocyte	10 µm	10^{-14}	10^6
Polystyrene bead	100 µm	10^{-15}	10^7

1.3.2.3. Forces on Particle/Cell Transport

The interaction of cells with velocity, pressure, gravity and electric fields in microchannels, results in cellular motion. The velocity field of fluid motion (created by an external pressure difference), directs the particle to fluid streamlines, which is submitted on its surface to pressure and viscous fluid stresses. The deviations result from the particle motion on fluid motion are due to gravity, electrical and magnetic fields, and particle-boundary interactions (90).

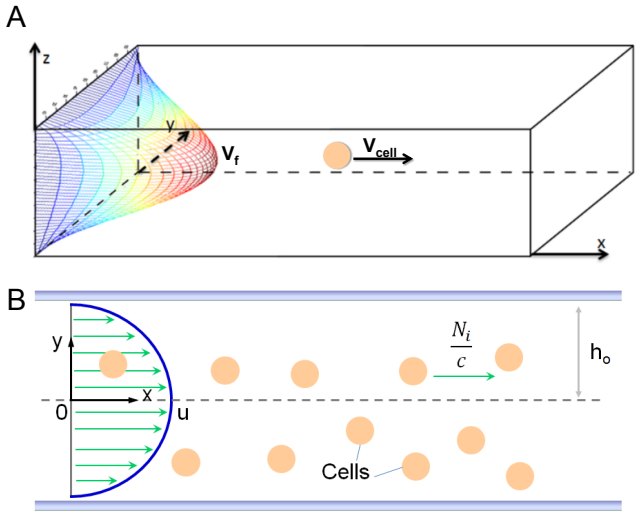

Figure 1.3.2.3.1 A) 3D illustration of cell migration by pressure driven flow, through a rectangular channel. B) 2D illustration of cell motion by pressure driven flow, through a rectangular channel with half-height h_0. Cell velocity Ni/c. Adapted from Ref.(91).

It is worth noting that, for simplicity of this discussion we will assume one dimensional motion in a rectangular channel, there are three groups of types of forces on a particle moving in an electrically conducting fluid: (i) *from external fields*, external pressure difference, electrostatic force, magnetic force and gravity; (ii) *from fluid particles*, Stokes drag and random force; (iii) *from the channel walls*, van der Waals force and electric double layer force.

(i) Forces from external fields

In the context of this thesis, and to simplifythis discussion, it will only be assumed as (i) force generated by the external field, the gravitational force (e.g., the force gravity on a 5 µm radius, 10^3 kg. m^{-3} density cell is 5 pN). The electrostatic and magnetic forces are assumed as negligible, once there were not applied during this project.

(ii) Forces from fluid particle

Regarding the (ii) forces coming from the fluid surrounding the particle; we can identify the Stokes drag and the random force.

Stokes drag

A friction force is induced by the interaction between the particle/cell and its surrounding viscous fluid (being restricted to Re<0.1), defined as Stokes drag (F_S) and discovered by G.G. Stokes (92, 93). The expression for the drag force has been improved along times, and Padmavathi et al. (94) defined the Stokes drag for a sphere in the flow with mixed slip-stick boundary conditions as,

$$F_S = \begin{cases} 4\pi\mu a\left(v_p - v\right) & for\ slip\ boundaries \\ 6\pi\mu a\left(v_p - v\right) & for\ no-slip\ boundaries \end{cases} \quad (1.19)$$

where μ is the fluid's viscosity, a is the radius of the cell, v_p is the particle velocity and v is the fluid velocity (94). It is important to note that the Stokes drag force exists if there is a difference between the fluid speed and the particle/cell speed. In case of an equilibrium state, it balances any other external forces (92-94).

In Paper I, assuming the case of the flow passing through a sphere at low Reynolds number (Re<<1), we used the Stokes' law to estimate the total drag force (F_S) on the T cells as a resultant force from pressure force and viscous shear stresses on the cell.

Random force

Brownian motion phenomena results when a suspended particle interacts with the surrounding fluid, and causes a random drifting of the particle (93). The force applied on the particle by fluid-particle interaction is the random force, R (91, 93). By numerical calculation, the random force on a particle k from the j^{th} surrounding particles can be defined by a Gaussian random process by,

$$R_k = \sum_{j=1}^{N}\left[A_j e^{\frac{2\pi i}{N}jk} + B_j e^{\frac{-2\pi i}{N}jk}\right] \quad (1.20)$$

where N is the total number of interacting fluid particles, and A_j and B_j arbitrary constant chosen from Gaussian distribution, and $i = \sqrt{-1}$ (91). By experimental measurement, Yuan et al (95) has determined the motion force exerted on nanoscale particles in a static dilution solution in a range of $0.013 - 0.17$pN.

(iii) Forces from the channel walls

The group of forces from the channel walls includes van der Waals attraction force and the electric double layer (EDL) repulsion force, and there are short forces due to the charged surfaces (the channel walls). The combination of the van der Waals attraction and EDL repulsion results in DLVO (Derjaguin, Landau, Verwey, and Overbeek) theory. However, these forces fall outside the scope of the Paper I. More information can be found in (91, 96, 97).

In conclusion, Table 3 summarize the possible forces on a particle or on a cell (assuming radius a= 5 μm), with correspondent order of magnitude of forces and their importance on cell motion.

Table 3. Summary of forces on a particle, with correspondent order of magnitude of forces on a cell and importance to cell motion. It is important to note that the primary forces are larger in ~ [3-5] order of magnitude than the secondary forces. Adapted from Ref. (91).

Force	Direction	Origin	Symbol		Magnitude (pN)	Importance to cell motion
External Field	Electromagnetic Field	Electric Field	F_{ext}	F_e	$\sim 10^3$	Primary
		Magnetic Field		F_m	$\sim 10^3$	Primary
	Earth	Gravity Field		F_g	< 5	Secondary
Stokes Drag	Fluid	Speed Difference	F_S		$\sim 10^3$	Primary
Random	Fluid	Brownian motion	R		0.013-0.17	Secondary
DLVO	Wall	Molecule Interaction	F_{DLVO}	F_{vdW}	< 4.6	Secondary
	Wall	Electric Double Layer (EDL)		F_{EDL}	< 40	Secondary

Cross-streamline motion from body forces

For deterministic cross-streamline motion, there are several interesting cases to be analyzed and related with the particle pathlines deviating or not from streamlines such as in a system with non-negligible inertia, a system where the particles are denser than the fluid, and a system where boundaries and fluid streams are introduced that strongly affect the nature of the particle motion (90). In our analysis for the convection (Paper I), we will assume inertialess flow without external force, where there is no motion across streamlines unless contact with a boundary occurs (85, 86, 90).

It is important to consider that cells can be influenced by gravity or electrical and magnetic forces. Regarding the gravity, a particle can float or sediment when its density varies from that of the fluid. In this way, density can influence the ability of the particle to trace fluid streamlines (90). However at the length scale of microsystems and consequent effects of Reynolds number, the particle motion due to density variations can be mitigated, once that these deviations are not a significant cause to the particle pathlines deviating from streamlines (85, 86, 90) .

1.3.3. Microfabrication techniques for microfluidics

In the past few decades, there has been a high interest in micromachining technologies. Currently, microelectromechanical systems (MEMS) can be found in every manufacturing and industry segment such as communication and information technologies, automotive, energy, aerospace, biomedical applications and biotechnology/pharmaceutical processes. The semiconductor industry began its

growth in 1968 with the fabrication of semiconductor devices as diodes, transistors, integrated circuits and more complex electronic components.

In this context, the concept and evolution of microfluidics are totally fused with the advances in micro- and nanofabrication largely developed for the semiconductor industry, and carried out in a cleanroom environment. A typical process can involve successive steps as mask-based photolithography, wet and dry etching, thin film deposition, lift-off, characterization, soft lithography and replica molding, bonding and biofunctionalization. Monocrystalline silicon (Si), glass, or a combination between glass and silicon can be used as base material. As a strategic fabrication technique for microfluidics, soft lithography and replica molding by using PDMS (polydimethylsiloxane) material have found widespread applications due to its low cost and easy to use. More recently, some maskless techniques as 3D printing and laser micro-machining have gained some attention since they simplify the other microfabrication techniques. This section briefly reviews the general standard techniques and materials used in the conception of microfluidic devices. For more details about the techniques focused on biological applications, readers may refer to Fundamentals of BioMEMS and Medical Microdevices by Saliterman (98, 99).

1.3.3.1. Photolithography

Photolithography, also termed optical lithography or UV lithography, is a standard method for pattern generation in the manufacturing of ICs, microchips and MEMS device (100). This process consists to transfer a pattern from a stencil to light-sensitive polymers (photoresists), which are reactive to ultraviolet (UV) light with wavelengths in the range of 193-436 nm. The pattern can be transferred in parallel through a photomask, which consists of opaque features on a transparent subtract, or direct writing with a focused electron-beam or direct laser writing, using an electronic database obtained by a CAD conversion (computer-aided design) (100). The main principle of a photomask is based on the blocking of radiation where it is not wanted (absorb radiation), using opaque material at the desired wavelength, and to transmit radiation where it is needed, using material with high transmission at the desired wavelength, in order to achieve the desired design. For common optical lithography, mask can be composed by quartz or glass as transparent material, and by Cr as opaque material (100).

Currently, there are multiple options of photomasks in the market as quartz, glass and film photomask (as polyester poly(ethyleneterephthalate) (PET) base with a photographic emulsion gel; resolution >50 μm), depending on our purposes/criteria of resolution and in small or large format (101). As current substrate, there are several types to be used as quartz, low expansion glass, sodalime glass. Regarding the opaque materials to be used to block light, it is possible to use chrome, emulsion or iron oxide. Considering the polarities of masks, two polarities are common, light field (LF, mostly clear) and dark field (DF, mostly dark) (101).

Another important metric of lithography is the registration determined by optical system and aligner. As aligners, there are three exposure systems for wafer lithography - Contact, Proximity and Projection – and each of them can be selected/used considering our criteria/proposes. The interval between photomask and resist surface can induce the diffraction pattern and consequently damage the resolution. Furthermore, contaminations in subtract, bubbles in the resist film, incomplete bake times, contamination of photomask by particles, and edge bead can also be assumed as possible accidental reasons bad lithographies (102).

Photoresist is a light-sensitive material that changes its molecular rearrangement when exposed to specific wavelengths of light. Photoresists generally consist in a mixture of three parts: base resin, which is solid in its undiluted state; casting solvent, as chemicals used to dissolve the resin, and photoactive compound (PAC), which acts to inhibit or promote the dissolution of the resin in the developer. The solvents define the viscosity of the resist, allowing their uniformity distribution on a flat substrate by spin-coating, and depending on the quantity of solvent, it results in different layer thicknesses. Afterwards in the process, the solvents are evaporated by baking the substrate on a hot plate, leaving behind photoactive molecules embedded in a polymer matrix (102).

The PAC acts to inhibit or promote the dissolution of the resin in the developer, by absorbing light at certain wavelengths and changing the solubility of the polymer. There are two types of light sensitive material, positive and negative photoresist. In a positive photoresist (e.g., PMMA or SPR), the portion of the resist which is exposed to light becomes soluble to the photoresist developer and the developed resist results as a mirror copy of the mask pattern. In negative photoresist (e.g., SU-8), the portion of the resist which is exposed to light becomes insoluble because the polymer chains become the crosslinking process, creating insoluble polymer networks to the photoresist developer. The developer dissolves unexposed portion of the photoresist, resulting an inverted pattern of the mask (102). Both positive and negative photoresists have their place in the semiconductor manufacturing industry, helping to produce a wide range of products with high quality considering their specifications/features. Positive photoresist when compared with negative photoresist, is characterized to give better contrast and less shadowing effects. Negative photoresist is characterized to have a faster photo speed, better adhesion capabilities to certain materials, wider process latitude and a considerable lower operating cost (100, 102).

SU-8 was originally developed by IBM in 1982 and is an epoxy-base negative tone photoresist designed for the lithography of ultra-thick resists. Currently, it is commercially available from Microchem Corporation (Westborough, MA, USA) (103) and Gersteltec Sàrl (Pully, Switzerland) (104) in several formulations and protocols. SU-8 consists on the epon SU-8 epoxy resin, which is a multifunctional glycidly ether derivative of bisphenol-A novolac, given that an epoxy group functionality of 8. The epoxy resin is dissolved in an organic solvent (cyclopentanone C_5H_8O) and with the addition of photoinitiator as of triarylsulfonium hexafluoroantimonate salt (98). SU-8 is available in different viscosities, depending on the quality of solvent, and resulting in different layer thicknesses. Multilayer processes can also be performed in order to achieve higher thicknesses.

SU-8 is sensitive to light at wavelengths in the range λ=350-400nm which coincides with the I-line (λ=365nm) of mercury lamps present in most contact aligners. When the light is absorbed, transforms the triarylsulfonium hexafluoroantimonate salt into a photoacid ($H^+SbF_6^-$). The photoacid acts as a catalyst in the cross linking reaction, where the H+ ions attack the cyclic chains of the epoxy groups and open them up deliver another H+ ions as an avalanche catalytic. This process is further accelerated by increment of temperature during post-exposure bake (PEB) (60-100°C). The open bonds cross-link to each other, resulting in insoluble areas to liquid developers (98).

SU-8 is also characterized by a great chemical, mechanical and thermal stability making it suitable for high-aspect-ratio structures with straight sidewalls and enables processing of thick films (>100µm) in a single spin (105).

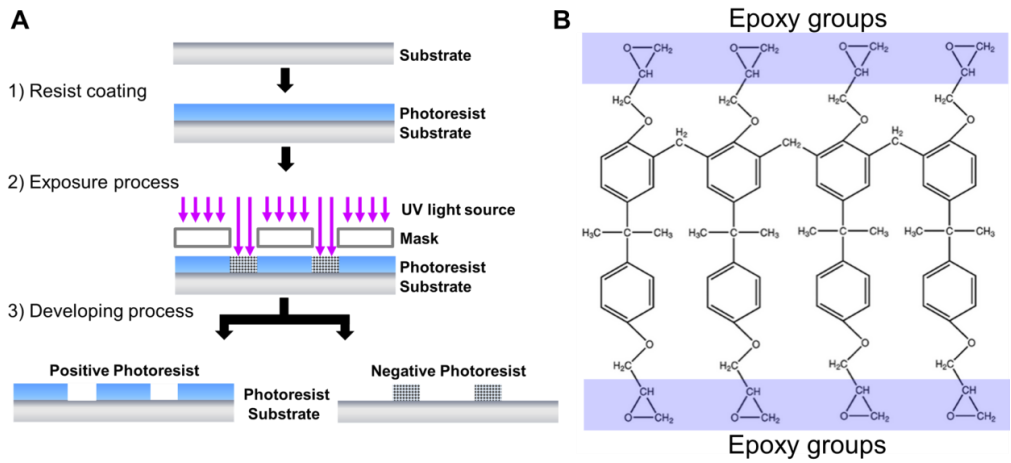

Figure 1.3.3.1.1 A) A comparison of positive and negative photoresist. B) SU-8 molecule. A single molecule contains 8 epoxy groups in a bisphenol-A novalac glycidly ether that forms a strong crosslinking network upon UV-light exposure.

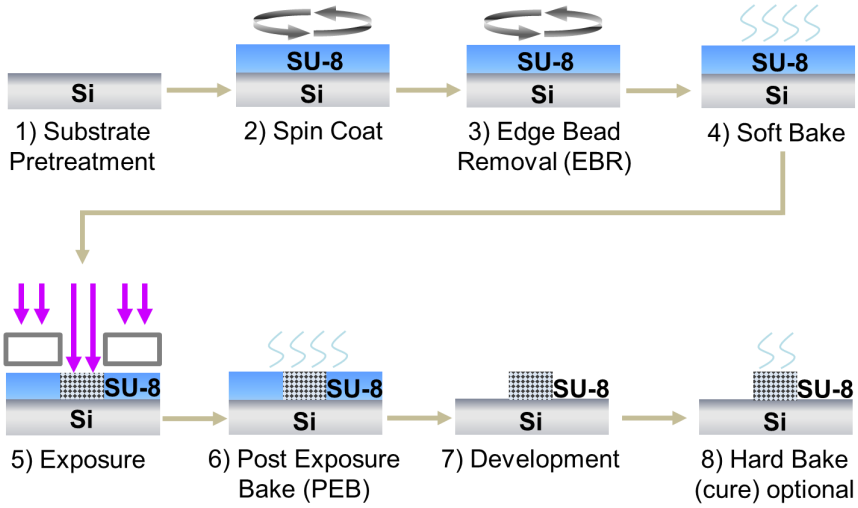

Figure 1.3.3.1.2 SU-8 photolithography process chart. **1) Substrate Pretreatment:** A Si wafer substrate should be cleaned and dried with chemical solutions (e.g., piranha solution) and/or oxygen plasma to remove contaminants and increase adhesion to the photoresist. A dehydration bake is performed with high temperature (>200°C for 10-15 min) to remove the adsorved de-ionized water on the surface. **2) Spin Coat:** Photoresist is uniformly spread by rapid rotation on a vacuum spin chuck. The final thickness is determined by resist properties (solvent chemistry and viscosity) and by rotation parameters used (ramp, spin speed and time). **3) Edge Bead Removal (EBR):** during the spin coat step on higher thickness of photoresist may occur on the edge of the substrate. In order to minimize bubbling problems during soft bake and focus offset problems during exposure, this thick bead should be removed. There are several methods to remove it considering literature and producers. 4) Soft Bake: the substrate is heated to evaporate solvents from the photoresist and improve the adhesion between resist and wafer. Baking time/temperatures are dependent on the resist thickness and solvent and some recommendations can be found in protocols provided by producer. **5) Exposure:** SU-8 is optimized for near UV (λ=350-400nm) exposure and i-line exposure tools are recommended. The optimal exposure dose will depend on film thickness (thicker films require higher dosage) and the intensity of the lamp. The photomask is aligned with direct physical contact (hard contact) with substrate, or there is a small proximity distance between resist surface

and mask (proximity printing). 6) **Post Exposure Bake (PEB):** Following exposure, PEB must be performed to selectively control the kinetics of the polymerization reaction initiated during exposure. **7) Development:** As a final step of pattern transfer, the substrate is developed with solution to remove non-crosslinked resist. **8) Hard Bake (optional):** This step is optional and an additional bake can be performed to improve the thermal or chemical stability of resist.

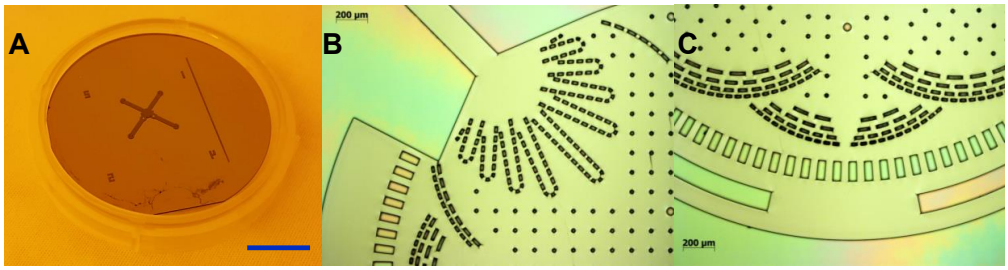

Figure 1.3.3.1.3 SU-8 master molds: A) Top view of a master mold made with SU-8 3050 with film thickness, 100µm. Scale bar: 1cm. B) & C) Magnification from A).

Mask aligners are the tools currently used in most microfabrication research laboratories and institutes with low-volume production facilities. The mask aligner consists on an alignment and exposure tool, where the mask is adjusted to a substrate with submicron precision. Normally, mask aligner can be used in direct physical contact (hard contact) or in proximity contact where there is a small proximity distance between resist surface and mask, and only the upper side of the wafer is exposed. Thus, the operator loads successively the mask and the wafer into the mask aligner. Mask aligner are also equipped with a backside microscope that allows alignment procedures using the loaded mask with an already exposed and developed wafer.

1.3.3.2. Soft Lithography and Replica Molding

Soft lithography consists on a collection of techniques for replicating microstructures and nanostructures based on printing, molding and embossing (106). As an alternative to photolithography and electron-beam lithography, this soft technique is based on the usage as a mask, a patterned elastomeric polymer (SU-8), and as pattern, soft materials such as polymers, gels and organic monolayers, as well as glass or silicon. Considering the simplicity and low-cost associated with this technique, associated to the high variability of materials that could be used, several tools of soft lithography have been frequently used in cell biology, fundamental biology and biomedical applications/devices (14).

Considering the scope of this work, the final result using soft techniques consists on a device made of poly-dimethylsiloxane (PDMS) replicated from a rigid master of SU-8 (106).

PDMS is a silicon-based organic elastomer with repeating monomer $SiO(CH_3)_2$ (**Figure 1.3.3.2.1**). Currently, Sylgard 184 has a PDMS-kit commercially available from Dow Corning (Dow Corning Corporations) (107), and this elastomer is supplied in a two component kit with a base (vinyl-terminated PDMS) and a curing agent (copolymers of methylhydrosiloxane and dimethylsiloxane mixed with a platinum complex) (108). When the two components are mixed, crosslinking reactions start with a hydrosilylation reaction takes place between vinyl ($SiCH=CH_2$) and hydrosilane (SiH) groups. The crosslinking is highly dependent on temperature and increase the viscosity until the formation solid elastomer. This cast molding against a mold made by photolithography is the current

standard method to soft lithography for microfluidics (106). Replica molding is a technique for duplicating three-dimensional structures in a single step by using the first PDMS replica as an inverted copy of the mold to transfer the pattern to the surface of another polymer (e.g., epoxy resins) (106).

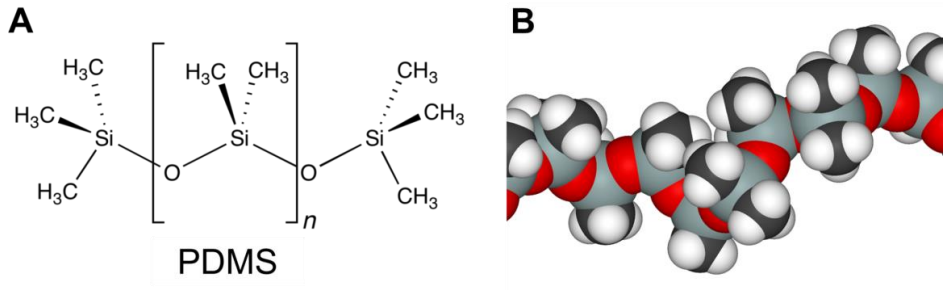

Figure 1.3.3.2.1 PDMS A) Chemical formula of PDMS. **B)** 3D structure. Adapted from Ref. (109).

In this case, the process to fabricate the PDMS replica is based on mixture of vinyl-terminated PDMS and curing agent in a ratio of 1:10, and afterwards degassed in a vacuum chamber. Then, the PDMS is poured on the SU-8 master, thermally cured (e.g., 70°C for 60min) and then peeled off the master. PDMS can be drilled to create inlets and outlets and bonded to glass substrate to create closed microfluidic devices (110).

In the sealing process, PDMS is typically bonded/sealed to PDMS or to another substrate. The bonding can be either reversible (e.g., van der Waals contact of PDMS-PDMS or PDMS-glass) or irreversible, with the assistance of plasma oxidation or bonding of procured PDMS to a fully cured PDMS (110). The reversible seal is fast and occurs at room temperature, however does not withstand high pressures (>30kPa). The irreversible sealing can be done with a number of substrates, as PDMS, glass, Si, SiO2, quartz, polystyrene, polyethylene; this sealing withstands pressures up to 200 kPa (110).

PDMS is characterized by repetitive units of -O-Si(CH_3)$_2$-, and when a PDMS replica is exposed on air or O_2 plasma, McDonald et al. suggested that the plasma introduces polar groups on the surface as silanol groups (Si-OH) at the expense of methyl groups (Si-CH_3) (108, 110). These silanol groups condense with appropriate groups (OH, COOH, ketone) on a surface. When the PDMS and glass are bonded, these two layers stablish conformal contact yielding Si-O-Si bonds with loss of a water.

Essentially, PDMS has been characterized as an excellent material, focusing on the optimization and standardization of biomicrosystems manufacturing for use with biological samples in aqueous solutions. In this sense, several aspects and advantages may be mentioned, such as, (i) features on the micro scale can be reproduced with high fidelity in PDMS by replica molding; (ii) it is optically transparent down to 280nm, so it can be used in a varied number of detection schemes (e.g., UV/Vis absorbance and fluorescence), (iii) it cures at low temperatures; (iv) it presents high permeability, elasticity and surface properties; (v) as a biomaterial, it is characterized as non toxic, stable, elastic resistant to degradation and durable (110). A more detailed discussion about all advantages/disadvantages of PDMS in microfluidic cell culture will be presented in the next section.

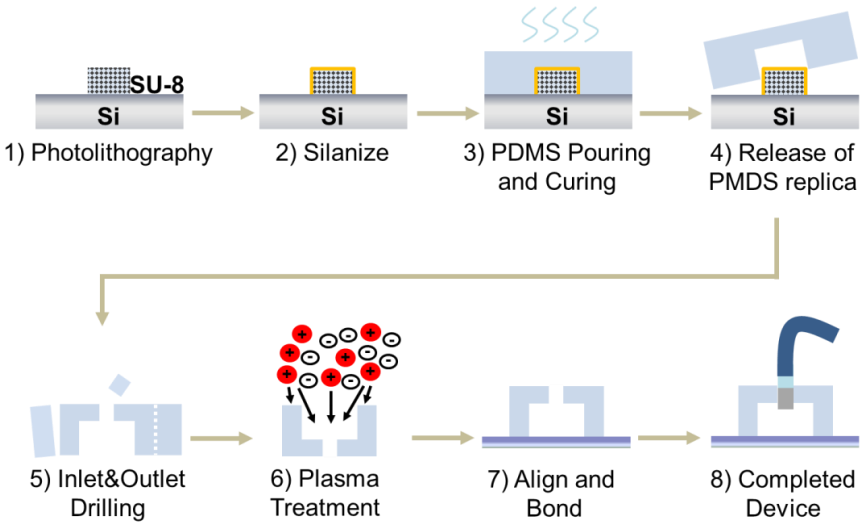

Figure 1.3.3.2.2 Soft lithography and Replica molding: 1) Photolithography: A SU-8 master is created by photolithography on a Si wafer (substrate). **2) Silanize:** The SU-8 master is covered with a fluorine-based silane. **3) PDMS Pouring and Curing:** PDMS elastomer is prepared by mixing siloxane oligomer and curing agent in a standard ratio 1:10, and afterwards degassed in a vacuum chamber to remove bubbles. PDMS is poured onto the master and then baked to cure the PDMS into the desired pattern. 4) **Release of PDMS replica:** The PDMS layer is peeled off of the SU-8 master and can now be used to make devices. The SU-8 master can be reused. **5) Inlet&Outlet Drilling:** The PDMS sheet is cut into individual pieces, and inlets/outlets are punched using a hole punch. **6) Plasma Treatment:** Exposure to oxygen plasma chemically activates the PDMS surface and allows it to be bonded to the glass. **7) Align and bond:** The device is aligned and bonded to a substrate. The device is ready for the biofunctionalization treatment. **8) Completed device:** Metal connectors and thin capillaries are coupled and attached to the device, which is now ready to be tested.

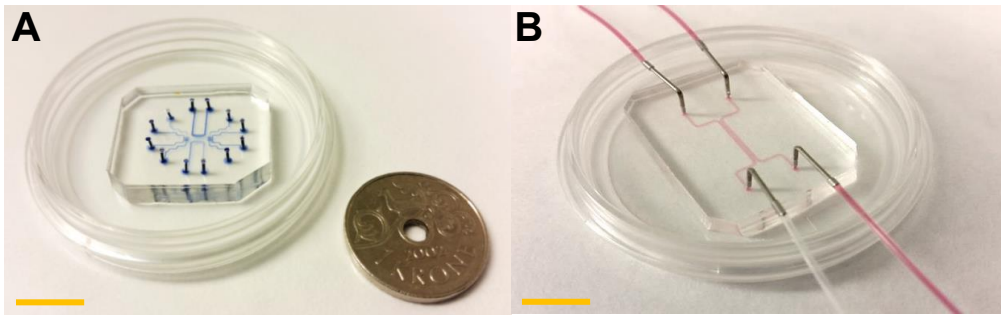

Figure 1.3.3.2.3 PDMS devices. A) Microfluidic device for cell migration (Paper II). Scale bar: 1cm. B) Microchannel device with metal connectors and thin capillaries for the perfusion system (Paper I). Scale bar: 1cm.

1.3.4. Microfluidics for immune cell-cell communication

1.3.4.1. Microfluidic cell culture

Most of the microfluidic technologies for cell culture to address specific problems and fundamental limitations in biology and clinical research, were developed more significantly over the last ten years (21).

Microfluidic cell culture allows controlling and manipulating the fluid flow, measured in microliters to femtoliters in precise and complex geometries, and simultaneously analyze the operation from a single cell to the tissues cultured on integrated and automated chips. **Table 1.3.4.1.1** compares the limitations of conventional cell culture to improvements addressed by microfluidic cell culture technology (111).

Table 1.3.4.1.1 Limitations and requirements from conventional cell culture to solutions addressed and to be addressed by microfluidic cell culture. Adapted from Ref. (111) from Elsevier.

Requirements	Conventional cell culture	Microfluidic cell culture
·Control of exchanged temperature and gases	Large fluid volumes prevent fast changes	Small volumes allow dynamic control
·Addition of nutrients and removal of metabolites	Uncontrolled and manual exchange of large volumes	Precisely measured, continuous or transient exchange of medias and waste.
·Stimulation with drugs/proteins and simultaneous imaging	Mostly not feasible	Feasible
·Parallelization of cellular assays	Not feasible	High capability for parallelization
·Automation of cell culture tasks	Bulky, expensive fluid-handling robots must be used	High capability for automation in compact, inexpensive format
·Single-cell manipulation and analysis	Manually involved, inaccurate, low throughput	Accurate and high-throughput

From the semiconductor industry and multiple approaches for manufacturing of microfluidic devices, soft lithography with poly-dimethylsiloxane (PDMS) has been the standard approach for cell culture applications. This fabrication technique is based on pouring a liquid polymer PDMS on an etched silicon substrate as a hard master with a 3D mold drawn in photoresist, and allowing it to polymerize into an optically clear rubber with open cavities in the form of small channels (cross section <1 mm x <1mm), or chambers with openings at both ends of the polymer block for flow perfusion (111-118).

As key features of PDMS cell culture systems, PDMS is (i) optically transparent, gas- and vapour-permeable elastomer; (ii) it allows fabrication of more complex and robust geometry and implementation of valves and actuators; (iii) relative cheap and easy set-up for fabricating small numbers of devices (in academic setting); (iv) easy bonding protocols (reversible or irreversible processes) for closing PDMS microchannel to glass, plastic, PDMS itself and other materials; and (v) its elasticity, which allows for easy removal and several reutilizations from delicate silicon master molds for replication (113, 119-122). Furthermore, optically it offers low level of autofluorescence and stable optical features, promoting image acquisition in real-time, high-resolution optical imaging of cellular responses to environmental cues (111).

Note that the materials used for the conception of microfluidic devices have been explored over the years. Early devices were fabricated from silicon and glass, but considering several limitations a long-term solution for cell biology research such as opacity to visible and ultraviolet light, their brittle and non-trivial bonding protocol for closing channels; other more flexible and cheaper materials and fabrication methods were explored. Other alternative materials as plastic, silk and paper were used for microfabrication by using laser etching, injection molding, photopolymerization and solid object printing (112).

The expansive use of PDMS in microfluidic chips has allowed the conception and miniaturization of micromechanical membrane valves, and, by parallelized fabrication by optical lithography and

alignment of flow and control layers, the rapid construction of multiples types of channels, chambers and valves in an integrated device (111, 112). Valves can be assumed as transistors in electronic devices, where they allow manipulating fluids at the microliter scale with precise spatial and temporal control of fluid flow, and the delivery of media, drugs and signaling factors through the microchannels to living cells inside the microchambers (123-125).

The advent of PDMS micromechanical membrane valves by multiplexing methods parallelized, the increment of incorporated microsensors inside the channels/chambers in order to monitor the mechan-biochemical parameters/signals/gradients in real time, and with the integration of computation systems to the transduction of all signals, has allowed the development of truly "lab-on-a-chip devices", improving the accuracy and throughput of biological assays by orders of magnitude (111, 112, 126-129). It is worth mentioning that the use of nanoliter-sized assay chambers mimics the compartmentalization of cell environments and reflects physiological conditions of cells or cell-populations in tissues, resulting in this way in increased precision and reduced consumption of costly reagents (111, 112, 130).

1.3.4.1.1. Advantages of microfluidic cell culture

Microfluidic cell culture devices have become particularly valuable for the analysis of single cell and tissue dynamics allowing controllability, parallelization, automation and excellent imaging properties.

Microfluidic chip allow the precise control over many system parameters, such as cell numbers and cell density in a given area and volume, cell monitoring with high spatial and temporal resolution and their individual retrieval during or following experiments, and placement of cells in complex geometries or 3D geometries in matrices as hydrogels (130, 131).

The multiple cell compartmentalization on a single chip allow the control of a multitude of single cells events, facilitating high parallelization of experiments and high throughput of samples and reactions, enhancing cell-based screening assays (e.g., in immunophenotyping assays monitoring single cell cytokine production in response to external stimuli (111, 132, 133)) , reproducibility, and on the reduction in reagents costs (134, 135).

The control of fluid flow is enormously useful, and allows the tissue-to-fluid ratio inside the microchannels to be adjusted to mimic physiological ratios - regulating nutrient/waste/drug concentrations at the level of single cells or small cell clusters (136); the generation of biophysical and chemical gradients - being exploited in several studies of directional cell migration and differentiation (112, 137-143); and the control of fluid shear stresses independently of gradients by varying flow rates or channel dimensions (112, 144, 145).

Control of cell patterning has proved very valuable. For instance, different cell types can be coated in numerous patterns by using several methods such as applying laminar streams to plate cells or ECM proteins (112, 137), positioning micropost between adjacent cell types (112, 146), microcontact printing ECM in distinct positions inside the channels (112, 147-149), or by directly incorporation of cells embebbed in 3D ECM gels (112, 150-154) or multicellular scaffolds from tissue engineering (112, 154-156). These microdevices are therefore well suited to control cell-cell and cell-matrix interactions, and to have remarkable impact and potential to study from human physiology models of human organ to the biological interactions down to the cell and molecular level (136).

Automation in microfluidic cell devices can be extended to culturing cells for several weeks under precise defined conditions without manual intervention, leading to standardized manipulation, monitoring and sampling of cultured cells, as well as allowing, in some particular cases where cells can present low rate of cell division and growth, a continuous mode of culture in same cell chamber by regular and constant replacement of media (111, 157).

As referred above, PDMS has offered a high potential for the explorations of BioMEMS for the live cell imaging, as well as in combination with fluorescent live cell imaging, allowing a powerful characterization of a multitude of cellular responses on a single cell, individual cell populations or tissue aggregates. With microfluidic devices, cell growth and regulation of cell number and size inside the chambers can be performed on real-time, as well as the monitorization and analysis of the dynamic of protein secretion and signaling pathways (111, 124, 158-169).

In this sense, making PDMS prototypes for iterating on a new design concept is easy approach; however additional issues start to appear for scale-up of systems and their commercialization.

1.3.4.1.2. Challenges and Troubleshooting to use microfluidic cell culture

Considering all advantages of PDMS, that allow its rapid expansion in both technological development and number of publications, it is worth mentioning, and as a consequence of their intensive use and results, that it have been identified several limitations including reliability, robustness, manufacturability and scalability on the implementation of this material in biomedical research (136, 170).

PDMS is a hydrophobic and porous material, and as a consequence PDMS has been found to adsorb hydrophobic molecules such as lipids or small molecules, from culture media into PDMS, which can influence critical cell signaling dynamics. In order to reduce the effects of adsorption to PDMS and to maintain good cell conditions, it is needed to replace the culture media constantly or permanently (for instance, by pumps). Furthermore, considering their small volume effects reflecting physiological cell microenvironment – faster consumption of nutrients and an increase of concentration of metabolites or secreted molecules – these small volumes also demands more frequent replacement of media.

Another pertinent aspect of PDMS is its porosity and permeability to gases, once during an experiment the liquid inside the microchannels can rapidly evaporate, making impossible to follow, for instance, for long time (days, weeks or months) cell perfusion experiments. In order to overcome this point, several aspects can be optimized such as to place the device in an environment with high humidity, for instance, by using conventional incubator connected to a humidifier, or by building on-chip media or PBS reservoirs in order to submerge totally the biochip inside the reservoir (162, 171-173). In addition, this incorporation also provides control on system of temperature and concentrations of oxygen and carbon dioxide.

If PDMS is not completely cured during a couple of hours between (60 – 80) °C (n.b., temperature and curing time are initially determined considering the complexity of the structure, for instance, a simple microchannel or a microchamber with several pillares), and/or by varying significantly the ratios of mixtures of silicone and curing agent, these factors can be toxic for cells (174).

Sterilization process by cleaning the device and glass with 70% of ethanol let it dry during some hours and to submit to the oxygen plasma, and further autoclave process or UV lamp, can improve biological compatibility and less inert to the cell adhesion. In this context, the PDMS surface can change

temporally the level of its hydrophobicity. This factor is a fundamental property for the bonding of the structure, for capillary driven devices and it also affects the level of adsorbance. As already mentioned, oxygen plasma can be applied in order to decrease the contact angle, though such hydrophilicity is unstable in air and fades away with time (~30 min). In this context, after application of oxygen plasma on the surface, the channels are ready for biofunctionalization process by coating it with proteins (matrigel), such as fibronectin or collagen (as used in Paper I), or mixture as dopamine solution in Tris-HCl (as used in Paper II and III).

Last, for manufacture and distribution of PDMS there are some restrictions about the scalability, because high throughput methods such as injection molding, rolling and embossing are not suitable for PDMS material.

Given these limitations with PDMS, in recent years microfluidic community have explored alternative materials for example thermoplastics, polystyrene and cyclic olefin copolymer, paper, wax and cloth (175-178). Polystyrene should be a good options over PDMS for many cell biology applications, because the use of polystyrene reduces many material property issues associated with PDMS, including the absorption of small molecules and evaporation though the device, and polystyrene can be handled and packaged easier for use and commercialization (112, 122, 179).

Cheaper materials as paper, wax and cloth have been explored for point-of-care applications in low-resource settings. Being cheap and easily incinerated, they are ideal choices for settings safe disposal of biological samples (180-182).

Another important aspect to be considered is the simplicity of final μTAS solutions, as the ultimate sophistication, for general cell assay design and application, which should be viewed through the lens of single-step, automated, portability, rapid-feedback and user-friendly and end-user (21).

The question how the user will interact with this new technology is a permanent and critical aspect discussed by biomedical engineers.

The ultimate use should be an ultra-simple to operate device and the provision of qualitative or quantitative output that can be transduced with low-cost and ubiquitous equipment (for example, by using a mobile-phone, camera or scanner). Consequently, these devices could be achieved by integrating a simple flow design with passive pumping, valving and in-line sensors (e.g., flow pressure, temperature, pH, oxygen, glucose, lactate, electrical conduction approaches), that only require a micropipette to operate, cheap photodetectors for the rapid optical readout or an incorporated microscopic and microfluorimetric imaging capabilities to screen overall system performance in real-time (112, 183, 184) .

The biosensing field integrates the optical, electrical, magnetic, acoustic and piezoelectric detection principles, and the biosensors are extensively used inside the microfluidic devices (112, 136). Considering their tremendous potential in the new digital era as smarter solutions (i.e., by the convergence of big data and the Internet of Things), the availability of such sensors would significantly enhance the system functionality and be of benefit for the translation of the model from the lab to the personalized medicine concept (136). More concretely and recently, several studies have reported the incorporation of sensing tools inside the microfluidic based culture such as a set of microelectrodes for monitoring the transendothelial electrical resistance (TEER) (185, 186), sensors coupled with microbioreactors for cell culture-based assays to control the cell culture parameters such as temperature, cell loading, media perfusion and detection (187), either sensors for studying the

mechanism of cellular metabolism and drug effects by rapid detection of concentration change of cellular acid metabolites in the extracellular microenvironment (188).

In recent years, a lot of efforts with this perspective behind have been developed in microfluidic area for biology, diagnostic and clinical research and applications (175, 189-197). In diagnostic area, an excellent example is the paper assays, which are single-step, portable, and user-friendly microfluidic solutions and where their technology is implicit but not visible, allowing their use as access diagnostic in the developing world and also increase their factor in developed world by enabling in-home testing and treatment (175, 181, 198).

Another good example in diagnostic and clinical research is the use of ultra-low volumes of biofluids for the sample processing and that can usually be accomplished rapidly and easily. A concrete example is the rapid purification and analysis of neutrophils, which have been developed in several studies in recent years for clinical and research applications (191, 199-201).

Other example - identified in this work, but being a project more ambitious in the early future, which have been gained attention from pharmaceutical manufacturer as AstraZeneca (21)- is the development of a platform which aggregates interests from biology, diagnostic, cell/drug development and cell treatment/therapy research (as, Immunotherapy) by using organ-on-a-chip or disease-on-a-chip. However being still in its initial phase, there are some challenges that should be resolved on its integration, for instance in our days, this approach requires the use of external pumps (syringe or peristaltic pumps) or pneumatic fluid (or pressure pump) to generate continuous perfusion to specific shear profiles (e.g., to mimic the shear stress on blood vessels or organoids) (112, 202, 203). And from the view presented above, it should be imperative to find simple approaches and limit the use of external apparatus and to cheaper appropriate materials, whenever possible.

1.3.4.2. Recent developments in microfluidic for immune cell culture systems

As it was discussed in **section 1.3.2**, Fundamentals of Microfluidics Devices, the principles of micromanipulation of biologic targets are dependent on the type of target and the level of selectivity and precision to be achieved. In this chapter, the objective consists to present recent developments in microfluidic for immune cell culture systems associated in the first plan with the study of the microfluidic flow as a carrier fluid, and in a second plan, with the study of the behavior of biotarget – macromolecules, cells, tissues, organs – in such microfluidic flows.

1.3.4.2.1. Microflow transport of biological targets

A variety of complex physiological processes use biochemical gradients of chemokines or growth factors, as a key mechanism to impart distinct signaling to cells in space and time (19, 204). Some cells, including fibroblast, leukocytes, endothelial and neutrophil cells, in the presence of delivered chemokine gradients become motile and display persistent, directed motion as single cells or collectives towards these molecules, a process known in the cell migration field as chemotaxis (205). This innate ability to migrate is implicit during the immunity response, wound healing, homeostasis, angiogenesis and metastatic progression (204, 206, 207). *In vivo*, soluble biochemical gradients arise through the diffusion of paracrine, autocrine and endocrine cell secretions, and from a direct interpretation of perceived concentration on cells, gradients can induce distinct signals to adjacent cells based on their proximity to the gradient source, such as differentiation and proliferation (204).

In this context, microfluidics provides a useful tool to examine complex interactions of various micro environmental components with spatial and temporal control in a wide range of applications in biology, pharmacological, biomedical, and clinical research. Microfluidic gradients generators in micro-compartmentalization have been used to create confined and separate compartments in a single-device, allowing high potential of parallelization, throughput screening and reproducibility (208). Additionally, 3D ECM compartmentalization has been another alternative to investigate signaling mechanism involved in chemotaxis, by incorporation and polymerization of ECM solution inside the compartments (19, 208-214). Although 3D ECM/hydrogels have also been utilized as cell self-organization matrices with one or more gradients at a time by molecular diffusion, these systems are still lacking of spatial and temporal controllable and reproducible chemotactic gradients (19).

Comparing to conventional cell migration assays, microfluidic devices can offer highly controlled chemical gradients, allowing a powerful and multiple research approach for studying gradient sensing and chemotaxis of different cell types conjugated with different types of flow-based or flow-free devices (19, 204, 215).

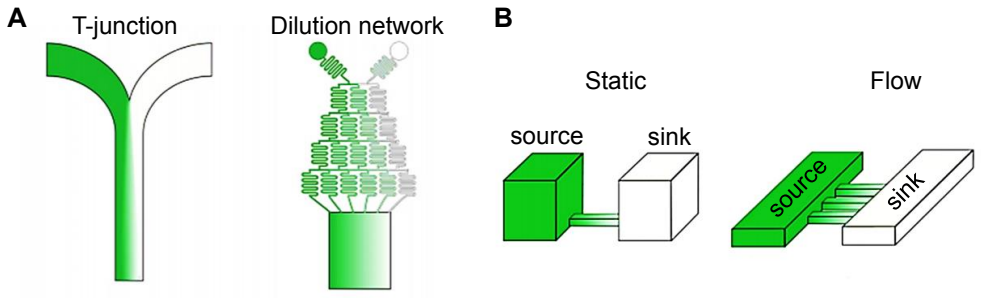

Figure 1.3.4.2.1.1 Microfluidic gradient generation designs. (A) Microfluidic gradient generators with only flow based. (B) Microfluidic gradient generators with only diffusion (204). Adapted from Lin B. et al., 2015. Originally published in *Front. Bioeng. Biotechnol.* https://doi.org/10.3389/fbioe.2015.00039. Copyright 2015.

The flow-based devices are defined as stationary steady dependent on laminar flow mixing in microchannels to generate highly controlled gradients profiles without changes over time at a specific point in space inside the system (19, 204, 215). On the other hand, and considering our focus in this work (Paper II), the flow-free devices are characterized as transient state where a concentration can change over-time, by free-diffusion of chemical or biological molecules in a static fluid environment between a source and a sink (19, 204, 215). These systems are less dependent on external setups, and the flow does not induce significant shear stress on cells as in the flow-devices, being advantageous for cells with low adhesiveness, in suspensions or normally residing in flow free environments (19, 204, 215). It is worth nothing that as opposed to flow-based devices, in transient systems the spatial gradient profile of diffusion may take a substantial amount of time to reach steady state, which may be depended on the distance, material and cell level expression (i.e., phenotypes to the stimulus), between source and sink (19, 204, 215).

For the conception of this type of devices, several strategies need to be adopted as physical barriers to increase the fluidic resistance in order to control the free chemical diffusion, such as decreasing the height of the connecting channel, integration of porous membranes or thin filters, or incorporations of resistive 3D extracellular matrix gels. Although this prerequisite increments the level of complexity of the microfabrication process, this step also contribute for the simplicity of device operation, without additional and external equipment, becoming more attractive to biologists (19, 204, 215).

Over recent years, innovations in developing new microfluidic devices for generating chemotaxis that mediate various immune responses, with flow or free diffusion system, have evidenced promising progress (216-222). Tong et al. assembled a microfluidic migration chamber that utilizes a self-sustaining chemotactic diffusion gradient to induce locomotion of single-cell with direct visualization of migratory tracks (218). Ricart *et al*. presented the DC migration in competing chemokine gradients on a 2D substrate by using a microfluidic network gradient generator (215, 217). Haessler *et al*. demonstrated using a flow-free microfluidic gradient device where cells significantly migrate towards the CCL21 gradient over a competing CCL19 gradient in 3D ECM (215, 216). However, these approaches still do not incorporate a controlled chemotactic stimulus 3D gel assays and require the use of expensive and external pumps and cumbersome tubing setups. Resolving this paradox requires several challenges in the development of *in vitro* models that can replicate key features of the complex immune cell behaviour in tissue, and more specifically, to ensure that effector cells produce enough signals to form a noticeable gradient over long periods of time that target cell can sense, and may evidence the directional decision making process toward free-diffusion biological gradients inherent to tissue resident immune cells.

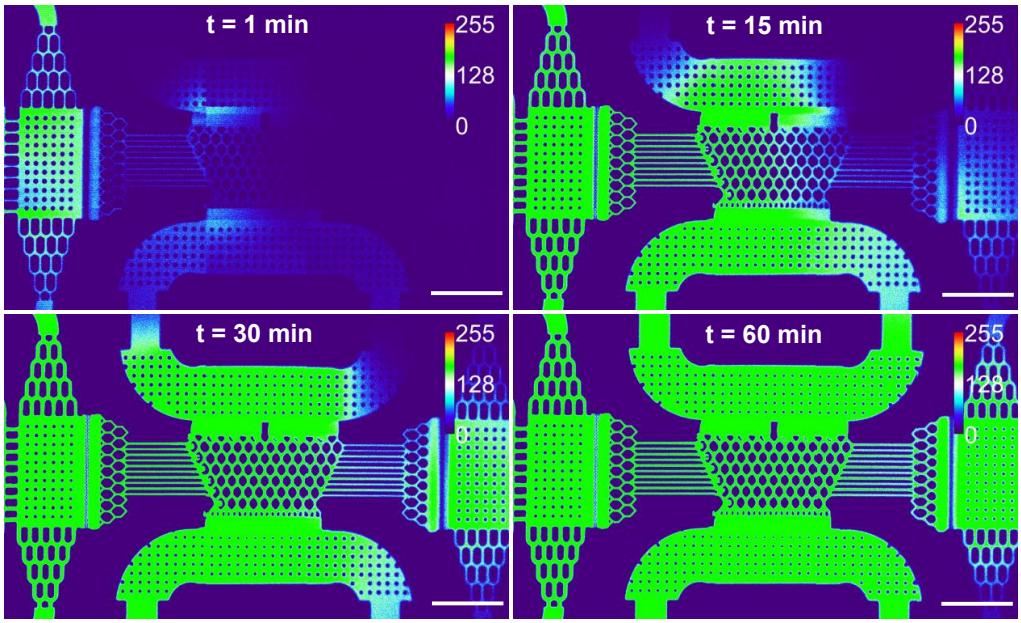

Figure 1.3.4.2.1.2 Example of a diffusion process inside a structure along time (Paper II). Fluorescent images representing the time evolution of the fluorescent dextran dye concentration profile across the structure at 1, 15, 30 and 60 min after loading in lateral feeding channel of the source side. Scale bar: 550µm.

1.3.4.2.2. Biological target: immune cell-cell communication

In this topic, microfluidics devices for cell-cell communication and their applications will be briefly detailed. The ability to study cell signaling in single level or in small population in microfluidics will open new avenues, increasing information and understanding of cell heterogeneity in cancer, stem cells, metastasis, oncology, immunology and more (4, 14, 214, 223). In particular, immunology and cancer research have been the biggest driving forces for the development of assays in microfluidics for cell-cell communication at single or multi cell level (4, 14, 214, 223, 224).

In this context, the immune cell-cell communication at a single-level-on-a-chip and of a small cell population in an tissue/organ-on-a-chip will be studied. It is worth mentioning that the mechanism of intercellular signaling to be studied will be subjacent to the type of device (4, 14, 214, 223-225). At single (or few cells on regime)-on-a-chip, these devices would mainly be used to study juxtacrine signaling, or paracrine signaling (< 50 μm), or gap junction signaling; at multi cell level as tissue/organ-on-a-chip would allow to study paracrine (> 50 μm), endocrine signaling and synaptic/direct signaling (4, 14, 214, 223-228).

1.3.4.2.2.1. Immune single cell-on-a-chip

At single level, the mechanisms of intercellular signaling of interests are juxtacrine and paracrine interactions that play a central role in immunity, responsible of initiating and mediating critical development (priming, selection, proliferation, differentiation) and functional (cytolysis, cytokine and antibody production) immune response (223).

Microfluidic at single-cell level offer the ability to study two cells next to or near each other in two orientations, horizontal or vertical. In this context, there are many methods and tools in microfluidics to pair cells in either vertical or horizontal orientation and to exert cell-scale control to define cell-cell interaction (4, 223). Microscale toolkit for single-cell analysis of intercellular interactions can be categorized in 7 types: (i) microwell arrays (229-234) ; (ii) hydrodynamic traps (9, 29, 232, 235-237) ; (iii) valves (238); (iv) droplets (148, 239-242); (v) micropits (243, 244); (vi) electrodes (245-250); and (vii) acoustofluidics (232, 251, 252) (**Figure 1.3.4.2.2.1.1**).

For microwell array, this technique consists to form discrete co-cultures by sequentially dispensing each cell population onto an array or by gravity. In general, microcell arrays are assumed as open systems; the horizontal and vertical cell pairing method using microwells have been developed and used in recent years (4, 223). For enclosed microfluidic systems, the cell manipulation and horizontal or vertical entrapment can be achieved by hydrodymanics, with traps, valves, droplet cell-encapsulation and micropit approach, and/or other physical phenomena as electrode-based (integrated electrodes use dielectrophoresis to trap/manipulate the cells at the electrode interface) or acoustofluidics (by surface acoustic waves approach) (4, 223).

For immune applications, much work have been carried out to recreate multiple dynamic aspects of *in vivo* immune migration, as to monitor spatial interactions of immune cell heterogeneity as such between T-cells and dendritic cells, to analyze their migration and the activation of killing lymphocytes (29, 170, 253-257). Considering the variety and complexity of examples in this field (257), it was decided to select and present some examples more direct and related with the background and type of platform developed in Paper I and Paper II.

At a single-cell level and with background more related with Paper I, more recently Dura *et al*. developed a microfluidic platform which allows high-throughput deterministic pairing of T cell to target cells with a defined contact time and to perform different scenarios for lymphocyte activation and stimulation in controlled microenvironments (9). Thus, the platform allows from different stimuli (B cells, antibodies or chemical agents) over time to capture the dynamic profile of Ca^{2+} response and to characterize how T-cell receptor (TCR) affinity affects Ca^{2+} spikes and the cytokines secreted. However, in this system the assays were performed toward early events of intercellular interactions (<20 min) and were not optimized to extend the measurements at various time scales (9). In this context, the same group by using the same platform decided to extend the measurements at 24h with NK cells (258). After cell loading and to keep the cells inside the traps after pairing, the devices were

disconnected from any external fluidic hardware while maintaining cell-cell interaction and pair within the array, between a standard incubator for culture and microscope imaging over ~24h culture period. The calcium flux to cytotoxicity was determined, as well as the strength of Ca^{2+} activation can be correlated with consequence in lysis and interferon-gamma (IFN-γ) production (258).

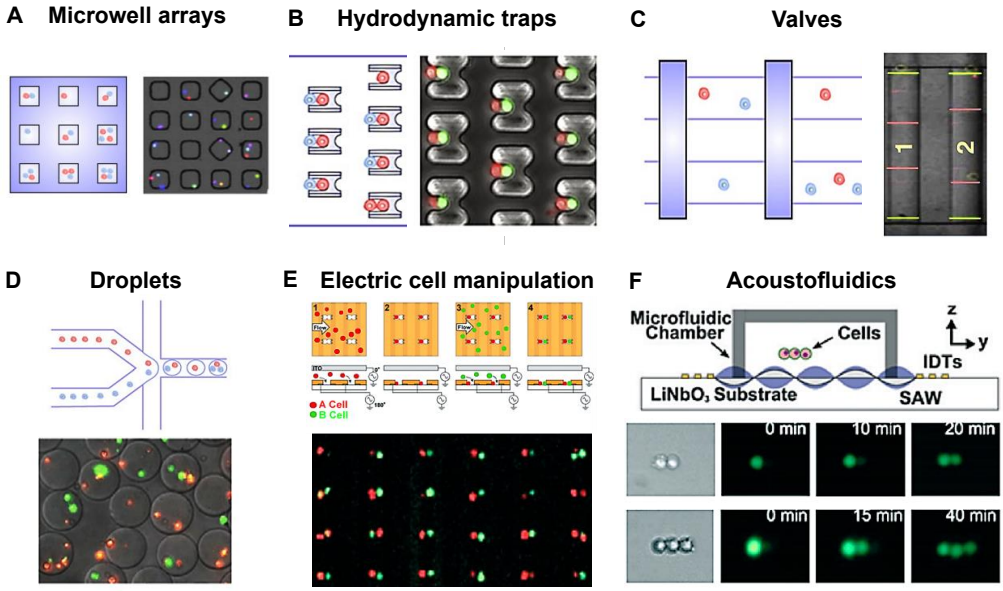

Figure 1.3.4.2.2.1.1 Microscale tools for single-cell analysis in intercellular communication. A) Microwell arrays: this system is a high-throughput method used to generate co-cultures by sequentially dispensing each cell onto the array and allowing cells to deposit into wells by gravity. B) Microfluidic cell hydrodynamic traps with specific size to hold two cells, only in order to ensure one-to-one interactions. C) Valves: control and manipulation of cell positions by hydrodynamic valves. D) Droplet approach for encapsulating cell pairs or clusters in picoliter emulsions of immiscible liquids. From Ref. (223) reprinted from Elsevier. E) Electrical manipulation: single cells can be manipulated and trapped horizontally or vertically via dielectrophoretic forces generated by non-uniform electric fields. Adapted from Ref.(4). D) Control and manipulation of cell by surface acoustic waves. Adapted from Ref. (4).

At the cluster-cell level and more related with the type of platform of Paper I, constant perfusion of compound such as nutrients and cytokines are an important technique used to investigate cell migration and adhesion. Kim and Moon *et al*. developed a model as inflammatory mimetic microfluidic chip, which measured cell leukocyte binding/attachment to cell adhesion molecules under flow conditions by controlling the types and ratio of adhesion molecules (259). In this approach, different coating levels and combinations of T cell attachment molecules (E-selectin; ICAM-1; VCAM-1) and immunosuppressive drugs (tacrolimus and cyclosporine) on the channel surfaces were used to analyze and measure the influences on adhesion under flow. This work addressed the deficiencies with *in vitro* and *in vivo* systems, proving to be as useful application in immunosuppressive drug screening (259). Sundd *et al*. used the perfusion to study neutrophil rolling under flow. In this model, microchannel surfaces were coated with different densities of P-selectin in order to identify the slings and tethers during cell rolling (260). They established that the sling length is dependent on the shear stress, and for high shear stress, this arrangement could demonstrate the mechanisms of how slings and tethers promote rolling (260).

At the cluster-level and in the context of Paper II, Jones *et al*. developed a platform, which mimics features of focal inflammation sites, by gradient formation that is relied on using the channels with a reduced cross section, allowing to establish the chemical gradient and without perfusion (261). For cell migration, this approach was characterized by the formation of chemotactic gradients inside the device mimicking inflammation by only free diffusion and in the absence of convection. The device was composed by 16 peripheral chemotactic chambers for chemoattractant diffusion tests, connected through the thin channels to a center chamber where cell were seeded and migrated towards them during 20 hours. Furthermore, a fluorescent elastase assay inside the chemotactic chambers was performed in order to demonstrate the cell recruitment by inflammatory conditons from the detection of elastin degradation by migrating cells. In addition, this device integrated channel bifurcations, which allow the observation among cells displaying increased chemokinesis, and their cell decision making process of chemotactical migration during their traffic through the bifurcation to higher gradient values. This microfluidic assay allowed analysis of the behavior of a mix of primary neutrophils and monocytes when subjected to various chemoattractant and immune modifiers. This platform evidenced a high output through the multiparameter observations of interesting points of inflammation process, uncovering more aspects of co-cultures of monocytes, neutrophils and, elastase and their migration (261).

Our group has also been developing over years platforms to analyze directly cell-cell migration (more specifically, interactions between LPS-primed bone marrow-derived dendritic cell (BMDC) - T cell, LPS-primed BMDC – immature BMDC and a combination of BMDC infected with *Mycobacterium avium* – T cell), which allows us to follow cell migration towards signaling of other cells, using gradient formation only by diffusion (20). The challenge in this platform has been the generation of free-diffusion gradients of cytokines and chemokines produced during infections and immune reactions by effector cells, in order to produce enough signal concentration to form a noticeable gradient over long periods of time (>24h) and that the target cell can sense. The implicated advances of this model using free-diffusion in transient state are the fact that the system circumvents the need for external pump, cells are not induced with shear stress, without convection the cells signaling produced to the diffusion gradients is not disturbed over time and it is advantageous for cells with low adhesiveness (as T cells). The device incorporated two compartments – infection side and migratory/recruitment side – were connected by a honeycomb network of bifurcated microchannels which allowed the diffusion of cells signaling agents over time. To control the free molecular diffusion, the conception of this device integrated physical barriers to increase the fluidic resistance, such as applying with a high ratio of height between chambers and small channels and the incorporation of thin filters (with openings of 2 x 2 μm), which also worked as bacterial filters on infection side, preventing bacteria and active cells enter on the network and permitting migration only from the recruitment reservoir. As a result, the network of bifurcated microchannels allowed to monitor in real-time the cellular decision-making process based on the evolution of produced gradients from immune response over time, and to follow cell decision on path length in a gradient context. The benefit of this device is the diverse output from multiparameter observations in several interesting points during the evolution of immune response, being a valuable tool for studying cellular migration and self-organization in infections, cancer, and tissue and wound repair (20).

1.3.4.2.2.2. Immune organ-on-a-chip | Disease-on-a-chip | Cancer-on-a-chip

As a result of natural evolution in microfluidic field and the continued interest to investigate, by biochemical mechanical and spatiotemporal control, the basic mechanism of organ physiology and

disease, the development of "organ-on-a-chip" has been a result of continued progress and integration of microfabrication techniques, 3D biology and microfluidic technology.

From a reductionist concept of an organ in the human body as individual tissue entity that serves a common function to the translational research, organ-on-a-chip can be assumed as a 3D microfluidic cell culture that mimics some functions of a biological organ by integration of microengineering. In order to achieve the main biological function of an organ, it is needed to incorporate elementary functions *in vitro* such as tissue microarchitecture, perfusion, spatiotemporal chemical gradients and mechanical forces such as cyclic strain, compression, and fluid shear stresses.

Over the past decade, many microfluidic 3D systems have been developed to recreate structures and functions of various organs such as liver (144, 146, 147, 156, 262-269), kidney (270-273), intestine (274-277), lung (202, 262, 278-281), heart (149, 153, 282-284), muscle (285), adipose tissue (156, 262), bone (286-288), marrow (289), breast (209, 290, 291), cornea (292), skin (293), blood vessels (128, 185, 202, 278, 294, 295), nerve (154, 296-299), and blood-brain barrier (145, 185, 300-302). Many of these models can represent the next step towards developing of modular complex of multi-organs-on-a-chip to a complete human-on-a-chip, promoting for completely animal-free screening (136, 303).

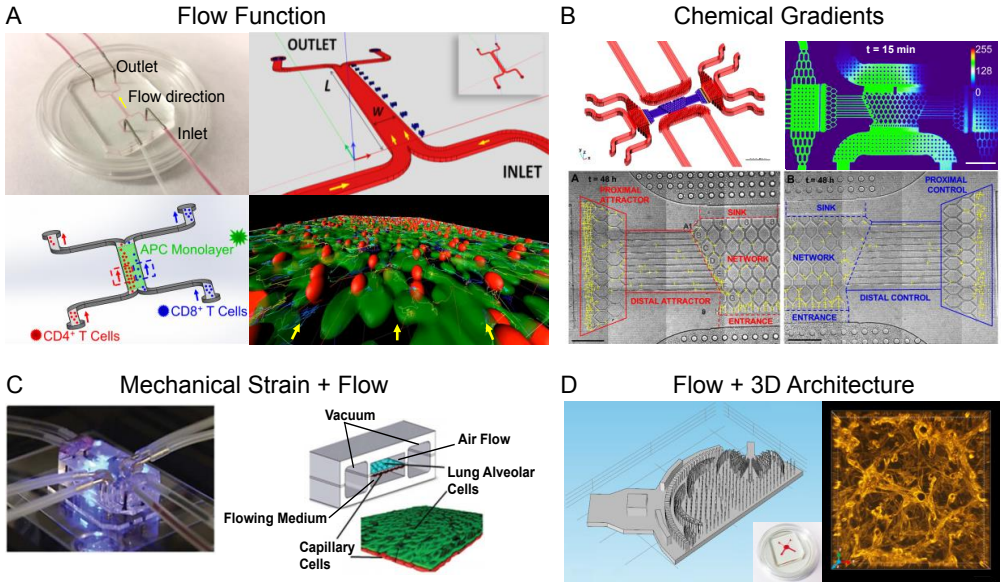

Figure 1.3.4.2.2.2.1 Chemical and mechanical microenvironments in microengineered organ-on-a-chip. A) Flow function (Paper I): microfluidic microchannel for cell attachment and detachment tests applying of continuous hydrodynamic flow that produces shear stress which mimics an inflammation process. B) Chemical gradients (Paper II): Diffusion flow-free platform to study cell migration in distinct compartments under inflammatory conditions. C) Mechanical Strain+Flow: A human breathing lung-on-a-chip fabricated in PDMS that recreates the structural cell organization, mechanical stimulus and microphysiological functionality of an alveolar-capillary interface of a living human lung. Reproduced from Ref. (202). D) Flow + 3D Architeture (Paper III/Manuscript): This cell chamber was developed to promote the growth of FRC scaffold around PDMS pillars/filters through the application of continuous flow, which produced both mechanical and chemical stimulus.

It is worth mentioning that the degree of complexity of the organ development achieved in many of these devices might be characterized by organoid level. In most studies, they are characterized as 3D miniaturized and simplified version of an organ created in vitro with realistic micro-anatomy and they can be derived from few cells (homo or heterotype) from a tissue, embryonic stem cell, as well as from the insertion of living tissue or biopsy samples (112).

These systems have revealed that induction of fluid flow and shear stress enhance the differentiation, function and long term of viability of several cell types. For example, Dongeun Huh *et al.* utilized human lung cells to develop an organ-level lung platform and cells kept their functional state for at least one month in culture (202). With this ability, some future studies could be performed on clinically relevant time scales for responses of chronic pathophysiological disease (112).

Furthermore, the permanent perfusion allows testing microenvironmental molecular signals, such as to study the adsorption, distribution, metabolism, elimination and toxicity (ADMET) of soluble molecules – such as chemicals, oxygen, cytokine gradients (e.g., directly induced from external source; or from autocrine, paracrine, justacrine, gap-juntion, synaptic signaling from cell populations), hormones secreted from a signaling cell (as endocrine signaling between organs), angiocrine cues (as soluble signals from endothelium), drugs – with precise control of actuation at the level of single cells or small cell clusters, and entirely *in vitro* assays rather than in animals, as a common method used in pharmaceutical industry (112). As well as, the study of interactions of circulating cells, such as various types of immune, blood, and tumor cells, or even interaction with bacteria or virus.

Additionally, the well-defined bioarchitecture of organ-on-a-chip and the control and predictability of flow behavior and particles distribution inside the microchannels, allow by simulations to model the fluid dynamics interacting among different metabolites, gases, cells and the inner structure of channels (112).

As the main attribute of microsystems engineering is their capability to build a synthetic culture system with control in many different parameters – the bioarchitecture of scaffolds; transcellular chemical, molecular and oxygen gradients; flow levels and mechanical foreign regimens; integration of high-throughput testing by fabrication of arrays from cell hosting chambers – and further, with the high freedom degree to vary these parameters/conditions "independently" while in simultaneous analysis of high-resolution, real-time imaging of molecular-scale events in a 3D organ context (112).

In this context, these tools are well suited to study human physiology and pathogenesis by effectively building microphysiological models of human organs and innovating many areas of basic research and drug development (136, 304).

Recent studies of translational medical research have suggested that many aspect of the human immune response may be focused more on complex human factors and conditions, than relying purely on mouse models or reconstituted "humanized" mice. In this context, microfluidics provides the tool to create advanced *in vitro* models of cell culture with potential to assist in understanding the physiological events that define the immune response in humans (14, 136, 304-308).

In this sense, such platforms would improve the predictability of human response to drugs and reducing expenses with the clinical studies, as well as to redefine this technology to develop personalized models/assays of health and disease to immunotherapy (14, 112, 136, 214, 304).

Ramadan and Gijs, 2015 (136) published an excellent review related with organ-on-a-chip models for translational immunology, and they categorized **the microfluid-base physiologically based in three**

models: physiologically based pharmacokinetic (PBPK) models, disease models and inflammation models.

The physiologically based pharmacokinetic (PBPK) models are entirely correlated with drug screening and the study of cell/tissue-drug interaction research, being both the major driving force for the progress of in vitro models of human organs (144, 178, 262, 303, 309-317).

The purpose of disease models is completely related with PBPK models, once the recreation of *in vitro* models of diseases within an "*in vivo*-like" microenvironment enables studying the cellular interactions within and with the matrix, and from the control of the physio-mechanical properties to understand the fundamental biological processes and consequently to explore new therapeutic strategies (210, 279, 290, 313, 316, 318-324) .

Inflammation models are related with the focus on this thesis and with Paper III. Currently, several studies have evidenced that inflammation and immune responses are implicated in the pathogenesis with a variety of diseases, such as chronic vascular diseases (325), myocardial ischemia (326), acute cerebral stroke Alzheimer's (327-329), diabetes (330, 331), hypertension (332) and cancer (5-7). And as consequence, in the recent years inflammation has been gained special attention in clinical research.

Immune organs-on-chip

As it was referred at the beginning of this dissertation, the inflammation is a process resulting from a tightly regulated cascade of immunological, physiological and behavior processes that are triggered and regulated by cytokines. In this sense, ongoing research to identify tissues, cells, proteins and genes implicated in the normal inflammation cascade and in the dysfunctional cell signaling continues to provide new insights into the biological processes. However, the complexity of various forms of inflammation considering their location in the tissue, type of tissue, timing, magnitude of inflammation spans, etc., demands quantitative and qualitative analyses/assays, from new *in vitro* models (333, 334).

In this context, epithelial tissues – intestine, lung and skin – have gained attention in the recent years, considering their role in the regulation of immune homeostasis and inflammation as first protective barriers that physically separate an organism from the outside world. Recent research in signaling pathways controlling epithelial cells responses from microbial, immunological, physical and chemical attack on tissue inflammation, have been developed considering these specific organs-on-a-chip, including gut (275, 335-337), lung (202, 338) and skin (339).

Furthermore, with an urgent need and interest to engineering functional and living immune tissues, which can recreate the immune cell development and reactions at innate and adaptive levels and with control of spatiotemporal analysis of living systems, more and more studies have developed several strategies for the conception of a minimal functional unit as organoid, or as organ-on-chip in immune engineering (340). As the main driving force after the conception of ex vivo 3D immune tissue/reactions, is the high potential for rapid development of high affinity antigen-specific antibody secreting cells, target-specific T cells, as well as new paths towards immunotherapies and vaccines (36, 340, 341).

Several studies have been focused on the factors that influence the immune cell-immune cell interactions, immune cell-stromal cell interactions, signaling proteins that induce autocrine-paracrine signaling, and extracellular ligands (36, 304, 340-344).

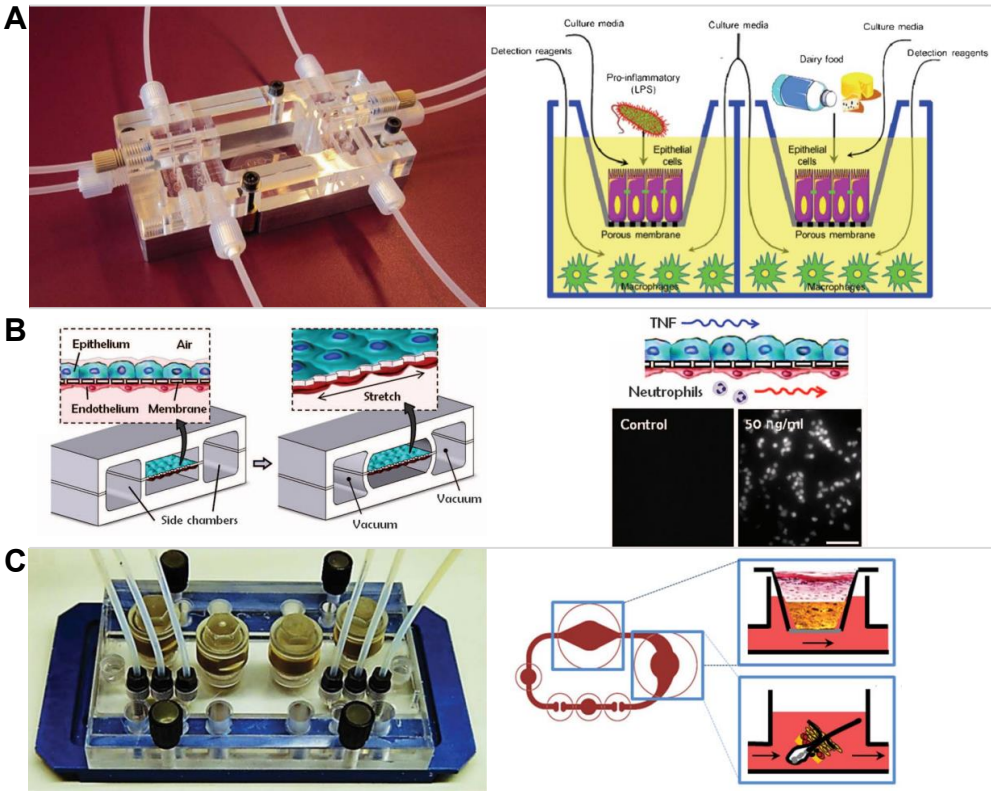

Figure 1.3.4.2.2.2.2 Dynamic organ-on-a-chip systems of human (a) gut, (b) lung and (c) skin containing subsets of immune cells. A) Microfluidic NutriChip interface unit (left image) for the co-culture of gut epithelial cells and macrophages and a representation of underlying tissue culture principle (right image). Reproduced from Ref. (335) from the Royal Society of Chemistry. B) Representation of the dynamic lung mimic device with compartmentalized microchannels to recreate the alveolar-capillary barrier, mimicking physiological breathing movements by using vacuum to the side chambers (left image). Fluorescently labelled human neutrophils (white dots) after introduction into the vascular microfluidic channel, interact to the activated endothelium cells (right image). From (202) reprinted from AAAS. C) A photograph microfluidic Multi-organ-chip (MOC) platform (left image) with built in micropump and microchannel circuit with pulsatile flow of medium and incorporating two 3D tissue culture spaces as shown in the shematic representation (right image). Reproduced from Ref. (339) from the Royal Society of Chemistry.

As applications of microfluidics devices at organ-on-a-chip level to immunology, microfluidics has been used to recreate 3D complex immune structures on-chip to analyze the effects on concentration and spatiotemporal diffusion of paracrine signaling in cell-cell communication (345), to assess leukocyte extravasation and its interstitial migration in 3D microenvironment (346), to mimic and understand the importance the lymphatic drainage in vascularization (347, 348), and to study the migratory ability of leukocytes and their spontaneous organization during cancer (349).

However, only a few *in vitro* platforms - but not as organ-on-a-chip level - have been established in the last years to mimic human immunity response and reaction from the T cell- DC interaction, with emphasis on T cell activation on a stromal network, in a 3D complex way using tissue and organoid

models (43, 342, 343, 350-353). Based on this approach and from the bioreactor concept, Christoph Giese and colleagues in 2006 developed, through a bioreactor, a process to support self-assembly of human lymphatic tissues, and to recreate the human artificial lymph node (HuALN) architecture *in vitro* to follow the T-cell activation (342, 343). This system consisted to integrate macroporous matrix sheets in a bioreactor and to provide by continued monetarization over maximum 14 days of cell feeding rates, gas supply and recirculating systems. Operated during 14 days, this system proved long-term viability and reactivity of lymphatic tissue with a significant TNF-α response profile with LPS stimulation at day 11. In addition, the functionality of this system was also proved by supporting T and B cell swarming within a functional primed DC network, and T cell clustering (342, 343).

Ashley Ross and colleagues developed the lymph node slice-on-a-chip as a system for local chemical stimulation of lymph node tissue on a microfluidic device with 200-300 μm spatial resolution sufficient to follow discrete regions as the B cell and T cell zones (353). The system consisted in the assembling and alignment of 3 layer of PDMS related with the channels, ports and perfusion chamber respectively. The control of spread and quantity of proteins in these channels, and consequent diffusion and convection through the tissue, was regulated by flow rates. The stimulation of a model therapeutic, as glucose-conjugated albumin was performed to specific regions of the lymph node simultaneously in order to mimic the complex intercellular signaling. This experiment allowed to target and to follow the level of retention of the drug in different B cell and T cell zone, proving the use of this platform for future studies for detecting immune responses in small clusters of cells in lymph node and the development of new drugs (353).

However, none of these studies have been able to reproduce an artificial lymph node *in vitro* with the ability to produce a dynamic system very similar to lymphatic system - specially particular regions as paracortex T cell zone, which can support the artificial tissue as a scaffold allowing cells self-assemble into tissues by control of molecular and biophysical mechanisms - and simultaneously, to follow the immune responses in human health and disease tissue. In this context, our Paper III emerges to find new answers for this challenge and needs at organ-on-chip level in immunoengineering.

Challenges and Troubleshooting to use organ-on-a-chip for translational immunology

The development of individual micro-physiological models *in vitro* and afterwards, their lego-integration of multi-microphysiological models, definitely offer a high potential to provide a deeper understanding of the physiological events on the origin and progression of diseases, becoming in this way one of the outstanding challenges in modern medicine (112, 136, 354).

Furthermore, when compared to the use of conventional *in vitro* assays or the *in vivo* animal models, the high-throughput screening of a large number of compounds with different stimuli-response in real-time and the ability to monitor in real time the signaling and cell-cell or organ-organ interactions, attribute these microphysiological models a strong potential to achieve a compact immune analysis system for disease modeling, drug discovery, toxicology and personalized medicine (112, 136).

Although there have been recent success demonstrating that these micro-physiological models can mimic specific organ-level functions, many challenges are still ahead and need to be overcome in order to be adopted as current in vitro models and as alternative to animal models (112, 136).

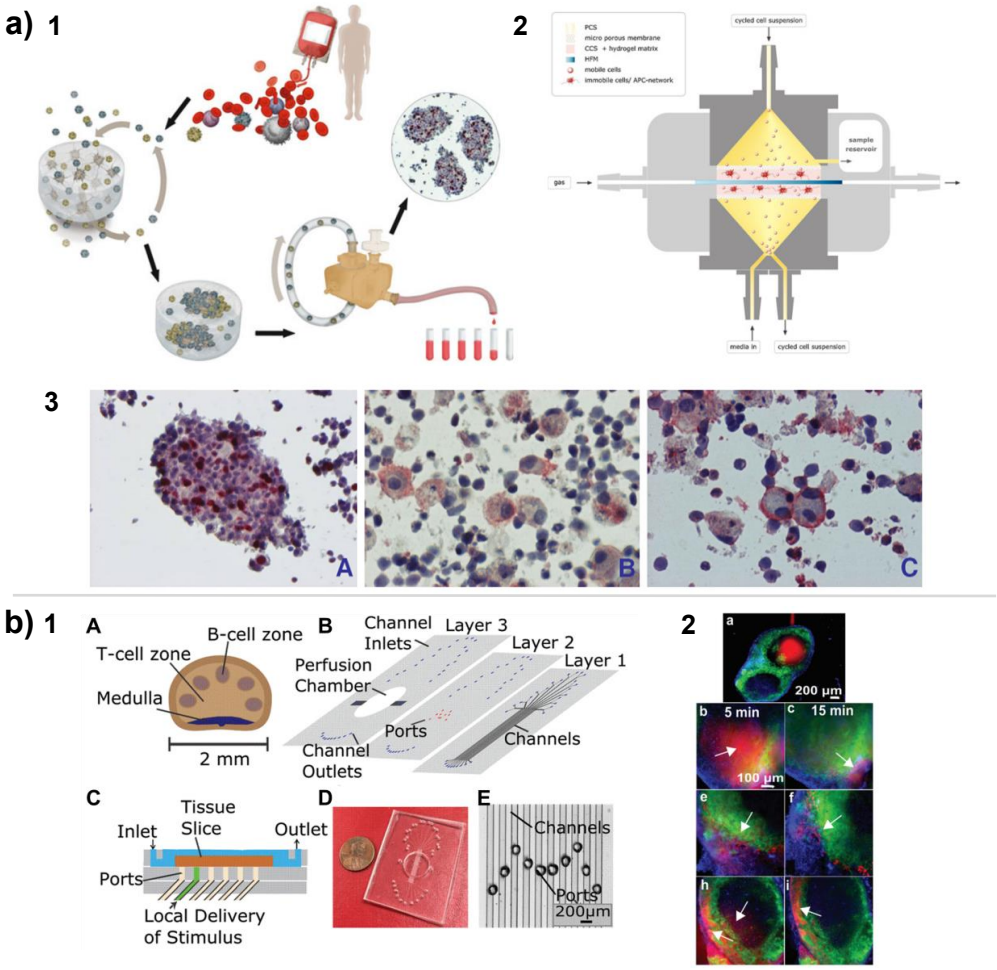

Figure 1.3.4.2.2.2.3 a) Human Artificial Lymph Node 1. Overview of the HuALN used for substance testing: different cells of the native immunity are separated from donor leukocytes, differentiated into mature cells (e.g. DCs), seeded in 3D macroporous matrix sheets and incorporated into a bioreactor device. **2.** Schematic representation of the bioreactor where media and cell suspension flow vertically, and gas supply perfuses into the system horizontally. **3.** Upon tissue culture completion, follicle-like spheroid formation and proliferation (image A; red staining), plasma cell (image B; red staining), and antigen-specific binding on plasma cells (image c; red staining) was confirmed histologically tissue slices. From (344) reprinted from Elsevier. **b) Lymph node slice-on-chip 1.** Schematic representation of microfluidic for local stimulation of lymph-node slices: A) key structural features of the lymph node; B) view of 3 PDMS layers with channels, ports and perfusion chamber; C)side-view of the device; D) photograph of platform; E) micrograph of the ports aligned over the microchannels**. 2.** Local stimulation of the T-cell and B-cell regions of lymph node slices on-chip a) Delivery of glucose-BSA (red) to the T cell zone. Images collected 5 min and 15 min after delivery to the T cell zone (b,c), B cell zone (e,f) and intersection of the two zones (h,i). Reproduced from Ref. (353) from The Royal Society of Chemistry.

Simplifying the resolution by decomposing the challenges into parts, the target of the single organ models should be previously established according to current challenges, some already mentioned in **1.3.3.1.2** section, including the reliability, robustness, manufacturing and scalability, integration of sensors, and cell source, before advancing on more complex multi-organs systems (136).

Some pertinent issues from microfluidic technology as the lack of a standard fabrication method, bubble formation during experiments, lack of standard "micro-macro" interfacing tools and the compatibility of an organ-on-a-chip system with respective biological protocol, are still big challenges for organ-on-a-chip technology (136). Furthermore, at this organ-level additional requirements for robustness and reliability are needed to be considered as to maintain the tissue/organ culture environment in ideal conditions keeping the organs models intact for a long time (e.g., weeks or months). And consequently, some solutions are needed to develop and integrate on the systems such as incorporation of automated sample injection, processing and collection, real-time monitoring and feedback system about analytes or biological substances (e.g. metabolities) which pass through different tissues mimicking the in vivo conditions (136, 354).

Another important aspect to be solved in order to validate *in vitro* models is to find a common cell culture media or blood substitute, which provide the necessary nutrients and growth promoting factors to keep the cells in an active state in an organ-model. A possible solution could be the development "in vivo-like" integrated organs on a chip with a vascular connecting network as a better approximation to the biological models (136, 214, 354, 355).

Regarding type of cells, the major advantage of the organ-on-a-chip is the employment of human cells in order to overcome some differences in metabolism between humans and animals. In this system, it is possible to adopt as a cell source immortalized cell lines, human pluripotent stem-cells (hPSC) (356), or primary cells and tissues biopsies - which are the most advantageous cell sources for microphysiological models, but due to ethical and regulation aspects, there are still limitations about the use of primary cell source for developing organ models on a chip (136).

1.3.5. Potential of ImmuneMicrofluidics

In the recent years, microfluidics have proved to have a great potential for the pharmaceutical and biotechnology industries (112, 357). Eric Sackman *et al.* has recently published a comprehensive review about the evolution made by lab-on-a-chip microtechnologies in recent years, and discussed in detail the impact of this technology on the challenges and opportunities in clinical and research area (21). The authors discussed in detail the status of various microfluidic applications, proposing them into three categories: (i) point-of-care testing devices for low-resources settings; (ii) research and clinical applications; (iii) in vitro models for drug discovery, diagnostics and research applications (21).

Access to health care in developing countries is very limited as the reduced access of the means or infrastructures to perform diagnostic tests and analyses. In this sense, it is urgent to reinvent alternative solutions to perform these tests and analyses as microfluidic technology. Over the years μTAS technology has developed platforms to perform a variety of diagnostic test with built-in analysis capability that are compatible with the infrastructures in the developing world. As mentioned above on the topic **1.3.4.1.2**, there are mandatory requisites to be followed for the development of this technology such as portability, ultra-simple to operate, rapid feedback where the provision of qualitative or quantitative output can be measured with low-cost equipment as a mobile-phone camera or scanner, and the materials to be used in these devices should be destructible (to avoid contamination), cheap and easy scalability to manufacture (21).

In the past years, several studies have reported the meaningful contributions of microfluidic to healthcare in the developing world, such as Chin and colleagues in 2011 developed a biochip that runs an ELISA-like assay in 20 minutes by using small amount of blood from a lancet puncture (175).

Rapidly assaying biofluids as research and clinical microfluidic applications offers new approaches to explore microscale properties that enable new applications in clinical assays. Among these properties are the possibility of using tultra-low volume of biofluids to be processed in rapid and easy bioassays, faster purification and cell analysis (201), and fast target analytes sorting across multiphase barriers by the dominance of surface tension at the microscale (193, 194). These techniques take advantages to reduce volume of sample processing from roughly hours to a few minutes, and improved sensitivities for protein or genetic purification assay by reducing the number of wash cycles required to carry out a macroscale experiment (21).

As a new class of microfluidic devices, organ-on-a-chip assays are definitely characterized by their high potential for drug discovery, diagnostic and research applications allowing the validation and prioritization of drug candidates, and the study the molecular mechanism of action and toxicities (14, 21, 112, 357). Considering the current paradigm of the pharmaceutical industry, in recent years with unsustainable R&D cost (358), the exclusivity on blockcluster drugs that is soon expiring for several companies, and fewer new drugs being approved by the Food and Drug Administration (FDA; as described by Hay *et al* (359), only 10,4% of all drugs that enter a phase I clinical trial will gain market approval), new alternative strategies for drug development are urgent to mitigate the costs (14, 21, 112, 357). In this context, new approaches are needed in order to improve R&D productivity and to increase the probability of new drugs to enter in the market (14, 21, 112, 357).

The final purpose would be a sophisticated human organs-on-a-chip assay which may help to test new drugs, to identify new biomarkers of drug efficacy, toxicity, disease response as well as for personalized cell therapy, being a value for clinical trials by increasing their predictability before an human testing (14, 21, 112, 316, 357).

As it was mentioned above, given the complexity of organ functioning and regulatory requirements, much more work is still required in order to adopt organ-on-a-chip methods in drug R&D. Although early developments in this area have been encouraging and promising such as in April 11, 2017 FDA communicated and signed collaborative agreement with EMULATE to use organ's-on-chips technology as toxicology testing platforms (360).

1.3.5.1. Immunotherapy: Vaccines and Oncological Research

Microfluidic technology is a prominent technology and with high potential to research and reprogram the interactions between tumor and immune cells (T cell education), as well as on the development of personalized medicine through cell targeted therapies or immunotherapies. This technology presents several advantages as on their ability to manipulate cell interactions in a reduced volume, with tight control of the microenvironment and real time monitoring.

Considering their versatility, Boussommier-Calleja *et al* (14) have propose that microfluidic assays could be further integrated as study platforms for cancer tests incorporating for example cancer-associated fibroblasts in order to model the immune response via the secretion of cytokines (361). Or with similar analogy to the organ-on-a-chip, to recapitulate for example the systemic nature of the

metastatic process in order to analyze the role and interplay of several types of immune responses simultaneously (136).

Furthermore, another potential (and ambitious challenge) of microfluidics to be exploited, would be the development of cell platforms for T cell education and for tests of cell-based vaccines for immunotherapies through manipulation of immune cell (14, 362).

In this sense, microfluidic system would have the potential to address personalized medicine not only at the diagnostic level, but also at treatment level by building patient-specific organ-on-a-chip microfluidic platform through patient-derived pluripotent stem cells (136).

2. OBJECTIVES

The overall objective of this thesis was to develop and optimize microfluidic devices to analyze the immune cell-cell interactions and reactions for extended periods of time. To achieve this main goal, four intermediate sub-projects and structures were developed:

- **Project 1:** Microfluidic device in stationary stage to analyze the T cell:DC interactions on a DC monolayer layer bound over a glass surface to understand the intercellular dynamics and physiological conditions in the LN (Paper I).

- **Project 2** *Patterns on glass for cell adhesion and sorting*: Microfluidic device in stationary stage to analyze the T cell:DC interactions and T cell: DC: FRC interactions. Gold patterns inside a microchannel was biofunctionalized with a series of antibodies specific to T cells, DCs or FRCs, and the glass was blocked to prevent non-specific cell-binding.

- **Project 3:** Microfluidic device in transient state to analyze immunological processes – infections and immune reactions – by the observation of immune cells migration and decision making process in targeted cells through the signaling of other effector cells, which produce a signaling gradient of cytokines over long periods of time (Paper II).

- **Project 4:** Microfluidic cell chamber in stationary stage to mimic the microarchitecture of immune environment and cell behavior in the T cell zone of a LN, being considered as a LN-T cell zone-on-the-chip (Paper III).

3. METHODS

In this chapter, a general sequence of key methods and techniques that was followed during the development of 3 papers will be provided. More detailed and specific materials and methods are described in each paper.

It is important to mention that during the period of this PhD, four projects were developed and of which result three papers:

- **Project 1**, *The intercell dynamics of T cells and dendritic cells in a lymph node-on-a-chip flow device,* associated with **Paper I**;
- **Project 2,** *Patterns on glass for cell adhesion and sorting - Fabrication and testing of a patterned microfluidic channel for cell-cell interaction in the Immune System;*
- **Project 3,** *Immune cells moving in a microchannel network in search of targets,* associated with **Paper II**;
- **Project 4,** *Lymph node-on-a-chip: mimicking the microphysiology of the T cell zone,* associated with **Paper III/Manuscript**.

In this work, the fabrication of the microfluidic devices was performed at NTNU NanoLab cleanroom. Cell preparations and experiments were done at the Department of Clinical and Molecular Medicine, Faculty of Medicine NTNU (Trondheim, Norway).

3.1. Fabrication of microfluidic devices

3.1.1. Mask design and numerical simulation of microfluidics

For the conception of microfluidic devices, the first step consists to design the microchannels, in function of the main principles and purposes behind of each work, using AutoCAD 2014 and AutoCAD 2017 drawing software (Autodesk Inc., Europe). After the conception, the design was simulated in COMSOL Multiphysics 4.4. software in order to determine the velocity profile and corresponding wall shear stress profile in the microfluidic structure used for each study. Next step was to analyze the results generated by simulations, in function of the main parameters that we want to achieve (e.g., specific values of flow velocities or shear stress in specific positions inside the microchannel). Several design/simulations iterations were performed in order to achieve the final goal.

During this PhD project, three different photomasks were conceived, designed and purchased from JD PHOTO DATA (UK) (363) and Compugraphics Ltd. (Germany and UK) (101): (i) a film photomask of polyester poly(ethyleneterephthalate) (PET) base with a photographic emulsion gel (resolution >50μm) represented by **Figure 3.1.1.1** and associated with **Paper I**; and two soda lime photolithography masks coated with a thin chrome metal layer: (ii) **Figure 3.1.1.2**, photomask with 2 microchannels and several patterns, and (iii) **Figure 3.1.1.4**, with several cell chambers and associated with **Paper III/Manuscript**. In the sequence of previous work developed by Øyvind Halaas group, NTNU and Nimi Gopalakrishnan (20), (iv) microfabrication and sealing processes were optimized by using the photomask of **Figure 3.1.1.3,** associated with **Paper II**.

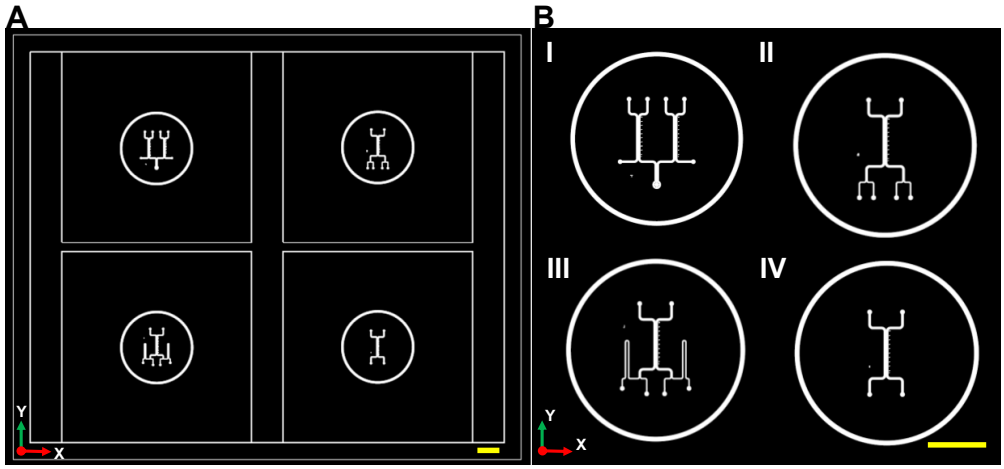

Figure 3.1.1.1 Photomask 1 (Paper I). Film photomask of PET base with a photographic emulsion gel (resolution >50µm) from JD PHOTO DATA (UK), with a disposition of four microchannels: **A)** General vision of real disposition of photomask. Scale bar: 1cm. **B)** Magnification on the configuration of four microchannel. **I)** Structure with two microchannels (length 1cm and width 1000µm) to run simultaneously two cell perfusion experiments from three main entries. **II)** Structure with four inlets to the main channel (length 1cm and width 1000 µm), in order to run a cell perfusion experiment applying 4 different solutions on cells. **III)** Structure with four inlets (two inlets with short length, and other two inlets high length) to the main channel (length 1cm and width 1000 µm), in order to run a cell perfusion experiment applying 4 different solutions on cells and playing with mass transport. **IV)** Simple channel (length 1cm and width 1000 µm) with two inlets and two outlets. Scale bar: 1cm.

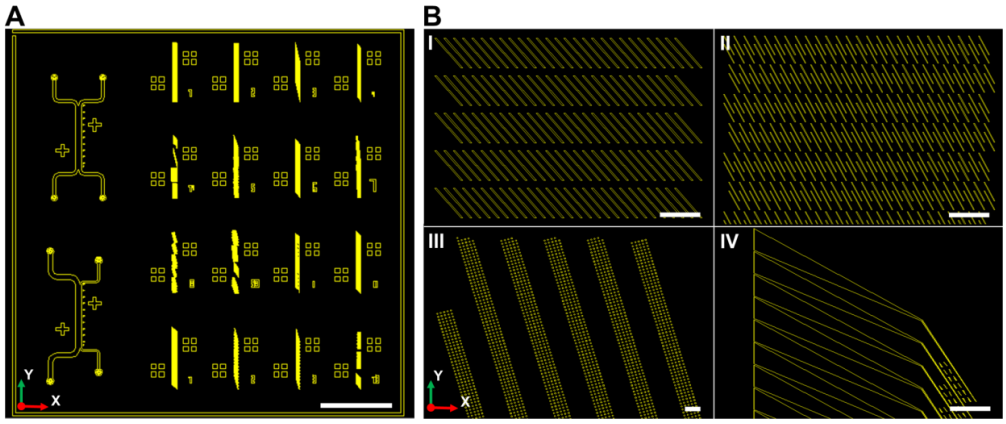

Figure 3.1.1.2 Photomask 2 (Project 2). Soda lime photolithography mask coated with a thin chrome metal layer from Compugraphics Ltd. (Germany and UK) (101). **A)** General vision of real disposition of photomask. Scale bar: 1cm. This photomask is composed by two microchannels, both 1cm in length and 1mm in width. The difference between the two channels lies in the inlets and outlets, only varying their dimensions of aperture – a *symmetric microchannel* with 500µm per each inlet to outlet, and another *asymmetric microchannel* with 750µm to 250µm per inlets and 750m and 250µm per outlets. This mask was designed to make Au patterns on a glass substrate, which will be aligned with PDMS *symmetric* or *asymmetric channel*. Several pattern types were design with diverse configurations, such as long and thin stripes, dots and bend patterns. Scale bar: 1cm. **B)** Magnification on the configuration of some pattern designs. **I)** Long and thin stripes with (5µmx100µm; with

interval between stripes of 20µm). Scale bar: 100µm. **II)** Long and thin stripes with (2µmx50µm; with interval between stripes of 10µm). Scale bar: 100µm. **III)** 6 stripes defined with dots, where each stripe is defined with 5 dots per line; each dot with 4µm of diameter and with interval per dot, 5µm. Scale bar: 50µm. **IV)** Bend patterns: triangular part with length 600µm and base 100µm, with a terminal thin line with a length 400µm and width 2µm. Scale bar: 100µm.

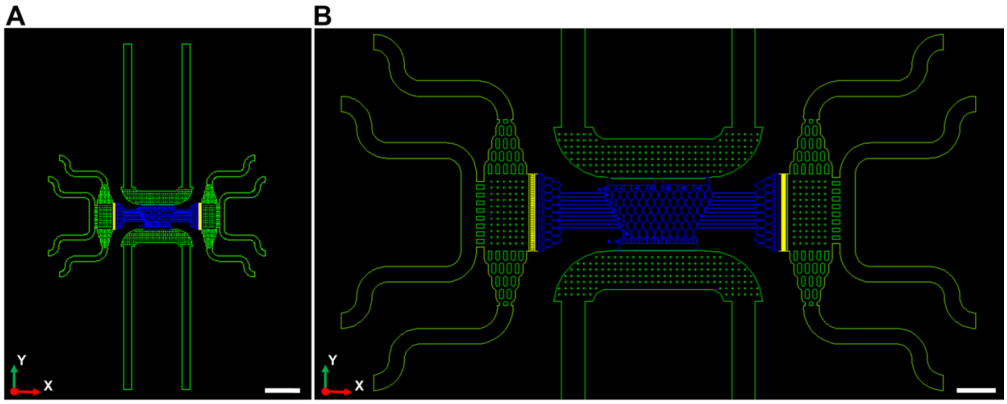

Figure 3.1.1.3 Photomask 3 (Paper II). Soda lime photolithography mask coated with a thin chrome metal layer from Compugraphics Ltd. (Germany and UK) (101). **A)** General vision of real disposition on photomask. Scale bar: 1cm. **B)** Magnification of the main structure, where it is possible to identify 3 layers (representing with different colours): first layer (yellow), thin filters with a capillaty network cross section of 2µm x 2µm; second layer (blue), microchannel migration network with a hexagonal capillary network cross section of 6µm x 6µm; and third layer (green), cell compartments had a thickness of 28µm and two types of rectangular chambers with width x length of 550µm x 1000µm (as side of infection: attractor and control chambers) and 550µm x 2000µm (migratory, entrance and sink chambers). Scale bar: 500µm.

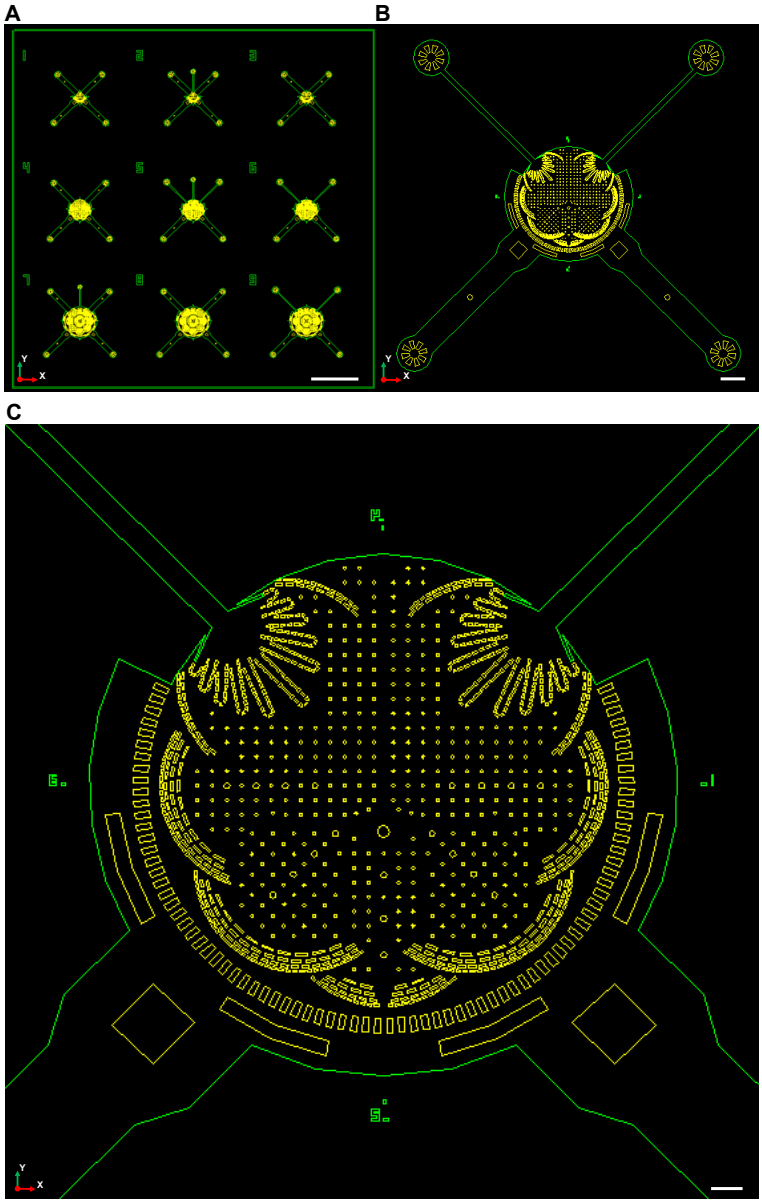

Figure 3.1.1.4 Photomask 4 (Paper III/Manuscript). Soda lime photolithography mask coated with a thin chrome metal layer from Compugraphics Ltd. (Germany and UK) (101). **A)** General vision of real disposition on photomask. Scale bar: 1cm. **B)** Magnification of the main structure selected, where it is possible to identity two thin inlets (with a cross section area, 200µm x 100µm) and two large (with a cross section area, 1000µm x 100µm), and a main circular cell chamber with an outer diameter of 4mm. Scale bar: 1000mm. **C)** Magnification of the circular cell chamber: the cell chamber is composed by inlets (top channels) with two independent systems of 11 protuberances with juxtaposed rectangular pillars (20µm x 40µm) with interval between pillars of 20µm; the inner of the chamber (with inner diameter of 3mm without filters) is completely supported by round pillars with 25µm and 50µm of diameter and spaced between them by 100µm; and the outer perimeter of the cell chamber composed by two levels of filters. 1st level of filters with thin juxtaposed rectangular pillars in 4 concentric circular lines of filters (10 sets in all chamber; composed by individual pillars from 100µm x 20µm (as maximum) to 40µm x 20µm (as minimum) with interval between pillars

of 50µm and 20µm, respectively); 2nd level of filters with a large single circular line around the cell chamber (composed by individual pillars 150µm x 50µm with interval between pillars of 50µm). Scale bar: 200µm.

Examples of COMSOL simulations executed during the design phase, in order to simulate the wall shear stress determined inside of a microchannel with cross section of 1000µm x 100µm (Paper I), as well as the flow velocity profile inside of a cell chamber (Paper III).

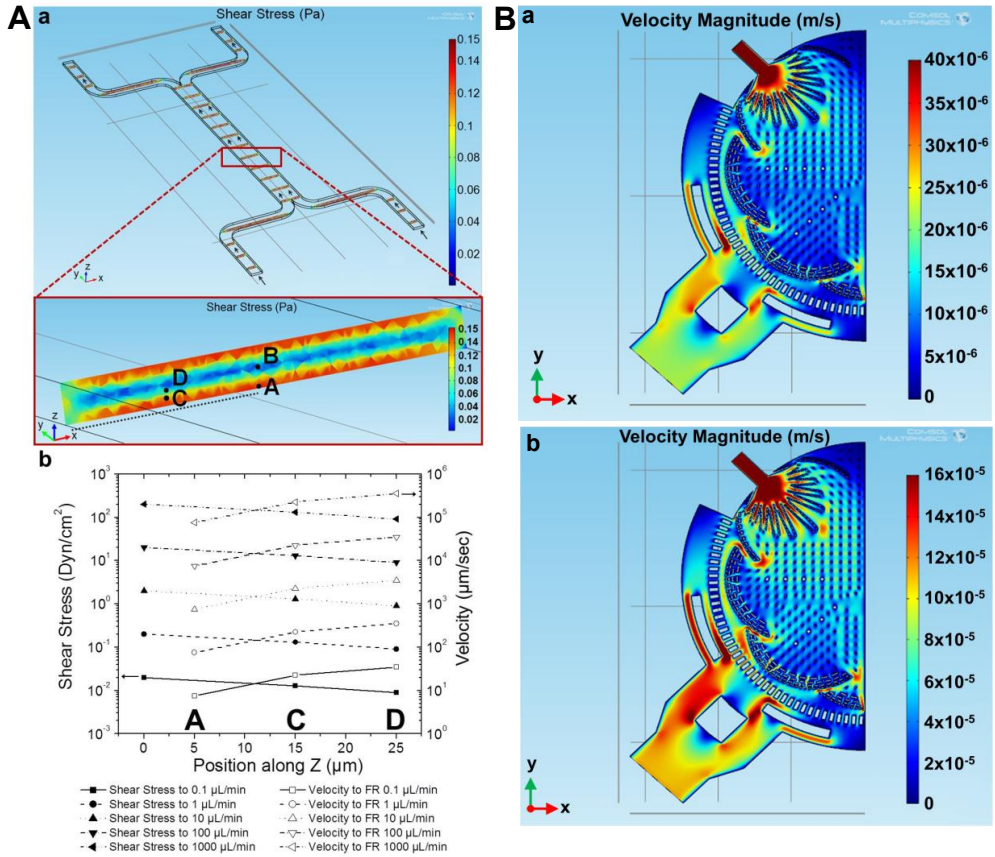

Figure 3.1.1.5 Simulations in Comsol. A) Shear stress profile (**Paper I**). a) 2D graphics from COMSOL Multiphysics 4.4 simulation of a rectangular channel cross section. b) Shear stress in a rectangular channel cross section as a function of different positions along the Z axis at different flow rates (µL min^{-1}). **B)** Velocity profile (**Paper III**). Representation in 2D graphic of half of the cell chamber at Z plane of 50µm, with flow rate of **a)** 100 nl min^{-1} with a mean maximum velocity range determined for the fluid passing through the chamber of 5-15 x 10^{-6} m s^{-1}, and **b)** 500 nl min^{-1} with a mean maximum velocity range determined for the fluid passing through the chamber of 2.5-7.5 x 10^{-6} m s^{-1}.

3.1.2. Photolithography

Photolithography (optical lithography) was performed for all structures during this PhD project (Paper I-III), and its work flow consisted of (as mentioned in **Section 1.3.3 and Figure 1.3.3.2**): (i) wafer cleaning and surface preparation; (ii) photosensitive film (photoresist) application; (iii) alignment of

mask and wafer; (iv) exposure of the photoresist; (v) development of patterns; (vi) inspection and characterization of patterns.

It is important to refer that during this process, three different elements are converged to a final result: *Optics* through the radiation generation, propagation, focusing diffraction and interference; *Chemistry* with photochemical reactions in the resist and development; and *Mechanics* as mask to wafer alignment (364).

The general cleaning procedure consisted by: wafer cleaning and surface preparation, where a 2" wafer was cleaned by ultrasonication in acetone for 5 min, followed by flushing with IPA in order to prevent the acetone from drying on the surface. The solvents were dried off the wafer using a stream of N_2 gas. Plasma ashing was performed to remove organic residues (Femto model from Diener Electronics). A dehydration bake on a 150°*C* hot plate for 15-20min was then performed to drive out any remaining solvent on the wafer. This was followed by 10min at a cold plate.

Considering the specifications and advantages referred on the **Section 1.3.3.** regarding the usage of SU-8, during this project all structures were fabricated using a wide range of SU-8 available on the facilities of NTNU Nanolab: as adhesion layer of photoresist, it was used SU-8 5 from MicroChem (2-7μm) (365); for "thin" layers (2-7μm), SU-8 5 from MicroChem (365); and for "ultra-thick" layers (50-200μm), SU-8 2100 (366) and SU-8 3050 from MicroChem (367).

The third photomask consisted on a complex microfabrication with three layers of photoresist with different thicknesses. For the third layer (cell compartments; **Figure 3.1.1.3**), a positive photoresist (maP-1275 from Micro Resist Technology GmbH (368), was used. A total thickness of 28μm was attained by making a multilayer process (14μm per layer).

All samples were exposed in Karl Suss MA6 Mask Aligner (365 nm), a versatile UV maskaligner capable to process samples from 5mm x 5mm up to 100mm wafers. It was used 4 exposure modes E-flood (no mask), Proximity, Soft and Hard, using i-line (λ=365nm) of the mercury lamp. The photomask was loaded on a mask holder, the resist-covered wafer was loaded on the desired chuck, and both were aligned, brought into contact, and exposed. The exposure time (s) was determined based on the necessary dose (mJ cm^{-2}) given by the photoresist manufacturer and on light power of the mask aligner (mW cm^{-2}) known upon calibration. The resolution was determined by mask dimensions and diffraction at mask edges. Contact/proximity lithography systems consisted to define a gap between the mask and the wafer as an adjustable parameter, with values from zero up, and final image on substrate was 1:1 size, with the same size of the original mask.

During this project, several lithographic processes were optimized as function of each photomask and of the desired result for the final structure.

To determine the optimum exposure time for a negative resist, it is important to refer that the process to be followed is the inverse criteria to be used for positive resists. When we are starting with a new process, we should test exposure times varying between 50% and 200% of the expected ideal value (105, 364). For the SU-8 (a negative photoresist), the optimum exposure time is determined by the degree of cross-linking and sidewall profile. In this case, the dimensions of features in the masters are equal to the dimensions of features in the photomask. In case SU-8 dimensions are larger than expected, we are overexposing and consequently we need to decrease the time. In the opposite way, if the dimensions are smaller than in the model, we are underexposing, and as a result we need to increase the time. In this context, performing iterative steps, the optimum exposure time is obtained.

In a final stage, the samples were developed following the recommendations/protocol of NanoLab staff and producers. For negative resists (SU-8 resists), the developer MrDev 600 (369) was used and for positive resist, the developer maD531 (370), at 20–25°C. At the end, the developed resist films were thoroughly rinsed with isopropanol and then dried. After the development, the master molds were characterized using a profilometer, Dektak 150 (Veeco).

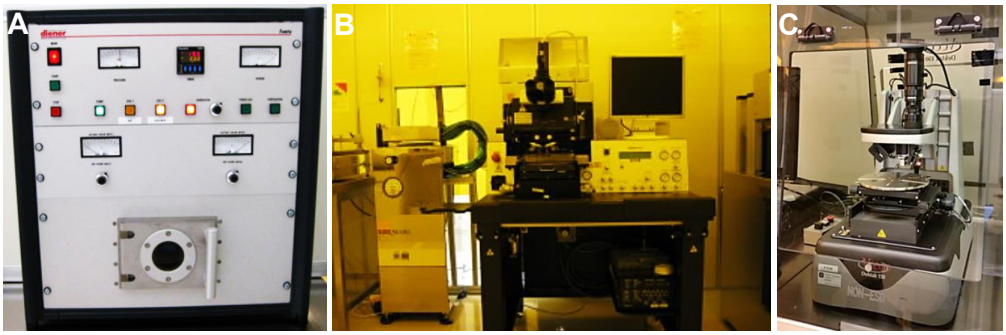

Figure 3.1.1.6 Equipments of Nanolab's cleamroom utilized during microfabrication process. A) Plasma Cleaner, Femto model from Diener Electronics. **B)** Karl Suss MA6 Mask Aligner (365 nm). **C)** Profilometer, Dektak 150, Veeco.

3.1.3. Soft lithography and replica molding

In Paper I-III, the 3D profiled master molds were silanized with trimethyl fluorosilane (Sigma-Aldrich) for 2h and then used for the soft lithography and replica molding processes. PDMS devices were produced by casting a mixture of Sylgard TM 184 (Dow Corning) (107) silicone with the curing agent in a proportion of 1:10, poured over the Si/photoresist master molds followed by heat-curing at 60-80°C during 2-4h. After curing, the PDMS (as solid elastomer) was peeled from the mold, the individual devices were cut to appropriate size and a needle (INSTECHLABS, US) with a blunt tip was used to drill the fluid connection access holes.

In Paper I-III, the individual devices were cleaned and sterilized with acetone and ethanol (70%) and dried with nitrogen. The PDMS replica was irreversibly sealed to a Ø50mm no.15 thickness sterilized cover glass (Menzel Gläser), using a plasma cleaner for surface activation (Femto model from Diener Electronics; 80 sccm O_2, ~80 W RF power for 2min). Then, the devices were further mounted onto 1mm high WillCo-dish®.

During this project, replica molding process was also developed and optimized by using epoxy glue, Permabond ES562 (371). The epoxy mold replication is a simple way to replicate Si master mold for microfluidic patterns on PDMS. This method has some advantages: (i) the epoxy mold conserves the resolution down to 1 µm; (ii) multiple and inexpensive replication of mold; (iii) this replica can be used more than 50 times over several months without significant ageing; (iv) can be cleaned with isopropanol (i.e., which is not possible with positive resists). This process was very useful during the fabrication of structures of Paper II, considering the complexity of the master mold (3 layers with different thicknesses).

This process consisted (372): (i) the first patterned PDMS obtained from the Si/photoresist master mold was placed with the channels/features up side over a cleaned piece of silicon wafer; (ii) Before usage, the epoxy glue was put at room temperature (22°C, 2h); (iii) the epoxy glue was poured on top

the PDMS (thickness ~ 2-3mm); (iv) the system was degassed to remove bubbles during 2h; (v) The epoxy glue was cured in the PDMS convection oven at 120°C for 50 min; (vi) the epoxy mold was peeled from the PDMS master; and, (vii) the replica structure was inspected on the microscope and the heights of the channels/features were measured in a profilometer.

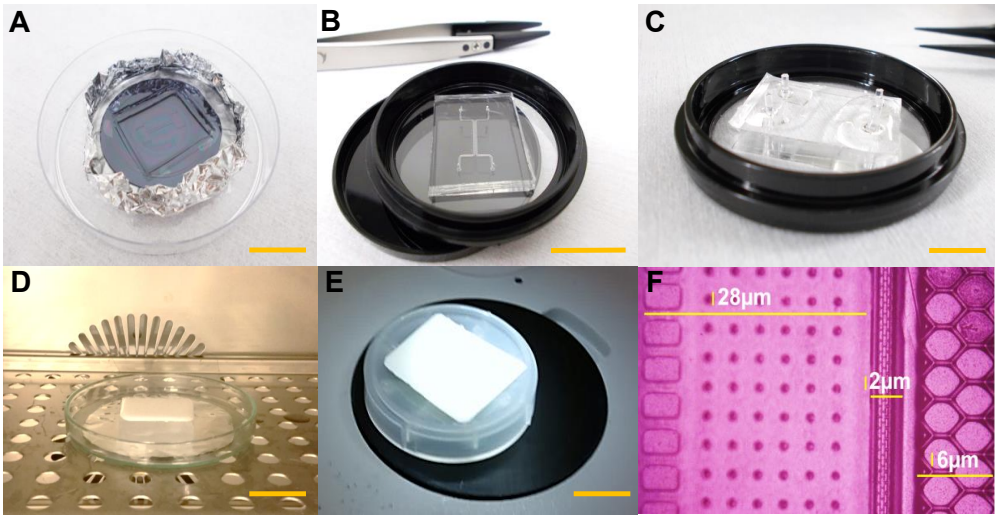

Figure 3.1.1.7 Soft lithography and replica molding. A) Soft lithography: PDMS was poured over the master mold and cured; PDMS replica is obtained by peeling from the mold. Scale bar: 1cm. **B)** PDMS biochip on a glass substrate of WillCo-dish®. Scale bar: 1cm. **C)** PDMS biochip with connectors (plastic capillaries) for macro to microfluidic interfacing. Scale bar: 1cm. **D)** Replica molding using the epoxy glue: PDMS mold was completely covered with a homogenous layer of epoxy glue 2-3mm. Scale bar: 1cm. **E)** Final epoxy mold. Scale bar: 1cm. **F)** Profile measurements from a test mold obtained by profilometer: compartments with pillars with height 28µm; filters with height 2µm and small network with height 6µm (Paper II).

3.1.4. Biofunctionalization

During the evolution of this project and considering the goals per each biodevice, the bottom of the microchannel were tested and coated with several types of biomaterials such as collagen (Col; 50 µgml−1, diluted with 1×PBS; Sigma Aldrich) (22) (associated with Paper I), fibronectin (FN; 50µg ml^{-1}, diluted with PBS; Bio-Techne, R&D Systems Europe Limited) (22) (associated with Paper I), and dopamine solution (Sigma Aldrich; 0.1%w/v in 10mM Tris-HCl (pH 8.5)) (373) (associated with Paper II and Paper III/Manuscript), to form a matrix for cell attachment and incubated at 4 °C overnight.

3.1.5. Patterns on glass for cell adhesion and sorting

Other techniques and processes

During this PhD, a co-development with a master student project in Nanotechnology - *Fabrication and testing of a Biopatterned Microfluidic Channel for cell-cell interactions in the immune systems*, by Lisa Svartdal 2015 NTNU (374) - was performed. The goal was to fabricate microfluidic channels bond to a glass substrate which included gold patterns. The gold patterns were used to specifically bind immune cells in specific areas and observe cell rolling upon continuous perfusion of a solution containing cells **(Figure 3.1.1.2)**.

Procedures of photolithography (process associated with photomask 2, **Figure 3.1.1.2**: SU-8 negative photoresist for the master mold; and SPR 700 1.0 positive photoresist for gold pattern glass;), electron beam evaporation (gold pattern glass), lift-off (gold pattern glass), soft-lithography (SU-8 master mold/PDMS) and plasma bonding (PDMS microchannel and gold pattern glass) to create an enclosed, patterned microchannel were optimized and performed during this work. The general steps towards creating a microfluidic device for the study of cell-cell interactions consisted of:

(1) Designing a photomask with microchannels and several pattern designs **(Figure 3.1.1.2)**.

(2) Creating by photolithography of microchannel master molds with SU-8 photoresist.

(3) Fabricating by soft lithography the PDMS microchannels.

(4) Creating a 15nm thin gold pattern on a glass slide by photolithography with positive resist, e-beam evaporation and lift-off process.

(5) Bonding the glass and the PDMS to create an enclosed system with inlets and outlets.

(6) Biofunctionalization the gold pattern and backfilling the glass.

(7) Binding antibodies to the gold patterns.

(8) Injecting the correct corresponding cell-type: LN FRCs, DCs and T cells. For perfusion and cell injection inside the microchannels, syringe pumps were used, and whole system was observed and monitored on an EVOS FL Auto Cell Imaging System (Invitrogen).

Details associated with the preparation of glass substrate for Au patterns with photolithography, electron beam evaporation and lift-off process, will be briefly reported in this section.

Photolithography

Thin glass slides (thickness ~150µm; Ø50mm) from Menzel Gläser, were cleaned (acetone, ethanol, IPA, deionized water, and blow dried with N_2-gas), pre-treated in plasma cleaner and submitted with the dehydration bake. For the photolithography process, the NTNU Nanolab protocol was followed (375), using as positive photoresist, SPR 700 1.0 resist (from Dow® Electronic Materials MEGAPOSIT™; thickness ~1µm) (376), and as developer, MF 26A (MicroChem) (377). This type of glass and the thin layer of gold (~15nm) were chosen in order to ensure the transparency and to allow optimal resolution for inspecting the samples in a high resolution confocal fluorescence microscope.

Electron Beam Evaporation

By using Electron-Beam Evaporator (Vacuum Classic 500, Pfeiffer), a 3nm thin adhesion layer of titanium (Ti) and a 15nm thin layer of gold (Au) were evaporated onto the resist patterned glass. This process was performed using an automatic procedure at ~10^{-7} Torr, 18°C.

Lift-Off

Lift-off process is characterized as a simple and easy method for patterning deposited thin films. This process consists in a photoresist layer patterned by photolithography on top of which a thin film is deposited. Finally, the photoresist is dissolved by a solvent (acetone) or resist strip solution, removing the material on top of it. Thus, the thin film remains where there was no photoresist. In this process, the Ti/Au layer that was evaporated directly onto the glass, will remain, while the metal deposited on

top of the SPR 700.10 resist will be removed together with the resist. The lift-off process was performed with acetone applying ultra-sounds to accelerate the removal.

Biofunctionalization

The gold pattern was conjugated with carboxy-PEG-thiol, streptavidin and biotinylated antibody and the glass was backfield with PLL-g-PEG to prevent non-specific cell binding. In order to analyze the cell interactions and behaviors with Au patterns using different cell types, several biochips were prepared with four different biotinylated antibodies: anti-CD8 for $CD8^+$ T cells (BD Bioscience Pharmingen), anti-MHC I for $CD4^+$ T cells (BD Bioscience Pharmingen), podoplanin (PDPN; eBioscience) for mouse lymph node fibroblast reticular cells (FRCs), and anti-CD11c for $CD11c^+$ dendritic cells (BD Bioscience Pharmingen). For more details readers may consult Lisa Svartdal master thesis (374).

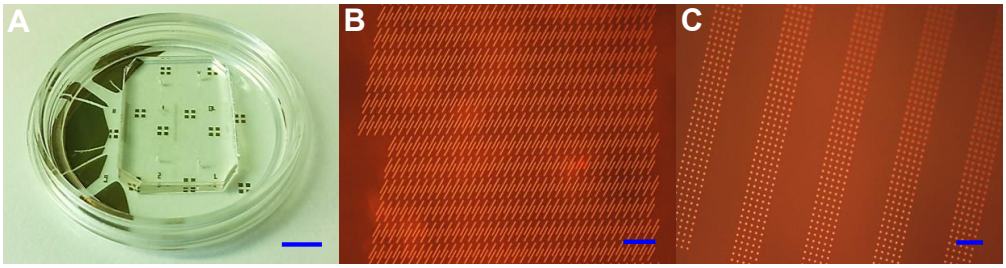

Figure 3.1.1.8 Au patterns on glass for cell adhesion and sorting. A) PDMS channel bonded to glass patterned with gold. Au patterns: B) Long and thin stripes with (2µmx50µm; with interval between stripes of 10µm). Scale bar: 100µm. C) 6 stripes defined with dots, where each stripe is defined with 5 dots per line; each dot with 4µm of diameter and with interval per dot, 5µm. Scale bar: 50µm. Adapted from Ref. (374).

3.2. Cell analysis

3.2.1. Cells and Staining cells

In Paper I-III, the range of *in vitro* experiments converged with the use of the same type of cells. During these studies, several cell types were used such as, mouse lymph node fibroblast reticular cells (FRCs), from peripheral LNs, inguinal and axillary of adult male mouse (C57BL/6); primary bone marrow-derived dendritic cells (BMDC) generated from adult male mouse (C57BL/6); enhanced green fluorescent protein (eGFP)+murine dendritic cell line "MutuDC 1940", as kindly provided by Prof. Hans Acha-Orbea, University of Lausanne; non-adherent ovalbumin specific MHC class II restricted (MF2.2D9) $CD4^+$ T cells (here in after referred to as OVAII) and MHC class I restricted (RF33.70) $CD8^+$ T cell hybridomas (here in after referred to as OVAI) were gifts from Dr. Kenneth Rock, University of Massachusetts, Worcester. More details about cell preparation and medium can be found in Paper I-III.

In Paper I-III, the cell staining of T cells was performed with 1µM Cell Tracker™ Deep Red Dye (378) (Invitrogen), or 5µM Cell Tracker™ Orange CMTMR (5-(and-6)-(((4-chloromethyl)-benzoyl)amino)tetramethylrhodamine) (379) (Invitrogen) for 30 minutes according to protocols (more details can be found in Paper I and Paper II), and also with 0.5x solution CytoPainter Live Cell Labelling Kit- Blue Fluorescence ab187966 (Abcam) (380) for 45min according to protocols (more details can be found in Paper III). FRCs were stained with 0.5x solution CytoPainter Cell proliferation

Staining Reagent - Deep Red Fluorescence ab176736 (Abcam) (381) for 20min according to protocols (more details can be found in Paper III).

The CellTracker™ Deep Red Dye and CellTracker™ Orange CMTMR (5-(and-6)-(((4 chloromethyl)benzoyl)amino)tetramethylrhodamine) are characterized to be a fluorescent dye well suited for monitoring cell movement and tracking movements (considering the high motility of T cells), and have been designed to freely pass through cell membranes and are transformed into cell-impermeant reaction products. The CellTracker™ Deep Red Dye red excitation/emission spectra is 630/650nm whereas the CellTracker™ Orange CMTMR excitation/emission spectra is 541/565nm. The combination of these two dyes is therefore ideal for multiplexing purpose. By using of eGFP+murine dendritic cell line "MutuDC 1940" inside the channel, with excitation/emission 488/510nm) (378, 379), a 3 colors multiplexing can be performed (more details can be found in Paper I and Paper II).

In paper III, considering the level of cell interaction analyzed FRC-DC(eGFP)-T cell, the FRCs cells were stained with CytoPainter Cell proliferation Staining Reagent - Deep Red Fluorescence ab176736 (Abcam), characterized as a fluorescent dye well suited for multiplexing with excitation/emission 633/(628-643)nm (381). The T cells were staining with CytoPainter Live Cell Labelling Kit- Blue Fluorescence ab187966, characterized to become strongly fluorescent upon entering into live cells, and it is also a fluorescent dye well suited for multiplexing with excitation/emission 410/450nm (380) (more details can be found in Paper III).

3.2.2. Antigen-presentation assays

In Paper I-III, antigen presentation assays were performed in all devices/experiments. This common method consists to pre-incubate dendritic cells with 100 ng/ml LPS for 2-5h. After 2-5h, dendritic cells were incubated with the ovalbumin OVA323-339 I-Ab-(MHC class II)-presented peptide (ISQAVHAAHAEINEAGR) (here after called OVAII peptide) or the OVA257-264 Kb (MHC class I)-presented peptide (SIINFEKL) (here after called OVAI peptide), both at 10 $\mu g\ ml^{-1}$ and 100ng ml^{-1} lipopolysaccharide (LPS, Sigma) for 1h, for antigen presentation to $CD4^+$ or $CD8^+$ T cells, respectively. More details can be found in Paper I-III.

3.2.3. Microfluidic setup and Device's loading procedure

The cells were imaged using a Zeiss LSM 510 inverted confocal microscope, which was equipped with an on-stage incubator with controlled temperature, CO_2 pressure and humidity for long term cell experiment (**Figure 3.1.1.10**) (Paper I-III). The microscope and digital camera were controlled via Carl Zeiss Zen 2009 (Version 6.0 SP2). In an initial stage of this PhD, for the image acquisition it was also used the EVOS FL Auto Cell Imaging System (Invitrogen), as an auto imaging system for long-term monitoring of cell cultures and time-lapse cell imaging.

As a standard experimental setup, in Paper I and Paper III two syringes were loaded previously on the same or in two independent syringe pumps (PHD 2000, Harvard Apparatus, Holliston, MA), and the software of perfusion was defined in function of the syringe diameter. The syringe pumps were mounted near the confocal incubator. The sterile device was inserted on the microscope, being connected to two syringes by polyethylene capillaries and metal connectors (Instech Solomon).

Cells interactions were visualized in 2D and 3D at different times, using a fully rendered multidimensional data set and a scheme of monochrome Z-stacks, resulting in a "top view" projection.

By using Zeiss LSM 510 inverted laser scanning confocal microscope, time lapse fluorescence and differential contrast (DIC) images were also captured using 10x objective and 20x objective, while the devices were maintained at 37 °C, 5% CO_2.

As the device's loading procedure, in Paper I-III several modalities of cell loading were performed, considering the specificity of device/project. In general, cells can be introduced into the microchannel or microchamber by micropipetting with reduced volume (>2µl) from the inlets or by continuous perfusion at a specific flow rate of a cell solution using a syringe.

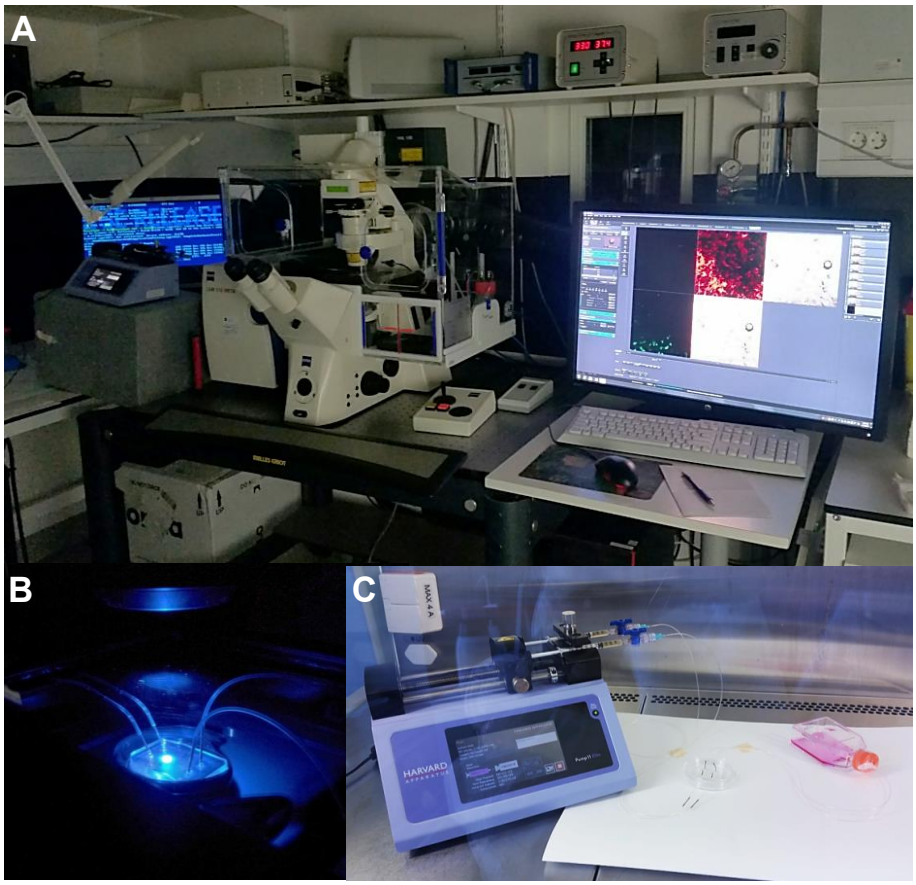

Figure 3.1.1.10 Details of the schematic illustrating the standard experimental setup. A) Zeiss LSM 510 inverted confocal microscope, which was equipped with an on-stage incubator with controlled temperature, CO_2 pressure and humidity for long term cell experiment. The syringe pump was mounted near the confocal in order to avoid dead volumes of capillaries, and the sterile device was inserted on the microscope holder. **B)** Biochip when fluorescence was applied. **C)** The assembly of a perfusion system consisted, in the following sequence, to connect the waste container with outlet plastic capillaries + metal connectors, and then with the biochip. The inlets capillaries + metal connectors were prepared, the syringes were loaded with medium solution (or cell solution) and the perfusion software of syringe pump was defined with the diameter and volume of the syringe used. The inlet capillaries were connected to the syringes, and then "syringes + inlet capillaries" were mounted and locked on the pump. The inlet capillaries were loaded with a solution through the pump, in order to remove all the air inside the capillaries, the perfusion software was "run" and the inlet connectors inserted on the inlets of biochip. The biochip was maintained either inside the cell incubator or inside the confocal incubator.

3.2.4. Microscopy

During this PhD project, a Zeiss LSM 510 inverted confocal microscope and an EVOS FL Auto Cell Imaging System (Invitrogen) were used for cell image acquisition. These two equipments were an excellent approach to study cell:cell interaction (72).

Zeiss LSM 510 inverted confocal microscope is a sophisticated laser scanning confocal microscope (LSCMs), with a Meta detector (polychromatic detector) and high speed scanner (Live). This microscope is equipped with seven laser lines - Diode 405nm, Ar 458, 477, 488 and 514nm, diode 561nm and diode 640nm - , and 5 lenses - 5X Plan-Apochromat/0.16 NA, 10X Plan-Neo/0.3 NA, 20X Plan-Apo/0.75 NA with DIC capability, 40X Plan-Neo/1.3 NA Oil with DIC capability, 63X Plan-Apo/1.4 NA Oil with DIC capability-, and allows all scan combinations of line, X, Y, Z and time (382).

The laser scanning confocal microscope is a specialized type of light microscope, in which a laser beam is scanned across the specimen in a raster and the emitted fluorescent light or reflected light signal, sensed by a photomultiplier tube and displayed in pixels on a computer monitor. The key to the confocal effect is the pinhole. A variable pinhole aperture, positioned in a plane confocal with the specimen, prevents the out of focus light to reach the detector and allows for optical sectioning. As main advantage, LSCM can provide excellent image quality, however with a slower image acquisition and often a limited choice of excitation wavelengths.

The EVOS FL Auto Cell Imaging System (Invitrogen) (382, 383) is a simple friendly microscope which integrates an incubator as chamber, enabling precise control of temperature, humidity and gases for long term experiments. This system consists in an automated, digital, inverted multi-channel fluorescence and transmitted light imaging system with color and B/W cameras, high-resolution mosaic tiling, multi - position well scanning, live cell imaging, area scanning, image stitching, and time-lapse imaging. This microscope is equipped with eight light cubes - TagBFP, CFP, GFP, RFP, Cy5, Cy7, Texas Red, YFP - , and 5 lenses - 4x, 10x, 20x, 40x, 60x all with long working distance, no immersion.

Figure 3.1.1.11 A) Zeiss LSM 510 inverted confocal microscope. B) EVOS FL Auto Cell Imaging System (Invitrogen).

3.2.5. Statistical analysis

Cell measurements were quantified from the fluorescence micrographs obtained by Zeiss LSM510, and analyzed using Bitplane Imaris 8.1.2, Matlab R2014 (XTensions) and ImageJ software. Statistical

analysis of all collected data from Imaris was performed using ORIGIN® (ORIGINLAB) or GraphPad Prism (GraphPad Software) software.

4. SUMMARY AND DISCUSSION OF PAPERS

4.1. Summary of papers

4.1.1. Paper I

In this study, we investigated the T cell:DC interactions in a microfluidic device to understand the intercellular dynamics and physiological conditions in a LN. We explored the mechanism, dynamics and basic cell behavior of attachment and detachment of antigen-specific and unspecific $CD8^+$ T cells and $CD4^+$ T cells to activated antigen presenting or non-activated DCs. Investigating these interactions as a function of the tangential force *via* shear stress in a continuous flow on a microfluidic channel allowed to mimic the natural principle of interaction that occurs *in vivo*, in this way determining the natural dynamic rate of attachment and detachment of T cell:DC. These results established basic principles and approaches to allow further exploration of the immunological synapse.

In T cell:DC interactions, when an antigen is present, the initiating interaction leads to a highly organized structure of immunological synapse known as the central, peripheral and distal supramolecular activation complexes (SMACs). This process of attachment starts within seconds after conjugation and reaches a maximum strength at around 30min, before cell activity causes some changes in adhesion subsequent detachment. According to several studies (70-72, 74-84, 384), the formation of SMAC is dependent on the mechanical force, cell-cell contact area and time, shear stress, expression of surface molecules (such as TRC and LFA-1), cytoskeleton dynamics, antigen affinities and all phenotype.

In this work, our objective was to first allow the establishment of these interactions with low shear stress and then successively increase the flow rates to determine the threshold shear stress necessary to break the inter-cell conjugation (with shear stress values found inside capillary venules 0.01-1Dyn cm^{-2}, and inside the arteries, >50Dyn cm^{-2}) (23, 385).

First, the DC monolayer adhesion and T cell:DC interactions was characterized under a shear stress of 0.01Dyn cm^{-2}. We observed random migration of antigen-specific T cells onto the antigen-presenting DC monolayer independent of the flow direction with a mean T cell:DC dwell time of 12.8min and a mean velocity of 6µm min^{-1}.

To further characterize the T cell:DC interactions and assess the longevity and strength of the contacts, we investigated the antigen specific *vs.* unspecific attachment and detachment of $CD8^+$ and $CD4^+$ T cells to DCs under varying shear stress. In our system, $CD4^+$ T cells presented long stable contacts with APCs, whereas $CD8^+$ T cells showed transient interactions with DCs. By varying the shear stress from 0.01 to 100Dyn cm^{-2}, it was evident that there was a much stronger attachment (shear stress up to 1-12Dyn cm^{-2}) of antigen-specific than unspecific T cells to stationary DCs. The mechanical force of cell:cell interaction associated with the pMHC-TRC coupling under controlled tangential shear force was estimated to be in the range 0.25-4.8nN.

Finally, having established the influence of shear stress (by varying the flow rates) on the dynamic behavior of the conjugates, the dynamics and rate of attachment of T cells to activated antigen-loaded DCs in a continuous flow was studied, mimicking in this way the natural principle of interaction that occurs *in vivo*. The T cell:DC interaction was allowed for a degree of freedom of orientation to establish contact induced by the tangential mechanical force applied over time by the flow (called attachment & detachment approach). In this approach, we also explored the laminar flow in microchannels by the application of two different stream lines, one with $CD4^+$ T cells and one with $CD8^+$ T cells over a common DC monolayer previously activated with either LPS+OVA II peptide, or LPS+OVA I peptide or untouched DCs at a low flow rate determined from previous experiments. At low shear stresses, there was a steady accumulation of antigen specific $CD4^+$ T cells or $CD8^+$ T cells on DC activated with LPS+OVA II peptide or LPS+OVA I, respectively. This shows that the T cells

bind specifically to DCs cells only if they are properly activated. If the DCs cells are not activated or with an unspecific activation, even a low shear stress is enough to allow the detachment of T cells. As in the previous experiments, the T cells specifically attached to activated DCs were found to be released only at large shear stress (12Dyn cm^{-2}).
This microphysiological model provides new possibilities to recreate a controlled mechanical force threshold of pMHC-TCR binding, allowing to investigate the possibility of using these principles as tools towards immunological research and in the development of novel immunotherapeutic approach.

4.1.2. Paper II

In the second study, we developed a novel approach for building and operating a simple and flexible microfluidic chip mimicking immunological compartmentalization with real-time, bulk, single-cell and subcellular interrogation options. With this chip, we explored the behavior and migration of naïve and/or effector T cells to distinct microcompartments "tissues" composed of DCs under different inflammatory stimuli. Preference was given to tissue paths that would favor a migration strategy and the single cell decision-making process driving collective cell behavior. This biochip was conceived as a flow-free device that allowed the continuous and dynamic generation of chemotactic gradients produced by living cells maintaining in this way a gradient over a longer period time.
This system was characterized at the transient state, where molecular concentration can change over time, by free-diffusion in a static fluid environment between a source and a sink, and with reduced shear stress for cells in suspension or with low adhesiveness.
In order to design this high performing flow free device, several structural strategies were integrated and finely tailored according to cell physiology and need. Although the requisites have contributed to the simplicity of device operation by not requiring additional equipment (e.g., pumps), they increased the complexity of the microfabrication process. The device consisted on multiple cell chambers, separated by a hexagonal network of microchannels with cell-sized cross sections (6µm x 6µm), and with embedded filter compartmentalization (2µm x 2µm) that allow the passage of molecules but not of the cells. The design criteria for the device were: (i) Confine cells and bacteria (representing the inflammatory foci), but allow their molecular products to diffuse through the system to form a dynamic gradient; (ii) Connect the inflammatory focus chamber, i.e. the attractor side, to a reservoir of immune cells to be recruited through microchannels with a cell-sized cross-section; (iii) Interconnect the microchannels in a network to avoid hydrostatic forces and historic events affecting single cell movement and allow cells to make choices based on local differences in chemotactic factors; (iv) Introduce a second chamber, i.e. the control side, to better control specific recruitment to inflammatory foci; (v) Introduce a sink to maintain the on-chip produced gradients for a longer time; (vi) Introduce side-channels that can be used to add substances during an ongoing experiment without disturbing the cells.
Initially, we characterized the free diffusion gradient inside the device with a fluorescent dextran, Rh-Dex (3kDa), which is smaller (therefore with higher diffusion coefficient) than typical cytokines produced during inflammation and immune response (e.g., MW CCL19 8.8kDa).
Modelling and testing confirmed the function of these compartments to maintain a differential unidirectional gradient between attractor and control side after loading. The time frames for molecular diffusion were found to be similar to what is expected in tissues.
We set up different inflammatory cell culture foci in the attractor chamber to examine the overall bulk performance of the device using LPS-stimulated macrophages, T cells activated by antigen-presenting cells as well as lymph node fibroblast, dendritic cell and T cell co-cultures.
A directional migration of both dendritic cells and T cells towards the inflammatory foci was observed. The hexagonal network layout allowed us to follow and observe the motility and decision-

making process of individual cells: Bone Marrow Dentritic Cells (BMDCs), OVA I and OVA II T cells moved along microchannels as elongated cells. They extended fast-moving protrusions at the leading edge and at intersections. It was observed that the cells paused to probe both alternative pathways several times before making a decision on which direction to go, accumulating close to the inflammatory cue. The cells were tracked individually and a highly variable travel distance with a mean speed of 9μm min^{-1} was found.
Our device is unique in providing a structured environment for automated long-term high-resolution interrogation of the process of complex immune cell recruitment and migration towards cell-produced gradients, at the collective as well as the individual cell level. We believe our system can be used to compare different systemic or genetic contributions to immune system effects and defects as well as a model system for tissue repair.

4.1.3. Paper III/Manuscript

Our aim in the third study was to develop a microfluidic cell chamber to artificially mimic the T cell zone of LN, in order to recreate interactions induced *via* shear stress from the natural dynamic rate of attachment of T cell:DC:FRC in a continuous flow. This further allowed investigation on the recodification and education of T cell priming by APC during dynamics stages of immune responses.
In order to design and conceive these cell chambers, several prerequisites/strategies and bioprinciples were integrated to mimic artificially microphysiological features on a T cell zone of LN on-the-chip: (i) to promote the T cell:DC encounters with a network of FRCs acting as attachment scaffold for pro-inflammatory antigen-carrying dendritic cells arrived from sites of infection/inflammation; (ii) to allow the application of successive increment of flow rates similar as a normal inflammation process; (iii) to mimic the natural attachment process of T cell to DC during immune interaction; (iv) to offer to the operator additional control and monitoring of the whole system in real time.
This chamber consisted in two thin inlets with a cross section area of 200μmx100μm, a main circular cell chamber with an outer diameter of 4mm, two large outlets with a cross section area of 1000μmx100μm, and to maximize the control of velocity profile inside the chamber, the same height 100μm was defined in the whole device.
LNs are characterized to display a complex micro-immune-architecture. During the adaptive immune response, stromal cell networks have key role in guiding immune cells to the lymph node compartments, providing cytokine and chemokine gradient field for lymphocyte activation or regulation. The paracortex T cell zone as a meeting point for APC and T cell interactions is defined with a highly dense FRC trabecular network with the function of resisting tension and providing cell filtering (56-58, 60, 386, 387).
In this context, the main circular cell chamber was composed by an inner chamber (3mm of diameter) completely supported by round PDMS pillars (with diameters of 25 μm and 50μm, and spaced by 100 μm) and without filters. The outer diameter of cell chamber was composed by two levels of filters. Our strategy with a uniform disposition of PDMS pillars on the central cell chamber, was to give the largest possible spacing between pillars in order to minimize the fluid velocity. This strategy also provides an artificial substrate/scaffold for FRC growth, without the need to use polymeric hydrogels.
Considering the complexity of the tissue architecture of LN, we recreated a slice of a spherical volume of a LN with a thickness of 100μm, defining an inner diameter of the main chamber with 3mm. These dimensions correspond to ~15% from the total spherical volume of LN (d=2mm). The cell occupation in this reduced volume (0.6μl) was defined as 29% for FRCs, 3% for DCs and 7% for T cells, resulting in 40% of occupied area and therefore 60% of empty space.
Initially, the cell chamber was simulated to predict the flow behavior, velocity and shear stress values at an *h* position of 5μm from the channel edge corresponding to the localization of the DC or T cell on

glass or on FRC scaffold (assuming a no-slip condition, where the velocity of the fluid at the boundary is zero). From the simulations, the mean maximum velocity range determined for the fluid passing through the chamber at 100nl min^{-1} on a XY plane at Z=50µm was 5-15x10^{-6}m s^{-1} (or 300-900µm min^{-1}) with a correspondent range of shear stress at 5µm above the boundary of (0.001-0.004)Dyn cm^{-2}. At 500nl min^{-1} on a XY plan at Z=50µm, the maximum velocity was 2.5-7.5x 10^{-5}m s^{-1} (or 1500-4500µm min^{-1}) with a correspondent range of shear stress at 5µm above the boundary (0.007-0.02)Dyn cm^{-2}.

An important aspect is that the conception of this design, allowed achieving low values of shear stress starting from 5x10^{-5}Dyn cm^{-2} up to high values 0.02Dyn cm^{-2}, giving the operator a significant range of control on mechanical forces to be exerted on FRC scaffolds and on cell interactions. This range integrates the low range of shear stress of the physiological values for complex flow in the lymph node published until now 0.005 to 0.05Dyn cm^{-2} (43, 384, 388).

Initially, we promoted the FRC trabecular network construction inside the chamber, through the application of perfusion flow that induced both chemical stimuli (e.g., nutrient, biological activation) and mechanical stimuli (e.g., shear stress, fluid velocity). This was attained upon continuous perfusion during 48h at 100nl min^{-1} with a corresponding shear stress of 0.001 to 0.004Dyn cm^{-2}. To explore the characterization of the full construction of the 3D meshwork by FRC with perfusion, cell chambers with FRC were submitted to the detachment/disruption test with successive increment of flow rate every 20 min from 50nl min^{-1} to 500nl min^{-1}. From the results and the simulation data, we can assume that the range of shear stress supported by this system with high cell density during initial loading (10-20x10^{6}cells ml^{-1}) is 0.0007 to 0.008Dyn cm^{-2}. In the device tested in this work, these shear stresses are attained for flows ranging from 50nl min^{-1} to 200nl min^{-1} corresponding to the fluid velocities values between a minimum for normal cell growth around 150µm min^{-1} and a maximum supported by the stromal mesh 1800µm min^{-1}. For shear stresses above 0.008Dyn cm^{-2}, cell detachment and structural self-destruction start to be observed.

Two tests were further performed on a system with 2 types of cells: (i) the analysis of DC motility interacting with FRC scaffold when submitted to successive increment of flow rates (50nl min^{-1} to 500nl min^{-1}) and shear stress (0.0007-0.02Dyn cm^{-1}), and (ii) the analysis of natural attachment of T cell flowing over a FRC scaffold at 100nl min^{-1} with a shear stress range of (0.001-0.004Dyn cm^{-1}). In both caces, it was detected high motility with mean velocity of ~10µm min^{-1}.

Finally, in the system with 3 types of cell interaction T cell:DC:FRC, it was studied interactions with and without cognate activation using LPS+OVAII peptide, where DCs were pre-loaded to interact with FRC scaffold during 1h.T cells were then flown over the DC:FRC scaffold in order to analyse the natural attachment by sucessive increment of flow rate (100 to 300nl min^{-1}) as an immediate response to inflammation. These results evidenced that without cognate interactions, T cell and DC show a motility of 5µm min^{-1}, random movements and “stop and go” interactions during 3min. With cognate interactions, it was visible a decrease of DC and T cell velocity to 2.5µm min^{-1}, where T cells moved in characteristic lipping patterns making serial contacts with the same or with neighbouring DC during 7min.

We successfully demonstrated the ability of our system to selectively promote adhesion of antigen-specific T cells through serial contacts, as well as an application to be used as a research tool and as a clinical development tool (e.g. *in vitro* immunization, personalized cancer vaccination, immunotherapeutic approaches for cancer and autoimmune diseases).

4.1.4. Appendix A - *Patterns on glass for cell adhesion and sorting*

As it was described above in **section 3.1.5**, *Patterns on glass for cell adhesion and sorting* corresponds to the co-development with a master student in Nanotechnology during one year - *Fabrication and testing of a Biopatterned Microfluidic Channel for cell-cell interactions in the immune systems*, by Lisa Svartdal 2015 NTNU (374) – where the microfabrication process, cell procedures and analyses were optimized as a part of this PhD project.

In this study, a microfluidic channel bonded to a gold patterned glass was designed and fabricated. The idea is to define restricted and specialized areas for cell attachment and cell repulsion. The specialized areas were highly specific receptor-antibody bonded to gold patterns to which immune cells can bind.

Three main objectives were defined for this master project: (i) first, to recreate the T cell rolling undergo on the insides of the vascular endothelial vessel by pumping T cells onto thin patterns with antibodies. The goal was to recreate the cell rolling and sorting, by establishing transient antibody-receptor bonds via control of flow rate (and shear stress) along the channel, and by sorting them along the design of the antibody patterns. The pattern adopted for this approach was based on (389). (ii) The second objective consisted to pattern the microchannel with LN FRCs with constant fluid perfusion, to recreate FRC scaffold for DCs adhesion and encounters between DCs and T cells. (iii) The third goal consisted to bind DCs in the gold restricted areas, to activate them with a peptide and to injected T cells in order to follow interactions between the two cell types in a controlled manner, and further, to sort T cells after their activation with the geometry of Au patterns.

Initially, we have designed and fabricated Au patterned microfluidic channels through photolithography, electron beam evaporation, soft lithography, plasm bonding and protein bioconjugation. The gold pattern was conjugated with carboxy-PEG-thiol, streptavidin and biotinylated antibody and the glass was blocked with PLL-g-PEG to prevent non-specific cell binding. Considering the three main objectives defined for this project, biotinylated antibodies specific for T cells (anti-CD8), LN FRC (anti-podoplanin) and DCs (anti-CD11c) were used to bind to the streptavidin.

The main results were very promising (374): it was documented that when T-cells were injected into channels with low flow rates (10-50nl min^{-1}) on the thin, long, bioconjugated gold patterns, T cells showed a tendency to adhere to the pattern, and when injected with high flow rate (>100nl min^{-1}), it was possible to observe T cell rolling on anti-CD8. It was also possible to create microchannels with FRCs and DCs specific to the bioconjugated gold pattern throughout entire channel. In both cases, when T cells were injected into the patterned channels, interactions between T cell:DC were detected and reported.

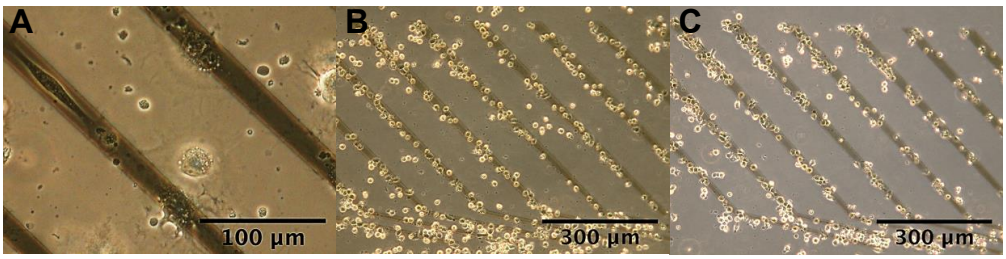

Figure 4.1.4.1 Cell tests. A) LN FRCs inside a microchannel 1 hour after injection. LN FRCs were stretching out on the Au pattern. B) & C) A microchannel patterned with CD11c was injected with gfcDCs: B) 10 min after injection, and C) after 18h. Adapted from Ref. (374). For more details readers may consult Lisa Svartdal master thesis (374).

Considering the limitation of time, the initial results obtained were satisfactory to define a continuation of the project. This also open new horizons for the development of microchannels with DCs immobilized on a patterned surface which to specific antibodies that allow the activation of T cells. These microchannels would also allow to sort cells from a heterogeneous solution by antibody pattern interactions. However, there are some aspects for a re-evaluation, which stand out PLL-g-PEG control, characterization of cell expression on Au-patterns, and redesign with larger pattern for the LN FRC.

4.2. General discussion

The overall aim of this work was to design and fabricate microfluidic platforms to investigate cellular interactions of the adaptive immune responses. Narrowing the focus to more specific sub-goals, during this PhD project were developed three classes of microfluidic devices: (i) in Paper I, a microfluidic channel to promote the cognate physical interactions between naïve T cells:APC under varying shear stress and to estimate the mechanical force associated with the immunological synapse formation (SMACs); (ii) in Paper II, a diffusion flow-free platform to study the immune cell migration towards inflammatory foci; and (iii) in Paper III (created from the background of Paper I and Paper II), a microfluidic cell chamber that mimics the microphysiological environment of T cell zone of LN and allows the analyses of interactions between FRCs, DCs and T cells, characterizing their motility, interaction time and trajectories, which were proven to be very similar to reported *in vivo* values.

In all devices and experiments, practice of scientific methodology was followed: in the study of cell *in vitro*, it was recreated the *in vivo* conditions within practical limits, to ensure that the obtained results might be representative for the *in vivo* case and adopted as *a control*. During these studies, when the system was perturbed by a variable to study the phenomenon of interest, the effect of this perturbation was followed by optical detection through direct microscopic observation, or indirect methods as molecular biology analysis, or as a combination of both.

The evolution of the microfluidic design, fabrication and experiments along this PhD consisted in a sequential and refined integration from the background and feedback of previous works/papers.
In this context from the Paper I, we wanted to understand the practical limits of shear stress range that can be supported by T cells and DCs and their interactions inside the microchannel, to ensure that the obtained results might be representative for the in *vivo* case. In this sense, it was identified the need to create a microfluidic platform which could support low range of shear stress (<0.01Dyn cm^{-2}) by using the syringes pumps, leading in this way, to the conception of the cell chamber design of Paper III.
From Paper II, an important aspect elucidated from the experiments was the identification that FRCs could grow in 3D and enwrap the pillars forming a meshwork assembly inside the attractor and control chambers.
Furthermore, and in simultaneous with the project of Appendix A, preliminary perfusion tests inside a microchannels patterned with LN FRCs during 24-48h, were performed and evidenced that mechanical stimulus induced the development along time of a FRC scaffold, which could only supported shear stress until 0.01Dyn cm^{-2} (associated with flow rate of 100nl min^{-1}).
In this context, some of the main bioprinciples/criteria to redesign a new cell chamber for Paper III were defined:

1) to define a circular chamber (with diameter >2mm, considering the form and normal dimensions of LN) with significant density of pillars and filters inside a main chamber to slow the fluidic flow

(due to an increased resistance within the chamber) and to trap the cells, in order to achieve shear stress values lower than 0.01Dyn cm^{-2};

2) to explore and take all advantages of multiphysics simulations of microfluidics - considering the software integration (AutoCAD and COMSOL) and the laminar and predictable behavior with a linear scaling of fluid flow inside the cell chamber - to determine specific velocity and shear stress profile in specific position inside the chamber;
3) to promote the grow of LN FRCs with continuous perfusion to form a 3D FRC meshwork, mimicking the T cell zone architecture, as an open lattice network without ECM filling interface (and without the need to use polymeric hydrogels);
4) with the mechanical stimulation of FRCs in 3D meshwork under flow to induce pressure, drag, and shear forces, and gradient forces, leading to the production of chemokines and other proteins, which change the behavior and motility of T cell and DC, as well as their interactions;
5) to perform cell tests with successive increment of flow rates, in order to simulate a normal inflammation process;
6) and also during these cell tests, by control of the flow rate, to mimic the natural attachment and detachment process of T cells to DCs or FRCs during immune interaction by fluid flow.

Regarding the microfabrication methodology, the general focus was based on the use of commercially available substrates and materials, and of common lithographic procedures, in order to avoid potential cost and time for optimizations. Thus, the substrates used in all systems were standard Si wafer (2 in) and cover glasses (Menzel Gläser; Ø50mm no.15 thickness). As materials used for microstructures, positive and negative photoresists (SU-8), PDMS and biomaterials (e.g., fibronectin and podoplanin) are all available and can be utilized in standard clean room processes.

Another important aspect implicit in the fabrication of structures, was the creation of systems/platforms, which could be easily integrated into the established work-flows and instrumentation. A clear example was our option to use a thin transparent glass as substrates in all our systems, allowing high-numerical aperture imaging in inverted microscope set-ups.

Furthermore, in the continuation of this vision, we also tried to expand the spectrum to the user-friendly assays, in order to integrate a single-step, automated and user-friendly microsystem, where the technology was not visible, and the user could focus on interpreting the results. This result was clearly achieved in Paper II, although from an engineering perspective it was the most complex device microfabricated in this thesis, from the execution point of view the experiments were quite simple requiring only to load manually solutions (with or without cells) on the device. This clarified us about the concept of simplicity-on-the-chip for a biologist operator, through his time of execution with cell loading and analyses, and without additional equipment (as syringe pumps).

From the tissue/organ-on-a-chip perspective, in Paper I and Paper III some facts and challenges were detected during execution of experiments and are presented here, as alternative tools for future works:
i) It would be very useful to integrate on-the-chip a system of PDMS membrane valves, sensors (for temperature, pH, cell loading, media perfusion and detection) and pumps;
ii) At the level of "micro-macro" interfacing tools and during a continuous perfusion system, it would be useful to have individual metal inlet connectors adapted with a small port to allow the direct injection by micropipetting of a small amount of drug or cells inside the chip, avoiding issues associated with dead volumes, time and bubbles formation.
iii) It would be important to develop a system to switch solutions directly connected with a main inlet/channel/chamber, from syringe pumps. This system could be associated with a recirculation

system, where the medium exchanges would be quite fast without dead volumes time and bubbles formation.
iii) At macro level, during these studies it was visible the need to develop a portable incubator box for the chip with the same standard dimensions of a confocal central holder which could display several parameters of the cell culture on-the-chip (e.g., temperature, O_2, CO_2 and humidity).

However, considering many challenges that are still ahead for the conception of an integrated lymph node-on-a-chip with a vascular connection network for better cell-cell interactions, the main purposes for Paper I and Paper III were successfully achieved, adapting several times strategies and solutions to overcome limitations. For example, in order to maintain our systems with continuous perfusion for long term (2-7days) inside the incubator, all the chip was soaked in PBS and covered with a complementary lid (with two entries for connectors), in order to keep the ideal level of humidity for the system. This strategy also overcame the appearance of bubbles inside the chip that occurred when the fluid was flown at constant speed inside the inlets along time.

Design Principles and Multiphysics Simulations

The organ's tissue architecture is intrinsically correlated with its function. *In vitro*, cells are gifted to self-assemble into organized micro-organoid. However in the absence of structural, mechanical and biochemical cues they are incapable of spontaneously self-assembling in macro-organ as an anatomically correct complex tissue (390).

During this PhD study, in the conception of the design of microfluidic devices, it was crucial to have a forecast and global understanding about the dynamic of structural, mechanical and biochemical cues that were involved in each case-study/platform, through finite-elements multiphysics simulations. In this sense, the platforms involved in the study of the Paper I, III and Appendix A, were projected for *stationary system* at a continuous perfusion. This allowed the analysis of the influence of continuous flow induction to generate specific shear stress profile on cell-cell interactions. Thus, all of these platforms were previously designed and simulated using COMSOL Multiphysics in order to predict the velocity ranges and shear stress profiles inside the biochips, in order to compare and to mimic the micro physiological parameters reported *in vivo*.

As a complementary vision, in the study of Paper II, the challenge was focused at the *transient system* to analyze the direct effect of signaling agents flow-free diffusion on cell migration, using a single-step and user-friendly system. Although several requisites have contributed to the simplicity on the device operation, they increased the complexity of the simulation and microfabrication process due to the different height of the microchannels. In this sense, because of the simulation complexity and given the compartmentalization of continuous and dynamic biochemical gradients produced by a determined number of living cells over time, an experimental analysis of the diffusion gradient with was performed inside the microfluidic device using fluorescent dextran. In this experimental approach, Rh-Dex (3kDa) was used once it is smaller (therefore with higher diffusion coefficient) than typical cytokines produced during inflammation and immune response (e.g, MW CCL19 8.8kDa). More details about this approach can be found in Paper II.

Microfabrication – Photolithography, Soft-lithography and Replica molding

In terms of photolithography processes for microfluidic devices fabrication, in Paper I, III and Appendix A, a standard procedure with two SU-8 layers were performed: an adhesion layer, with a 3-7μm thin layer of photoresist, and a second layer as a test layer, with the desired thickness (e.g. 50, 75, 100, 150, 200μm).

It is worth noting that during the time of this PhD, several lithography processes were optimized as function of each photomask and of the desired result for the final structure. In fact, the structures presented on Paper I and Paper III, although having the same thickness 100μm, they were achieved with different SU-8s (and protocols): (i) in Paper I, SU-8 2100 of MicroChem was used; and (ii) in Paper III, the chosen photoresist was SU-8 3050, considering that this resist is an improved formulation of SU-8 2000 with better level of adhesion and less coating stresses, along with the capability of performing very high aspect ratio (over 5:1) aspect ratio structures. In the particular case of Paper III structure, the high aspect ratio was ideal for the fabrication of features inside the cell chamber.

In the case-study of Paper II, the complex multilayer process involved the utilization of layer of positive photoresist (MaP-1275, Micro Resist Technology GmbH; this layer was associated with cell compartments characterized with a thickness of 28μm and two types of rectangular chambers with a width x length of 550μm x 1000μm and 550μm x 2000μm), which is more difficult to use in a soft lithography process. In fact, this positive resist demonstrated low adhesion and was easily breakable after first time of soft lithography. Furthermore, IPA couldn't be used to clean the mold for further utilization because it dissolved the positive photoresist destroying the master mold. In this context, a replica molding process was developed alternatively to the fabrication of a mold each time that a microfluidic device was required. This allowed multiple and inexpensive replication of the mold (over 50 times) with the advantage to be cleaned quickly with IPA leaving no residues. Thus, our replica molding process was based on the optimization protocol with a specific epoxy glue, Permabond ES562 (371).

Regarding the soft lithography, in the studies of Paper I, II, III and Appendix A, all PDMS devices were fabricated following the standard commercial procedures of Sylgaard TM 184 (Dow Corning) silicone with the curing agent in a proportion of 1:10, poured over the Si/photoresist or epoxy master mold followed by heat-curing at 65-70°C for 1-2h. However, it is important to refer that structures with a high density of micropillars or filters, a slightly increase of the curing temperature to 80°C during 2-3h was performed. At these temperatures, the PDMS has more tendency to dry and slightly shrink becoming easier to peel off the PDMS from the master mold and to guarantee the quality/integrity of the pillars and the master mold.

Biofunctionalization for short and long term perfusion

In all devices, the PDMS replica was irreversibly sealed to a Ø50mm no1.5 thickness sterilized cover glass, using a plasma cleaner for surface activation. Considering the post-processing of the PDMS, a crucial aspect to be noted is associated with the surface cleanness affecting the contact angle (or hydrophobicity) of the structure. This factor is a fundamental property for the PDMS bonding to the glass surface, in capillary driven devices and it also affects the level of adsorbance of biological entities. In this context, the oxygen plasma can be applied to decrease the contact angle, though such hydrophilicity is unstable in air and fades away within ~15-30min (108, 110).

In this context, during the evolution of this work significant steps in the biofunctionalization process were reached, in order to guarantee the normal execution of cell experiments with short and long term continuous perfusion (e.g, appearance of bubbles inside the channels, by surface conversion due to dehydration or biomaterial dissolution).

Initially, as it was mentioned in Paper I, the microchannels were prepared after plasma activation with an extracellular matrix protein coating, fibronectin (FN) and collagen (Col). From this approach, it was evidenced that on the FN-coated surface, DCs spreaded uniformly along the microchannel in accordance with expected morphology: long dendrites and a larger surface area. In contrast, in Col-coated microchannels, DCs were poorly dispersed and with thinner and shorter dendrites. These results evidenced that FN-coated surfaces have shown a beneficial effect on the DC function. Our initial option to apply FN as an ECM, was based on the detailed ultrastructural studies of lymph micro-anatomy and on individual molecular components of LN paracortex developed in several studies (387). In the T cell cortex, the reticular network, as fundamental element of the inter- and peri-follicular stroma made of collagen fibers and fibroblastic reticular cells wrapping the fibers, presents two major individual extracellular matrix components, fibronectin and laminin-1. Our findings of a positive effect on FN-coating on the DC monolayer and dendritic length were in line with the literature (22), evidencing the impact of this ECM on the phenotypical and functional properties of DCs and its influence on DC induced T cell differentiation.

Despite the FN-coating capacity to enhance cell adhesion and proliferation during 24h, for long term experiment (more than >24h), using these microchannels in continuous perfusion, it was detected cell sheet aggregation and detachment. Furthermore, the appearance of bubbles was observed. We hypothesize that this may be a result of the surface conversion due to the successive protein dissociation.

In this way, several alternatives were explored finding good results for long term perfusion with polydopamine (PD)-coated PDMS surfaces. By adopting the same experimental protocol from (373), this ECM revealed significant changes in surfaces wettability due to the presence of hydroxyl and secondary amines groups in long term experiments (>48h). Polydopamine is considered as a bio-inspired material in Bone Tissue Engineering showing a reduced *in vivo* toxicity of implanted biomaterials, and thus suggested as a surface coating reagent for cell studies. The chemistry of dopamine in weak alkaline conditions undergoes oxidative polymerization, resulting in a strong adsorption onto a wide variety of substrates by covalent bonding and strong intermolecular interactions (373).

Structural, mechanical and biochemical cues on immune cell-cell communication

As a primary requirement for accurate recreation and analysis of structured monolayer tissues or scaffolds on-the-chip and with cell-cell interactions, was the acquisition of clean, detailed and multiscale digital imaging data through the confocal microscopy. This type of light microscope allows an excellent image quality acquisition, though with a consequent slower image acquisition process and a limited choice of excitation wavelengths. By using the Zeiss LSM 510 confocal microscope, it was possible to visualize and capture in 2D and 3D at different times (time lapse fluorescence and differential interference contrast images), using a fully rendered multidimensional data set and a scheme of monochrome Z-stacks, resulting in a “top view” projection. Another advantage was the simple integration among software for cell analysis treatment where fluorescence micrographs can be

analyzed using Bitplane Imaris 8.1.2 or ImageJ software, and more explored through the customized Matlab scripts (or XTensions) in function on our desired parameters.

Passive and active mechanical stimuli were explored in all studies. As passive mechanical stimuli, we can identify the stiffness of the surrounding microenvironment as on substrat cover with FN and Col in Paper I and II, or PD-coated PMDS pillars in Paper III. In addition, we can also identify a confined geometry of basic tissue structures, as a mimicked hexagonal capillary network with cross section of 6μm x 6μm presented in Paper II.

Cells can sense these mechanical cues via integrin-mediated signal transduction and focal adhesions (sensitive as a balance between stiffness and the content of extracellular matrix) (391, 392). This integrin is a molecular complex that promotes deformability in specific environment and dynamically remodels in response by external inputs (393-396). Cells can also sense mechanical cues by triggering signaling cascade with a wide array of biological ramification. It should be noted that other physicochemical properties, including the distribution of adhesion ligands and the hydrophobicity/hydrophilicity of the environment, have also been shown to affect the cell behavior (390).

As active or imparted mechanical cues, in Paper I and Paper III the structural scaffolds and cell-cell interactions were submitted and affected by shear stress force and tugging forces from their neighbors. We reported, cell attachment and detachment test were performed to explore the mechanism, dynamics and basic cell behavior of attachment and detachment of antigen-specific and unspecific T cells to activated antigen-presenting or non-activated DCs in 2D monolayer of cells (Paper I) or 3D FRC scaffold (Paper III), during flow at different shear stress. Furthermore, basic principles of cell motility and mechanical force associated with immunological synapse formation were observed and analyzed using this technology.

In addition, during the evolution of this PhD, platforms were developed considering the bioprinciple requisites to achieve low values of shear stress, starting from $5x10^{-5}$Dyn cm^{-2} to 0.02Dyn cm^{-2} (Paper III), as well as high level of destructivity with shear stress of 100Dyn cm^{-2} (Paper I). With these ranges, the operator has significant freedom to control the mechanical forces applied on FRC scaffolds and on cell interactions. It should be noted that this range integrates the low range of shear stress of the physiological values for complex flow in lymph nodes published until now in literature 0.005 to 0.05Dyn cm^{-2} (43, 372, 388).

Considering that shear stress and hydrodynamic forces are able to dynamically remodel cell by changing their volume or aspect ratio, which are key features that induce the molecular signaling gradients within cells (390), we studied the 3D FRC trabecular network construction by perfusion around the PD-coated PDMS pillars on a chip. By continued perfusion during 48h, we successfully achieved a FRC meshwork where FRCs tended to align and enwrap the PDMS pillars spaced by 100μm with a height of 100μm in a homogenous dispersion. Despite the difficulty to determine microphysiologically relevant flow velocities in the LN, our experiments and simulation data showed, by cellular behavior observation, that the range of shear stress supported by this system with high cell density during initial loading ($10\text{-}20x10^{6}$cells ml^{-1}) is 0.0007 to 0.008Dyn cm^{-2}. In the device tested in this work (Paper III), these shear stresses are attained for flows ranging from 50nl min^{-1} to 200nl min^{-1} corresponding to the fluid velocities on cells between a minimum for normal cell growth (assuming, FRCs tested in our platforms) around 150μm min^{-1} and as maximum supported by the stromal mesh 1800μm min^{-1}.

Together, these data suggest that the construction and organization of a meshwork by FRC cells is the combination of several aspects: (i) the mechanical stimulation of FRCs in 3D meshwork under flow induced pressure, drag, and shear forces, and gradient forces inducing the production chemokines and other proteins; (ii) a vigorous flow rate through the system allows an enhanced delivery of nutrients and gases; (iii) the direct collision/interaction of DCs, T cells and proteins with FRC mesh induce the production of chemokines gradients and adhesion molecules, working as spatio-temporal guide for immune interactions or homeostasis (as Spatiotemporal Biochemical Signaling cue). Additionally, for this system in particular, the maximum value of shear stress supported by FRC scaffold was found to be around 0.008-0.01Dyn cm^{-2}, corresponding to a high level of fluid velocity: ~1800µm min^{-1}. More details can be found on Paper III/Manuscript.

For this wide range of control of shear stress on cell-cell interactions (Paper III), several types of cell attachment/detachment tests were performed in order to mimic the natural adaptive inflammation process. Cells motility parameters (i.e. average velocity, displacement and interaction time) were characterized and compared to the ones reported *in vivo*. For distinct cell tests, the final results were convergent and are in line to studies performing *in vivo*.

From Paper I, and through the application of cell attachment/detachment tests with high level of shear stresses (from 0.01 to 100Dyn cm^{-2}), it was possible by a successive increment of shear profile on T cell:DC interactions to determine the mechanical strength on the immunological synapse formation (a range estimated to be 0.25-4.8nN), and the suitable velocities for differentially breaking the bond of antigen-specific vs non-specific interactions.

Regarding the study of Spatiotemporal Biochemical Signaling cue, the platform of Paper II was conceived to explore a complementary vision of adaptive immune response through chemotaxis effect on cell-behavior in absence of active forces on cells. By recapitulating distinct compartments of tissues under condition of inflammation, it was possible to compare time-dependent signals through the cell migration, and to explore the decision-making process in migration strategy under specific paths and geometries (hexagonal capillary network).

Towards the Immuneengineering

Demonstrating the viability of these microfluidic platforms to mimic the complexity involved in immune reactions, the next challenge is to use these platforms for a more in-deep investigation of intercellular signaling on immunological synapse given different stimuli, and to explore new therapeutic targets for diagnostic and immunotherapy.

5. CONCLUSION AND OUTLOOK

Microfluidic technology has emerged in the past decade as important biomedical tool for the study of immune-cancer cell interactions. This technology represents an important trade-off between the *in vivo* and the compartmentalization of microphysiology in *in vitro* platform, allowing precise control of the cellular biophysical and biochemical stimuli. It further allows coupling with *on-chip* technologies for detection, sorting and 3D cell growth, resulting in biochips with a remarkable potential for point-of-care testing, drug screening tests, and translational cancer and autoimmune research.

In this context, during the evolution of this project all efforts were focused on the conception of microfluidic platforms that allowed the investigation of interactions between naïve T cells and dendritic cells, by recreating the microenvironment of a T cell zone of LN, and to explore the immune cell migration under inflammatory conditions.

In Paper I, a microchannel device was developed to explore the mechanism, dynamics and basic cell behavior of attachment and detachment of antigen-specific and unspecific $CD4^+$ and $CD8^+$ T cells to activated or non-activated DC monolayer during continuous flow at different shear stresses. In this study, we observed random migration of antigen-specific T cells onto the antigen-presenting DC monolayer with a mean T cell:DC dwell time of 12.8min and a mean velocity of 6μm min^{-1} at a shear stress of 0.01Dyn cm^{-2}. In this study, we further identified that the range of mechanical force associated with the immunological synapse formation was ~0.25-4.8nN.

With this platform, we successfully demonstrated the ability of this system to selectively promote adhesion of antigen-specific T cells through serial contacts. Furthermore, we found antigen-specific attachment and detachment at different shear stresses, suggesting that a shear stress of 0.1-1Dyn cm^{-2} can be used to selectively allow cell-based affinity isolation of antigen specific T cells towards unknown antigen. By contrast to static cultures or passive channels, this platform can be used to analyze – in parallel and in real time, and through control over adhesion – the effect of different treatments, inhibitors, activators or immunogens. This system can also be used as research tool to understand T cell development and activation, contribution of different cell types in immunization protocols, and generation to specific immune responses. It can also be utilized as a clinical development tool towards *in vitro* immunization and immunotherapeutic approaches.

In Paper II, a single-step and user-friendly diffusion flow-free platform was created to study cell migration. The microfabrication process involved 3 different photoresist heights and was further transformed to a unique epoxy mold for easy and reproducible replica molding. With this system, migration models in distinct microcompartments under inflammatory conditions and single decision-making process driving collective cell behavior were observed and analyzed. During this study, this platform confirmed to provide a structured environment for automated long-term high-resolution interrogation of the process of immune cell recruitment and migration towards cell-produced gradients at a single to collective cell level. This platform allowed us to identify the directional migration of T cells and DCs towards the inflammation foci (with a mean speed 9μm min^{-1}). Furthermore, through the hexagonal network, we observed at a single level the decision-making process at intersections, where cells probe both alternative paths before making a decision in which direction to advance.

Through these real-time observations, this platform can be used to study the individual cell decision-making leading to collective behavior in the immune system, and to compare different systemic or genetic contributions to immune system effects/defects as a model system for tissue repair.

In the sequence of the previous studies and as an integration of Paper I and Paper II, Paper III consisted on the development of a microfluidic cell chamber that mimicked the microphysiology of T cell zone of LN. This chamber was conceived for the growth of FRC scaffold through the application of perfusion flow, which induced both chemical stimuli (e.g., nutrient, biological activation) and

mechanical stimuli (e.g., shear stress, fluid velocity). This was attained upon continuous perfusion during 48h at 100nl min^{-1} with a corresponding shear stress 0.001 to 0.004Dyn cm^{-2}.

This platform allowed in a second stage, to analyze the cell behavior with 2 types of cells, in order to simplify the level of cellular interactions as intermediate system testing. Two types of cells tests were performed: (i) DC motility analysis in a FRC scaffold when submitted to successive increment of flow rates (50nl min^{-1} to 500nl min^{-1}); and (ii) the analysis of natural attachment of T cell flowing over a FRC scaffold. From these tests, high cell motility was observed to DCs and T cells, both with a mean velocity of ~10µm min^{-1}.

At a third stage, cell tests were performed with three cell types present on the T cell zone of a LN - T cells, DCs, and FRCs. The cells motility was then analyzing in terms of average velocity, distance and time and the results we compared to the ones reported *in vivo*. These tests consisted in the study with and without cognate interactions using LPS+OVA II peptide activation in order to analyze the natural attachment of DCs and T cells in successive increment of flow rate (100 to 300nl min^{-1}), mimicking an immediate response to inflammation. These results evidenced that without activation, T cells and DCs presented a mean velocity of ~5µm min^{-1}, random movements and "stop and go" interactions during 3min. With cognate interactions, it was visible a significant decrease of DC and T cell velocity to ~2.5µm min^{-1}, where T cells moved in characteristic looping patterns making serial contacts with the same or with neighboring DCs, with interval of interactions around ~7min. These results were consistent to studies performed *in vivo*, demonstrating that this microfluidics device mimics the cell behavior in the T cells zone of LN, being a LN-T cell zone-on-the-chip.

In this sense, this platform opens new horizons as a tool for the investigation of intercellular signalling of immune synapse, or as a clinical development tool towards *in vitro* immunization, personalized cancer vaccination, immunotherapeutic approaches for cancer and autoimmune diseases.

In terms of microfluidic technology and microfabrication processes, several NanoMicroEngineering challenges regarding system integration and platform development still need to be solved. Creative lego-integrated solutions aiming for a simpler and practical cell platform for the end-user is still required. In this perspective and in the sequence of this PhD project, the concrete challenges to be developed in order to increase the level of control of the operator in multiple variables simultaneously during experiments, would be: (i) the integration of valves; (ii) sensors (for temperature, pH, cell loading, media perfusion and detection) and pumps; (iii) the creation of "micro-macro" interfacing tools" and a general system to switch the feeding solutions; and, (iv) a portable incubator box for the chip with the same standard dimensions of a confocal central holder, which could display several parameters of the cell culture on-the-chip (e.g., O_2, CO_2 and humidity).

REFERENCES

1. Conniot J, Silva JM, Fernandes JG, Silva LC, Gaspar R, Brocchini S, et al. Cancer immunotherapy: nanodelivery approaches for immune cell targeting and tracking. Frontiers in chemistry. 2014;2:105.
2. Guo F, French JB, Li P, Zhao H, Chan CY, Fick JR, et al. Probing cell-cell communication with microfluidic devices. Lab on a chip. 2013;13(16):3152-62.
3. Swartz MA, Hirosue S, Hubbell JA. Engineering approaches to immunotherapy. Science translational medicine. 2012;4(148):148rv9.
4. Vu TQ, de Castro RM, Qin L. Bridging the gap: microfluidic devices for short and long distance cell-cell communication. Lab on a chip. 2017;17(6):1009-23.
5. Li Q, Withoff S, Verma IM. Inflammation-associated cancer: NF-kappaB is the lynchpin. Trends in immunology. 2005;26(6):318-25.
6. Karin M, Greten FR. NF-kappaB: linking inflammation and immunity to cancer development and progression. Nature reviews Immunology. 2005;5(10):749-59.
7. Philip M, Rowley DA, Schreiber H. Inflammation as a tumor promoter in cancer induction. Seminars in cancer biology. 2004;14(6):433-9.
8. Nahavandi S, Tang SY, Baratchi S, Soffe R, Nahavandi S, Kalantar-zadeh K, et al. Microfluidic platforms for the investigation of intercellular signalling mechanisms. Small. 2014;10(23):4810-26.
9. Dura B, Dougan SK, Barisa M, Hoehl MM, Lo CT, Ploegh HL, et al. Profiling lymphocyte interactions at the single-cell level by microfluidic cell pairing. Nature communications. 2015;6:5940.
10. Bousso P. T-cell activation by dendritic cells in the lymph node: lessons from the movies. Nature reviews Immunology. 2008;8(9):675-84.
11. Miller MJ, Safrina O, Parker I, Cahalan MD. Imaging the single cell dynamics of CD4+ T cell activation by dendritic cells in lymph nodes. The Journal of experimental medicine. 2004;200(7):847-56.
12. Miller MJ, Wei SH, Parker I, Cahalan MD. Two-photon imaging of lymphocyte motility and antigen response in intact lymph node. Science. 2002;296(5574):1869-73.
13. Mirsky HP, Miller MJ, Linderman JJ, Kirschner DE. Systems biology approaches for understanding cellular mechanisms of immunity in lymph nodes during infection. Journal of theoretical biology. 2011;287:160-70.
14. Boussommier-Calleja A, Li R, Chen MB, Wong SC, Kamm RD. Microfluidics: A new tool for modeling cancer-immune interactions. Trends in cancer. 2016;2(1):6-19.
15. Boyden S. The chemotactic effect of mixtures of antibody and antigen on polymorphonuclear leucocytes. The Journal of experimental medicine. 1962;115:453-66.
16. Zigmond SH. Ability of polymorphonuclear leukocytes to orient in gradients of chemotactic factors. The Journal of cell biology. 1977;75(2 Pt 1):606-16.
17. Zicha D, Dunn GA, Brown AF. A new direct-viewing chemotaxis chamber. Journal of cell science. 1991;99 (Pt 4):769-75.
18. Muinonen-Martin AJ, Veltman DM, Kalna G, Insall RH. An improved chamber for direct visualisation of chemotaxis. PloS one. 2010;5(12):e15309.
19. Somaweera H, Ibraguimov A, Pappas D. A review of chemical gradient systems for cell analysis. Analytica chimica acta. 2016;907:7-17.
20. Gopalakrishnan N, Hannam R, Casoni GP, Barriet D, Ribe JM, Haug M, et al. Infection and immunity on a chip: a compartmentalised microfluidic platform to monitor immune cell behaviour in real time. Lab on a chip. 2015;15(6):1481-7.
21. Sackmann EK, Fulton AL, Beebe DJ. The present and future role of microfluidics in biomedical research. Nature. 2014;507(7491):181-9.
22. Garcia-Nieto S, Johal RK, Shakesheff KM, Emara M, Royer PJ, Chau DY, et al. Laminin and fibronectin treatment leads to generation of dendritic cells with superior endocytic capacity. PloS one. 2010;5(4):e10123.
23. Young EW, Wheeler AR, Simmons CA. Matrix-dependent adhesion of vascular and valvular endothelial cells in microfluidic channels. Lab on a chip. 2007;7(12):1759-66.

24. Girard JP, Moussion C, Forster R. HEVs, lymphatics and homeostatic immune cell trafficking in lymph nodes. Nature reviews Immunology. 2012;12(11):762-73.
25. Bianchi E, Molteni R, Pardi R, Dubini G. Microfluidics for in vitro biomimetic shear stress-dependent leukocyte adhesion assays. Journal of biomechanics. 2013;46(2):276-83.
26. Whitesides GM. The origins and the future of microfluidics. Nature. 2006;442(7101):368-73.
27. Manz A, Graber N, Widmer HM. Miniaturized Total Chemical-Analysis Systems - a Novel Concept for Chemical Sensing. Sensor Actuat B-Chem. 1990;1(1-6):244-8.
28. Reyes DR, Iossifidis D, Auroux PA, Manz A. Micro total analysis systems. 1. Introduction, theory, and technology. Analytical chemistry. 2002;74(12):2623-36.
29. Faley S, Seale K, Hughey J, Schaffer DK, VanCompernolle S, McKinney B, et al. Microfluidic platform for real-time signaling analysis of multiple single T cells in parallel. Lab on a chip. 2008;8(10):1700-12.
30. Wu M, Swartz MA. Modeling tumor microenvironments in vitro. Journal of biomechanical engineering. 2014;136(2):021011.
31. Portillo-Lara R, Annabi N. Microengineered cancer-on-a-chip platforms to study the metastatic microenvironment. Lab on a chip. 2016;16(21):4063-81.
32. Katt ME, Placone AL, Wong AD, Xu ZS, Searson PC. In Vitro Tumor Models: Advantages, Disadvantages, Variables, and Selecting the Right Platform. Frontiers in bioengineering and biotechnology. 2016;4:12.
33. Suematsu S, Watanabe T. Generation of a synthetic lymphoid tissue-like organoid in mice. Nature biotechnology. 2004;22(12):1539-45.
34. Ruddle NH, Akirav EM. Secondary lymphoid organs: responding to genetic and environmental cues in ontogeny and the immune response. Journal of immunology. 2009;183(4):2205-12.
35. Irvine DJ, Stachowiak AN, Hori Y. Lymphoid tissue engineering: invoking lymphoid tissue neogenesis in immunotherapy and models of immunity. Seminars in immunology. 2008;20(2):137-46.
36. Cupedo T, Stroock A, Coles M. Application of tissue engineering to the immune system: development of artificial lymph nodes. Frontiers in immunology. 2012;3:343.
37. Forster R, Davalos-Misslitz AC, Rot A. CCR7 and its ligands: balancing immunity and tolerance. Nature reviews Immunology. 2008;8(5):362-71.
38. Shields JD, Kourtis IC, Tomei AA, Roberts JM, Swartz MA. Induction of lymphoidlike stroma and immune escape by tumors that express the chemokine CCL21. Science. 2010;328(5979):749-52.
39. Swartz MA, Lund AW. Lymphatic and interstitial flow in the tumour microenvironment: linking mechanobiology with immunity. Nature reviews Cancer. 2012;12(3):210-9.
40. Koning JJ, Mebius RE. Interdependence of stromal and immune cells for lymph node function. Trends in immunology. 2012;33(6):264-70.
41. Clark RA, Yamanaka K, Bai M, Dowgiert R, Kupper TS. Human skin cells support thymus-independent T cell development. The Journal of clinical investigation. 2005;115(11):3239-49.
42. Randolph GJ, Beaulieu S, Lebecque S, Steinman RM, Muller WA. Differentiation of monocytes into dendritic cells in a model of transendothelial trafficking. Science. 1998;282(5388):480-3.
43. Tomei AA, Siegert S, Britschgi MR, Luther SA, Swartz MA. Fluid flow regulates stromal cell organization and CCL21 expression in a tissue-engineered lymph node microenvironment. Journal of immunology. 2009;183(7):4273-83.
44. Actor JK. Introductory Immunology Basic Concepts for Interdisciplinary Applications. London: Academic Press,; 2014. Available from: http://www.sciencedirect.com/science/book/9780124200302 MIT Access Only.
45. Owen JA, Punt J, Stranford SA, Jones PP, Kuby J. Kuby immunology. 7th ed. New York: W.H. Freeman; 2013. xxvii, 692, 109 p. p.
46. Wiig H, Swartz MA. Interstitial fluid and lymph formation and transport: physiological regulation and roles in inflammation and cancer. Physiological reviews. 2012;92(3):1005-60.
47. Systems L-AotLaI. Available online: https://courses.lumenlearning.com/ap2/chapter/anatomy-of-the-lymphatic-and-immune-systems/ (accessed on 24 July 2017).

48. Moura Rosa PG, Nimi; Halaas, Øyvind. Immunity on a Chip. MicroTAS 2015 Gyeongju, South Korea ; Gyeongju, South Korea. 2015.
49. Miller MJ, Hejazi AS, Wei SH, Cahalan MD, Parker I. T cell repertoire scanning is promoted by dynamic dendritic cell behavior and random T cell motility in the lymph node. Proceedings of the National Academy of Sciences of the United States of America. 2004;101(4):998-1003.
50. MadMograph MA. Available online: http://animation801.rssing.com/chan-14669195/all_p1.html#item2 (accessed on 24 July 2017).
51. Mueller SN, Germain RN. Stromal cell contributions to the homeostasis and functionality of the immune system. Nature reviews Immunology. 2009;9(9):618-29.
52. Andorko JI, Hess KL, Jewell CM. Harnessing biomaterials to engineer the lymph node microenvironment for immunity or tolerance. The AAPS journal. 2015;17(2):323-38.
53. Drayton DL, Liao S, Mounzer RH, Ruddle NH. Lymphoid organ development: from ontogeny to neogenesis. Nature immunology. 2006;7(4):344-53.
54. Turley SJ, Fletcher AL, Elpek KG. The stromal and haematopoietic antigen-presenting cells that reside in secondary lymphoid organs. Nature reviews Immunology. 2010;10(12):813-25.
55. Card CM, Yu SS, Swartz MA. Emerging roles of lymphatic endothelium in regulating adaptive immunity. The Journal of clinical investigation. 2014;124(3):943-52.
56. Gretz JE, Anderson AO, Shaw S. Cords, channels, corridors and conduits: critical architectural elements facilitating cell interactions in the lymph node cortex. Immunological reviews. 1997;156:11-24.
57. Gretz JE, Kaldjian EP, Anderson AO, Shaw S. Sophisticated strategies for information encounter in the lymph node: the reticular network as a conduit of soluble information and a highway for cell traffic. Journal of immunology. 1996;157(2):495-9.
58. Gretz JE, Norbury CC, Anderson AO, Proudfoot AE, Shaw S. Lymph-borne chemokines and other low molecular weight molecules reach high endothelial venules via specialized conduits while a functional barrier limits access to the lymphocyte microenvironments in lymph node cortex. The Journal of experimental medicine. 2000;192(10):1425-40.
59. Katakai T, Hara T, Sugai M, Gonda H, Shimizu A. Lymph node fibroblastic reticular cells construct the stromal reticulum via contact with lymphocytes. The Journal of experimental medicine. 2004;200(6):783-95.
60. Bajenoff M, Egen JG, Koo LY, Laugier JP, Brau F, Glaichenhaus N, et al. Stromal cell networks regulate lymphocyte entry, migration, and territoriality in lymph nodes. Immunity. 2006;25(6):989-1001.
61. Bogle G, Dunbar PR. T cell responses in lymph nodes. Wiley interdisciplinary reviews Systems biology and medicine. 2010;2(1):107-16.
62. Ma Z, Discher DE, Finkel TH. Mechanical force in T cell receptor signal initiation. Frontiers in immunology. 2012;3:217.
63. Mempel TR, Henrickson SE, Von Andrian UH. T-cell priming by dendritic cells in lymph nodes occurs in three distinct phases. Nature. 2004;427(6970):154-9.
64. Bousso P, Robey E. Dynamics of CD8+ T cell priming by dendritic cells in intact lymph nodes. Nature immunology. 2003;4(6):579-85.
65. Lin J, Miller MJ, Shaw AS. The c-SMAC: sorting it all out (or in). The Journal of cell biology. 2005;170(2):177-82.
66. Celli S, Lemaitre F, Bousso P. Real-time manipulation of T cell-dendritic cell interactions in vivo reveals the importance of prolonged contacts for CD4+ T cell activation. Immunity. 2007;27(4):625-34.
67. Shakhar G, Lindquist RL, Skokos D, Dudziak D, Huang JH, Nussenzweig MC, et al. Stable T cell-dendritic cell interactions precede the development of both tolerance and immunity in vivo. Nature immunology. 2005;6(7):707-14.
68. Zinselmeyer BH, Dempster J, Gurney AM, Wokosin D, Miller M, Ho H, et al. In situ characterization of CD4+ T cell behavior in mucosal and systemic lymphoid tissues during the induction of oral priming and tolerance. The Journal of experimental medicine. 2005;201(11):1815-23.
69. Linderman JJ, Riggs T, Pande M, Miller M, Marino S, Kirschner DE. Characterizing the dynamics of CD4+ T cell priming within a lymph node. Journal of immunology. 2010;184(6):2873-85.

70. Dustin ML. The immunological synapse. Cancer immunology research. 2014;2(11):1023-33.
71. Dustin ML, Tseng SY, Varma R, Campi G. T cell-dendritic cell immunological synapses. Current opinion in immunology. 2006;18(4):512-6.
72. Huppa JB, Davis MM. T-cell-antigen recognition and the immunological synapse. Nature reviews Immunology. 2003;3(12):973-83.
73. Grakoui A, Bromley SK, Sumen C, Davis MM, Shaw AS, Allen PM, et al. The immunological synapse: a molecular machine controlling T cell activation. Science. 1999;285(5425):221-7.
74. Monks CR, Freiberg BA, Kupfer H, Sciaky N, Kupfer A. Three-dimensional segregation of supramolecular activation clusters in T cells. Nature. 1998;395(6697):82-6.
75. Markey KA, Gartlan KH, Kuns RD, MacDonald KP, Hill GR. Imaging the immunological synapse between dendritic cells and T cells. Journal of immunological methods. 2015;423:40-4.
76. Springer TA. Adhesion receptors of the immune system. Nature. 1990;346(6283):425-34.
77. Hosseini BH, Louban I, Djandji D, Wabnitz GH, Deeg J, Bulbuc N, et al. Immune synapse formation determines interaction forces between T cells and antigen-presenting cells measured by atomic force microscopy. Proceedings of the National Academy of Sciences of the United States of America. 2009;106(42):17852-7.
78. Li YC, Chen BM, Wu PC, Cheng TL, Kao LS, Tao MH, et al. Cutting Edge: mechanical forces acting on T cells immobilized via the TCR complex can trigger TCR signaling. Journal of immunology. 2010;184(11):5959-63.
79. Puech PH, Nevoltris D, Robert P, Limozin L, Boyer C, Bongrand P. Force measurements of TCR/pMHC recognition at T cell surface. PloS one. 2011;6(7):e22344.
80. Wang JH, Reinherz EL. The structural basis of alphabeta T-lineage immune recognition: TCR docking topologies, mechanotransduction, and co-receptor function. Immunological reviews. 2012;250(1):102-19.
81. Campi G, Varma R, Dustin ML. Actin and agonist MHC-peptide complex-dependent T cell receptor microclusters as scaffolds for signaling. The Journal of experimental medicine. 2005;202(8):1031-6.
82. Varma R, Campi G, Yokosuka T, Saito T, Dustin ML. T cell receptor-proximal signals are sustained in peripheral microclusters and terminated in the central supramolecular activation cluster. Immunity. 2006;25(1):117-27.
83. Yokosuka T, Sakata-Sogawa K, Kobayashi W, Hiroshima M, Hashimoto-Tane A, Tokunaga M, et al. Newly generated T cell receptor microclusters initiate and sustain T cell activation by recruitment of Zap70 and SLP-76. Nature immunology. 2005;6(12):1253-62.
84. Kaizuka Y, Douglass AD, Varma R, Dustin ML, Vale RD. Mechanisms for segregating T cell receptor and adhesion molecules during immunological synapse formation in Jurkat T cells. Proceedings of the National Academy of Sciences of the United States of America. 2007;104(51):20296-301.
85. Tian W-C, Finehout E. Microfluidics for biological applications. New York: Springer Science + Business Media; 2008. xix, 416 p. p.
86. Berthier J, Silberzan P. Microfluidics for biotechnology. 2nd ed. Boston: Artech House; 2010. xv, 483 p. p.
87. Bruus H. Theoretical microfluidics. Oxford ; New York: Oxford University Press; 2008. 346 p p.
88. Kirby BJ. Micro- and nanoscale fluid mechanics : transport in microfluidic devices. New York: Cambridge University Press; 2010. xxiii, 512 p. p.
89. HA S. An introduction to fluid mechanics for microfluidic flows. CMOS Biotechnology ed H Lee, D Ham and R M Westervelt (New York: Springer). 2007.
90. Smith JP, Barbati AC, Santana SM, Gleghorn JP, Kirby BJ. Microfluidic transport in microdevices for rare cell capture. Electrophoresis. 2012;33(21):3133-42.
91. Peng Z. Modeling of Particle and Biological Cell Transport in Microchannels: The Ohio State University; 2011.
92. Stokes GG, Larmor J, Rayleigh JWS. Mathematical and physical papers. Cambridge,: University Press; 1880.

93. Bird RB, Stewart WE, Lightfoot EN. Role of Transport Phenomena in Chemical-Engineering Teaching and Research - Past, Present, and Future. Abstr Pap Am Chem S. 1979(Apr):35-&.
94. Padmavathi BS, Amaranath T, Nigam SD. Stokes-Flow Past a Sphere with Mixed Slip Stick Boundary-Conditions. Fluid Dyn Res. 1993;11(5):229-34.
95. Yuan LB, Liu ZH, Yang J. Measurement approach of Brownian motion force by an abrupt tapered fiber optic tweezers. Appl Phys Lett. 2007;91(5).
96. Bhattacharjee S, Elimelech M. Surface element integration: A novel technique for evaluation of DLVO interaction between a particle and a flat plate. J Colloid Interf Sci. 1997;193(2):273-85.
97. Verwey EJ. Theory of the stability of lyophobic colloids. The Journal of physical and colloid chemistry. 1947;51(3):631-6.
98. Dietzel A. Microsystems for pharmatechnology : manipulation of fluids, particles, droplets, and cells. Cham: Springer,; 2016. Available from: http://dx.doi.org/10.1007/978-3-319-26920-7 MIT Access Only.
99. Saliterman S. Fundamentals of bioMEMS and medical microdevices. Hoboken, NJ

Bellingham, Wash.: Wiley-Interscience ;

SPIE Press; 2006. xxvii, 610 p. p.
100. Chakraborty S, SpringerLink (Online service). Microfluidics and microfabrication. New York: Springer,; 2010. Available from: SpringerLink http://dx.doi.org/10.1007/978-1-4419-1543-6 MIT Access Only.
101. Compugraphics. Available online: http://www.compugraphics-photomasks.com/our-capabilities/master-photomasks/ (accessed on 24 July 2017).
102. Levinson HJ, Society of Photo-optical Instrumentation Engineers. Principles of lithography. Bellingham, Wash. (1000 20th St. Bellingham WA 98225-6705 USA): SPIE,; 2010. Available from: http://dx.doi.org/10.1117/3.865363.
103. MicroChem. Available online: http://www.microchem.com/ (accessed on 24 July 2017).
104. Solutions. GE. Available online: http://www.gersteltec.ch/ (accessed on 24 July 2017).
105. Lee KY, LaBianca N, Rishton SA, Zolgharnain S, Gelorme JD, Shaw J, et al. Micromachining applications of a high resolution ultrathick photoresist. J Vac Sci Technol B. 1995;13(6):3012-6.
106. Weibel DB, Diluzio WR, Whitesides GM. Microfabrication meets microbiology. Nature reviews Microbiology. 2007;5(3):209-18.
107. DowCorning. Available online: http://www.dowcorning.com/ (accessed on 24 July 2017).
108. Xia YN, Whitesides GM. Soft lithography. Angew Chem Int Edit. 1998;37(5):550-75.
109. Wikipedia. Available online: https://en.wikipedia.org/wiki/Polydimethylsiloxane (accessed on 24 July 2017).
110. McDonald JC, Duffy DC, Anderson JR, Chiu DT, Wu H, Schueller OJ, et al. Fabrication of microfluidic systems in poly(dimethylsiloxane). Electrophoresis. 2000;21(1):27-40.
111. Mehling M, Tay S. Microfluidic cell culture. Current opinion in biotechnology. 2014;25:95-102.
112. Bhatia SN, Ingber DE. Microfluidic organs-on-chips. Nature biotechnology. 2014;32(8):760-72.
113. Duffy DC, McDonald JC, Schueller OJ, Whitesides GM. Rapid Prototyping of Microfluidic Systems in Poly(dimethylsiloxane). Analytical chemistry. 1998;70(23):4974-84.
114. Singhvi R, Kumar A, Lopez GP, Stephanopoulos GN, Wang DI, Whitesides GM, et al. Engineering cell shape and function. Science. 1994;264(5159):696-8.
115. Chen CS, Mrksich M, Huang S, Whitesides GM, Ingber DE. Geometric control of cell life and death. Science. 1997;276(5317):1425-8.
116. Folch A, Toner M. Cellular micropatterns on biocompatible materials. Biotechnology progress. 1998;14(3):388-92.
117. Kane RS, Takayama S, Ostuni E, Ingber DE, Whitesides GM. Patterning proteins and cells using soft lithography. Biomaterials. 1999;20(23-24):2363-76.
118. Folch A, Ayon A, Hurtado O, Schmidt MA, Toner M. Molding of deep polydimethylsiloxane microstructures for microfluidics and biological applications. Journal of biomechanical engineering. 1999;121(1):28-34.

119. Quake SR, Scherer A. From micro- to nanofabrication with soft materials. Science. 2000;290(5496):1536-40.
120. Unger MA, Chou HP, Thorsen T, Scherer A, Quake SR. Monolithic microfabricated valves and pumps by multilayer soft lithography. Science. 2000;288(5463):113-6.
121. Aumiller GD, Chandros.Ea, Tomlinso.Wj, Weber HP. Submicrometer Resolution Replication of Relief Patterns for Integrated Optics. J Appl Phys. 1974;45(10):4557-62.
122. Berthier E, Young EW, Beebe D. Engineers are from PDMS-land, Biologists are from Polystyrenia. Lab on a chip. 2012;12(7):1224-37.
123. Novo P, Volpetti F, Chu V, Conde JP. Control of sequential fluid delivery in a fully autonomous capillary microfluidic device. Lab on a chip. 2013;13(4):641-5.
124. Bennett MR, Pang WL, Ostroff NA, Baumgartner BL, Nayak S, Tsimring LS, et al. Metabolic gene regulation in a dynamically changing environment. Nature. 2008;454(7208):1119-22.
125. Chen YA, King AD, Shih HC, Peng CC, Wu CY, Liao WH, et al. Generation of oxygen gradients in microfluidic devices for cell culture using spatially confined chemical reactions. Lab on a chip. 2011;11(21):3626-33.
126. Douville NJ, Tung YC, Li R, Wang JD, El-Sayed ME, Takayama S. Fabrication of two-layered channel system with embedded electrodes to measure resistance across epithelial and endothelial barriers. Analytical chemistry. 2010;82(6):2505-11.
127. Nguyen TA, Yin TI, Reyes D, Urban GA. Microfluidic chip with integrated electrical cell-impedance sensing for monitoring single cancer cell migration in three-dimensional matrixes. Analytical chemistry. 2013;85(22):11068-76.
128. Liu MC, Shih HC, Wu JG, Weng TW, Wu CY, Lu JC, et al. Electrofluidic pressure sensor embedded microfluidic device: a study of endothelial cells under hydrostatic pressure and shear stress combinations. Lab on a chip. 2013;13(9):1743-53.
129. Eklund SE, Thompson RG, Snider RM, Carney CK, Wright DW, Wikswo J, et al. Metabolic discrimination of select list agents by monitoring cellular responses in a multianalyte microphysiometer. Sensors. 2009;9(3):2117-33.
130. Chiu DT, Jeon NL, Huang S, Kane RS, Wargo CJ, Choi IS, et al. Patterned deposition of cells and proteins onto surfaces by using three-dimensional microfluidic systems. Proceedings of the National Academy of Sciences of the United States of America. 2000;97(6):2408-13.
131. Gottwald E, Giselbrecht S, Augspurger C, Lahni B, Dambrowsky N, Truckenmuller R, et al. A chip-based platform for the in vitro generation of tissues in three-dimensional organization. Lab on a chip. 2007;7(6):777-85.
132. Mata A, Boehm C, Fleischman AJ, Muschler G, Roy S. Growth of connective tissue progenitor cells on microtextured polydimethylsiloxane surfaces. Journal of biomedical materials research. 2002;62(4):499-506.
133. Huang NT, Chen W, Oh BR, Cornell TT, Shanley TP, Fu J, et al. An integrated microfluidic platform for in situ cellular cytokine secretion immunophenotyping. Lab on a chip. 2012;12(20):4093-101.
134. Woodruff K, Fidalgo LM, Gobaa S, Lutolf MP, Maerkl SJ. Live mammalian cell arrays. Nature methods. 2013;10(6):550-2.
135. Vyawahare S, Griffiths AD, Merten CA. Miniaturization and parallelization of biological and chemical assays in microfluidic devices. Chemistry & biology. 2010;17(10):1052-65.
136. Ramadan Q, Gijs MA. In vitro micro-physiological models for translational immunology. Lab on a chip. 2015;15(3):614-36.
137. Takayama S, Ostuni E, LeDuc P, Naruse K, Ingber DE, Whitesides GM. Subcellular positioning of small molecules. Nature. 2001;411(6841):1016.
138. Li Jeon N, Baskaran H, Dertinger SK, Whitesides GM, Van de Water L, Toner M. Neutrophil chemotaxis in linear and complex gradients of interleukin-8 formed in a microfabricated device. Nature biotechnology. 2002;20(8):826-30.
139. Prentice-Mott HV, Chang CH, Mahadevan L, Mitchison TJ, Irimia D, Shah JV. Biased migration of confined neutrophil-like cells in asymmetric hydraulic environments. Proceedings of the National Academy of Sciences of the United States of America. 2013;110(52):21006-11.
140. Du Y, Hancock MJ, He J, Villa-Uribe JL, Wang B, Cropek DM, et al. Convection-driven generation of long-range material gradients. Biomaterials. 2010;31(9):2686-94.

141. Lo CM, Wang HB, Dembo M, Wang YL. Cell movement is guided by the rigidity of the substrate. Biophysical journal. 2000;79(1):144-52.
142. Kass L, Erler JT, Dembo M, Weaver VM. Mammary epithelial cell: influence of extracellular matrix composition and organization during development and tumorigenesis. The international journal of biochemistry & cell biology. 2007;39(11):1987-94.
143. Kim S, Kim HJ, Jeon NL. Biological applications of microfluidic gradient devices. Integrative biology : quantitative biosciences from nano to macro. 2010;2(11-12):584-603.
144. Carraro A, Hsu WM, Kulig KM, Cheung WS, Miller ML, Weinberg EJ, et al. In vitro analysis of a hepatic device with intrinsic microvascular-based channels. Biomedical microdevices. 2008;10(6):795-805.
145. Griep LM, Wolbers F, de Wagenaar B, ter Braak PM, Weksler BB, Romero IA, et al. BBB on chip: microfluidic platform to mechanically and biochemically modulate blood-brain barrier function. Biomedical microdevices. 2013;15(1):145-50.
146. Lee PJ, Hung PJ, Lee LP. An artificial liver sinusoid with a microfluidic endothelial-like barrier for primary hepatocyte culture. Biotechnology and bioengineering. 2007;97(5):1340-6.
147. Kane BJ, Zinner MJ, Yarmush ML, Toner M. Liver-specific functional studies in a microfluidic array of primary mammalian hepatocytes. Analytical chemistry. 2006;78(13):4291-8.
148. Tumarkin E, Tzadu L, Csaszar E, Seo M, Zhang H, Lee A, et al. High-throughput combinatorial cell co-culture using microfluidics. Integrative biology : quantitative biosciences from nano to macro. 2011;3(6):653-62.
149. Agarwal A, Goss JA, Cho A, McCain ML, Parker KK. Microfluidic heart on a chip for higher throughput pharmacological studies. Lab on a chip. 2013;13(18):3599-608.
150. Baker BM, Trappmann B, Stapleton SC, Toro E, Chen CS. Microfluidics embedded within extracellular matrix to define vascular architectures and pattern diffusive gradients. Lab on a chip. 2013;13(16):3246-52.
151. Nguyen DH, Stapleton SC, Yang MT, Cha SS, Choi CK, Galie PA, et al. Biomimetic model to reconstitute angiogenic sprouting morphogenesis in vitro. Proceedings of the National Academy of Sciences of the United States of America. 2013;110(17):6712-7.
152. Han S, Yan JJ, Shin Y, Jeon JJ, Won J, Jeong HE, et al. A versatile assay for monitoring in vivo-like transendothelial migration of neutrophils. Lab on a chip. 2012;12(20):3861-5.
153. Khanal G, Chung K, Solis-Wever X, Johnson B, Pappas D. Ischemia/reperfusion injury of primary porcine cardiomyocytes in a low-shear microfluidic culture and analysis device. The Analyst. 2011;136(17):3519-26.
154. Tsantoulas C, Farmer C, Machado P, Baba K, McMahon SB, Raouf R. Probing functional properties of nociceptive axons using a microfluidic culture system. PloS one. 2013;8(11):e80722.
155. Li CY, Wood DK, Huang JH, Bhatia SN. Flow-based pipeline for systematic modulation and analysis of 3D tumor microenvironments. Lab on a chip. 2013;13(10):1969-78.
156. Viravaidya K, Shuler ML. Incorporation of 3T3-L1 cells to mimic bioaccumulation in a microscale cell culture analog device for toxicity studies. Biotechnology progress. 2004;20(2):590-7.
157. Gomez-Sjoberg R, Leyrat AA, Pirone DM, Chen CS, Quake SR. Versatile, fully automated, microfluidic cell culture system. Analytical chemistry. 2007;79(22):8557-63.
158. Cookson S, Ostroff N, Pang WL, Volfson D, Hasty J. Monitoring dynamics of single-cell gene expression over multiple cell cycles. Molecular systems biology. 2005;1:2005 0024.
159. Falconnet D, Niemisto A, Taylor RJ, Ricicova M, Galitski T, Shmulevich I, et al. High-throughput tracking of single yeast cells in a microfluidic imaging matrix. Lab on a chip. 2011;11(3):466-73.
160. Frank T, Tay S. Flow-switching allows independently programmable, extremely stable, high-throughput diffusion-based gradients. Lab on a chip. 2013;13(7):1273-81.
161. Han Q, Bagheri N, Bradshaw EM, Hafler DA, Lauffenburger DA, Love JC. Polyfunctional responses by human T cells result from sequential release of cytokines. Proceedings of the National Academy of Sciences of the United States of America. 2012;109(5):1607-12.
162. Lecault V, Vaninsberghe M, Sekulovic S, Knapp DJ, Wohrer S, Bowden W, et al. High-throughput analysis of single hematopoietic stem cell proliferation in microfluidic cell culture arrays. Nature methods. 2011;8(7):581-6.

163. Ricicova M, Hamidi M, Quiring A, Niemisto A, Emberly E, Hansen CL. Dissecting genealogy and cell cycle as sources of cell-to-cell variability in MAPK signaling using high-throughput lineage tracking. Proceedings of the National Academy of Sciences of the United States of America. 2013;110(28):11403-8.
164. Rowat AC, Bird JC, Agresti JJ, Rando OJ, Weitz DA. Tracking lineages of single cells in lines using a microfluidic device. Proceedings of the National Academy of Sciences of the United States of America. 2009;106(43):18149-54.
165. Son S, Tzur A, Weng Y, Jorgensen P, Kim J, Kirschner MW, et al. Direct observation of mammalian cell growth and size regulation. Nature methods. 2012;9(9):910-2.
166. Taniguchi Y, Choi PJ, Li GW, Chen H, Babu M, Hearn J, et al. Quantifying E. coli proteome and transcriptome with single-molecule sensitivity in single cells. Science. 2010;329(5991):533-8.
167. Tay S, Hughey JJ, Lee TK, Lipniacki T, Quake SR, Covert MW. Single-cell NF-kappaB dynamics reveal digital activation and analogue information processing. Nature. 2010;466(7303):267-71.
168. Vedel S, Tay S, Johnston DM, Bruus H, Quake SR. Migration of cells in a social context. Proceedings of the National Academy of Sciences of the United States of America. 2013;110(1):129-34.
169. Yamanaka YJ, Szeto GL, Gierahn TM, Forcier TL, Benedict KF, Brefo MS, et al. Cellular barcodes for efficiently profiling single-cell secretory responses by microengraving. Analytical chemistry. 2012;84(24):10531-6.
170. Halldorsson S, Lucumi E, Gomez-Sjoberg R, Fleming RM. Advantages and challenges of microfluidic cell culture in polydimethylsiloxane devices. Biosensors & bioelectronics. 2015;63:218-31.
171. Berthier E, Warrick J, Yu H, Beebe DJ. Managing evaporation for more robust microscale assays. Part 1. Volume loss in high throughput assays. Lab on a chip. 2008;8(6):852-9.
172. Wu MH, Dimopoulos G, Mantalaris A, Varley J. The effect of hyperosmotic pressure on antibody production and gene expression in the GS-NS0 cell line. Biotechnology and applied biochemistry. 2004;40(Pt 1):41-6.
173. Dezengotita VM, Kimura R, Miller WM. Effects of CO2 and osmolality on hybridoma cells: growth, metabolism and monoclonal antibody production. Cytotechnology. 1998;28(1-3):213-27.
174. Melin J, Quake SR. Microfluidic large-scale integration: the evolution of design rules for biological automation. Annual review of biophysics and biomolecular structure. 2007;36:213-31.
175. Chin CD, Laksanasopin T, Cheung YK, Steinmiller D, Linder V, Parsa H, et al. Microfluidics-based diagnostics of infectious diseases in the developing world. Nature medicine. 2011;17(8):1015-9.
176. Henry AC, Tutt TJ, Galloway M, Davidson YY, McWhorter CS, Soper SA, et al. Surface modification of poly(methyl methacrylate) used in the fabrication of microanalytical devices. Analytical chemistry. 2000;72(21):5331-7.
177. Browne AW, Rust MJ, Jung W, Lee SH, Ahn CH. A rapid prototyping method for polymer microfluidics with fixed aspect ratio and 3D tapered channels. Lab on a chip. 2009;9(20):2941-6.
178. Nilghaz A, Wicaksono DH, Gustiono D, Abdul Majid FA, Supriyanto E, Abdul Kadir MR. Flexible microfluidic cloth-based analytical devices using a low-cost wax patterning technique. Lab on a chip. 2012;12(1):209-18.
179. Domansky K, Leslie DC, McKinney J, Fraser JP, Sliz JD, Hamkins-Indik T, et al. Clear castable polyurethane elastomer for fabrication of microfluidic devices. Lab on a chip. 2013;13(19):3956-64.
180. von Lode P. Point-of-care immunotesting: approaching the analytical performance of central laboratory methods. Clinical biochemistry. 2005;38(7):591-606.
181. Martinez AW, Phillips ST, Whitesides GM, Carrilho E. Diagnostics for the developing world: microfluidic paper-based analytical devices. Analytical chemistry. 2010;82(1):3-10.
182. Yager P, Edwards T, Fu E, Helton K, Nelson K, Tam MR, et al. Microfluidic diagnostic technologies for global public health. Nature. 2006;442(7101):412-8.
183. Wikswo JP, Curtis EL, Eagleton ZE, Evans BC, Kole A, Hofmeister LH, et al. Scaling and systems biology for integrating multiple organs-on-a-chip. Lab on a chip. 2013;13(18):3496-511.

184. Wikswo JP, Block FE, 3rd, Cliffel DE, Goodwin CR, Marasco CC, Markov DA, et al. Engineering challenges for instrumenting and controlling integrated organ-on-chip systems. IEEE transactions on bio-medical engineering. 2013;60(3):682-90.
185. Booth R, Kim H. Characterization of a microfluidic in vitro model of the blood-brain barrier (muBBB). Lab on a chip. 2012;12(10):1784-92.
186. Ferrell N, Desai RR, Fleischman AJ, Roy S, Humes HD, Fissell WH. A microfluidic bioreactor with integrated transepithelial electrical resistance (TEER) measurement electrodes for evaluation of renal epithelial cells. Biotechnology and bioengineering. 2010;107(4):707-16.
187. Huang SB, Wang SS, Hsieh CH, Lin YC, Lai CS, Wu MH. An integrated microfluidic cell culture system for high-throughput perfusion three-dimensional cell culture-based assays: effect of cell culture model on the results of chemosensitivity assays. Lab on a chip. 2013;13(6):1133-43.
188. Hu N, Wu C, Ha D, Wang T, Liu Q, Wang P. A novel microphysiometer based on high sensitivity LAPS and microfluidic system for cellular metabolism study and rapid drug screening. Biosensors & bioelectronics. 2013;40(1):167-73.
189. Walker G, Beebe DJ. A passive pumping method for microfluidic devices. Lab on a chip. 2002;2(3):131-4.
190. Butler KL, Ambravaneswaran V, Agrawal N, Bilodeau M, Toner M, Tompkins RG, et al. Burn injury reduces neutrophil directional migration speed in microfluidic devices. PloS one. 2010;5(7):e11921.
191. Sackmann EK, Berthier E, Young EW, Shelef MA, Wernimont SA, Huttenlocher A, et al. Microfluidic kit-on-a-lid: a versatile platform for neutrophil chemotaxis assays. Blood. 2012;120(14):e45-53.
192. Jowhar D, Wright G, Samson PC, Wikswo JP, Janetopoulos C. Open access microfluidic device for the study of cell migration during chemotaxis. Integrative biology : quantitative biosciences from nano to macro. 2010;2(11-12):648-58.
193. Berry SM, Alarid ET, Beebe DJ. One-step purification of nucleic acid for gene expression analysis via Immiscible Filtration Assisted by Surface Tension (IFAST). Lab on a chip. 2011;11(10):1747-53.
194. Berry SM, Strotman LN, Kueck JD, Alarid ET, Beebe DJ. Purification of cell subpopulations via immiscible filtration assisted by surface tension (IFAST). Biomedical microdevices. 2011;13(6):1033-42.
195. Berthier E, Warrick J, Casavant B, Beebe DJ. Pipette-friendly laminar flow patterning for cell-based assays. Lab on a chip. 2011;11(12):2060-5.
196. Gorkin R, Park J, Siegrist J, Amasia M, Lee BS, Park JM, et al. Centrifugal microfluidics for biomedical applications. Lab on a chip. 2010;10(14):1758-73.
197. Berthier E, Guckenberger DJ, Cavnar P, Huttenlocher A, Keller NP, Beebe DJ. Kit-On-A-Lid-Assays for accessible self-contained cell assays. Lab on a chip. 2013;13(3):424-31.
198. Watkins NN, Hassan U, Damhorst G, Ni H, Vaid A, Rodriguez W, et al. Microfluidic CD4+ and CD8+ T lymphocyte counters for point-of-care HIV diagnostics using whole blood. Science translational medicine. 2013;5(214):214ra170.
199. Kotz KT, Xiao W, Miller-Graziano C, Qian WJ, Russom A, Warner EA, et al. Clinical microfluidics for neutrophil genomics and proteomics. Nature medicine. 2010;16(9):1042-7.
200. Warner EA, Kotz KT, Ungaro RF, Abouhamze AS, Lopez MC, Cuenca AG, et al. Microfluidics-based capture of human neutrophils for expression analysis in blood and bronchoalveolar lavage. Laboratory investigation; a journal of technical methods and pathology. 2011;91(12):1787-95.
201. English D, Andersen BR. Single-step separation of red blood cells. Granulocytes and mononuclear leukocytes on discontinuous density gradients of Ficoll-Hypaque. Journal of immunological methods. 1974;5(3):249-52.
202. Huh D, Matthews BD, Mammoto A, Montoya-Zavala M, Hsin HY, Ingber DE. Reconstituting organ-level lung functions on a chip. Science. 2010;328(5986):1662-8.
203. Tsai M, Kita A, Leach J, Rounsevell R, Huang JN, Moake J, et al. In vitro modeling of the microvascular occlusion and thrombosis that occur in hematologic diseases using microfluidic technology. The Journal of clinical investigation. 2012;122(1):408-18.

204. Lin B, Levchenko A. Spatial manipulation with microfluidics. Frontiers in bioengineering and biotechnology. 2015;3:39.
205. Singer SJ, Kupfer A. The directed migration of eukaryotic cells. Annual review of cell biology. 1986;2:337-65.
206. Roussos ET, Condeelis JS, Patsialou A. Chemotaxis in cancer. Nature reviews Cancer. 2011;11(8):573-87.
207. Gregorieff A, Clevers H. Wnt signaling in the intestinal epithelium: from endoderm to cancer. Genes & development. 2005;19(8):877-90.
208. Wong AP, Perez-Castillejos R, Christopher Love J, Whitesides GM. Partitioning microfluidic channels with hydrogel to construct tunable 3-D cellular microenvironments. Biomaterials. 2008;29(12):1853-61.
209. Sung KE, Yang N, Pehlke C, Keely PJ, Eliceiri KW, Friedl A, et al. Transition to invasion in breast cancer: a microfluidic in vitro model enables examination of spatial and temporal effects. Integrative biology : quantitative biosciences from nano to macro. 2011;3(4):439-50.
210. Zervantonakis IK, Hughes-Alford SK, Charest JL, Condeelis JS, Gertler FB, Kamm RD. Three-dimensional microfluidic model for tumor cell intravasation and endothelial barrier function. Proceedings of the National Academy of Sciences of the United States of America. 2012;109(34):13515-20.
211. Kaji H, Camci-Unal G, Langer R, Khademhosseini A. Engineering systems for the generation of patterned co-cultures for controlling cell-cell interactions. Biochimica et biophysica acta. 2011;1810(3):239-50.
212. Huang CP, Lu J, Seon H, Lee AP, Flanagan LA, Kim HY, et al. Engineering microscale cellular niches for three-dimensional multicellular co-cultures. Lab on a chip. 2009;9(12):1740-8.
213. Amadi OC, Steinhauser ML, Nishi Y, Chung S, Kamm RD, McMahon AP, et al. A low resistance microfluidic system for the creation of stable concentration gradients in a defined 3D microenvironment. Biomedical microdevices. 2010;12(6):1027-41.
214. Sung KE, Beebe DJ. Microfluidic 3D models of cancer. Advanced drug delivery reviews. 2014;79-80:68-78.
215. Wu J, Wu X, Lin F. Recent developments in microfluidics-based chemotaxis studies. Lab on a chip. 2013;13(13):2484-99.
216. Haessler U, Pisano M, Wu M, Swartz MA. Dendritic cell chemotaxis in 3D under defined chemokine gradients reveals differential response to ligands CCL21 and CCL19. Proceedings of the National Academy of Sciences of the United States of America. 2011;108(14):5614-9.
217. Ricart BG, John B, Lee D, Hunter CA, Hammer DA. Dendritic cells distinguish individual chemokine signals through CCR7 and CXCR4. Journal of immunology. 2011;186(1):53-61.
218. Tong Z, Balzer EM, Dallas MR, Hung WC, Stebe KJ, Konstantopoulos K. Chemotaxis of cell populations through confined spaces at single-cell resolution. PloS one. 2012;7(1):e29211.
219. Hoerning A, Koss K, Datta D, Boneschansker L, Jones CN, Wong IY, et al. Subsets of human CD4(+) regulatory T cells express the peripheral homing receptor CXCR3. European journal of immunology. 2011;41(8):2291-302.
220. Ricart BG, Yang MT, Hunter CA, Chen CS, Hammer DA. Measuring traction forces of motile dendritic cells on micropost arrays. Biophysical journal. 2011;101(11):2620-8.
221. Haessler U, Kalinin Y, Swartz MA, Wu M. An agarose-based microfluidic platform with a gradient buffer for 3D chemotaxis studies. Biomedical microdevices. 2009;11(4):827-35.
222. Nandagopal S, Wu D, Lin F. Combinatorial guidance by CCR7 ligands for T lymphocytes migration in co-existing chemokine fields. PloS one. 2011;6(3):e18183.
223. Dura B, Voldman J. Spatially and temporally controlled immune cell interactions using microscale tools. Current opinion in immunology. 2015;35:23-9.
224. Chattopadhyay PK, Gierahn TM, Roederer M, Love JC. Single-cell technologies for monitoring immune systems. Nature immunology. 2014;15(2):128-35.
225. Mittelbrunn M, Sanchez-Madrid F. Intercellular communication: diverse structures for exchange of genetic information. Nature reviews Molecular cell biology. 2012;13(5):328-35.
226. Kumar NM, Gilula NB. The gap junction communication channel. Cell. 1996;84(3):381-8.
227. Walker GM, Zeringue HC, Beebe DJ. Microenvironment design considerations for cellular scale studies. Lab on a chip. 2004;4(2):91-7.

228. Brownlee C. Role of the extracellular matrix in cell-cell signalling: paracrine paradigms. Current opinion in plant biology. 2002;5(5):396-401.
229. Varadarajan N, Julg B, Yamanaka YJ, Chen H, Ogunniyi AO, McAndrew E, et al. A high-throughput single-cell analysis of human CD8(+) T cell functions reveals discordance for cytokine secretion and cytolysis. The Journal of clinical investigation. 2011;121(11):4322-31.
230. Yamanaka YJ, Berger CT, Sips M, Cheney PC, Alter G, Love JC. Single-cell analysis of the dynamics and functional outcomes of interactions between human natural killer cells and target cells. Integrative biology : quantitative biosciences from nano to macro. 2012;4(10):1175-84.
231. Vanherberghen B, Olofsson PE, Forslund E, Sternberg-Simon M, Khorshidi MA, Pacouret S, et al. Classification of human natural killer cells based on migration behavior and cytotoxic response. Blood. 2013;121(8):1326-34.
232. Christakou AE, Ohlin M, Vanherberghen B, Khorshidi MA, Kadri N, Frisk T, et al. Live cell imaging in a micro-array of acoustic traps facilitates quantification of natural killer cell heterogeneity. Integrative biology : quantitative biosciences from nano to macro. 2013;5(4):712-9.
233. Olofsson PE, Forslund E, Vanherberghen B, Chechet K, Mickelin O, Ahlin AR, et al. Distinct Migration and Contact Dynamics of Resting and IL-2-Activated Human Natural Killer Cells. Frontiers in immunology. 2014;5:80.
234. Elitas M, Brower K, Lu Y, Chen JJ, Fan R. A microchip platform for interrogating tumor-macrophage paracrine signaling at the single-cell level. Lab on a chip. 2014;14(18):3582-8.
235. Skelley AM, Kirak O, Suh H, Jaenisch R, Voldman J. Microfluidic control of cell pairing and fusion. Nature methods. 2009;6(2):147-52.
236. Kemna EW, Wolbers F, Vermes I, van den Berg A. On chip electrofusion of single human B cells and mouse myeloma cells for efficient hybridoma generation. Electrophoresis. 2011;32(22):3138-46.
237. Dura B, Liu Y, Voldman J. Deformability-based microfluidic cell pairing and fusion. Lab on a chip. 2014;14(15):2783-90.
238. Ma C, Fan R, Ahmad H, Shi Q, Comin-Anduix B, Chodon T, et al. A clinical microchip for evaluation of single immune cells reveals high functional heterogeneity in phenotypically similar T cells. Nature medicine. 2011;17(6):738-43.
239. Konry T, Golberg A, Yarmush M. Live single cell functional phenotyping in droplet nano-liter reactors. Scientific reports. 2013;3:3179.
240. Chabert M, Viovy JL. Microfluidic high-throughput encapsulation and hydrodynamic self-sorting of single cells. Proceedings of the National Academy of Sciences of the United States of America. 2008;105(9):3191-6.
241. Edd JF, Di Carlo D, Humphry KJ, Koster S, Irimia D, Weitz DA, et al. Controlled encapsulation of single-cells into monodisperse picolitre drops. Lab on a chip. 2008;8(8):1262-4.
242. Hu H, Eustace D, Merten CA. Efficient cell pairing in droplets using dual-color sorting. Lab on a chip. 2015;15(20):3989-93.
243. Jang JH, Huang Y, Zheng P, Jo MC, Bertolet G, Zhu MX, et al. Imaging of Cell-Cell Communication in a Vertical Orientation Reveals High-Resolution Structure of Immunological Synapse and Novel PD-1 Dynamics. Journal of immunology. 2015;195(3):1320-30.
244. Biggs MJ, Milone MC, Santos LC, Gondarenko A, Wind SJ. High-resolution imaging of the immunological synapse and T-cell receptor microclustering through microfabricated substrates. Journal of the Royal Society, Interface. 2011;8(63):1462-71.
245. Choi K, Ng AH, Fobel R, Wheeler AR. Digital microfluidics. Annual review of analytical chemistry. 2012;5:413-40.
246. Kirschbaum M, Jaeger MS, Schenkel T, Breinig T, Meyerhans A, Duschl C. T cell activation on a single-cell level in dielectrophoresis-based microfluidic devices. Journal of chromatography A. 2008;1202(1):83-9.
247. Kirschbaum M, Jaeger MS, Duschl C. Correlating short-term Ca(2+) responses with long-term protein expression after activation of single T cells. Lab on a chip. 2009;9(24):3517-25.
248. Sen M, Ino K, Ramon-Azcon J, Shiku H, Matsue T. Cell pairing using a dielectrophoresis-based device with interdigitated array electrodes. Lab on a chip. 2013;13(18):3650-2.

249. Abonnenc M, Borgatti M, Fabbri E, Gavioli R, Fortini C, Destro F, et al. Lysis-on-chip of single target cells following forced interaction with CTLs or NK cells on a dielectrophoresis-based array. Journal of immunology. 2013;191(7):3545-52.
250. Rollo E, Tenaglia E, Genolet R, Bianchi E, Harari A, Coukos G, et al. Label-free identification of activated T lymphocytes through tridimensional microsensors on chip. Biosensors & bioelectronics. 2017;94:193-9.
251. Guo F, Li P, French JB, Mao Z, Zhao H, Li S, et al. Controlling cell-cell interactions using surface acoustic waves. Proceedings of the National Academy of Sciences of the United States of America. 2015;112(1):43-8.
252. Guo F, Mao Z, Chen Y, Xie Z, Lata JP, Li P, et al. Three-dimensional manipulation of single cells using surface acoustic waves. Proceedings of the National Academy of Sciences of the United States of America. 2016;113(6):1522-7.
253. Romain G, Senyukov V, Rey-Villamizar N, Merouane A, Kelton W, Liadi I, et al. Antibody Fc engineering improves frequency and promotes kinetic boosting of serial killing mediated by NK cells. Blood. 2014;124(22):3241-9.
254. Liadi I, Singh H, Romain G, Rey-Villamizar N, Merouane A, Adolacion JR, et al. Individual Motile CD4(+) T Cells Can Participate in Efficient Multikilling through Conjugation to Multiple Tumor Cells. Cancer immunology research. 2015;3(5):473-82.
255. Tauriainen J, Gustafsson K, Gothlin M, Gertow J, Buggert M, Frisk TW, et al. Single-Cell Characterization of in vitro Migration and Interaction Dynamics of T Cells Expanded with IL-2 and IL-7. Frontiers in immunology. 2015;6:196.
256. Forslund E, Sohlberg E, Enqvist M, Olofsson PE, Malmberg KJ, Onfelt B. Microchip-Based Single-Cell Imaging Reveals That CD56dimCD57-KIR-NKG2A+ NK Cells Have More Dynamic Migration Associated with Increased Target Cell Conjugation and Probability of Killing Compared to CD56dimCD57-KIR-NKG2A- NK Cells. Journal of immunology. 2015;195(7):3374-81.
257. Junkin M, Tay S. Microfluidic single-cell analysis for systems immunology. Lab on a chip. 2014;14(7):1246-60.
258. Dura B, Servos MM, Barry RM, Ploegh HL, Dougan SK, Voldman J. Longitudinal multiparameter assay of lymphocyte interactions from onset by microfluidic cell pairing and culture. Proceedings of the National Academy of Sciences of the United States of America. 2016;113(26):E3599-608.
259. Kim SK, Moon WK, Park JY, Jung H. Inflammatory mimetic microfluidic chip by immobilization of cell adhesion molecules for T cell adhesion. The Analyst. 2012;137(17):4062-8.
260. Sundd P, Gutierrez E, Koltsova EK, Kuwano Y, Fukuda S, Pospieszalska MK, et al. 'Slings' enable neutrophil rolling at high shear. Nature. 2012;488(7411):399-403.
261. Jones CN, Dalli J, Dimisko L, Wong E, Serhan CN, Irimia D. Microfluidic chambers for monitoring leukocyte trafficking and humanized nano-proresolving medicines interactions. Proceedings of the National Academy of Sciences of the United States of America. 2012;109(50):20560-5.
262. Sin A, Chin KC, Jamil MF, Kostov Y, Rao G, Shuler ML. The design and fabrication of three-chamber microscale cell culture analog devices with integrated dissolved oxygen sensors. Biotechnology progress. 2004;20(1):338-45.
263. Chao P, Maguire T, Novik E, Cheng KC, Yarmush ML. Evaluation of a microfluidic based cell culture platform with primary human hepatocytes for the prediction of hepatic clearance in human. Biochemical pharmacology. 2009;78(6):625-32.
264. Legendre A, Baudoin R, Alberto G, Paullier P, Naudot M, Bricks T, et al. Metabolic characterization of primary rat hepatocytes cultivated in parallel microfluidic biochips. Journal of pharmaceutical sciences. 2013;102(9):3264-76.
265. Cheng S, Prot JM, Leclerc E, Bois FY. Zonation related function and ubiquitination regulation in human hepatocellular carcinoma cells in dynamic vs. static culture conditions. BMC genomics. 2012;13:54.
266. Allen JW, Bhatia SN. Formation of steady-state oxygen gradients in vitro: application to liver zonation. Biotechnology and bioengineering. 2003;82(3):253-62.

267. Sivaraman A, Leach JK, Townsend S, Iida T, Hogan BJ, Stolz DB, et al. A microscale in vitro physiological model of the liver: predictive screens for drug metabolism and enzyme induction. Current drug metabolism. 2005;6(6):569-91.
268. Toh YC, Lim TC, Tai D, Xiao G, van Noort D, Yu H. A microfluidic 3D hepatocyte chip for drug toxicity testing. Lab on a chip. 2009;9(14):2026-35.
269. Novik E, Maguire TJ, Chao P, Cheng KC, Yarmush ML. A microfluidic hepatic coculture platform for cell-based drug metabolism studies. Biochemical pharmacology. 2010;79(7):1036-44.
270. Baudoin R, Griscom L, Monge M, Legallais C, Leclerc E. Development of a renal microchip for in vitro distal tubule models. Biotechnology progress. 2007;23(5):1245-53.
271. Jang KJ, Mehr AP, Hamilton GA, McPartlin LA, Chung S, Suh KY, et al. Human kidney proximal tubule-on-a-chip for drug transport and nephrotoxicity assessment. Integrative biology : quantitative biosciences from nano to macro. 2013;5(9):1119-29.
272. Jang KJ, Suh KY. A multi-layer microfluidic device for efficient culture and analysis of renal tubular cells. Lab on a chip. 2010;10(1):36-42.
273. Snouber LC, Letourneur F, Chafey P, Broussard C, Monge M, Legallais C, et al. Analysis of transcriptomic and proteomic profiles demonstrates improved Madin-Darby canine kidney cell function in a renal microfluidic biochip. Biotechnology progress. 2012;28(2):474-84.
274. Esch MB, Sung JH, Yang J, Yu C, Yu J, March JC, et al. On chip porous polymer membranes for integration of gastrointestinal tract epithelium with microfluidic 'body-on-a-chip' devices. Biomedical microdevices. 2012;14(5):895-906.
275. Kim HJ, Huh D, Hamilton G, Ingber DE. Human gut-on-a-chip inhabited by microbial flora that experiences intestinal peristalsis-like motions and flow. Lab on a chip. 2012;12(12):2165-74.
276. Kim HJ, Ingber DE. Gut-on-a-Chip microenvironment induces human intestinal cells to undergo villus differentiation. Integrative biology : quantitative biosciences from nano to macro. 2013;5(9):1130-40.
277. Mahler GJ, Esch MB, Glahn RP, Shuler ML. Characterization of a gastrointestinal tract microscale cell culture analog used to predict drug toxicity. Biotechnology and bioengineering. 2009;104(1):193-205.
278. Huh D, Leslie DC, Matthews BD, Fraser JP, Jurek S, Hamilton GA, et al. A human disease model of drug toxicity-induced pulmonary edema in a lung-on-a-chip microdevice. Science translational medicine. 2012;4(159):159ra47.
279. Huh D, Fujioka H, Tung YC, Futai N, Paine R, 3rd, Grotberg JB, et al. Acoustically detectable cellular-level lung injury induced by fluid mechanical stresses in microfluidic airway systems. Proceedings of the National Academy of Sciences of the United States of America. 2007;104(48):18886-91.
280. Fritsche CS, Simsch O, Weinberg EJ, Orrick B, Stamm C, Kaazempur-Mofrad MR, et al. Pulmonary tissue engineering using dual-compartment polymer scaffolds with integrated vascular tree. The International journal of artificial organs. 2009;32(10):701-10.
281. Tavana H, Zamankhan P, Christensen PJ, Grotberg JB, Takayama S. Epithelium damage and protection during reopening of occluded airways in a physiologic microfluidic pulmonary airway model. Biomedical microdevices. 2011;13(4):731-42.
282. Grosberg A, Alford PW, McCain ML, Parker KK. Ensembles of engineered cardiac tissues for physiological and pharmacological study: heart on a chip. Lab on a chip. 2011;11(24):4165-73.
283. Cheng W, Klauke N, Sedgwick H, Smith GL, Cooper JM. Metabolic monitoring of the electrically stimulated single heart cell within a microfluidic platform. Lab on a chip. 2006;6(11):1424-31.
284. Giridharan GA, Nguyen MD, Estrada R, Parichehreh V, Hamid T, Ismahil MA, et al. Microfluidic cardiac cell culture model (muCCCM). Analytical chemistry. 2010;82(18):7581-7.
285. Grosberg A, Nesmith AP, Goss JA, Brigham MD, McCain ML, Parker KK. Muscle on a chip: in vitro contractility assays for smooth and striated muscle. Journal of pharmacological and toxicological methods. 2012;65(3):126-35.
286. Park SH, Sim WY, Min BH, Yang SS, Khademhosseini A, Kaplan DL. Chip-based comparison of the osteogenesis of human bone marrow- and adipose tissue-derived mesenchymal stem cells under mechanical stimulation. PloS one. 2012;7(9):e46689.

287. Zhang Y, Gazit Z, Pelled G, Gazit D, Vunjak-Novakovic G. Patterning osteogenesis by inducible gene expression in microfluidic culture systems. Integrative biology : quantitative biosciences from nano to macro. 2011;3(1):39-47.
288. Zhang W, Lee WY, Siegel DS, Tolias P, Zilberberg J. Patient-specific 3D microfluidic tissue model for multiple myeloma. Tissue engineering Part C, Methods. 2014;20(8):663-70.
289. Torisawa YS, Spina CS, Mammoto T, Mammoto A, Weaver JC, Tat T, et al. Bone marrow-on-a-chip replicates hematopoietic niche physiology in vitro. Nature methods. 2014;11(6):663-9.
290. Song JW, Cavnar SP, Walker AC, Luker KE, Gupta M, Tung YC, et al. Microfluidic endothelium for studying the intravascular adhesion of metastatic breast cancer cells. PloS one. 2009;4(6):e5756.
291. Torisawa YS, Mosadegh B, Bersano-Begey T, Steele JM, Luker KE, Luker GD, et al. Microfluidic platform for chemotaxis in gradients formed by CXCL12 source-sink cells. Integrative biology : quantitative biosciences from nano to macro. 2010;2(11-12):680-6.
292. Puleo CM, McIntosh Ambrose W, Takezawa T, Elisseeff J, Wang TH. Integration and application of vitrified collagen in multilayered microfluidic devices for corneal microtissue culture. Lab on a chip. 2009;9(22):3221-7.
293. O'Neill AT, Monteiro-Riviere NA, Walker GM. Characterization of microfluidic human epidermal keratinocyte culture. Cytotechnology. 2008;56(3):197-207.
294. Shin M, Matsuda K, Ishii O, Terai H, Kaazempur-Mofrad M, Borenstein J, et al. Endothelialized networks with a vascular geometry in microfabricated poly(dimethyl siloxane). Biomedical microdevices. 2004;6(4):269-78.
295. van der Meer AD, Orlova VV, ten Dijke P, van den Berg A, Mummery CL. Three-dimensional co-cultures of human endothelial cells and embryonic stem cell-derived pericytes inside a microfluidic device. Lab on a chip. 2013;13(18):3562-8.
296. Xiao RR, Zeng WJ, Li YT, Zou W, Wang L, Pei XF, et al. Simultaneous generation of gradients with gradually changed slope in a microfluidic device for quantifying axon response. Analytical chemistry. 2013;85(16):7842-50.
297. Shi M, Majumdar D, Gao Y, Brewer BM, Goodwin CR, McLean JA, et al. Glia co-culture with neurons in microfluidic platforms promotes the formation and stabilization of synaptic contacts. Lab on a chip. 2013;13(15):3008-21.
298. Park HS, Liu S, McDonald J, Thakor N, Yang IH. Neuromuscular junction in a microfluidic device. Conference proceedings : Annual International Conference of the IEEE Engineering in Medicine and Biology Society IEEE Engineering in Medicine and Biology Society Annual Conference. 2013;2013:2833-5.
299. Ziegler L, Grigoryan S, Yang IH, Thakor NV, Goldstein RS. Efficient generation of schwann cells from human embryonic stem cell-derived neurospheres. Stem cell reviews. 2011;7(2):394-403.
300. Shayan G, Choi YS, Shusta EV, Shuler ML, Lee KH. Murine in vitro model of the blood-brain barrier for evaluating drug transport. European journal of pharmaceutical sciences : official journal of the European Federation for Pharmaceutical Sciences. 2011;42(1-2):148-55.
301. Shayan G, Shuler ML, Lee KH. The effect of astrocytes on the induction of barrier properties in aortic endothelial cells. Biotechnology progress. 2011;27(4):1137-45.
302. Achyuta AK, Conway AJ, Crouse RB, Bannister EC, Lee RN, Katnik CP, et al. A modular approach to create a neurovascular unit-on-a-chip. Lab on a chip. 2013;13(4):542-53.
303. Sung JH, Shuler ML. A micro cell culture analog (microCCA) with 3-D hydrogel culture of multiple cell lines to assess metabolism-dependent cytotoxicity of anti-cancer drugs. Lab on a chip. 2009;9(10):1385-94.
304. Giese C, Marx U. Human immunity in vitro - solving immunogenicity and more. Advanced drug delivery reviews. 2014;69-70:103-22.
305. Seok J, Warren HS, Cuenca AG, Mindrinos MN, Baker HV, Xu W, et al. Genomic responses in mouse models poorly mimic human inflammatory diseases. Proceedings of the National Academy of Sciences of the United States of America. 2013;110(9):3507-12.
306. Webb DR. Animal models of human disease: inflammation. Biochemical pharmacology. 2014;87(1):121-30.

307. Vudattu NK, Waldron-Lynch F, Truman LA, Deng S, Preston-Hurlburt P, Torres R, et al. Humanized mice as a model for aberrant responses in human T cell immunotherapy. Journal of immunology. 2014;193(2):587-96.
308. Esch MB, King TL, Shuler ML. The role of body-on-a-chip devices in drug and toxicity studies. Annual review of biomedical engineering. 2011;13:55-72.
309. Wu MH, Huang SB, Lee GB. Microfluidic cell culture systems for drug research. Lab on a chip. 2010;10(8):939-56.
310. Zheng XT, Yu L, Li P, Dong H, Wang Y, Liu Y, et al. On-chip investigation of cell-drug interactions. Advanced drug delivery reviews. 2013;65(11-12):1556-74.
311. Ebrahimkhani MR, Neiman JA, Raredon MS, Hughes DJ, Griffith LG. Bioreactor technologies to support liver function in vitro. Advanced drug delivery reviews. 2014;69-70:132-57.
312. Viravaidya K, Sin A, Shuler ML. Development of a microscale cell culture analog to probe naphthalene toxicity. Biotechnology progress. 2004;20(1):316-23.
313. Ma H, Xu H, Qin J. Biomimetic tumor microenvironment on a microfluidic platform. Biomicrofluidics. 2013;7(1):11501.
314. Buchanan C, Rylander MN. Microfluidic culture models to study the hydrodynamics of tumor progression and therapeutic response. Biotechnology and bioengineering. 2013;110(8):2063-72.
315. Jeon JS, Zervantonakis IK, Chung S, Kamm RD, Charest JL. In vitro model of tumor cell extravasation. PloS one. 2013;8(2):e56910.
316. Wlodkowic D, Cooper JM. Tumors on chips: oncology meets microfluidics. Current opinion in chemical biology. 2010;14(5):556-67.
317. Niu Y, Bai J, Kamm RD, Wang Y, Wang C. Validating antimetastatic effects of natural products in an engineered microfluidic platform mimicking tumor microenvironment. Molecular pharmaceutics. 2014;11(7):2022-9.
318. Huang Y, Agrawal B, Sun D, Kuo JS, Williams JC. Microfluidics-based devices: New tools for studying cancer and cancer stem cell migration. Biomicrofluidics. 2011;5(1):13412.
319. Sarkar S, Bustard BL, Welter JF, Baskaran H. Combined experimental and mathematical approach for development of microfabrication-based cancer migration assay. Annals of biomedical engineering. 2011;39(9):2346-59.
320. Ingber DE. Can cancer be reversed by engineering the tumor microenvironment? Seminars in cancer biology. 2008;18(5):356-64.
321. Szot CS, Buchanan CF, Freeman JW, Rylander MN. 3D in vitro bioengineered tumors based on collagen I hydrogels. Biomaterials. 2011;32(31):7905-12.
322. Wang G, McCain ML, Yang L, He A, Pasqualini FS, Agarwal A, et al. Modeling the mitochondrial cardiomyopathy of Barth syndrome with induced pluripotent stem cell and heart-on-chip technologies. Nature medicine. 2014;20(6):616-23.
323. Wang R, Chadalavada K, Wilshire J, Kowalik U, Hovinga KE, Geber A, et al. Glioblastoma stem-like cells give rise to tumour endothelium. Nature. 2010;468(7325):829-33.
324. Ricci-Vitiani L, Pallini R, Biffoni M, Todaro M, Invernici G, Cenci T, et al. Tumour vascularization via endothelial differentiation of glioblastoma stem-like cells. Nature. 2010;468(7325):824-8.
325. Ross R. Atherosclerosis--an inflammatory disease. The New England journal of medicine. 1999;340(2):115-26.
326. Anselmi A, Abbate A, Girola F, Nasso G, Biondi-Zoccai GG, Possati G, et al. Myocardial ischemia, stunning, inflammation, and apoptosis during cardiac surgery: a review of evidence. European journal of cardio-thoracic surgery : official journal of the European Association for Cardio-thoracic Surgery. 2004;25(3):304-11.
327. Qi JP, Wu H, Yang Y, Wang DD, Chen YX, Gu YH, et al. Cerebral ischemia and Alzheimer's disease: the expression of amyloid-beta and apolipoprotein E in human hippocampus. Journal of Alzheimer's disease : JAD. 2007;12(4):335-41.
328. del Zoppo GJ. Microvascular responses to cerebral ischemia/inflammation. Annals of the New York Academy of Sciences. 1997;823:132-47.
329. Kontos CD, Wei EP, Williams JI, Kontos HA, Povlishock JT. Cytochemical detection of superoxide in cerebral inflammation and ischemia in vivo. The American journal of physiology. 1992;263(4 Pt 2):H1234-42.

330. Shoelson SE, Lee J, Goldfine AB. Inflammation and insulin resistance. The Journal of clinical investigation. 2006;116(7):1793-801.
331. Sun S, Ji Y, Kersten S, Qi L. Mechanisms of inflammatory responses in obese adipose tissue. Annual review of nutrition. 2012;32:261-86.
332. Suematsu M, Suzuki H, Delano FA, Schmid-Schonbein GW. The inflammatory aspect of the microcirculation in hypertension: oxidative stress, leukocytes/endothelial interaction, apoptosis. Microcirculation. 2002;9(4):259-76.
333. Ashley NT, Weil ZM, Nelson RJ. Inflammation: Mechanisms, Costs, and Natural Variation. Annu Rev Ecol Evol S. 2012;43:385-406.
334. Schmid-Schonbein GW. Analysis of inflammation. Annual review of biomedical engineering. 2006;8:93-131.
335. Ramadan Q, Jafarpoorchekab H, Huang C, Silacci P, Carrara S, Koklu G, et al. NutriChip: nutrition analysis meets microfluidics. Lab on a chip. 2013;13(2):196-203.
336. Kim J, Hegde M, Jayaraman A. Co-culture of epithelial cells and bacteria for investigating host-pathogen interactions. Lab on a chip. 2010;10(1):43-50.
337. Andersen TE, Khandige S, Madelung M, Brewer J, Kolmos HJ, Moller-Jensen J. Escherichia coli uropathogenesis in vitro: invasion, cellular escape, and secondary infection analyzed in a human bladder cell infection model. Infection and immunity. 2012;80(5):1858-67.
338. Nesmith AP, Agarwal A, McCain ML, Parker KK. Human airway musculature on a chip: an in vitro model of allergic asthmatic bronchoconstriction and bronchodilation. Lab on a chip. 2014;14(20):3925-36.
339. Atac B, Wagner I, Horland R, Lauster R, Marx U, Tonevitsky AG, et al. Skin and hair on-a-chip: in vitro skin models versus ex vivo tissue maintenance with dynamic perfusion. Lab on a chip. 2013;13(18):3555-61.
340. Singh A. Biomaterials innovation for next generation ex vivo immune tissue engineering. Biomaterials. 2017;130:104-10.
341. O'Sullivan D, Pearce EL. Targeting T cell metabolism for therapy. Trends in immunology. 2015;36(2):71-80.
342. Sardi M. LA, and Giese C. Modeling Human Immunity In Vitro: Improving Artificial Lymph Node Physiology by Stroimal Cells

IN VITRO TOXICOLOGY. 2016;2(3):8.
343. Giese C, Demmler CD, Ammer R, Hartmann S, Lubitz A, Miller L, et al. A human lymph node in vitro--challenges and progress. Artificial organs. 2006;30(10):803-8.
344. Giese C, Lubitz A, Demmler CD, Reuschel J, Bergner K, Marx U. Immunological substance testing on human lymphatic micro-organoids in vitro. Journal of biotechnology. 2010;148(1):38-45.
345. Byrne MB, Trump L, Desai AV, Schook LB, Gaskins HR, Kenis PJ. Microfluidic platform for the study of intercellular communication via soluble factor-cell and cell-cell paracrine signaling. Biomicrofluidics. 2014;8(4):044104.
346. Molteni R, Bianchi E, Patete P, Fabbri M, Baroni G, Dubini G, et al. A novel device to concurrently assess leukocyte extravasation and interstitial migration within a defined 3D environment. Lab on a chip. 2015;15(1):195-207.
347. Wong KH, Truslow JG, Khankhel AH, Chan KL, Tien J. Artificial lymphatic drainage systems for vascularized microfluidic scaffolds. Journal of biomedical materials research Part A. 2013;101(8):2181-90.
348. Bonvin C, Overney J, Shieh AC, Dixon JB, Swartz MA. A multichamber fluidic device for 3D cultures under interstitial flow with live imaging: development, characterization, and applications. Biotechnology and bioengineering. 2010;105(5):982-91.
349. Agliari E, Biselli E, De Ninno A, Schiavoni G, Gabriele L, Gerardino A, et al. Cancer-driven dynamics of immune cells in a microfluidic environment. Scientific reports. 2014;4:6639.
350. Seifert M, Lubitz A, Trommer J, Konnig D, Korus G, Marx U, et al. Crosstalk between immune cells and mesenchymal stromal cells in a 3D bioreactor system. The International journal of artificial organs. 2012;35(11):986-95.
351. Kobayashi Y, Kato K, Watanabe T. Synthesis of functional artificial lymphoid tissues. Discovery medicine. 2011;12(65):351-62.

352. Okamoto N, Chihara R, Shimizu C, Nishimoto S, Watanabe T. Artificial lymph nodes induce potent secondary immune responses in naive and immunodeficient mice. The Journal of clinical investigation. 2007;117(4):997-1007.
353. Ross AE, Belanger MC, Woodroof JF, Pompano RR. Spatially resolved microfluidic stimulation of lymphoid tissue ex vivo. The Analyst. 2016.
354. van der Helm MW, van der Meer AD, Eijkel JC, van den Berg A, Segerink LI. Microfluidic organ-on-chip technology for blood-brain barrier research. Tissue barriers. 2016;4(1):e1142493.
355. Miura T, Yokokawa R. Tissue culture on a chip: Developmental biology applications of self-organized capillary networks in microfluidic devices. Development, growth & differentiation. 2016;58(6):505-15.
356. Yin X, Mead BE, Safaee H, Langer R, Karp JM, Levy O. Engineering Stem Cell Organoids. Cell stem cell. 2016;18(1):25-38.
357. Neuzi P, Giselbrecht S, Lange K, Huang TJ, Manz A. Revisiting lab-on-a-chip technology for drug discovery. Nature reviews Drug discovery. 2012;11(8):620-32.
358. Avorn J. The $2.6 billion pill--methodologic and policy considerations. The New England journal of medicine. 2015;372(20):1877-9.
359. Hay M, Thomas DW, Craighead JL, Economides C, Rosenthal J. Clinical development success rates for investigational drugs. Nature biotechnology. 2014;32(1):40-51.
360. Staff DW. FDA Signs Collaborative Agreement With Emulate To Use Organ's-On-Chips Technology As Toxicology Testing Platform 2017. Available from: http://www.diagnosticsworldnews.com/2017/04/11/fda-signs-collaborative-agreement-with-emulate-to-use-organs-on-chips-technology-as-toxicology-testing-platform.aspx.
361. Hirt C, Papadimitropoulos A, Mele V, Muraro MG, Mengus C, Iezzi G, et al. "In vitro" 3D models of tumor-immune system interaction. Advanced drug delivery reviews. 2014;79-80:145-54.
362. Restifo NP, Dudley ME, Rosenberg SA. Adoptive immunotherapy for cancer: harnessing the T cell response. Nature reviews Immunology. 2012;12(4):269-81.
363. DATA JP. Available online: http://www.jd-photodata.co.uk/index.php/photomask.html (accessed on 24 July 2017).
364. Franssila S. Introduction to microfabrication. Chichester, West Sussex, England ; Hoboken, NJ: J. Wiley; 2004. xvii, 401 p. p.
365. 5 MS-. Available online: http://www.microchem.com/pdf/SU8_2-25.pdf (accessed on 24 July 2017).
366. 2100-2150 MS-. Available online: http://www.microchem.com/pdf/SU-82000DataSheet2100and2150Ver5.pdf (accessed on 24 July 2017).
367. 3000 MS-. Available online: http://www.microchem.com/pdf/SU-8%203000%20Data%20Sheet.pdf (accessed on 24 July 2017).
368. ma-P 1275 m-PH. Available online: http://www.microresist.de/en/products/positive-photoresists/uv-lithography/ma-p-1275-ma-p-1275hv (accessed on 24 July 2017).
369. 600 Dm. Available online: http://microresist.de/sites/default/files/downloads/flyer_negative_resists_July2015_2.pdf (accessed on 24 July 2017).
370. maD351 D. Available online: http://microresist.de/sites/default/files/downloads/flyer_positive_resists_July2015_0.pdf (accessed on 24 July 2017).
371. ES562 EG-P. Available online: http://www.permabond.com/wp-content/uploads/2016/04/ES562_TDS.pdf (accessed on 24 July 2017).
372. Moura Rosa PEmr-P. Available online: http://forum.nano.ntnu.no/t/epoxy-mold-replication-protocol/45 (accessed on 24 July 2017).
373. Chuah YJ, Koh YT, Lim K, Menon NV, Wu Y, Kang Y. Simple surface engineering of polydimethylsiloxane with polydopamine for stabilized mesenchymal stem cell adhesion and multipotency. Scientific reports. 2015;5:18162.
374. Svartdal LG. Fabrication and testing of a Biopatterned Microfluidic Channel for Cell-Cell Interactions in the Immune System. Trondheim: Norwegian University od Science and Technology; 2015.

375. Protocol NNn-uS. Available online: https://github.com/NanoLabStaff/nanolab/wiki/SPR700-1um (accessed on 24 July 2017).
376. Photoresist DEMMS-P. Available online: http://www.capitolscientific.com/microlithography-dow-electronic-materials/dow-electronic-materials-megaposit-spr-700-positive-photoresist-series-for-lithography (accessed on 24 July 2017).
377. Developer M-A. Available online: https://wcam.engr.wisc.edu/Public/Safety/MSDS/Developer%20MF-26A.pdf (accessed on 24 July 2017).
378. Dye CDR. Available online: https://www.thermofisher.com/order/catalog/product/C34565 (accessed on 24 July 2017).
379. Dye COC. Available online: https://www.thermofisher.com/order/catalog/product/C2927 (accessed on 24 July 2017).
380. (Abcam) CLCLK-BFa. Available online: http://www.abcam.com/live-cell-labeling-kit-blue-fluorescence-ex405nm-cytopainter-ab187966.html (accessed on 24 July 2017).
381. (Abcam) CCpSR-DRFa. Available online: http://www.abcam.com/cell-proliferation-staining-reagent-deep-red-fluorescence-cytopainter-ab176736.html (accessed on 24 July 2017).
382. NTNU CaMICFC. Available online: https://ntnu.corefacilities.org/service_center/3045/?tab=equipment (accessed on 24 July 2017).
383. (Invitrogen) EFACIS. Available online: https://www.thermofisher.com/no/en/home/life-science/cell-analysis/cellular-imaging/cell-imaging-systems/evos-fl-auto.html (accessed on 24 July 2017).
384. . Available from: Random force http://www.nyu.edu/classes/tuckerman/stat.mech/lectures/lecture24/.
385. Valignat MP, Theodoly O, Gucciardi A, Hogg N, Lellouch AC. T lymphocytes orient against the direction of fluid flow during LFA-1-mediated migration. Biophysical journal. 2013;104(2):322-31.
386. Bajenoff M, Glaichenhaus N, Germain RN. Fibroblastic reticular cells guide T lymphocyte entry into and migration within the splenic T cell zone. Journal of immunology. 2008;181(6):3947-54.
387. Kaldjian EP, Gretz JE, Anderson AO, Shi Y, Shaw S. Spatial and molecular organization of lymph node T cell cortex: a labyrinthine cavity bounded by an epithelium-like monolayer of fibroblastic reticular cells anchored to basement membrane-like extracellular matrix. International immunology. 2001;13(10):1243-53.
388. Dafni H, Israely T, Bhujwalla ZM, Benjamin LE, Neeman M. Overexpression of vascular endothelial growth factor 165 drives peritumor interstitial convection and induces lymphatic drain: magnetic resonance imaging, confocal microscopy, and histological tracking of triple-labeled albumin. Cancer research. 2002;62(22):6731-9.
389. Choi S, Karp JM, Karnik R. Cell sorting by deterministic cell rolling. Lab on a chip. 2012;12(8):1427-30.
390. Kaushik G, Leijten J, Khademhosseini A. Concise Review: Organ Engineering: Design, Technology, and Integration. Stem cells. 2017;35(1):51-60.
391. Taylor-Weiner H, Ravi N, Engler AJ. Traction forces mediated by integrin signaling are necessary for definitive endoderm specification. Journal of cell science. 2015;128(10):1961-8.
392. Wen JH, Vincent LG, Fuhrmann A, Choi YS, Hribar KC, Taylor-Weiner H, et al. Interplay of matrix stiffness and protein tethering in stem cell differentiation. Nature materials. 2014;13(10):979-87.
393. Fuhrmann A, Engler AJ. The cytoskeleton regulates cell attachment strength. Biophysical journal. 2015;109(1):57-65.
394. Oakes PW, Banerjee S, Marchetti MC, Gardel ML. Geometry regulates traction stresses in adherent cells. Biophysical journal. 2014;107(4):825-33.
395. Spanjaard E, de Rooij J. Mechanotransduction: vinculin provides stability when tension rises. Current biology : CB. 2013;23(4):R159-61.
396. Young JL, Kretchmer K, Ondeck MG, Zambon AC, Engler AJ. Mechanosensitive kinases regulate stiffness-induced cardiomyocyte maturation. Scientific reports. 2014;4:6425.

Paper I

Lab on a Chip

PAPER

View Article Online
View Journal | View Issue

Cite this: *Lab Chip*, 2016, **16**, 3728

The intercell dynamics of T cells and dendritic cells in a lymph node-on-a-chip flow device†

Patrícia Moura Rosa,[ac] Nimi Gopalakrishnan,[ac] Hany Ibrahim,[b] Markus Haug[b] and Øyvind Halaas*[a]

Received 31st May 2016,
Accepted 12th August 2016

DOI: 10.1039/c6lc00702c

www.rsc.org/loc

T cells play a central role in immunity towards cancer and infectious diseases. T cell responses are initiated in the T cell zone of the lymph node (LN), where resident antigen-bearing dendritic cells (DCs) prime and activate antigen-specific T cells passing by. In the present study, we investigated the T cell : DC interaction in a microfluidic device to understand the intercellular dynamics and physiological conditions in the LN. We show random migration of antigen-specific T cells onto the antigen-presenting DC monolayer independent of the flow direction with a mean T cell : DC dwell time of 12.8 min and a mean velocity of 6 μm min^{-1}. Furthermore, we investigated the antigen specific *vs.* unspecific attachment and detachment of $CD8^+$ and $CD4^+$ T cells to DCs under varying shear stress. In our system, $CD4^+$ T cells showed long stable contacts with APCs, whereas $CD8^+$ T cells presented transient interactions with DCs. By varying the shear stress from 0.01 to 100 Dyn cm^{-2}, it was also evident that there was a much stronger attachment of antigen-specific than unspecific T cells to stationary DCs up to 1–12 Dyn cm^{-2}. The mechanical force of the cell : cell interaction associated with the pMHC–TCR match under controlled tangential shear force was estimated to be in the range of 0.25–4.8 nN. Finally, upon performing attachment & detachment tests, there was a steady accumulation of antigen specific $CD8^+$ T cells and $CD4^+$ T cells on DCs at low shear stresses, which were released at a stress of 12 Dyn cm^{-2}. This microphysiological model provides new possibilities to recreate a controlled mechanical force threshold of pMHC–TCR binding, allowing the investigation of intercellular signalling of immune synapses and therapeutic targets for immunotherapy.

Introduction

Immunoengineering is an emerging field that links biology, pharmaceutics, biomedicine and biophysics with engineering aiming at developing new strategies for molecular and cellular immunotherapies.[1] The immune system is particularly suited for engineering approaches due to the natural and dynamic self-governing of the cells involved in initiating an immune response. The immune system is a complex process involving many cell types, responses and microenvironments in several anatomical sites and immunological organs. In response to inflammatory signals, tissue-resident dendritic cells (DCs) acquire local antigens and migrate to lymph nodes to present MHC-bound peptide antigens to T cells recruited from blood. The adaptive immune response is then initiated by the cognate physical interactions between naïve T cells and antigen-presenting cells (APCs). Afterwards, the primed/activated T cells enter the lymph and blood and are recruited to inflammation sites where new T cell : target cell interactions take place. Although numerous *in vivo* and *in vitro* studies describe the molecules and responses involved in these interactions, a comprehensive understanding of the lymph node immune physiology and dynamics considering physical parameters (*i.e.* influence of shear stress, the duration and stability of the interaction, the magnitude of force sustained at the T cell–APC interface, the relative motions between the two plasma membranes at the T cell–DC interface, the number of sequential T cell : DC interactions, recirculation requirements) underlying molecular mechanisms to achieve priming, activation and proliferation is still lacking.[1–4]

Conventional techniques involved in the study of cell interaction dynamics and their behaviour inside lymph nodes, such as dissection, confocal microscopy and intravital multiphoton microscopy, have been used in the analysis of LNs in mice, rat, sheep and humans,[3,5,6] albeit with severe limitations in access and control.[5,7] On the other hand,

[a] *Department of Cancer Research and Molecular Medicine, Norwegian University of Science and Technology, 7489 Trondheim, Norway. E-mail: oyvind.halaas@ntnu.no*
[b] *Centre of Molecular Inflammation Research (SFF-CEMIR), Department of Cancer Research and Molecular Medicine, Norwegian University of Science and Technology, 7489 Trondheim, Norway*
[c] *NTNU Nanolab, Norwegian University of Science and Technology, 7489 Trondheim, Norway*

† Electronic supplementary information (ESI) available. See DOI: 10.1039/c6lc00702c

traditional cell culture dish systems are lacking suitable promoters for migration, intracellular signalling, proliferation, and differentiation because of the absence of an extracellular matrix (ECM)[1,8,9] and the presence of haptotactic gradients,[2] shear stress and other hemodynamic forces,[1,10] which are important for successful T cell : DC interaction. To better understand the specialized junction between a T lymphocyte and an APC, the immunological synapse formation and the induction of efficient T cell activation, it is also important to consider that the mechanical forces are an integral part of T cell : APC physiology and a driving force to the mechanism of TCR triggering by pMHC,[11–15] and recent studies on cell–cell adhesion using micropipette aspiration techniques[16] and atomic force microscopy (AFM)[17] have been conducted. One particular technique that has also been established as an important tool for the study of cell adhesion is single-cell force spectroscopy (SCFS) by AFM, allowing the process analysis under near-physiological conditions.[18,19] However, AFM is limited in the investigation of long-term adhesion, considering the characteristic dynamic motility and interaction between T cell and APC during the synapse formation.

To overcome these limitations and to find important clues to better understand the process of T cell : DC interaction during immune responses, we pursued a simple lymph node mimetic microfluidic system. This system is becoming important to model physiological functions of tissues or organs in 3D over time.

In recent years, attention has been focused on additional strategies for understanding the dynamic immune cell interactions. Recently, several studies on monolayers of heterotypic cell–cell interactions have demonstrated that combining the fluid flow with mechanical forces similar to those found *in vivo* can affect the cell shape, function, interaction and differentiation process.[1,20–25] These methods and techniques address some questions related to the effects of biochemical treatments and environmental *stimuli* to the cell adhesion and cell : cell interaction, offering potential for monitoring, studying and profiling stem cell interaction, multistep adhesion cascade of the entry of lymphocytes through high endothelial venules (HEVs) (rolling, sticking, crawling, transmigration),[24] and cancer metastasis. Additionally, these techniques can be also used to study therapeutic targets of different drugs.[1,23,26–28]

At the single-cell level of cell : cell interactions, five main classes of microscale tools have been described: microwell arrays, valve microfluidics, droplet microfluidics, microfluidic cell trap arrays[29] and electrical cell manipulation.[30] Dura *et al.* reported, in one particular study of microfluidic cell trap arrays, an approach to demonstrate the dynamic interactions between CD8 T cells and APC, to perform measurements on both patterns and to characterize the activation process of CD8 T cells.[31]

In this study, we developed a microfluidic platform that allows the real-time study of flowing lymphocytes dynamically interacting with adherent dendritic cells. This new technique lays the foundation for studies on cell–cell interaction dynamics with variable velocity, shear stress, deformation rates and migratory motility in different biological settings relevant to the adaptive immune system.

The shear stress of interest in this study relates to the shear stress inside the T cell zones of LNs,[3] where, in the presence of cognate antigen, T cells arbitrarily migrate along the fibroblastic reticular cell (FRC) network to contact the cognate antigen presented by adherent APCs. During this stage, T cell speed decreases and turning behavior increases, resulting in serial contacts with multiple DCs for 2 h.[2,3,32–39] The interstitial flow velocity measured in normal and tumor-associated inflamed skin ranges from 0.005 to 0.05 Dyn cm^{-2},[33] which served as our guide for choosing shear stresses representing physiological conditions, but we also probed the shear stress tolerance in our system.

We first investigated the T cell behavior on the DC monolayer at low flow rates. Next, we investigated the flow rates needed to break the cell : cell interactions and the DC adherence to the fibronectin surface. Finally, we investigated the antigen-specific attachment of T cells to DCs during continuous flow. This study demonstrates that this microfluidic platform can be a valuable tool for investigating T cell : APC interactions related to cell signaling and activation highly relevant to immunological R&D.

Materials and methods

A. Cells

Adherent murine tumor dendritic cell (MutuDC; expressing GFP) lines derived from spleen tumors in CD11c:SV40LgT-transgenic C57BL/6 mice were obtained from Hans Acha-Orbea, University of Lausanne, and non-adherent ovalbumin specific MHC class II restricted (MF2.2D9) $CD4^+$ T cells (hereinafter referred to as OVAII) and MHC class I restricted (RF33.70) $CD8^+$ T cell hybridomas (hereinafter referred to as OVAI) were gifts from Dr. Kenneth Rock, University of Massachusetts, Worcester. MutuDC lines were cultured in 75 cm^2 cell culture flasks with culture medium (CM) composed of IMDM media containing 8% fetal calf serum (FCS), 10 mM HEPES, 1.7% L-glutamine, and 0.1 μM ciprofloxacin, with 50 μM 2-mercaptoethanol (2-Me), considering the minor modification for this cell type according to ref. 40. MF2.2D9 and RF33.70 T cells were cultured in 75 cm^2 cell culture flasks with complete growth medium consisting of RPMI-1640 cell medium, mixed with 50 μM 2-Me, 20 mM HEPES, glutamine, 10% FCS and antibiotics (CIPRO).[41]

B. Peptide preparation

OVA peptides and variants were purchased from BioSite, Anaspec. All peptides were dissolved in dimethylsulfoxide (10 mg ml^{-1}) and stored at −20 °C.

C. Fabrication of a microfluidic system

The microfluidic device was fabricated in polydimethylsiloxane (PDMS) by rapid prototyping soft lithography using

SU-8 photoresist masters, according to published procedures.[42] The microchannel was designed using AutoCAD 2014 drawing software (Autodesk Inc., Europe). To form the optical mask, a film negative with the desired microchannel size was prepared by a commercial photomask manufacturer (Compugraphics Ltd., UK). It was purchased as a soda lime photolithography mask (3″ × 3″ × 0.060″) coated with a thin chrome metal layer. The master for the microfluidic device was fabricated using a two-layer SU-8 process. A 7 μm-thin layer of photoresist (SU-8 5, MicroChem) was used as an adhesion layer, and it was spun at 2000 rpm for 120 s over a 2 inch Si wafer. The wafer was then fully exposed to ultraviolet light (UV light). After post-exposure baking (1 min at 65 °C + 1 min at 95 °C), the second layer of photoresist (SU-8 2100, MicroChem) was spun at 4000 rpm for 30 s to yield feature heights of 100 μm. The wafer was exposed to UV light through the mask to generate the microchannel patterns. After post-exposure baking (5 min at 65 °C and 12 min at 95 °C) and development, the mold was hard-baked for 20 min at 150 °C.

To produce the PDMS replica, Sylgard™ 184 (Dow Corning) silicone was mixed with the curing agent in a proportion of 1 : 10, poured over the mold and baked at 70 °C for 2 h. After curing, the PDMS was peeled from the mold, individual devices were cut to appropriate sizes and a needle with a blunt tip was used to make the fluid connection access holes. The individual devices were cleaned with acetone and ethanol (70%) and dried with nitrogen. The PDMS replica was irreversibly sealed with a cover glass (from Menzel Gläser, Ø 50 mm diameter and 150 μm thickness, compatible with high numerical aperture (high-NA) fluorescence imaging), using a plasma cleaner for surface activation. The devices were further mounted onto 1 mm high WillCo-dish®.

The bottom of the channel was coated with collagen (Col) (50 μg ml^{-1}, diluted with 1× PBS) or fibronectin (FN) (50 μg ml^{-1}, diluted with PBS; Bio-Techne, R&D Systems Europe Limited) to form a matrix for cell attachment[8] and incubated at 4 °C overnight. After coating, the device was washed 3 times with PBS, loaded with culture medium, and finally incubated at 37 °C and 5% CO_2 for 2 h. Fig. 1(a) shows the microfluidic device fabricated as described above and following the insertion of metal catheters (Instech Solomon, ID = 0.8 mm) into the access holes in the PDMS and coupling to polyethylene tubes (Instech Solomon). The microfluidic device includes two inlets and two outlets feeding the main microchannel, as illustrated in Fig. 1(b). The main microchannel is 10 mm long, 1000 μm wide, and 100 μm high, and one ruler was defined along the side of the channel to facilitate the identification of a particular site of the microchannel when using the optical microscope.[43]

D. Simulation of wall shear stress and further validation by experimental conditions

COMSOL Multiphysics 4.4 software was used to simulate the wall shear stress (WSS) profile in the microfluidic structure used in this study. This finite elements simulation solved the Navier–Stokes equation (assuming non-slipping walls) to calculate the velocity profile inside a rectangular channel (height = 0.01 cm and width = 0.1 cm). Then, assuming a constant dynamic viscosity along the channel, the profile of shear stress can be calculated along the rectangular cross section using eqn (1), where τ is the shear stress in Dyn cm^{-2}, μ is the dynamic viscosity in Dyn s cm^{-2} (for cell medium at 37 °C, 0.78 × 10^{-2} Dyn s cm^{-2} (ref. 9)), u is the velocity of the fluid along the boundary in cm s^{-1}, and y is the height above the boundary in cm.

$$\tau(y) = \mu \frac{\partial u}{\partial y} \quad (1)$$

Different flow rates, ranging from 100 nL min^{-1} to 1000 μL min^{-1}, were applied at the inlet, and atmospheric pressure (1.01295 × 10^6 Dyn cm^{-2}) was imposed at the outlet.

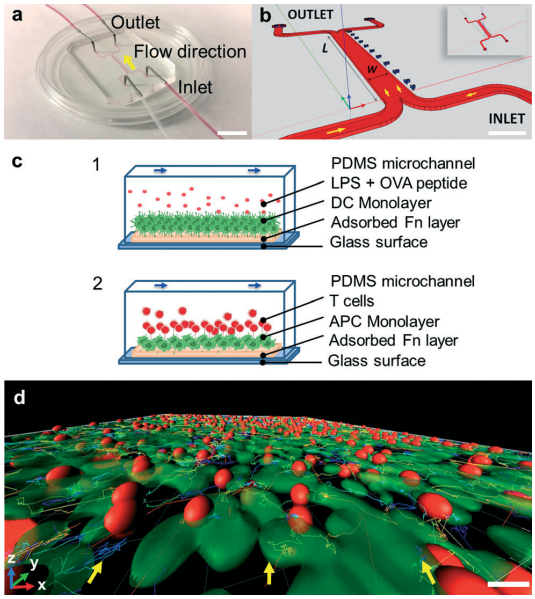

Fig. 1 Microfluidic device for immune cell–cell interactions. a) The PDMS biochip on a glass substrate. b) The device is composed of one main flow channel with 2 inlets and 2 outlets. Dimensions of the microchannel: length 10 mm, width 1 mm, and height 100 μm. The direction of the flow is indicated by yellow arrows. c) Dynamic DC : T-cell interactions during flow. Cross-sectional view of the microchannel: (1) the dendritic monolayer and LPS and OVA peptide activation in order to mimic an inflammatory biochemokine response. (2) T cell loading and T cell : DC interaction. The arrow indicates flow direction. d) Representation of the 3D dynamic interaction of T cells (red dots) and the DC monolayer (green monolayer) from real 3D confocal visualization, using Bitplane Imaris (yellow arrows indicate the flow direction). Scale bars: a) 1 cm, b) 1 mm, and d) 10 μm.

E. Antigen presentation assays, cell staining and loading procedure, and microfluidic setup

Dendritic cells. Dendritic cells were loaded onto the device and left to adhere to the fibronectin coating for 20 min and

then preincubated with 100 ng ml^{-1} LPS for 2 h. After 2 h, the cells were incubated with the ovalbumin OVA323-339 I-A^b (MHC class II)-presented peptide (ISQAVHAAHAEINEAGR) (hereafter called the OVAII peptide) or the OVA257-64 K^b (MHC class I)-presented peptide (SIINFEKL) (hereinafter called the OVAI peptide), both at 10 μg ml^{-1} and 100 ng ml^{-1} lipopolysaccharide (LPS, Sigma) for 1 h, for antigen presentation to CD4$^+$ or CD8$^+$ T cells, respectively.

Staining cells. Cells were removed from flasks and stained with 1 μM Cell Tracker™ Deep Red Dye or 5 μM Cell Tracker™ Orange CMTMR (5-(and-6)-(((4-chloromethyl)-benzoyl)amino)tetramethylrhodamine) (Invitrogen) for 30 minutes according to protocols and resuspended to a final concentration of ~5 × 10^6 cells per ml.

Microfluidic setup. The cells were imaged using a Zeiss LSM 510 inverted confocal microscope, which was equipped with an on-stage incubator with controlled temperature, CO_2 pressure and humidity for long term cell tracking. The microscope and digital camera were controlled *via* Carl Zeiss Zen 2009 (Version 6.0 SP2). Syringe pumps (PHD 2000, Harvard Apparatus, Holliston, MA) were used to insert cells and fluids into the microfluidic structure [Fig. 1(a)–(c)]. T cell : DC interactions were visualized in 2D and 3D at different times, using a fully rendered multidimensional data set and a scheme of monochrome *z*-stacks, resulting in a "top view" projection. Time lapse fluorescence and differential interference contrast (DIC) images were captured with a 20× objective using a Zeiss LSM 510 inverted laser scanning confocal microscope while the devices were maintained at 37 °C. The fluorescence micrographs were analysed using Matlab R2014, Bitplane Imaris 7.6 and ImageJ software. Cells were manually tracked over time from maximum intensity top-view image sequences. The instantaneous velocities of T cells and DCs were calculated from the distance moved between successive time points (~s each).

F. Mechanical strength assay of pMHC–TCR

The microfluidic system described above was used in this work to measure the detachment of cells at a certain tangential force *via* the controlled shear stress threshold of pMHC–TCR binding for specific and non-specific antigen activation of CD4$^+$ T cells and CD8$^+$ T cells. In order to generate specific stimulation, CD4$^+$ MF2.2D9 T cell and CD8$^+$ RF33.70 T cell will recognise OVAII/I-A^b peptide and OVAI/K^b peptide, respectively. As a way to promote these interactions, one uniform DC monolayer activated or not with LPS and OVA II or I peptide was prepared, and CD4$^+$ or CD8$^+$ T cells were loaded by pipetting from the inlet of the microchannel [Fig. 1(b)]. To allow formation and to strengthen these interactions, the microchannel co-culture was incubated at 37 °C for 30 min. The microchip was then mounted on the confocal microscope and connected with the syringe pump. For these cell detachment assays, the flow rate was increased every 20 min (from 100 nL min^{-1} to 1000 μL min^{-1}) to probe the shear stress by five orders of magnitude (from 0.01 to 100 Dyn cm^{-2}). The number of cell–cell interactions was determined by time-lapse microscopy in two different positions in the same channel and plotted as a function of shear stress. In this approach, the same experimental setup was used to investigate the cell rolling and the cell tracing, when these interactions are subjected to an increase in shear stress.

G. Adhesion cell assay for interaction of T cells and DCs

To probe the dynamics of cell attachment, T cells were introduced into the microchannel by continuous flow, as opposed to the static no-flow establishment of cell : cell adhesion in protocol F. A microchannel with a uniform DC monolayer with and without activation with LPS and OVA II peptide (or OVA I peptide) was connected to the syringe pumps with CD4$^+$ T cells and CD8$^+$ T cells, and T cell loading was performed at 0.01 Dyn cm^{-2} for 80 minutes with continuous perfusion on the two inlets, allowing the presence of two parallel flow streams with two different T-cell lines along the microchannel. Then, the two initial cell syringes with CD4$^+$ and CD8$^+$ T cells were replaced by two syringes with medium, starting the detachment approach: the flow rate was increased 10-fold every 10 min (from 100 nL min^{-1} to 1 mL min^{-1}) to test effect of the wall shear stress from 0.01 to 100 Dyn cm^{-2}. In this context, this experimental approach was used to investigate the model of cell–cell interaction, the cell surface distribution, the cell rolling and the cell tracing at an increasing shear stress.

H. Statistical analysis

Measurements of the T cell : DC interaction and DC monolayer were obtained and quantified using time series (Zeiss LSM510) across 12 independent experiments, at two separate locations, 4 mm and 7 mm from the beginning of the initial bifurcation of the microchannel. Considering that the results obtained in both positions were similar in all experiments, we opted to mention just one position, 7 mm, to simplify the description of this work. For cell counting, any T cell interacting with a DC that did not move for 30 s was considered adherent. For statistical clustering treatment, multiple stack samples at the same time were obtained and compared using Matlab R2014, Bitplane Imaris 7.6 and ImageJ software with the multidimensional data set assembled using custom written scripts to resolve cell count and stages of antigen recognition and CD4$^+$/CD8$^+$ T cell activation over time [Fig. 1(d)].

Results and discussion

Simulations: flow configuration and shear stress profile

In order to understand the progressive distribution of shear stress along a cross-section (*XZ*) at any position (*Y*) of the rectangular microchannel and for the different flow rates that were experimentally applied, a series of simulations were performed in COMSOL Multiphysics 4.4. In this context, biomimetic microfluidic systems are particularly suited for studies of cell adhesion and cell–cell interaction dynamics with variable velocity, shear stress, deformation rates and

migratory motility. The shear stress of interest in this study is related to the conditions found during an inflammation process, characterized by an increment of shear stress inside the T cell zones of LNs during stage II,[3] where in the presence of cognate antigen, T cells arbitrarily migrate along the fibroblastic reticular cell (FRC) conduit networks to contact the cognate antigen present in the surrounding APCs. During this initial stage of cognate interactions between T cells and DCs, T cells interacting with multiple DCs slow down their migratory speed, and eventually stop during the first 2 h.[2,3,32,34–36,38,39,44] Assuming the complexity of estimating the hydrodynamic properties in the highly confined microenvironment of T cell zones inside LNs, several studies that focused on the microvasculature suggest that the shear stress tested can be representative of the range of interstitial flow velocities measured in normal and tumor-associated inflamed skin, with a range of 0.005 to 0.05 Dyn cm^{-2}.[37]

As a result, in Fig. 2(a), we can observe that the shear stress is negligible at the centre of the channel and increases when approaching the edges of the channel, where the cells are immobilized and interacting. From the model, we found the shear stress values for the different flow rates used in our system (Fig. 2(a) and (b)) at the positions (*X*, *Y*, *Z*) of (A) the DC monolayer (500, *Y*, 5), (B) the center of the channel (500, *Y*, 50), (C) the representative region on the top of the T cell experiencing higher work (750, *Y*, 15) and (D) the representative region of a detached T cell (750, *Y*, 25).

In this way, it is possible to adjust the extrinsic shear force to the intrinsic inter-cell force of cell : cell adhesion to mimic lymph node conditions and to promote selective binding of antigen-specific *vs.* non-specific T cells to the DC monolayer. At low shear stress (0.01 to 0.05 Dyn cm^{-2}, associated with flow rates ranging from 100 nL min^{-1} to 500 nL min^{-1})[37] corresponding to physiological values for complex flow in the lymph node microenvironment,[15,45,46] cell speeds of 8–25 μm per second were generated, so cells have about 1 second to establish firm contact with another cell.

In the second phase, these established T cell : DC interactions were submitted to a successive increment of shear stress values (from 0.01 to 100 Dyn cm^{-2}) to determine the mechanical strength of the cell : cell interaction and the suitable speeds for differentially breaking the bond of antigen-specific *vs.* non-specific interactions.[4,10,13,47] We assessed the activation of DCs showing expression of MHC class II and CD80/86 by flow cytometry (data not shown).

Our objective in this work is to explore the mechanism, dynamics and basic cell behaviour of attachment and detachment of antigen-specific and unspecific $CD8^+$ T cells and $CD4^+$ T cells to activated antigen-presenting or non-activated DCs during flow at different shear stresses to establish some basic principles and approaches to allow further exploration of these phenomena.

In T cell : DC interactions, when an antigen is present, the initiating interaction leads to a highly organized structure of the immunological synapse known as the central, peripheral and distal supramolecular activation complexes (SMACs). The

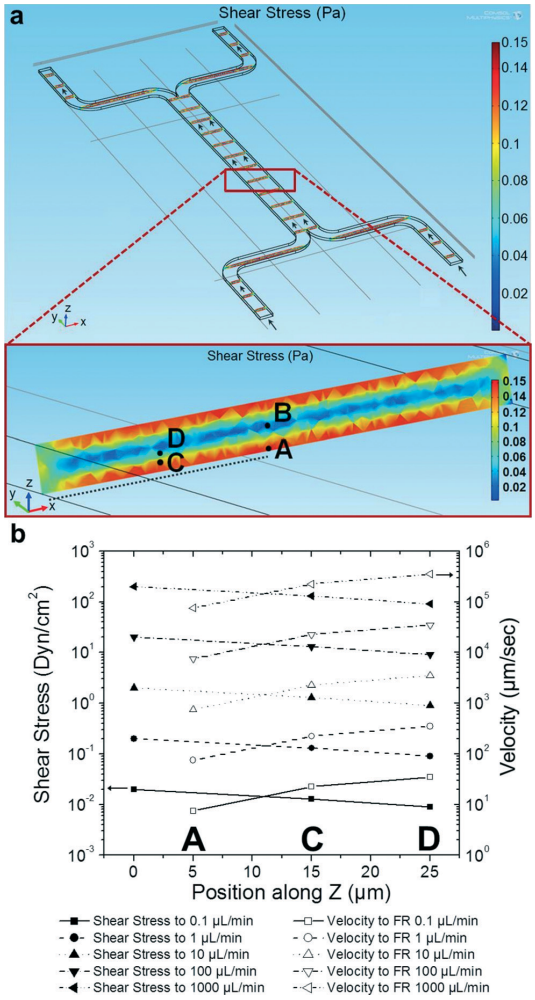

Fig. 2 Shear stress profile. a) 2D graphics from COMSOL Multiphysics 4.4 simulation of a rectangular channel cross section. b) Shear stress in a rectangular channel cross section as a function of different positions along the *Z* axis at different flow rates (μL min^{-1}).

formation of SMAC is dependent on the mechanical force, cell–cell contact area and time, shear stress, expression of surface molecules (such as TCR and LFA-1), cytoskeleton dynamics, antigen affinities and cell phenotype. In this work, our objective is to first allow establishment of these interactions with low shear stress before successive increment of flow rates mimicking the evolution of inflammatory stages.

The process of attachment starts within seconds after conjugation and reaches a maximum strength at around 30 min before cell activity causes changes in adhesion and subsequent release.[18] In this sense, we find it likely that T cells interact with DCs in a history dependent manner where in particular the detachment is dynamic and reliant on previous

encounters, making it likely that other flow-change regimes would change cell behaviour. In this work, we sought however to find the working limits of our system, and more work is needed to fully understand the mechanisms of attachment and release.

Characterization of DC monolayer adhesion and T cell : DC interactions under 0.01 Dyn cm^{-2}

The interaction of dendritic cells to adsorbed films of fibronectin (FN) and collagen (Col) was optimized, showing that after 1 h on the FN-coated surface, DCs spread uniformly along the microchannel, with a characteristic morphology with long dendrites and a larger surface area, in accordance with the expected morphology and overall function. In contrast, in Col coated microchannels, DCs were poorly dispersed and have thinner and shorter dendrites, similarly to what is observed in uncoated glass. All subsequent experiments were therefore performed in FN-coated channels, as ECM components have shown a beneficial effect on the DC function.[8,9,48–50] Our findings of a positive effect of FN coating on the DC surface area and dendritic length are in line with these studies.[8,9,48]

The DCs normally found in lymph nodes having migrated from peripheral tissues and able to prime T cells are proinflammatory expressing co-stimulatory molecules and secrete cytokines and chemokines. We activated the DCs with LPS for a total of 3 h after the initial DC loading and adherence. The DC monolayer acquired a mature phenotype, increasing in size presumably as a part of a strategy to increase the probability of encounters with naive antigen specific T cells.

To better understand the intercell dynamics, we co-incubated OVAII-peptide specific MHC class II-restricted CD4$^+$ T cells on LPS-activated OVAII-peptide presenting DCs for 30 min before starting the perfusion at 0.01 Dyn cm^{-2} for 2 h, a shear stress representative of the interstitial tissue flow velocity.[37] By tracking single cells over time, the trajectories of CD4$^+$ T cells could be established. For the initial 30 min with perfusion, the interactions had a mean duration of 12.8 min, the mean velocity of T cells was 6.0 μm min^{-1} (n = 422 cells), and most of the T cells crawled around allowing dynamic serial contacts with the same or with neighbouring DCs (Fig. 3 and Video S1†). This cell behaviour is very similar to what is found *in vivo*.[3,37] In fact, Miller *et al.* reported that *in vivo* the interactions were prolonged in the presence of an antigen with a mean time of 11.4 min and remained intermittent with a mean velocity of 5.4 μm min^{-1}.[3]

We also observed the tendency of CD4$^+$ T cells to move against the direction of flow (Fig. S1 and Movie S1†), as also reported in ref. 38 even though the collective analysis showed more or less random movement, independent of flow direction.[3] This discrepancy can be explained by that our DCs are not completely confluent, which introduces gaps in the contra-flow crawling substrate not present in the monolayers of ICAM-1-Fc, that the density of ICAM-1 on the DC surface probably is lower than that on the ICAM-1-Fc covered surface, and that T cells and DCs interact dynamically to influence each other's behaviour compared to the mono-cell behaviour reported by Valignat *et al.*[38]

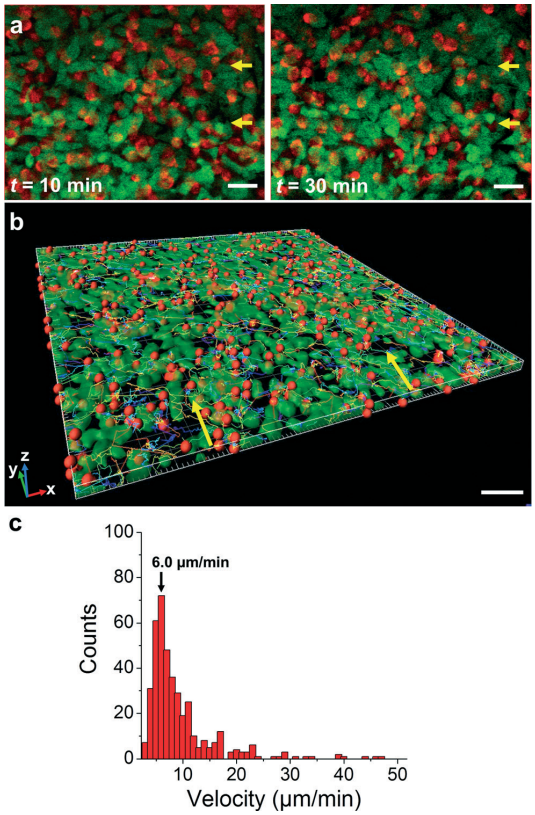

Fig. 3 Dynamic cognate T cell : DC interactions. a) Time-lapse images of cognate interactions between T cells (red) and APCs (green) over 30 min were examined by confocal microscopy. The yellow arrows indicate the direction of flow. b) Three-dimensional model of interactions of T cells (red dots) and the APC monolayer (green monolayer) using ImarisTrack. c) Distributions of instantaneous CD4$^+$ T cell velocities, measured over 30 min at times of 0–2 h (n = 422 cells) restricted to 35 μm from the surface. Scale bars: a) 15 μm and b) 50 μm.

DC : T cell interactions at low shear stress variations

To further characterize the T cell : DC interactions and assess the longevity and strength of the contacts, we allowed CD4$^+$ and CD8$^+$ T cells to adhere to activated antigen-presenting or control DCs for 30 min as previously described, at a physiological shear stress ranging from 0.01 to 0.15 Dyn cm^{-2} increasing every 20 minutes for a total of 4 h.

The magnitude of the shear stress in Fig. 4(b) is lower compared to Fig. 4(a) for the same flow rates since T cell positions are farther from the surface (as evidenced in Fig. 2), which decreases the shear stress. According to the model

presented in Fig. 2, these specific positions (A, C, D in Fig. 2) along the cross section of the channel for the different flow rates used in our system were selected to estimate the specific value of shear stress applied on specific cell positions: Fig. 4(b) describes the magnitude of shear stress in the region of a T cell interacting with a DC monolayer (position C (750, *Y*, 15); Fig. 2), and Fig. 4(a) represents the shear stress that dendritic cells (position A (500, *Y*, 5); Fig. 2) are submitted to.

There was a successive decrease in the number of DCs that adhered to the FN layer, and activated DCs adhered more firmly to the fibronectin substrate than the unactivated cells (Fig. 4(a)).

We also observed that the morphology of the DC changed to an elongated shape, with an enlarged contact area to the FN substrate, thus resulting in higher adhesive properties.[10,25,51]

The number of T cell : DC interactions also decreased along with an increase in shear stress but showing a much slower detachment rate from LPS-activated antigen-loaded DCs compared to the control DCs (Fig. 4(b)). The overall half-life of $CD4^+$ T cell contact to control DC was on the order of 75 min, whereas the half-life of the interaction with activated antigen-loaded DCs was more than 4 h indicating that the activation and antigen provided more stable conjugation of the cell pairs.

The cross-talk of T cell : DC involves several receptor–ligand interactions (as co-stimulatory and adhesion molecules) and the delivery of soluble mediators responsible for modulating the outcome of T cell activation, such as clonal expansion and differentiation.[6] The sustained adhesion of $CD4^+$ T cells to DCs at a progressive increase in shear stress could be explained by two possible regulation mechanisms:[10,49,52] (i) the integrin activation step on T cells allowing a stable leukocyte adhesion and (ii) the presence of high density of specific contacts of pMHC at the surface of APCs.

When T cells roll over the DC monolayer, and when the recognition is established by TCR binding to peptide-MHC of the APC, the TCR triggers a signalling cascade. Others have established that mechanical forces are involved in

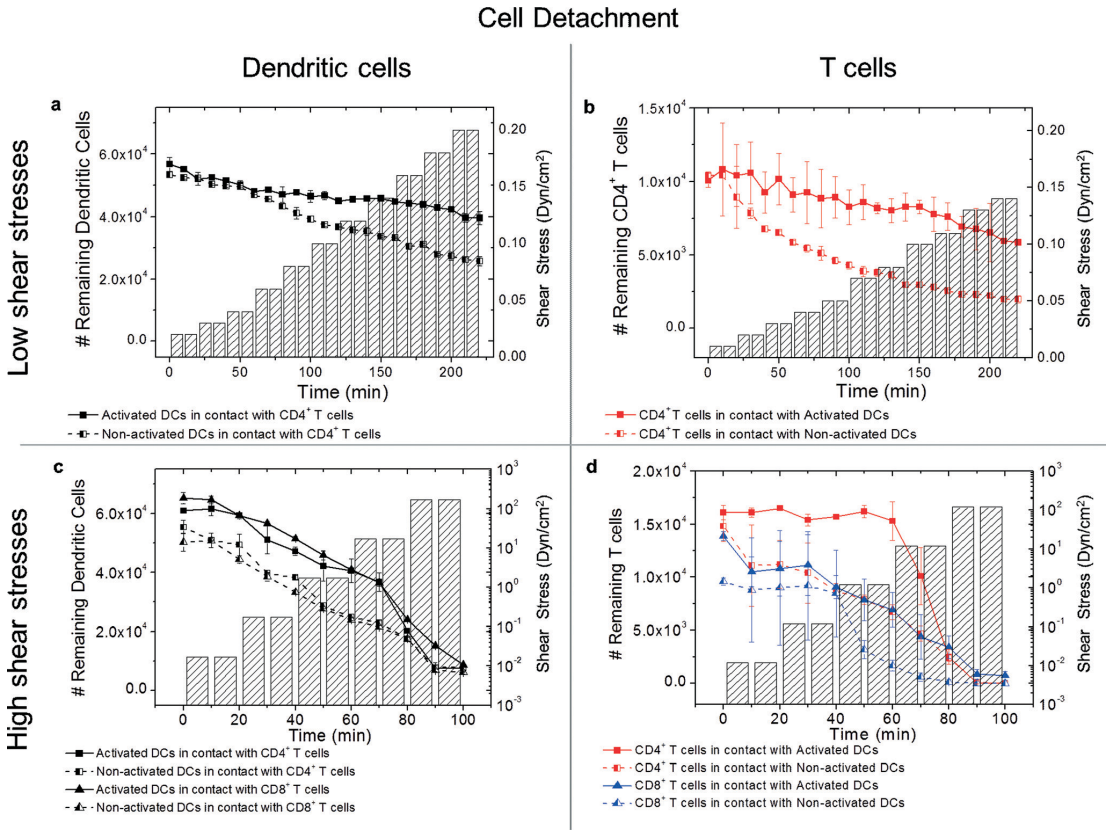

Fig. 4 T cell : DC interactions based on bond affinity and number: experimental distributions of high and low affinity bonds associated, respectively, with and without activation with LPS and OVA II peptide or OVA I peptide, increasing the velocity every 20 min. Low shear stress variations: detachment of a) dendritic cells and b) T cells; high shear stress variations: detachment of c) dendritic cells and d) T cells.

discriminating endogenous from foreign pMHC and in the activation of TCR triggering, described in several studies *via* traction force microscopy (TFM), atomic force microscopy (AFM), optical tweezers (OT) and biomembrane force probe (BFP).[4,13,18,46,53–55] Reinherz *et al.* describe the importance of tangential but not perpendicular mechanical force on the TCR complex activation, evidencing the need for force during the activation and, by this, defining the TCR as an anisotropic mechanosensor.[46,54] Once established, the TCR–peptide MHC interactions will resist shearing forces.[46,47] Reinherz *et al.* present as main implications associated with this directional-specific physical force that (i) TCR activation may be promoted due to the torque application, and the angle of interaction between the pMHC–TCR lever arm length and force vector will affect the torque;[15] (ii) shear stress can promote catch bonds at the TCR–pMHC interface, which are strengthened by tensile force, improving binding and ligand specificity; (iii) the total force exerted to the T cell surface is defined by the movement of the T cell membrane relative to the T cell : APC contact zone and the sensitivity is built into the TCR mechanosensor function.[45,46] Thus, a low shear force promoted antigen-specific T cell adhesion to DCs.

DC : T cell interactions at high shear stress variations

We next sought to determine the threshold shear stress necessary to break the inter-cell conjugation at shear stress values found inside capillary venules (0.01–1 Dyn cm^{-2}) and inside the arteries (>50 Dyn cm^{-2}).[9,38]

For the same reasons mentioned above, the magnitude of the shear stress shown in Fig. 4(d) is lower compared to that shown in Fig. 4(c) because the T cells are assumed to be farther from the surface than the DC monolayer, decreasing in this way the shear stress they are submitted to.

The DCs detached from the FN layer with a steady rate with no clear threshold level for shear stress (Fig. 4(c)). There was a tendency that activated DCs adhered more firmly to the substrate than the non-activated ones, particularly at intermediate shear stresses. There was no influence of the presence of $CD4^+$ or $CD8^+$ T cells on the detachment rate of DCs. Having established the background instability of the DC layer, we next assessed the detachment of $CD8^+$ and $CD4^+$ T cells from activated antigen-loaded and from control DCs.

The number of $CD4^+$ T cells conjugated to DCs was fairly stable at low shear stress but dropped abruptly above 12 Dyn cm^{-2} (Fig. 4(d)). The number of $CD4^+$ T cells adhering to peptide-presenting DCs after the initial rinse (*i.e.* after 10 min of perfusion) was significantly higher than that adhering to non-activated DCs, and the difference remained high until a threshold shear stress of 12 Dyn cm^{-2} was reached, when all T cells were released. In addition, the cytotoxic $CD8^+$ T cells showed a higher affinity to peptide-presenting DCs than to non-activated DCs, even though these interactions were a lot less stable and were steadily decreasing also at lower shear stresses. These observations show clearly that $CD4^+$ T cells have strong interactions with the activated peptide-loaded APCs, and therefore, we can infer that this activation was antigen-specific and that our system can possibly be used to selectively affinity isolate antigen-specific T cells and can be used as a microphysiological system of partial lymph node functionality.

The cell : cell interaction is dependent on the formation of SMAC, where a major contribution comes from ICAM-1–LFA-1 binding. This binding is again dependent on signalling through TCR, on mechanical force exerted on the ICAM-1–LFA-1 bond and on the expression level, type and stability of the ICAM-1 and LFA-1 molecules. The observed difference between $CD8^+$ and $CD4^+$ T cell release forces can be due to generally higher antigen-specific activation, determined by cytokine release, in this particular MF2.2D9 $CD4^+$ T cell clone compared to this particular RF33.70 $CD8^+$ T cell clone (data not shown). A further explanation can be that the MHC-level in MD2.2D9 is considerably higher than in the RF33.70 (data not shown), which should result in higher antigen-specific activation of the $CD4^+$ T cells. These release force numbers will probably vary much between different clones and cell pairs but will also probably lie within our reported ranges.

To account for the steady decrease in DC from the channel as well as to evaluate the efficiency in the formation and the stability of T cell : DC conjugates, we further analysed the relative T cell to DC ratios for different times and shear stresses. In our system, there was about one T cell for every five DCs initially. At low shear stresses, this ratio remained fairly constant over time for the interaction of $CD4^+$ T cells with activated peptide-loaded DCs (Fig. 5(a)), even though the number of DCs adherent to the fibronectin slowly decreased (Fig. 4(a)). This means that the adhesion of DCs to the substrate was neither strengthened nor weakened by conjugation to $CD4^+$ T cells. The ratio of $CD4^+$ T cells to resting DCs decreased to half of the initial ratio, suggesting that the binding strength in the conjugate was lower than the adherence of a DC to the substrate. This difference can be exploited to selectively retain antigen-specific T cells to a cognate activated DC. At higher shear stresses, the ratio of $CD4^+$ T cells to DCs was stable until the threshold shear stress of around 1.2 Dyn cm^{-2}, in which DCs, T cells and conjugates are released from the channel substrate (Fig. 5b). However, there was a higher ratio of T cells to activated Ag-loaded DCs than to resting DCs, suggesting higher binding forces. Considering that the high depletion of $CD4^+$ T cells occurs at 12 Dyn cm^{-2} and assuming the case of the flow past a sphere at low Reynolds numbers ($Re \ll 1$), we can estimate the total drag force (F_D) on the T cell as a grand resultant force from pressure force and viscous shear stresses on the cell, known as Stokes' law, $F_D = 6\pi\mu vR$. In this case, considering the variation range of flow rates tested in this system for the time associated with $0.0023 < Re < 2.6$ and the restrictions of Stokes' law to $Re < 0.1$, the expression for the drag force, $F_D = 6\pi\mu vR$, needs to be improved with an additional method of matched asymptotic expansions as suggested in ref. 56 leading to the derivation of Oseen's correction ($F_D = 6\pi\mu vR[1 + (3/8)Re]$) and being valid for Re up ~1. Assuming μ as the

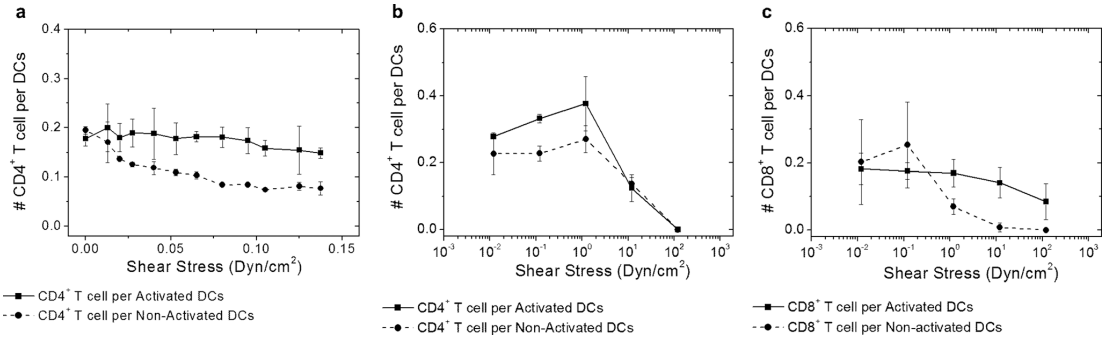

Fig. 5 Ratios of T cell per activated or non-activated DCs at different shear stress: a) retention of $CD4^+$ T cells on DCs during low levels of shear stress; b) retention of $CD4^+$ T cells on DCs during large variations of shear stress; and c) retention of $CD8^+$ T cells on DCs during large variations of shear stress.

dynamic fluid viscosity (for culture medium at 37 °C; 0.72×10^{-2} N s m^{-2}), R as the radius of the T cells (5 μm) and v as the fluid velocity (*i.e.* at a velocity of 0.033 m s^{-1} associated with Re = 2.6, when depletion of $CD4^+$ T cells occurs at 12 Dyn cm^{-2}),[56] we can estimate that a force of ~4.8 nN was applied to the T cells. The cell interaction dynamics in the CTL $CD8^+$ T cell systems was different, showing antigen-specific retention above 1.2 Dyn cm^{-2}. From this, we can estimate that for these cell lines the resultant force applied in the detachment of $CD4^+$ T cells on activated DCs is around ~4.8 nN, and for $CD8^+$ T cells on the non-activated system, it is around ~0.25 nN.

The antigen-specific T cell : DC interaction is strengthened by recruitment of LFA-1/ICAM-1 adhesion molecules to the immune synapse area. Shear stress on its own seems to have little influence on the adhesion molecule LFA-1; however, the chemokines CCL19 and CCL21 have an important influence on the upregulation of the active form of LFA-1 on DCs,[57] as well as the binding of TCR to pMHC.[18] LFA-1 then binds ICAM-1 on the T cells forming the immunological synapse, which seems to be strongest after 30 min and is stable for 1–2 h.[18,49,52]

Several groups have provided evidence about the mechanical force of the interaction between T cells and APC.[18,38,58] Hosseini *et al.* using single-cell force spectroscopy by AFM measured long-time interaction forces between T cells and APCs and demonstrated that in the presence of antigen interaction forces increased from 1 to 2 nN at early points, achieving at 30 min a maximum of interaction force of ~14 nN and decreasing the interaction forces after prolonged contact time (>60 min).[18,58] Valignat *et al.* investigated how migrational speed and directionality of T lymphocytes are influenced by variations of shear stress from 2 to 60 Dyn cm^{-2}, demonstrating that the force imposed by fluid flow in individual cells was estimated at around ~0.6 nN, corresponding to a shear stress of 60 Dyn cm^{-2} exerted on a typical cell surface.[38] The results obtained in this work match the interval of forces obtained by Hosseini *et al.* and Valignat *et al.*

Our observed differences in the intercell dynamics of $CD8^+$ and $CD4^+$ T cells to DCs, where the $CD4^+$ cell interaction with DC seemed to be longer and more stable than the relatively more transient $CD8^+$ T cell : DC interaction, are in line with other publications.[3] This fact suggests that this heterogeneity is part of a normal immune response and has an important role in diversifying the T cell fate.[6,59]

The detachment of T cell : DC contacts is also influenced by the strength of TCR signalling, the number of TCR–MHC interactions, and as a response to neighbouring chemokine environment, resulting in segregation and redistribution of established $CD4^+$ T cell : DC conjugates.[47,51,52]

It is also important to note that there is a major difference in shear stress experienced by DCs at 5 μm and T cells at 15 μm from the surface, as shown by retention of 70% and 40%

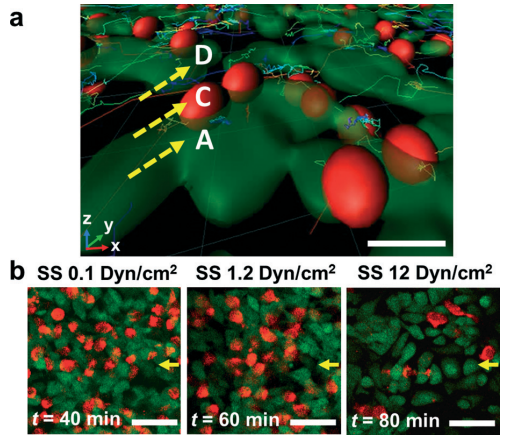

Fig. 6 Applying high shear stress variations between $CD4^+$ T cells with APCs: a) shear stress as a function of different positions (A, C and D) along the Z axis in a channel cross section, as illustrated in Fig. 2. b) Evolution of cell adhesion strength over time. Scale bars: a) 10 μm and b) 15 μm.

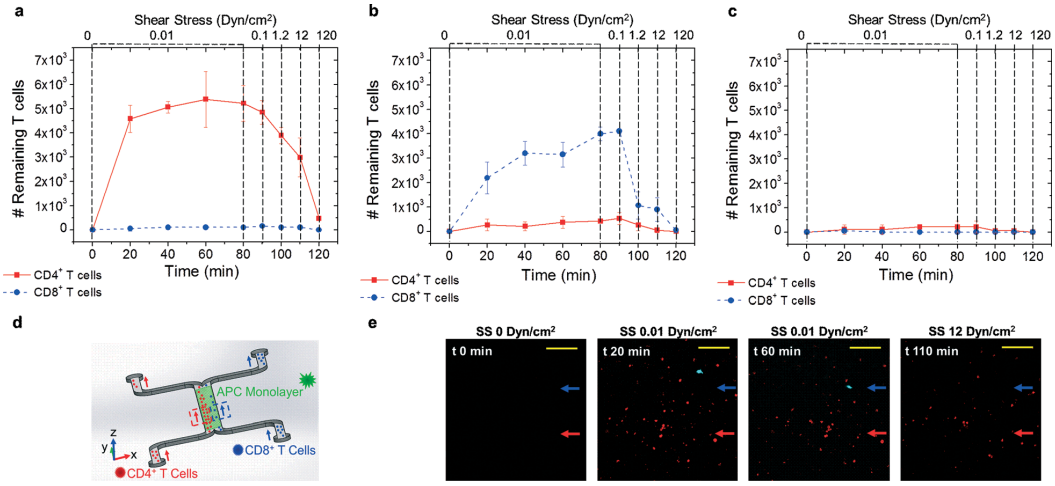

Fig. 7 Antigen specific attachment and shear stress induced detachment under continuous flow. $CD4^+$ T cells and $CD8^+$ T cells were continuously loaded by perfusion from the two inlets for 80 min at 0.01 Dyn cm^{-2} into previously activated and antigen-loaded DC microchannels allowing the presence of two parallel flow streams with two types of T-cells in parallel. After 80 min, cell perfusion was stopped and replaced with pure medium increasing the flow rate 10-fold every 10 min (from 100 nL min^{-1} to 1 mL min^{-1}) corresponding to wall shear stress from 0.01 to 100 Dyn cm^{-2}. a) Antigen-specific interactions of $CD4^+$ T cells with OVA II loaded DCs *vs.* antigen-unspecific $CD8^+$ cells. b) Antigen-specific interactions of $CD8^+$ T cells with OVA I loaded DCs *vs.* antigen-unspecific $CD4^+$ cells. c) Antigen-independent attachment of $CD8^+$ and $CD4^+$ T cells to antigen-free DCs. d) Schematic illustration of the cell-loading and pairing protocol. The main channel is coated with a monolayer of adherent DCs (in green). The directions of the flow of $CD8^+$ and $CD4^+$ T cells are indicated, respectively, by red and blue arrows. e) Representative images used for analyses of cell attachment of $CD4^+$ T cells (red) and $CD8^+$ T cells (cyan) to DCs for 60 min at 0.01 Dyn cm^{-2} (attachment phase) and 110 min at 12 Dyn cm^{-2} (detachment phase). Scale bar: c) 50 μm.

at 20 Dyn cm^{-2} for activated and non-activated DCs, respectively (Fig. 4(c) and 6), whereas only 10% of T cells remained after 10 Dyn cm^{-2} for 20 minutes (Fig. 4(d)). Thus, the force of binding of DCs to the FN is much stronger and lasting than T cells binding to DCs, as may be representative of forces inside lymph node conduits where DCs line the hollow tubes and T cells are in the center flow in between.[2,10,51]

Adhesion cell model for a specific interaction of T cells and DCs

Having established the influence of shear stress on the dynamic behaviour of the conjugates at different flow rates, we next wanted to establish the dynamics and rate of attachment of T cells to activated antigen-loaded DCs in a continuous flow, rather than by a preceding static synapse-forming stage. In this approach, the T cell : DC interaction is not forced but allows for a degree of freedom of orientation to establish contact, due to the tangential mechanical force applied over time by the flow. We also exploited the laminar flow in microfluidic devices by applying two different streamlines, one with $CD4^+$ T cells and one with $CD8^+$ T cells over a common DC monolayer previously activated with either LPS + OVA II peptide, LPS + OVA I peptide or untouched DCs at a low flow rate determined from previous experiments. We found a much higher degree of antigen-specific adhesion using this approach (Fig. 7) than the detachment approach. For the activated DC monolayer preincubated with LPS + OVA II peptide for 80 min and applying low shear stress (0.01 Dyn cm^{-2}), we found highly specific adhesion of antigen-specific $CD4^+$ T cells compared to the non-specific $CD8^+$ T cells (Fig. 7(a)). The number of $CD4^+$ T cell interactions was approximately constant over time with ~6.4×10^3 $CD4^+$ T cells to ~6.0×10^4 APCs, reflecting an interaction ratio of 11% compared to virtually no binding of $CD8^+$ T cells. After the initial 80 min attachment, the flow was switched to medium and subjected to increasing flow rates every 10 minutes. As shown in Fig. 7(a), we observed a successive detachment of $CD4^+$ T cells with a successive increment of shear stress from 0.01 to 12.0 Dyn cm^{-2} and a strong decrease when increasing the shear stress to 120.0 Dyn cm^{-2}. On the other hand, the non-specific interaction of $CD8^+$ T cells was only broken when submitted to a high shear stress in the range of 12.0–120.0 Dyn cm^{-2}.

This subsequent detachment was similar to what we found in the statically attached T cells (Fig. 4 and 5), with depletion of $CD4^+$ T cells occurring from 12 Dyn cm^{-2} and associated with a force of 4.8 nN. In this context, this attachment approach provides a simple way to control the natural formation of T cell : DC contact similar to the observations from *in vivo* experiments, with an interaction ratio of T cells to APCs of 11% compared to the 33% (~2.0×10^4 $CD4^+$ T cells per ~6.0×10^4 APCs) of the detachment approach. These results also show that the lower quantity of interactions in this attachment approach can be explained by the fact that the

total number of T cells interacting on the DC monolayer was lower and dependent on the balance between the convection velocity and sedimentation velocity that promotes cell rolling, adhesion and posterior interaction.

According to P. Bousso *et al.*, in the absence of antigen recognition, $CD8^+$ T cells may tend to encounter DCs that have already established a cognate interaction with other $CD4^+$ T cells, as an eventual result of chemokine expression and production (CCL3 and CCL4).[6] This fact may explain the reason why some $CD8^+$ T cells bound non-specifically to the DCs.

In addition, under the reverse conditions (Fig. 7(b)), $CD8^+$ cells selectively bound to Ag-loaded DCs, whereas few $CD4^+$ cells nonspecifically bound. Over 80 min with the same shear stress (0.01 Dyn cm^{-2}), the number of $CD8^+$ T cells that interacted during this approach was $\sim 4.0 \times 10^3$ T cells to $\sim 6.0 \times 10^4$ APCs, meaning an interaction ratio of ~7%. In the subsequent detachment, we observed an early depletion of specific $CD8^+$ T cells at 1.2 Dyn cm^{-2} and a successive detachment with increasing shear stress of 0.12–12 Dyn cm^{-2}, with no cells remaining at 120 Dyn cm^{-2}.

This attachment approach can be assumed as a complementary method of the initial detachment approach. This allows the confirmation of cell detachment behaviour and the shear stress applied to detach the cells in both approaches and highlights the existence of the heterogeneity response as part of a normal immune response and having an important role in diversifying the T cell fate.[6]

Conclusion

During T cell priming and activation, a few antigen-presenting dendritic cells residing in the lymph node interact with a large number of T cells entering the lymph node from the blood, scanning for match in TCR with peptide on MHC molecules on the DCs.

In this work, we have explored the mechanism, dynamics and basic cell behaviour of attachment and detachment of antigen-specific and unspecific $CD8^+$ cytotoxic T cells and $CD4^+$ T helper cells to activated or non-activated DCs during flow at different shear stresses. The main goal of this study is to investigate the interaction induced by the tangential force *via* shear stress from the natural dynamic rate of attachment of T cells : DC in a continuous flow, as a way to mimic the natural principle of interaction that occurs *in vivo* and to investigate the possibility of using these principles as tools towards immunological research and in development of novel immunotherapeutic approaches.

We successfully demonstrated the ability of our system to selectively promote adhesion of antigen-specific T cells through serial contacts. Furthermore, we found antigen-specific attachment and detachment at different shear stresses, suggesting that a shear stress of 0.1–1 Dyn cm^{-2} can be used to allow cell-based affinity isolation of antigen specific T cells towards unknown antigens.

In contrast to static cultures or passive channels, our system can be used to compare, in parallel and in real time, through control over adhesion, the effect of different treatments, inhibitors, activators or immunogens. The applications can be used as a research tool to understand lymph node organogenesis, T cell development and activation, contribution of different cell types in immunization protocols, and generation of specific immune responses and as a clinical developmental tool towards *in vitro* immunization, personalized cancer vaccination, immunotherapeutic approaches for cancer and autoimmune diseases *etc.*, all through re-creation of the natural T cell activation lymph node organ. Further investigations are needed to verify the feasibility of the approach on a clinical scale.

Acknowledgements

The Research Council of Norway is acknowledged for the support to the Norwegian Micro- and Nano-Fabrication Facility, NorFab (197411/V30). The microfabrication process was performed at the NTNU NanoLab (NorFab), Norwegian University of Science and Technology. Experiments were performed at the Cellular and Molecular Imaging Core Facility (CMIC), Norwegian University of Science and Technology. CMIC is funded by the Faculty of Medicine at NTNU and Central Norway Regional Health Authority.

References

1 M. A. Swartz, S. Hirosue and J. A. Hubbell, Engineering approaches to immunotherapy, *Sci. Transl. Med.*, 2012, **4**(148), 148rv9.
2 J. P. Girard, C. Moussion and R. Forster, HEVs, lymphatics and homeostatic immune cell trafficking in lymph nodes, *Nat. Rev. Immunol.*, 2012, **12**(11), 762–773.
3 M. J. Miller, O. Safrina, I. Parker and M. D. Cahalan, Imaging the single cell dynamics of $CD4^+$ T cell activation by dendritic cells in lymph nodes, *J. Exp. Med.*, 2004, **200**(7), 847–856.
4 Z. Ma, D. E. Discher and T. H. Finkel, Mechanical force in T cell receptor signal initiation, *Front. Immunol.*, 2012, **3**, 217.
5 H. P. Mirsky, M. J. Miller, J. J. Linderman and D. E. Kirschner, Systems biology approaches for understanding cellular mechanisms of immunity in lymph nodes during infection, *J. Theor. Biol.*, 2011, **287**, 160–170.
6 P. Bousso, T-cell activation by dendritic cells in the lymph node: lessons from the movies, *Nat. Rev. Immunol.*, 2008, **8**(9), 675–684.
7 M. J. Miller, S. H. Wei, I. Parker and M. D. Cahalan, Two-photon imaging of lymphocyte motility and antigen response in intact lymph node, *Science*, 2002, **296**(5574), 1869–1873.
8 S. Garcia-Nieto, R. K. Johal, K. M. Shakesheff, M. Emara, P. J. Royer and D. Y. Chau, *et al.*, Laminin and fibronectin treatment leads to generation of dendritic cells with superior endocytic capacity, *PLoS One*, 2010, **5**(4), e10123.

9 E. W. Young, A. R. Wheeler and C. A. Simmons, Matrix-dependent adhesion of vascular and valvular endothelial cells in microfluidic channels, *Lab Chip*, 2007, **7**(12), 1759–1766.
10 E. Bianchi, R. Molteni, R. Pardi and G. Dubini, Microfluidics for in vitro biomimetic shear stress-dependent leukocyte adhesion assays, *J. Biomech.*, 2013, **46**(2), 276–283.
11 P. A. van der Merwe, The TCR triggering puzzle, *Immunity*, 2001, **14**(6), 665–668.
12 Z. Ma and T. H. Finkel, T cell receptor triggering by force, *Trends Immunol.*, 2010, **31**(1), 1–6.
13 Y. C. Li, B. M. Chen, P. C. Wu, T. L. Cheng, L. S. Kao and M. H. Tao, *et al.*, Cutting Edge: Mechanical Forces Acting on T Cells Immobilized via the TCR Complex Can Trigger TCR Signaling, *J. Immunol.*, 2010, **184**(11), 5959–5963.
14 A. Grakoui, S. K. Bromley, C. Sumen, M. M. Davis, A. S. Shaw and P. M. Allen, *et al.*, Pillars article: The immunological synapse: a molecular machine controlling T cell activation, Science, 1999, 285, 221–227, *J. Immunol.*, 2015, **194**(9), 4066–4072.
15 S. T. Kim, Y. Shin, K. Brazin, R. J. Mallis, Z. Y. Sun and G. Wagner, *et al.*, TCR Mechanobiology: Torques and Tunable Structures Linked to Early T Cell Signaling, *Front. Immunol.*, 2012, **3**, 76.
16 C. Martinez-Rico, F. Pincet, E. Perez, J. P. Thiery, K. Shimizu and Y. Takai, *et al.*, Separation force measurements reveal different types of modulation of E-cadherin-based adhesion by nectin-1 and -3, *J. Biol. Chem.*, 2005, **280**(6), 4753–4760.
17 X. Zhang, E. P. Wojcikiewicz and V. T. Moy, Dynamic adhesion of T lymphocytes to endothelial cells revealed by atomic force microscopy, *Exp. Biol. Med.*, 2006, **231**(8), 1306–1312.
18 B. H. Hosseini, I. Louban, D. Djandji, G. H. Wabnitz, J. Deeg and N. Bulbuc, *et al.*, Immune synapse formation determines interaction forces between T cells and antigen-presenting cells measured by atomic force microscopy, *Proc. Natl. Acad. Sci. U. S. A.*, 2009, **106**(42), 17852–17857.
19 D. J. Muller and Y. F. Dufrene, Atomic force microscopy as a multifunctional molecular toolbox in nanobiotechnology, *Nat. Nanotechnol.*, 2008, **3**(5), 261–269.
20 S. N. Bhatia and D. E. Ingber, Microfluidic organs-on-chips, *Nat. Biotechnol.*, 2014, **32**(8), 760–762.
21 A. A. Khalili and M. R. Ahmad, A Review of Cell Adhesion Studies for Biomedical and Biological Applications, *Int. J. Mol. Sci.*, 2015, **16**(8), 18149–18184.
22 E. W. Esch, A. Bahinski and D. Huh, Organs-on-chips at the frontiers of drug discovery, *Nat. Rev. Drug Discovery*, 2015, **14**(4), 248–260.
23 D. Huh, Y. S. Torisawa, G. A. Hamilton, H. J. Kim and D. E. Ingber, Microengineered physiological biomimicry: organs-on-chips, *Lab Chip*, 2012, **12**(12), 2156–2164.
24 G. Lamberti, B. Prabhakarpandian, C. Garson, A. Smith, K. Pant and B. Wang, *et al.*, Bioinspired microfluidic assay for in vitro modeling of leukocyte–endothelium interactions, *Anal. Chem.*, 2014, **86**(16), 8344–8351.
25 C. Dong and X. X. Lei, Biomechanics of cell rolling: shear flow, cell-surface adhesion, and cell deformability, *J. Biomech.*, 2000, **33**(1), 35–43.
26 S. K. Kim, W. K. Moon, J. Y. Park and H. Jung, Inflammatory mimetic microfluidic chip by immobilization of cell adhesion molecules for T cell adhesion, *Analyst*, 2012, **137**(17), 4062–4068.
27 J. Y. Park, H. O. Kim, K. D. Kim, S. K. Kim, S. K. Lee and H. Jung, Monitoring the status of T-cell activation in a microfluidic system, *Analyst*, 2011, **136**(13), 2831–2836.
28 Y. Choi, E. Hyun, J. Seo, C. Blundell, H. C. Kim and E. Lee, *et al.*, A microengineered pathophysiological model of early-stage breast cancer, *Lab Chip*, 2015, **15**(16), 3350–3357.
29 S. Faley, K. Seale, J. Hughey, D. K. Schaffer, S. VanCompernolle and B. McKinney, *et al.*, Microfluidic platform for real-time signaling analysis of multiple single T cells in parallel, *Lab Chip*, 2008, **8**(10), 1700–1712.
30 B. Dura and J. Voldman, Spatially and temporally controlled immune cell interactions using microscale tools, *Curr. Opin. Immunol.*, 2015, **35**, 23–29.
31 B. Dura, S. K. Dougan, M. Barisa, M. M. Hoehl, C. T. Lo and H. L. Ploegh, *et al.*, Profiling lymphocyte interactions at the single-cell level by microfluidic cell pairing, *Nat. Commun.*, 2015, **6**, 5940.
32 P. Bousso and E. Robey, Dynamics of $CD8^+$ T cell priming by dendritic cells in intact lymph nodes, *Nat. Immunol.*, 2003, **4**(6), 579–585.
33 B. J. Burbach, R. B. Medeiros, K. L. Mueller and Y. Shimizu, T-cell receptor signaling to integrins, *Immunol. Rev.*, 2007, **218**, 65–81.
34 S. E. Henrickson, T. R. Mempel, I. B. Mazo, B. Liu, M. N. Artyomov and H. Zheng, *et al.*, T cell sensing of antigen dose governs interactive behavior with dendritic cells and sets a threshold for T cell activation, *Nat. Immunol.*, 2008, **9**(3), 282–291.
35 S. Hugues, L. Fetler, L. Bonifaz, J. Helft, F. Amblard and S. Amigorena, Distinct T cell dynamics in lymph nodes during the induction of tolerance and immunity, *Nat. Immunol.*, 2004, **5**(12), 1235–1242.
36 M. J. Miller, A. S. Hejazi, S. H. Wei, M. D. Cahalan and I. Parker, T cell repertoire scanning is promoted by dynamic dendritic cell behavior and random T cell motility in the lymph node, *Proc. Natl. Acad. Sci. U. S. A.*, 2004, **101**(4), 998–1003.
37 A. A. Tomei, S. Siegert, M. R. Britschgi, S. A. Luther and M. A. Swartz, Fluid flow regulates stromal cell organization and CCL21 expression in a tissue-engineered lymph node microenvironment, *J. Immunol.*, 2009, **183**(7), 4273–4283.
38 M. P. Valignat, O. Theodoly, A. Gucciardi, N. Hogg and A. C. Lellouch, T lymphocytes orient against the direction of fluid flow during LFA-1-mediated migration, *Biophys. J.*, 2013, **104**(2), 322–331.
39 K. W. Wucherpfennig, E. Gagnon, M. J. Call, E. S. Huseby and M. E. Call, Structural Biology of the T-cell Receptor: Insights into Receptor Assembly, Ligand Recognition, and Initiation of Signaling, *Cold Spring Harbor Perspect. Biol.*, 2010, **2**(4), 1–14.
40 S. A. Fuertes Marraco, F. Grosjean, A. Duval, M. Rosa, C. Lavanchy and D. Ashok, *et al.*, Novel murine dendritic cell

lines: a powerful auxiliary tool for dendritic cell research, *Front. Immunol.*, 2012, **3**, 331.

41 N. Gopalakrishnan, R. Hannam, G. P. Casoni, D. Barriet, J. M. Ribe and M. Haug, *et al.*, Infection and immunity on a chip: a compartmentalised microfluidic platform to monitor immune cell behaviour in real time, *Lab Chip*, 2015, **15**(6), 1481–1487.

42 J. C. McDonald, D. C. Duffy, J. R. Anderson, D. T. Chiu, H. Wu and O. J. Schueller, *et al.*, Fabrication of microfluidic systems in poly(dimethylsiloxane), *Electrophoresis*, 2000, **21**(1), 27–40.

43 P. Rosa, S. Tenreiro, V. Chu, T. F. Outeiro and J. P. Conde, High-throughput study of alpha-synuclein expression in yeast using microfluidics for control of local cellular microenvironment, *Biomicrofluidics*, 2012, **6**(1), 14109–141099.

44 T. R. Mempel, S. E. Henrickson and U. H. Von Andrian, T-cell priming by dendritic cells in lymph nodes occurs in three distinct phases, *Nature*, 2004, **427**(6970), 154–159.

45 J. H. Wang and E. L. Reinherz, A new angle on TCR activation, *Immunity*, 2011, **35**(5), 658–660.

46 J. H. Wang and E. L. Reinherz, The structural basis of a ss T-lineage immune recognition: TCR docking topologies, mechanotransduction, and co-receptor function, *Immunol. Rev.*, 2012, **250**, 102–119.

47 P. A. van der Merwe and O. Dushek, Mechanisms for T cell receptor triggering, *Nat. Rev. Immunol.*, 2011, **11**(1), 47–55.

48 M. J. Staquet, C. Jacquet, C. Dezutter-Dambuyant and D. Schmitt, Fibronectin upregulates in vitro generation of dendritic Langerhans cells from human cord blood $CD34^+$ progenitors, *J. Invest. Dermatol.*, 1997, **109**(6), 738–743.

49 T. Lammermann and M. Sixt, The microanatomy of T-cell responses, *Immunol. Rev.*, 2008, **221**, 26–43.

50 S. Celli, Z. Garcia and P. Bousso, CD4 T cells integrate signals delivered during successive DC encounters in vivo, *J. Exp. Med.*, 2005, **202**(9), 1271–1278.

51 D. Alvarez, E. H. Vollmann and U. H. von Andrian, Mechanisms and consequences of dendritic cell migration, *Immunity*, 2008, **29**(3), 325–342.

52 S. Celli, Z. Garcia, H. Beuneu and P. Bousso, Decoding the dynamics of T cell-dendritic cell interactions in vivo, *Immunol. Rev.*, 2008, **221**, 182–187.

53 J. Husson, K. Chemin, A. Bohineust, C. Hivroz and N. Henry, Force Generation upon T Cell Receptor Engagement, *PLoS One*, 2011, **6**(5), e19680.

54 S. T. Kim, K. Takeuchi, Z. Y. Sun, M. Touma, C. E. Castro and A. Fahmy, *et al.*, The alphabeta T cell receptor is an anisotropic mechanosensor, *J. Biol. Chem.*, 2009, **284**(45), 31028–31037.

55 P. H. Puech, D. Nevoltris, P. Robert, L. Limozin, C. Boyer and P. Bongrand, Force Measurements of TCR/pMHC Recognition at T Cell Surface, *PLoS One*, 2011, **6**(7), e22344.

56 R. B. Bird, W. E. Stewart and E. N. Lightfoot, *Transport phenomena*, 2nd, Wiley International Ed., J. Wiley, New York, 2002, vol. xii, p. 125.

57 C. Eich, I. J. de Vries, P. C. Linssen, A. de Boer, J. B. Boezeman and C. G. Figdor, *et al.*, The lymphoid chemokine CCL21 triggers LFA-1 adhesive properties on human dendritic cells, *Immunol. Cell Biol.*, 2011, **89**(3), 458–465.

58 S. Hoffmann, B. H. Hosseini, M. Hecker, I. Louban, N. Bulbuc and N. Garbi, *et al.*, Single cell force spectroscopy of T cells recognizing a myelin-derived peptide on antigen presenting cells, *Immunol. Lett.*, 2011, **136**(1), 13–20.

59 T. R. Mempel, S. E. Henrickson and U. H. von Andrian, T-cell priming by dendritic cells in lymph nodes occurs in three distinct phases, *Nature*, 2004, **427**(6970), 154–159.

Paper II

Journal Name

ARTICLE

Immune cells moving in a microchannel network in search of targets

Received 00th January 20xx,
Accepted 00th January 20xx

DOI: 10.1039/x0xx00000x

www.rsc.org/

Patrícia Moura Rosa,[a,c] Nimi Gopalakrishnan,[a,c] Giovanna Perinetti Casoni,[a] Rosanne van de Wijdeven,[a,c] Markus Haug[b] and Øyvind Halaas*[a]

A hallmark of the immune systems is cell-autonomous migration, homing and circulation between different immune organs and inflamed tissues based on soluble and immobilized chemotactic gradients and signals. In this work we developed and tested a microdevice that had features found in tissues, ie a tissue-mimicking device for the study of immune cell migration and homing towards inflammatory foci. We microfabricated a device consisting of multiple cell-chambers, separated by a hexagonal network of microchannels with cell-sized cross sections, and with embedded filters ensuring compartmentalization. Modelling and testing indicated time-frames for molecular diffusion similar to what is expected in tissues. We set up different inflammatory cell culture foci in attractor chambers using LPS-stimulated macrophages, T cells activated by antigen-presenting cells as well as lymph node fibroblast, dendritic cell and T cell co-cultures. A directional migration of both T cells and dendritic cells towards the inflammatori foci over that of control chambers was found. The hexagonal network layout allowed us also to observe decision-making process of individual cells at intersections, briefly arresting and probing both alternative paths before making a decision on which direction to go prior accumulating close to the inflammatory cue. The cells could be tracked individually and appeared to travel in all parts of the device. Our device is unique in providing a structured environment for automated long-term high-resolution interrogation of the processes of complex immune cell recruitment and migration towards cell-produced gradients at the collective as well as at the individual cell level.

Introduction

The immune system is comprised of a complex set of processes occurring during the body's response to infection, cancer and injury involving the orchestration of many cell types, cell functions, local microenvironments, organs and tissues all changing over time. Cellular mobility and self-reorganization in different body locations are a central hallmark of the whole immune system. This process is based on diffusive and bound factors guiding cells towards the locations where cell differentiation, activation or immune effector responses are appropriately initiated. In particular, the movement of innate and adaptive immune cells towards on-going tissue inflammation, as well as the trafficking to the lymph node, are fundamental for the correct activation and function of different types of leukocytes. These processes are tightly coordinated in the body and integrate a complex re-organization of both immune and stromal cells (fibroblasts, endothelial and epithelial cells) in relevant sites. For example, in response to local inflammatory signals, peripheral tissue-resident dendritic cells (DC) sample their surroundings and upon activation, enter the afferent lymphatic vessels, and migrate into the lymph nodes to present antigens to naïve T cells constantly recruited form the circulation. Afterwards, activated T cells exits to the lymph and blood, and migrates directionally to the inflammatory focus to fight the pathogens or cancer cells (1-3).

Although numerous *in vivo* and *in vitro* models have emerged to interrogate the cell motility involved in these immune interactions, a comprehensive understanding of naive and effector T cell migration *in vivo* is still lacking, such as the elucidation of cell migration models in distinct microcompartments of tissues under disease conditions, preferential tissue paths or geometries that would favor a migration strategy, whether immune cells have an internal clock regulating their pace and direction, and the decision-making process driving collective cell behaviour (1, 4-8). In order to enable a thorough delineation of the processes involved in directional decision-making in the immune system, we fabricated a microdevice allowing us to observe the process at the single cell as well as bulk level.

Traditional *in vivo* techniques for studying cell migration, such as dissection and intravital multiphoton microscopy, have provided good understanding of immune cell self-organization in immune reactions (1, 3, 4, 9, 10). Some of these approaches

[a] Department of Cancer Research and Molecular Medicine, Norwegian University of Science and Technology, 7489 Trondheim, Norway. E-mail: oyvind.halaas@ntnu.no
[b] Centre of Molecular Inflammation Research (SFF-CEMIR), Department of Cancer Research and Molecular Medicine, Norwegian University of Science and Technology, 7489 Trondheim, Norway
[c] NTNU Nanolab, Norwegian University of Science and Technology, 7489 Trondheim, Norway

Electronic Supplementary Information (ESI) available: [details of any supplementary information available should be included here]. See DOI: 10.1039/x0xx00000x

are based on genetic knockdown and overexpression experiments to disturb native molecular gradients and their receptors, or perturbations from exogenously supplied molecules through microinjection (5). However, these approaches are limited in image access, control of environmental conditions of biological substrates, maintenance of tissue cohesiveness and organization, as well as the possibility to perform gradient experiments for extended periods (1, 4, 5, 9).

In vitro, conventional methods such as macrochamber systems, pipette injection and hydrogels have been used to create concentration gradients for cell analysis (11). Transwell and Zigmond chambers, and subsequent design improvements of Dunn and Insall chambers have been used for chemotaxis studies for over five decades (11-14). Even though the Zigmond and the Dunn chambers allow for video imaging, the migration is not taking place in a spatially organized environment, and tracking of single cells results difficult. As a consequence, the assay readouts are mainly population based and are limited in options for perturbations during experiments and internal controls (11, 15). Moreover, conventional devices are generic and are not easily customized for specific purposes. For example, in bacterial infection studies, the lack of compartmentalization leads to bacterial spread in the entire system, making any long term conclusion infeasible (15). The micropipette method providing chemotactic factors locally into the open cell culture chambers is difficult to control and reproduce (11, 16, 17). Also 3D hydrogel systems are characterized by lack in spatial and temporal control and compartmentalization (11).

Compared to conventional cell migration assays, microfluidic devices offer highly controlled introduced or biologically produced gradients, allowing a powerful and multi-purpose research approach for studying gradient sensing and chemotaxis of different cell types either in flow-based or flow-free devices (5, 11, 18). The flow-based devices are characterized by a steady state being dependent on laminar flow mixing in microchannels that generates stable and local gradients profiles. The flow-free devices have instead a transient state, where molecular concentration can change over time, by free-diffusion in a static fluid environment between a source and a sink. Still, microfabrication technique allows to tightly control the changes over time greatly increasing experimental reproducibility. In addition, a static fluid environment reduces shear stress and is advantageous for cells in suspension or with low adhesiveness.

In order to design high performing flow-free devices, several structural strategies need to be integrated and finely tailored according to cell physiology and needs. Although these prerequisites increase the complexity of the microfabrication process, they contribute to the simplicity of device operation by not requiring complex operation such as pumping system (5, 11, 18). Tong *et al*. assembled a microfluidic migration chamber that utilizes a self-sustaining chemotactic diffusion gradient to induce locomotion of single cells coupled with direct visualization of migratory tracks (19). Ricart *et al.* studied DC migration in competing chemokine gradients on a 2D substrate by using a microfluidic network gradient generator (18, 20). Haessler *et al.* demonstrated using a flow-free microfluidic gradient device that cells significantly migrate towards the CCL21 gradient over a competing CCL19 gradient in 3D ECM (18, 21). However, these approaches are cumbersome and not very well controlled. In this context, and in the sequence of our previous work (15), we address a novel approach for building and operating a simple and flexible microfluidic chip system mimicking immunological compartmentalization with real-time, bulk, single-cell and sub-cellular interrogation options. We further demonstrate how such a design can be used for studying multiple immune cell behaviours and decision making processes, also allowing site-specific bacterial infections and in-experiment access.

Materials and Methods

A. Cells

C57BL/6 wild type mice were housed in the animal facility at the Department of Cancer Research and Molecular Medicine, Faculty of Medicine NTNU, St. Olavs University Hospital (Trondheim, Norway) and manipulated in accordance with the local Ethical Committee guidelines.

Unless otherwise stated, all cells were grown in complete medium was consisting of RPMI-1640 cell medium, 50 µM 2-mercaptoethanol, 20 mM HEPES, 2mM L-glutamine, 10% fetal calf serum (FCS) and 0.1 µM ciprofloxacin (6). Primary bone marrow-derived dendritic cells (BMDC) were generated from C57Bl/6 mouse bone marrow cells through 7 days of culture in 20 ng/ml GM-CSF (PeproTech) at 1×10^5 cells ml^{-1}. Fibroblast reticular cells (FRC) were obtained by culturing cells from mouse lymph nodes in complete medium for several weeks. The culture was shown to be 100% fibroblasts by podoplanin-positive and CD31-negative staining (not shown). Non-adherent ovalbumin specific MHC class II restricted (MF2.2D9) MHC class II restricted (MF2.2D9, referred to OVAII) and MHC class I restricted (RF33.70) $CD8^+$ T cell hybridomas (referred to as OVAI) were a gift from Dr Kenneth Rock, University of Massachusetts, Worcester. $CD4^+$ T cell (here after referred to as OVAII) were a gift from Dr Kenneth Rock, University of Massachusetts, Worcester. Adherent dendritic cells were matured by using 100 or 200 ng ml^{-1} LPS (Sigma) for indicated periods. Dendritic cells and FRC co-cultures were activated on chip by *E. Coli* Bioparticles (Thermo Fisher) at approximate ratio of 10 bioparticles per cell.

B. Design and fabrication of a microfluidic system

The microdevice was fabricated in polydimethylsiloxane (PDMS) by soft lithography with SU8 photoresist masters, according to published procedures (22) and using the standard photolithography techniques and facilities of NTNU NanoLab. The microfluidic device was designed using AutoCAD 2014 drawing software (Autodesk Inc., Europe), the photomasks were purchased from Compugraphics Ltd., UK), as a soda lime photolithography mask (3'' x3'' x0.060'') coated with a thin metal layer. The master for the microfluidic device was fabricated using a three-layer SU-8 process. The first layer (filters) was characterized with film thickness 2 µm with a

capillary network cross section of 2 µm x 2 µm, **Figure 1(b, c)** (yellow layer), the 2 µm-thin layer of photoresist (SU8 5, MicroChem) was spun at 8000 rpm for 30 s over a 2-inch Si wafer. The wafer was then exposed to ultraviolet light (UV light), at 120 mJ/cm^2 with hard contact. After post-exposure baking (1 min at 65 °C plus 1 min at 95 °C) and development, the mold was hard-baked for 3 min at 95 °C. After cooling, the mold was sacrificed with a 2nd layer (microchannel migration network), characterized with a hexagonal capillary network cross section of 6 µm x 6 µm, **Figure 1(b, c)** (blue layer).

The second layer of photoresist (SU8 5, MicroChem) was spun at 2500 rpm for 30 s. The wafer was aligned and exposed to UV light at 150 mJ/cm^2 hard contact followed by post-exposure baking and development. The third layer (cell compartments) had a thickness of 28 µm and two types of rectangular chambers with width x length of 550 µm x 1000 µm (as side of infection: attractor and control chambers) and 550 µm x 2000 µm (migratory, entrance and sink chambers, **Figure 1(b, c)** (red layer)). The third layer with a final film thickness 28 µm (MaP-1275, Micro Resist Technology GmbH) was spun twice at 2000 rpm for 30 s (per film thickness, 14 µm) in order to achieve the final thickness. The wafer was then aligned and multi-exposed in 2 cycles to UV light, at 120 mJ/cm^2 hard contact. After exposure, the resulting step heights were characterized using a profilometer (Dektak 150, Veeco). Then, this 3D profiled master mould was silanized with trimethyl fluorosilane (2h) and used for the replica moulding with PDMS.

PDMS devices were created by casting a mixture of Sylgaard TM 184 (Dow Corning) silicone with the curing agent in a proportion of 1:10, poured over the Si/photoresist master mold followed by heat-curing at 80°C for 2 h. After curing, the PDMS was peeled off from the mold, individual devices were cut to appropriate sizes and punched to make access holes. The individual devices were cleaned with acetone and ethanol (70%), and dried with nitrogen. The PDMS replica was bonded to a Ø50mm no1.5 thickness cover glass (Menzel Gläser), using a plasma cleaner for surface activation (Femto model from Diener Electronics; 80 sccm O2, ~80 W RF power for 2 min). The devices were further mounted onto 1 mm high WillCo-dish® (6). Surface modification was performed by pumping dopamine solution (Sigma Aldrich; 0.1%w/v in 10 mM Tris-HCl (pH 8.5) for 45 min (23). After dopamine coating, the surfaces were rinsed twice with Phosphate Buffered Saline (PBS) and stored in PBS. For experiments, all devices were equilibrated for >12 h in growth medium at 37 °C and 5% CO_2.

Figure 1(d) shows the microfluidic device fabricated as described above. The microfluidic device includes 6 inlets and 6 outlets in total, as illustrated in **Figure 1(b, d)**: basically being one inlet and outlet per compartment and one additional side-feeding channel for the gradient-producing compartments.

C. Characterization of free diffusion gradient

Dextran Tetramethylrhodamine biotin (3000MW; 2µM; InvitroGen) was used to visualize diffusion gradients inside the structure, and to determine the experimental real time for the concentration profile to reach a steady state in half of the

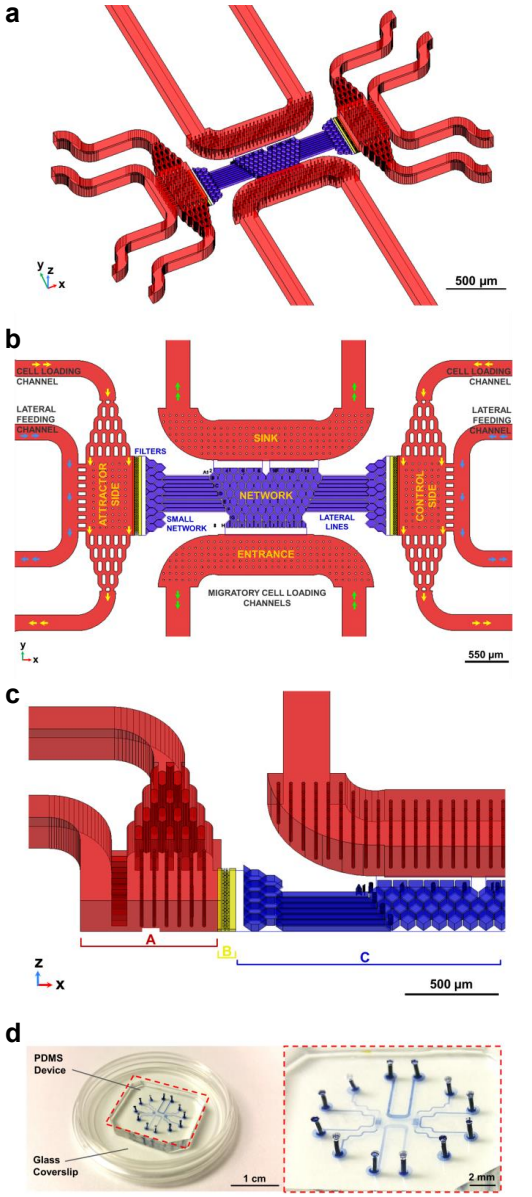

Figure 1| Microfluidic device for immune cell-cell interactions. a) General view in 3D. **b)** Front view: The device is characterized by the feature that entering cells can migrate through a network towards an attractor or control compartment. On the other side of the network there is a sink compartment specular to a migratory compartment. From the major network, lateral straight lines conduct to a smaller network in front of attractor/control compartments. The attractor/control compartments are connected with cell loading channels through a branched structure and with a lateral feeding channel. Arrows indicate the flow direction. **c)** Cross section of the device: profile of A section: attractor (or control) compartment with pillars with height 28 µm; B section: filters with height 2 µm; C section: small network, lateral lines and major network with height 6 µm. **d)** Photographs of the PDMS chip.

structure. The quantitative mass transport was processed and analysed using HeatMap Histogram (ImageJ plugin) (**Figure 2**).

D. Experimental procedures

Loading of chip: The devices were fully submerged in medium to prevent convection. All cells were injected, as 2µL cells at $20x10^6$ cells/ml. BMDCs were pre-stimulated or not with LPS for indicated times before loading onto chip. For antigen presentation experiments, DCs were loaded with 10µg/ml ovalbumin $OVA_{323-339}$ for peptide antigens (Anaspec) for 1h before being mixed at 1:3 ratio with T cell hybridomas MHC-restricted and specific for the peptide. The devices were imaged by a Zeiss LSM 510 inverted confocal microscope equipped with an on-stage incubator with controlled temperature, CO_2 pressure and humidity for long term cell tracking or kept in an incubator and monitored for segmented experiments. The microscope and digital camera were controlled via Carl Zeiss Zen 2009 (Version 6.0 SP2). Time lapse visible and fluorescence images were captured with a 10xobjective and 20×objective. Movies and pictured were analysed using open source software ImageJ and Bitplane Imaris.

E. Scoring

To evaluate the bulk movement of cells, the central network was divided into areas as shown in **Figure 3(a)**, cells inside the network closer to the attractor or control chamber as well as cells in the proximal and distal areas of the attraction or control chamber were counted by microscopy. The tracks of OVA I and OVA II cells were generated and analysed using the plugin Trackmate (ImageJ plugin).

Results and Discussion

The design criteria for the device were: 1) Confine cells and bacteria (representing the inflammatory foci), but allow their molecular products to diffuse through the system to form a dynamic gradient. 2) Connect the inflammatory focus chamber, ie the attractor side, to a reservoir of immune cells to be recruited through microchannels with a cell-sized cross-section. 3) Interconnect the microchannels in a network to avoid hydrostatic forces and historic events affecting single cell movement and allow cells to make choices based on local differences in chemotactic factors. 4) Introduce a second chamber, ie the control side, to better control specific recruitment to inflammatory foci. 5) Introduce a sink to maintain the on-chip produced gradients for a longer time. 6) Introduce side-channels that can be used to add substances during an ongoing experiment without disturbing the cells.

Characterization of free diffusion gradient

In order to understand the progressive distribution of diffusion gradient inside the device, tests were performed with 2µM fluorescent dextran (Rh-Dex 3kDa), which is smaller and with higher diffusion coefficient than typical cytokines produced during inflammation and immune responses (e.g., Mw CCL19 8.8 kDa) (24). To visualize the gradient, the Rh-Dex was loaded very carefully and quickly from the lateral feeding channel of the attractor side in a device fully submerged under PBS to

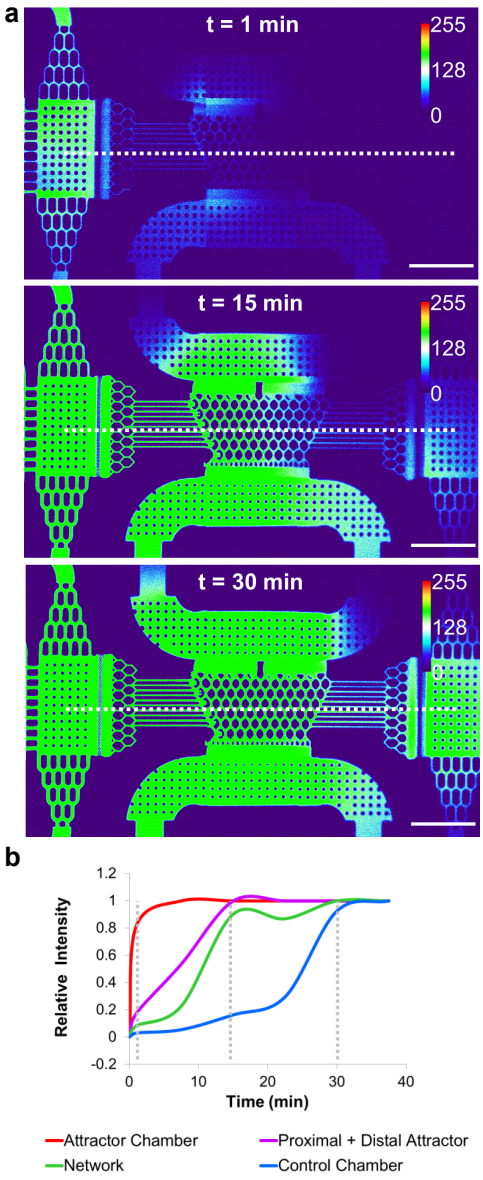

Figure 2| Device calibration using fluorescent dextran dye (DTB): a) Fluorescent images representing the time evolution of the DTB concentration profile across the structure at 1, 15, 30 min after loading in lateral feeding channel of the attractor side. Scale bar: 550 µm. **b)** Experimental time evolution of the relative intensity DTB concentration profile across Attractor Chamber, Proximal+Distal Attractor, Network and Control Chamber in the centre and mid plan of the structure, and with respective evolution of the DTB concentration profile at 1 min, 15 min, 30 min represented in dashed grey line in fluorescent images above. It takes about 15-20 min for the concentration profile to reach a steady state in half of the structure.

avoid convention. Only the lateral feeding channel and attractor chamber were filled with dye, a consequence of the design with narrow filters separating this chamber from the network. The device was imaged for 1h at 1min intervals. After 1 min (**Figure 2(a)**), dextran diffused from the attractor compartment to the proximal part of the network and started to enter the entrance and sink compartments. This confirmed the function of these compartments to maintain a differential unidirectional gradient between attractor and control side when loading. After further 15 min the dextran had reached the entrance and after 30 min the dextran had reached the control chamber. After 60min the device was in equilibrium and would not sustain gradients (not shown). Diffusion of protein in tissue is reported to be around 20-50µm^2/s (25), which is comparable to our observations that dextran travelled to the entrance in minutes. It must be stressed that our device is intended for use with living cells producing the chemotactic gradients continuously and dynamically on-chip, and thus will maintain a gradient over a longer period of time. We next examined the overall bulk performance of the device.

Collective bulk cell behaviour and overall functions

Chemotactic response of BMDCs towards LPSs stimulated BMDCs: We first investigated the migration of immature BMDCs (iBMDC) towards on-chip cell-generated chemokines to establish a timeline of cellular recruitment. LPS-activated BMDCs in the attractor compartment were used to simulate inflammation and to attract iBMDCs. We counted the number of iBMDCs in different areas of the chip as outlined in **Figure 3(a)**. The BMDCs gradually entered the network and migrated further towards the attractor compartment, accumulating in front of the filters, reaching a plateau after around 18-24h (**Figure 3(b)**). The timeline was different in other cell types which we investigated with the device, such as BMDCs and T cells (**Figure 4**). Though the number of cells travelling through the network and migrating to the attractor side varied between the different cell types and experiments, all cell types seemed to follow the same general pattern of reaching a plateau after around 24h. We further compared migration towards inflammation or empty chambers vs control cultures on the same chip (**Figure 3(c)**) and found that BMDCs also moved towards non-activated cultures, but still more towards the activated culture chambers. BMDC are sensitive cells and

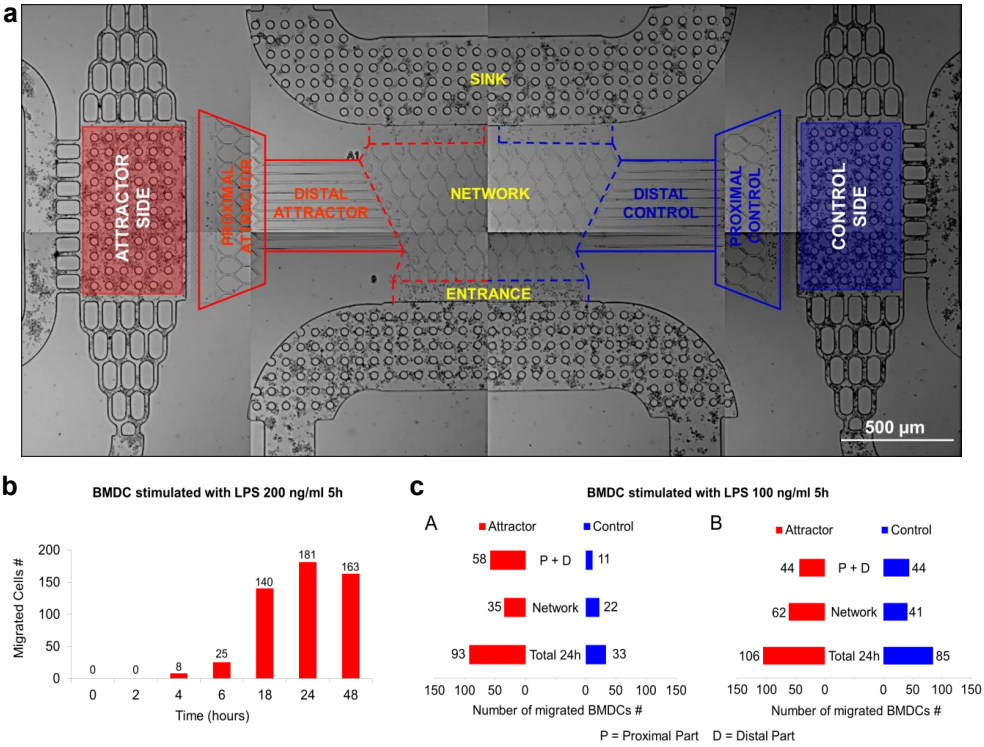

Figure 3| Chemotactic response of immature BMDCs (iBMDCs) towards LPS-stimulated BMDCs. a) Subareas for chemotaxis analysis: cells inside the different areas were counted (attractor area = red; control area = blue). Cell counts were quantified for the proximal (P) and distal (D) areas on the attractor and control side and the network area closer to the attractor or control chamber. **b)** Time-course of the chemotactic response of iBMDCs towards LPS stimulated BMDCs (200 ng/ml 5h) in the attractor compartment. Migration of iBMDCs entering the network quantified towards the attractor side from 0 - 48h after loading (P+D). **c)** Analysis of iBDMCs migration in different subareas of the device after 24h. Activated BMDC (100 ng/ml LPS 5h) were loaded inside the attractor chamber. A) empty control chamber or B) loading of non-activated BMDCS into the control chamber.

are easily triggered also by standard handling and we cannot rule out that the control cells had been partially activated.

Chemotactic response of CD8$^+$ T cells towards LPS stimulated BMDCs:

We further investigated the bulk migration of CD8+ T cells towards dendritic cells stimulated with LPS. CD8+ T cells are characterized by a high degree of motility towards target cells and inflammatory areas during immune responses. **Figure 4(a)** shows that recruitment of CD8+ T cells reaches a maximum of 244 recruited cells after 48h. At later time points (72-96h) we observed that cells started migrating away from the attractor chamber, suggesting that the gradient was no longer efficiently produced or that cells had been de-sensitized from long-term stimulation.

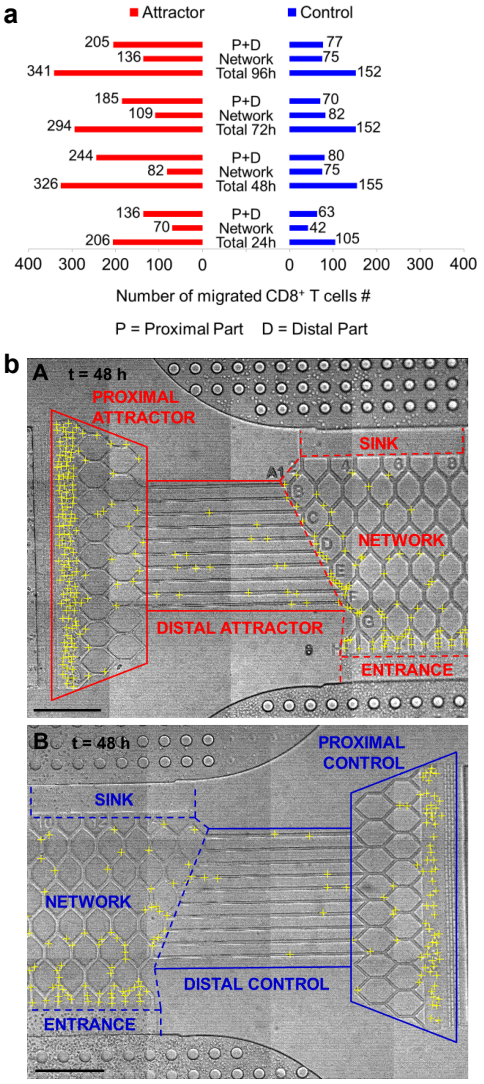

Figure 4| Chemotactic response of CD8$^+$ T cells towards LPS stimulated BMDCs: a) Chemotactic response and distribution of CD8$^+$ OVAI T cells over time towards LPS stimulated BMDCs (100 ng/ml LPS 5h) inside the attractor chamber and the control chamber (no cells). **b)** Chemotactic distribution of CD8$^+$ T cells in different areas of the device 48h after loading. Scale bar: **b)** 250 µm.

Lymph node mimicking

In the lymph node, a network of fibroblast reticular cells FRCs act as attachment scaffold for pro-inflammatory antigen-carrying dendritic cells arriving from sites of infection and inflammation. Here they continuously produce chemokines to attract more DCs, T cells and B cells from blood and lymph. We finally demonstrated that a co-culture of FRCs and DCs at ratio 1:3 in the presence of heat-killed *E. coli* bioparticles as pro-inflammatory stimulus efficiently recruited immature dendritic cells (**Figure 5**). Migration kinetics was similar to those observed with the other cell types in this work.

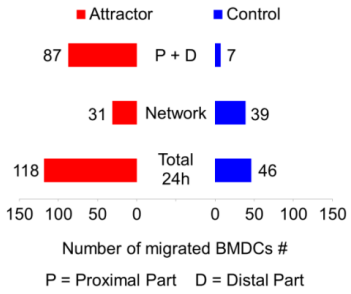

Figure 5| Chemotactic response of iBMDCs towards FRCs + BMDCs stimulated with *E. coli*. Lymph node inflammatory conditions were modelled with FRCs+ iBMDCs + *E. coli* inside the attractor chamber, the control chamber was empty. Chemotactic response of total number of iBMDC migration in different subareas of the device was quantified 24 hours after loading.

Individual cell behaviour and decision-making

Having established proof-of-principle for the bulk movement of cells in the device, we turned to observing individual cell behaviour. We were particularly interested in how cells probed the surroundings at intersections and what they did when encountering other cells. We followed for several hours both BMDCs, OVAI and OVAII T cells as they moved along microchannels as elongated cells and extended fast-moving protrusions at the leading edge, like they were sampling the surroundings. We observed that almost all the cells paused at junctions, often for several minutes to probe both alternative pathways several times before making a decision towards one opening (**Supplementary Video 1**). Cells often did not chose to move towards the gradient in all junctions, sometimes retraced their path before again moving forward, and seemed to probe the entire network (Figure 6 and **Supplementary Video 2**), even as the net effect was bulk movement towards the inflammation. Cell speed was highly variable and within

our 2-4h timeframes of video monitoring, cells also displayed a highly variable travel distance, with a mean speed of 9µm/min (half a cell length) traveling almost half a millimetre per hour. Cells seemed compelled to move around and most cells did not pause. All the motile cells we tested had the ability to quickly switch direction if they encountered other cells blocking the channels. This phenomenon we assume to be of mechanical origin and our device seems very well suited to interrogate the molecular mechanisms involved of the mechanoregulated interaction between mobile cells. Most T cells showed little interaction with other T cells, irrespective of type, and when cells met in the channels they moved independently, sometimes one or both cells switched direction, whereas other times cells simply squeezed past each other. Even though sometimes cells moved together after an encounter (**Supplementary Video 3**) there did not seem to be interrelated behaviour, such as travelling the same path their formation of cell-trains.

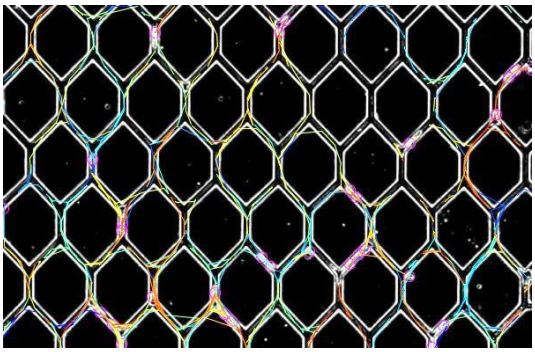

Figure 6| Tracks of OVAI and OVAII cells loaded onto the same chips from Supplementary video 2. The tracks represent 4h of movement and were generated using the plugin Trackmate embedded in ImageJ.

Conclusion

We have designed, fabricated and tested a multi-compartment device microchannel network enabling close real-time observations and bulk-effect interrogations of the decision making process of several cell types belonging to the immune system. We found cells to move actively and freely around the network, preferentially towards the inflammatory foci. We believe our system has promise towards understanding the individual cell decision-making leading to collective behaviour in the immune system and can be used to compare different systemic or genetic contributions to immune system effects and defects and as a model system for tissue repair.

Acknowledgement

The Research Council of Norway is acknowledged for the support to the Norwegian Micro- and Nano-Fabrication Facility, NorFab, project number 245963/F50. Microfabrication process was performed at the NTNU NanoLab (NorFab), Norwegian University of Science and Technology (NTNU).

Experiments were performed at the Cellular and Molecular Imaging Core Facility (CMIC), Norwegian University of Science and Technology (NTNU). CMIC is funded by the Faculty of Medicine at NTNU and Central Norway Regional Health Authority.

References

1. Trepat X, Chen Z, Jacobson K. Cell migration. Comprehensive Physiology. 2012;2(4):2369-92.
2. Girard JP, Moussion C, Forster R. HEVs, lymphatics and homeostatic immune cell trafficking in lymph nodes. Nature reviews Immunology. 2012;12(11):762-73.
3. Mirsky HP, Miller MJ, Linderman JJ, Kirschner DE. Systems biology approaches for understanding cellular mechanisms of immunity in lymph nodes during infection. Journal of theoretical biology. 2011;287:160-70.
4. Cahalan MD, Parker I, Wei SH, Miller MJ. Real-time imaging of lymphocytes in vivo. Current opinion in immunology. 2003;15(4):372-7.
5. Lin B, Levchenko A. Spatial manipulation with microfluidics. Frontiers in bioengineering and biotechnology. 2015;3:39.
6. Moura Rosa P, Gopalakrishnan N, Ibrahim H, Haug M, Halaas O. The intercell dynamics of T cells and dendritic cells in a lymph node-on-a-chip flow device. Lab on a chip. 2016;16(19):3728-40.
7. Mrass P, Petravic J, Davenport MP, Weninger W. Cell-autonomous and environmental contributions to the interstitial migration of T cells. Seminars in immunopathology. 2010;32(3):257-74.
8. Lammermann T, Germain RN. The multiple faces of leukocyte interstitial migration. Seminars in immunopathology. 2014;36(2):227-51.
9. Kedrin D, van Rheenen J, Hernandez L, Condeelis J, Segall JE. Cell motility and cytoskeletal regulation in invasion and metastasis. Journal of mammary gland biology and neoplasia. 2007;12(2-3):143-52.
10. Miller MJ, Wei SH, Parker I, Cahalan MD. Two-photon imaging of lymphocyte motility and antigen response in intact lymph node. Science. 2002;296(5574):1869-73.
11. Somaweera H, Ibraguimov A, Pappas D. A review of chemical gradient systems for cell analysis. Analytica chimica acta. 2016;907:7-17.
12. Zicha D, Dunn GA, Brown AF. A new direct-viewing chemotaxis chamber. Journal of cell science. 1991;99 (Pt 4):769-75.
13. Zigmond SH. Ability of polymorphonuclear leukocytes to orient in gradients of chemotactic factors. The Journal of cell biology. 1977;75(2 Pt 1):606-16.
14. Muinonen-Martin AJ, Veltman DM, Kalna G, Insall RH. An improved chamber for direct visualisation of chemotaxis. PloS one. 2010;5(12):e15309.
15. Gopalakrishnan N, Hannam R, Casoni GP, Barriet D, Ribe JM, Haug M, et al. Infection and immunity on a chip: a compartmentalised microfluidic platform to monitor immune cell behaviour in real time. Lab on a chip. 2015;15(6):1481-7.
16. Soon L, Mouneimne G, Segall J, Wyckoff J, Condeelis J. Description and characterization of a chamber for viewing and quantifying cancer cell chemotaxis. Cell motility and the cytoskeleton. 2005;62(1):27-34.
17. Servant G, Weiner OD, Neptune ER, Sedat JW, Bourne HR. Dynamics of a chemoattractant receptor in living neutrophils during chemotaxis. Molecular biology of the cell. 1999;10(4):1163-78.
18. Wu J, Wu X, Lin F. Recent developments in microfluidics-based chemotaxis studies. Lab on a chip. 2013;13(13):2484-99.
19. Tong Z, Balzer EM, Dallas MR, Hung WC, Stebe KJ, Konstantopoulos K. Chemotaxis of cell populations through

confined spaces at single-cell resolution. PloS one. 2012;7(1):e29211.
20. Ricart BG, John B, Lee D, Hunter CA, Hammer DA. Dendritic cells distinguish individual chemokine signals through CCR7 and CXCR4. Journal of immunology. 2011;186(1):53-61.
21. Haessler U, Pisano M, Wu M, Swartz MA. Dendritic cell chemotaxis in 3D under defined chemokine gradients reveals differential response to ligands CCL21 and CCL19. Proceedings of the National Academy of Sciences of the United States of America. 2011;108(14):5614-9.
22. McDonald JC, Duffy DC, Anderson JR, Chiu DT, Wu H, Schueller OJ, et al. Fabrication of microfluidic systems in poly(dimethylsiloxane). Electrophoresis. 2000;21(1):27-40.
23. Chuah YJ, Koh YT, Lim K, Menon NV, Wu Y, Kang Y. Simple surface engineering of polydimethylsiloxane with polydopamine for stabilized mesenchymal stem cell adhesion and multipotency. Scientific reports. 2015;5:18162.
24. Haessler U, Kalinin Y, Swartz MA, Wu M. An agarose-based microfluidic platform with a gradient buffer for 3D chemotaxis studies. Biomedical microdevices. 2009;11(4):827-35.
25. Sniekers YH, van Donkelaar CC. Determining diffusion coefficients in inhomogeneous tissues using fluorescence recovery after photobleaching. Biophysical journal. 2005;89(2):1302-7.

Figures

Immune cells moving in a microchannel network in search of targets

Patrícia Moura Rosa,[a,c] Nimi Gopalakrishnan,[a,c] Giovanna Perinetti Casoni,[a] Rosanne van de Wijdeven,[a,c] Markus Haug[b] and Øyvind Halaas*[a]

[a]Department of Cancer Research and Molecular Medicine, Norwegian University of Science and Technology, 7489 Trondheim, Norway

[b]Centre of Molecular Inflammation Research (SFF-CEMIR), Department of Cancer Research and Molecular Medicine, Norwegian University of Science and Technology, 7489 Trondheim, Norway

[c]NTNU NanoLab, Norwegian University of Science and Technology, 7489 Trondheim, Norway

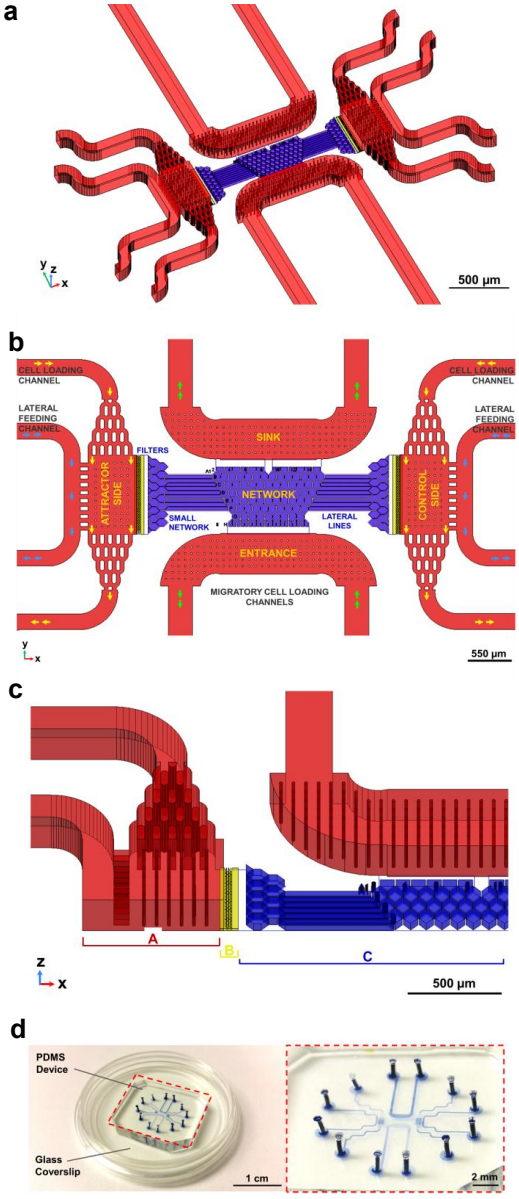

Figure 1| Microfluidic device for immune cell-cell interactions. a) General view in 3D. **b)** Front view: The device is characterized by the feature that entering cells can migrate through a network towards an attractor or control compartment. On the other side of the network there is a sink compartment specular to a migratory compartment. From the major network, lateral straight lines conduct to a smaller network in front of attractor/control compartments. The attractor/control compartments are connected with cell loading channels through a branched structure and with a lateral feeding channel. Arrows indicate the flow direction. **c)** Cross section of the device: profile of A section: attractor (or control) compartment with pillars with height 28 µm; B section: filters with height 2 µm; C section: small network, lateral lines and major network with height 6 µm. **d)** Photographs of the PDMS chip.

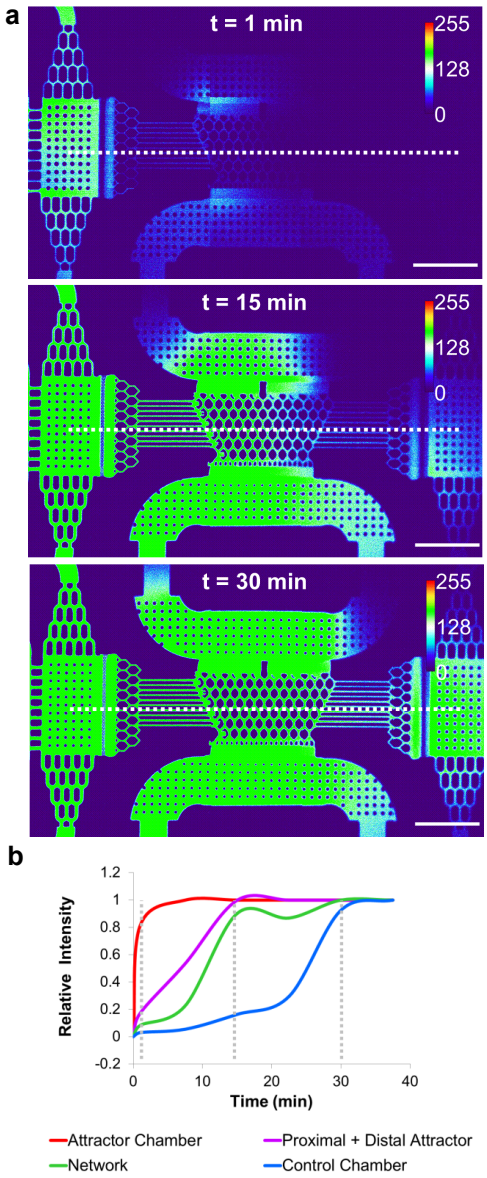

Figure 2| Device calibration using fluorescent dextran dye (DTB): a) Fluorescent images representing the time evolution of the DTB concentration profile across the structure at 1, 15, 30 min after loading in lateral feeding channel of the attractor side. Scale bar: 550 µm. **b)** Experimental time evolution of the relative intensity DTB concentration profile across Attractor Chamber, Proximal+Distal Attractor, Network and Control Chamber in the centre and mid plan of the structure, and with respective evolution of the DTB concentration profile at 1 min, 15 min, 30 min represented in dashed grey line in fluorescent images above. It takes about 15-20 min for the concentration profile to reach a steady state in half of the structure.

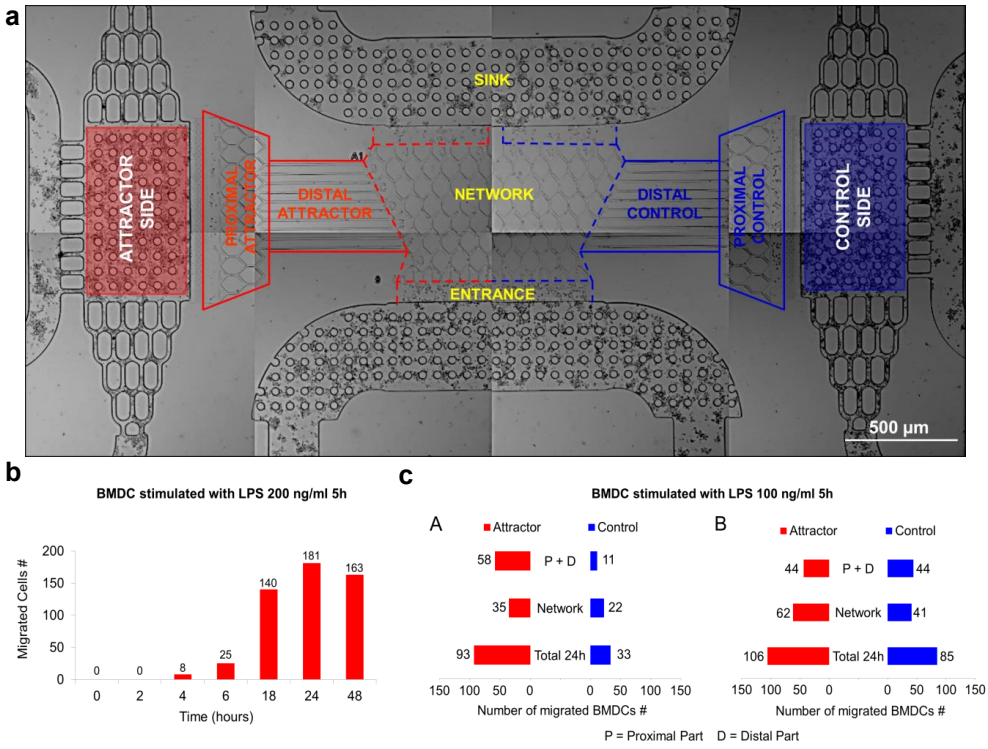

Figure 3| Chemotactic response of immature BMDCs (iBMDCs) towards LPS-stimulated BMDCs. a) Subareas for chemotaxis analysis: cells inside the different areas were counted (attractor area = red; control area = blue). Cell counts were quantified for the proximal (P) and distal (D) areas on the attractor and control side and the network area closer to the attractor or control chamber. **b)** Time-course of the chemotactic response of iBMDCs towards LPS stimulated BMDCs (200 ng/ml 5h) in the attractor compartment. Migration of iBMDCs entering the network quantified towards the attractor side from 0 - 48h after loading (P+D). **c)** Analysis of iBDMCs migration in different subareas of the device after 24h. Activated BMDC (100 ng/ml LPS 5h) were loaded inside the attractor chamber. A) empty control chamber or B) loading of non-activated BMDCS into the control chamber.

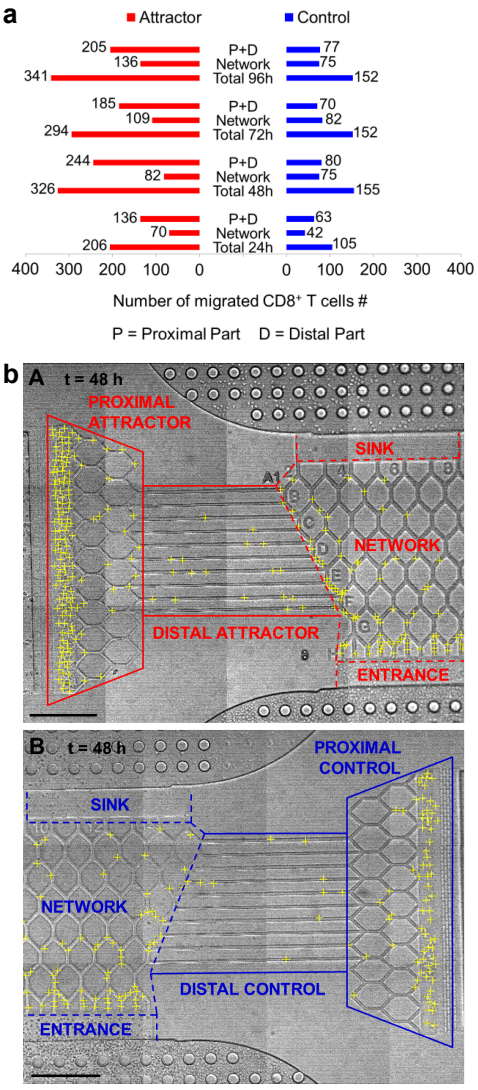

Figure 4| Chemotactic response of CD8$^+$ T cells towards LPS stimulated BMDCs: a) Chemotactic response and distribution of CD8$^+$ OVAI T cells over time towards LPS stimulated BMDCs (100 ng/ml LPS 5h) inside the attractor chamber and the control chamber (no cells). **b)** Chemotactic distribution of CD8$^+$ T cells in different areas of the device 48h after loading. Scale bar: **b)** 250 µm.

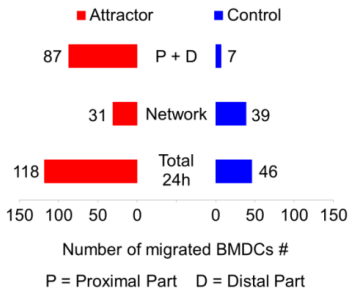

Figure 5| Chemotactic response of iBMDCs towards FRCs + BMDCs stimulated with *E. coli*. Lymph node inflammatory conditions were modelled with FRCs+ iBMDCs + *E. coli* inside the attractor chamber, the control chamber was empty. Chemotactic response of total number of iBMDC migration in different subareas of the device was quantified 24 hours after loading.

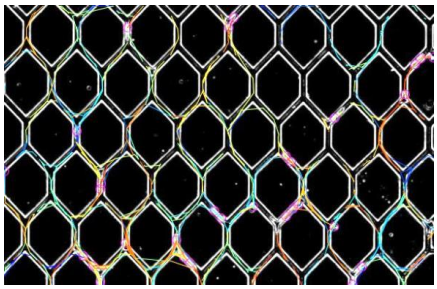

Figure 6| Tracks of OVAI and OVAII cells loaded onto the same chips from Supplementary video 2. The tracks represent 4h of movement and were generated using the plugin Trackmate embedded in ImageJ.

Supplemental Data

Immune cells moving in a microchannel network in search of targets

Patrícia Moura Rosa,[a,c] Nimi Gopalakrishnan,[a,c] Giovanna Perinetti Casoni,[a] Rosanne van de Wijdeven,[a,c] Markus Haug[b] and Øyvind Halaas*[a]

[a]Department of Cancer Research and Molecular Medicine, Norwegian University of Science and Technology, 7489 Trondheim, Norway

[b]Centre of Molecular Inflammation Research (SFF-CEMIR), Department of Cancer Research and Molecular Medicine, Norwegian University of Science and Technology, 7489 Trondheim, Norway

[c]NTNU NanoLab, Norwegian University of Science and Technology, 7489 Trondheim, Norway

Supplementary Video 1| Movement of OVAII cells 48h after seeding on chip. Video is a time lapse compilation of pictures taken every 3min for 2h.

Supplementary Video 2| Movement of OVAI and OVAII T-cells 6h after seeding on chip. Video is a time lapse compilation of pictures taken every 3minutes for 4h.

Supplementary Video 3| Interaction between OVAI/CD8 (fluorescent) and OVAII/CD4 T (not fluorescent) cells loaded on the same chip. Video is a time lapse compilation of pictures taken every 3minutes for 3.5h.

Paper III

Journal Name

ARTICLE

Lymph node-on-a-chip: mimicking the microphysiology of the T cell zone

Received 00th January 20xx,
Accepted 00th January 20xx

DOI: 10.1039/x0xx00000x

www.rsc.org/

Patrícia Moura Rosa,[a,c] Cecilie Lund,[a] Markus Haug[b] and Øyvind Halaas*[a]

Both natural and vaccine-promoted immunity towards cancers and infectious diseases are dependent on lymph node (LN) activity. LN are scattered around the body and act as meeting points for antigen, antigen-presenting cells and lymphocytes, resulting in specific immunity. The LN function is therefore of central importance in modern immunotherapy. The detailed study of cellular interactions within the LN has been limited by difficult *in vivo* tools or over-simplified *in vitro* tools. To overcome this limitation, we propose a microfluidic cell chamber that mimics the microphysiological environment of the T cell zone of LN, opening new horizons for the investigation and exploitation of T cell education.

Our microfluidic LN device was designed to immobilize activated DCs on a supporting fibroblast reticular cell (FRC) scaffold allowing T cells to be perfused, thus providing both a permissive microenvironment and mechanical cues necessary for T cell priming. The general performance of the device was assessed. First, the perfusion rate (shear stress) was fine tuned to guarantee a fully developed and stable FRC scaffold inside the microfluidic device. This was obtained by continuous perfusion for 48h at 100nl min^{-1} with a corresponding maximum fluid velocity, 300-900µm min^{-1} and range of shear stress, 0.001 to 0.004 Dyn cm^{-2}. Second, two intermediate system testing with 2 types of cells was performed: (i) analysis of dentritic cells (DCs) adherence and motility on a FRC scaffold when submitted to successive increment of flow rates (50nl min^{-1} to 500nl min^{-1}); and, (ii) the analysis of natural attachment of T cell flowing over a FRC scaffold. Both DCs and T cells adhered to the FRC scaffold and were motile on the scaffold with a mean velocity of ~10µm min^{-1}. Finally, the system was characterized with the three main cell types present in the T cell zone of a LN (T cell, DC and FRC) and compared to reported *in vivo* results. A study without and with cognate interactions using LPS+OVAII peptide activation was performed in order to analyse the natural attachment of DCs and T cells in sucessive increment of flow rate (100 to 300nl min^{-1}), mimicking immediate response to inflammation. These results evidenced that without cognate interactions, T cells and DC shown motiliy with ~5µm min^{-1}, random movements and interactions during 3 min as an intrinsic rhythmicity program of "stop and go". And with cognate interactions, it was visible a significant decrease of DC and T cell velocity to ~2.5µm min^{-1}, where T cells moved in characteristis looping patterns making serial contacts with the same or with neighbouring DCs, with interval of interactions around ~7min. The analysis of DC and T cell motility, interaction time and trajectories analysis indicated that our microfluidic device at least partially mimicks the T cell zone of LN being a LN-on-a-chip and opening new opportunities both in research and as a clinical development tool.

Introduction

Immunity is a complex process in the body's response to injuries or infections, involving an orchestra of many cells, organs and functions over space and time. The central organs in adaptive immune cell education are the lymph nodes (LN). LN are scattered around in the body acting as meeting points between a large number of circulating lymphocytes passing over and interacting with a few antigen-bearing dendritic cells immobilized on the stromal cell reticular network inside the LN. The LNs are very dynamic organs, increasing significantly their volume during infection and quickly regress at the end of inflammation. The LN architecture is composed of and controlled by different stromal cell types such as fibroblastic reticular cells (FRCs), follicular dendritic cells (FDCs), marginal reticular cells (MRCs), vascular endothelial cells of the high endothelial venules (HEV), and lymph node medullary fibroblast (MLF), providing an appropriate cellular scaffold for immune cell homing, adhesion, migration, interaction and segregation (1-3). The LN educates both B cells and T cells albeit in in different zones inside the LN, B cells in the cortex and T cells in the paracortex, or T cell zone. The antigen specific T cells are the major cellular force in the defence against infectious diseases and cancers. The priming, or initial education, of naïve T cells occurs in the T cell zone in lymph nodes (LN). (4-8). (8-10). In the T cell zone, the stromal scaffold is largely composed of reticular fibres, fibrous extracellular matrix and FRCs supporting the fibrous conduits. A remarkable contrast to the fibroblasts in most other connective tissue, where cells are embedded in the ECM, FRCs in the LN grow

[a] Department of Clinical and Molecular Medicine, Norwegian University of Science and Technology, 7489 Trondheim, Norway. E-mail: oyvind.halaas@ntnu.no
[b] Centre of Molecular Inflammation Research (SFF-CEMIR), Department of Clinical and Molecular Medicine, Norwegian University of Science and Technology, 7489 Trondheim, Norway
[c] NTNU Nanolab, Norwegian University of Science and Technology, 7489 Trondheim, Norway

Electronic Supplementary Information (ESI) available: [details of any supplementary information available should be included here]. See DOI: 10.1039/x0xx00000x

around/enwrap the thin strands of ECM, promoting their direct and continuous contact with immune cells passing through. In addition the stroma has a central role in immune-modulation affecting the stimulation, suppression or survival of T cells (2, 11-16).

During a response to a peripheral inflammatory signal, tissue-resident dendritic cells (DC) sample the microenvironments and upon activation, enter the blood and lymphatic vessels, and migrate into the lymph nodes to present their MHC-bound peptide antigens to naïve and memory T cells passing through the T cell zone. The T cells are recruited both from lymph and from blood through the HEV. The adaptive immune response is then initiated by the cognate physical interactions between naïve T cells and antigen-presenting cells (APC) residing in paracortex, resulting in activation and proliferation of antigen specific T cells. (6). These primed/activated T cells are thereafter drained by efferent lymphatic vessels, thus entering lymph and blood circulatory system before finally migrating directionally to the peripheral inflammatory foci to fight the pathogens or cancer cells (6, 7, 17). All progress towards reconstruction of the LN function could therefore be of major importance in cellular immunotherapeutic research and development.

LN function has been studied both *in vivo* and *in vitro*. *In vivo* several studies have been conducted using intravital multiphoton microscopy or dissection of LNs in animal models and humans, providing important insights into the cellular interactivity necessary for T cell priming (6, 18, 19). However, these techniques have some limitations in both relevance to human subjects, as well as technical limitations such as imaging access, control of environmental conditions, maintenance of tissue cohesiveness and organization, and long term experiments (6, 9, 20-23). Also traditional *in vitro* static 2D or 3D cell cultures are limited in physiological relevance related to architecture, microenvironment, tissue dynamics, mechanical forces and cell perfusivity which are important for successful T cell:DC interactions (9, 20, 23, 24). Thus, we still lack comprehensive understanding of the integral multicellular behavior necessary for efficient T cell priming. Most likely both a dynamic multicellular physiology, biomechanical forces and biochemical cues are needed to drive and regulate the cell activation. These factors can be integrated and facilitated in microphysiological model systems.

Recent developments in microfabrication and microfluidics technologies have provided exciting new tools to create advanced cell culture. Microfluidics represent a highly relevant compromise between the *in vivo* perfused organization of tissues and *in vitro* platforms allowing precise control of the cellular, biophysical and biochemical stimuli resulting in organ-on-a-chip platforms with a remarkable potential for drug screening, and as a platform for basic and translational cancer and autoimmune research (20, 23, 25). Moreover, these devices can eventually be coupled with on-chip technologies for cell handling and bioanalysis, adding unforeseen possibilities. In relation to cellular immunology, microfluidics has been used to study chemotaxis, cell: cell interaction and perform accurate measurements in the cell activation process (26-29). At a tissue-cell level, some studies have been developed in order to recreate a complex immunological structures on-chip (3, 30-32), migration and leukocyte extravasation in 3D environment (33) and to mimic lymphatic drainage (34, 35). We thus found it timely to seize the opportunity to approach a recreation of a LN in vitro, LN-on-a-chip, with the long-term aim of achieving *in vitro* immunization.

Our approach was to engineer a system aimed to mimic the T cell zone of a LN, by allowing FRC adhere to a perfusable scaffold where DCs and T cells can be perfused. Our previous study (30) indicated that such a device should allow growth in 3D to ensure better contact with adherent stationary cells and the perfused cells. Our device allows long term experiment (2-7 days) in continuous flows in a transparent device making it possible to monitor in real-time the dynamic interaction of T cells with dendritic cells immobilized in a 3D FRC network. We stepwise studied the formation of the 3D FRC network, the interaction of DCs and T cells with the FRC, and finally the antigen specific and unspecific interaction of T cells with DCs and FRC. This study demonstrates that this microfluidic cell chamber can be a valuable tool for investigating T cell:DC:FRC interaction, related to cell signalling and activation, illustrating the high potential to immunological R&D.

Materials and Methods

A. Animals

C57BL/6 wild type mice were housed in the Comparative Medicine core facility, Faculty of Medicine and Health Sciences NTNU, and manipulated in accordance with the local Ethical Committee guidelines.

B. Cells

LN FRCs: Peripheral LNs (inguinal and axillary) were pooled from an adult male mouse (C57BL/6). The lymph nodes were digested in an enzyme mix of DNaseI (Invitrogen) and Collagenase, and collected cells were cultured in RPMI 1640 supplemented with 25mM HEPES (Sigma-Aldrich) 50U ml^{-1} penicillin, 50µg ml^{-1} streptomycin, 2mM L-glutamine, 8% Fetal calf serum (FCS) and 50µM 2-Mercaptoethanol (ME) (Sigma-Aldrich) at 37°C, 5% CO_2. Non-adherent cells were removed after 24h and the adherent cells were cultured for several weeks. After 3-4 months of outgrowth the cell population was confirmed CD31-/PDPN+ by flow cytometry (data not shown).

DCs: The eGFP+ murine dendritic cell line "MutuDC 1940" (36) was kindly provided by Hans Acha-Orbea, University of Lausanne. These cells were cultured in IMDM plus 25mM HEPES (Gibco) supplemented with 50U ml^{-1} penicillin, 50µg ml^{-1} streptomycin, 2mM L-glutamine, 8% FCS and 50µM 2-ME (Sigma-Aldrich) at 37°C, 5% CO_2.

T cells: Non-adherent ovalbumin specific MHC class II restricted CD4+ T cell hybridomas (MF2.2D9), were a gift from Dr Kenneth Rock, University of Massachusetts, Worcester. These cells were maintained using the same culture medium and conditions as described for FRCs.

C. Ovalbumin treatment

Ovalbumin (A7641 Sigma-Aldrich) was dissolved in phosphate-buffered saline (PBS) to 10mg ml^{-1} and stored at -20°C. Adherent DCs were treated with Ovalbumin (10μg ml^{-1}) in combination with LPS (100 ng ml^{-1}) for 4-5h prior to experiment.

D. Design and fabrication of a microfluidic system

The microdevice was fabricated in polydimelthylsiloxane (PDMS) by rapid prototyping soft lithography with SU 8 photoresist masters, according to published procedures (37) and using the standard photolithography techniques and facilities at NTNU NanoLab.

The microfluidic device was designed using AutoCAD 2017 drawing software (Autodesk Inc., Europe), the photomasks were purchased from Compugraphics Ltd. (Jena Germany), as a soda lime photolithography mask (4'' x4'' x0.060'') coated with a thin chrome metal layer. The master for the microfluidic device was fabricated using a two-layer SU-8 process.

A 5μm-thin layer of photoresist (SU-8 5, MicroChem) was used as an adhesion layer, it was spun at 6000rpm for 30s over a 2 inch Si wafer and then, the wafer was fully exposed to ultraviolet light (UV light). 30min after the post-exposure baking (1min at 65°C + 1min at 95°C), the second layer of photoresist (SU-8 3050, MicroChem) was spun at 1000 rpm for 60s to yield feature heights of 100μm. The wafer was exposed to UV light through the mask to generate the microchamber patterns. After post-exposure baking (1min at 65°C + 5min at 95°C) and development, the master mold was characterized using a profilometer (Dektak 150, Veeco). And subsequently, the 3D profiled master mould was silanized with trimethyl fluorosilane (2h) and used for the replica moulding with PDMS. PDMS devices were produced by casting a mixture of Sylgaard TM 184 (Dow Corning) silicone with the curing agent in a proportion of 1:10, poured over the Si/photoresist master mould followed by heat-curing at 80°C for 2h. After curing, the PDMS was peeled off from the mould, and individual devices were cut to appropriate size (2cmx2cm). A needle (INSTECHLABS, US) with a blunt tip was used to drill the fluid connection access holes.

The individual devices were cleaned with acetone and ethanol (70%) and dried with nitrogen. The PDMS replica was irreversibly sealed to a Ø50mm no1.5 thickness sterilized cover glass (Menzel Gläser), using a plasma cleaner for surface activation (Femto model from Diener Electronics; 80 sccm O2, ~80 W RF power for 2min). Afterwards, the devices were further mounted onto 1mm high WillCo-dish® (30). Surface modification was performed by direct injection micropipetting of dopamine solution (Sigma Aldrich); 0.1%w/v in 10mM Tris-HCl (pH 8.5) for 45min (38). For experiments, all devices were equilibrated for >12 h in growth medium at 37°C and 5% CO_2. Before cell loadings, all devices were washed 3 times with PBS, loaded and covered with culture medium, and incubated at 37 °C and 5% CO_2 for 2h.

Figure 1A shows a photograph of the microfluidic cell chamber fabricated as described above. **Figure 1(B-E)** represent several constituent parts of the microfluidic microchamber from the top view. The device is characterized by two thin microchannel inlets with a cross section area of 200μmx100μm, a main circular cell chamber with total diameter of 4mm – including an external filter ring and an internal cell chamber with a diameter of 3mm completely filled with rounded pillars and internal filters – and two large microchannels as outlets with cross section area 1000μmx100μm.

The composition of inner cell chamber is defined from the inlets by two independent systems of 11 protuberances including juxtaposed rectangular pillars (20μm x 40μm) with thin interval between the rectangular pillars of 20μm; the core of cell chamber is scattered with circular pillars (with diameter of 25μm and 50μm, and spaced by 100μm), and the external perimeter of the cell chamber composed by two levels of cell retention filters to aid in cell loading and scaffold stability. The 1st level of filters (or internal filters) are characterized by thin juxtaposed rectangular pillars in 2 or 4 concentric circular lines of filters (10 set in total); composed by individual rectangular pillars with dimensions from 100μm x 200μm (as maximum) to 40μm x 20μm (as minimum) with interval between pillars of 50μm and 20μm, respectively. The 2nd level of filters (or external filter) is characterized by a large single circular line around the inner cell chamber (composed by individual rectangular pillars of 150μmx50μm with 50μm of interval between them).

Figure 1| Lymph node on-a-chip. A) Photograph of the PDMS biochip bonded to a glass substrate. Inlets, cell chamber and outlets are in red. Scale bar: 1cm. **B)** Top view of whole biochip: The device is characterized by two thin inlets with a cross section area of 200μmx100μm, a main circular cell chamber with an outer diameter of 4mm and two large outlets with a cross section area of 1000μmx100μm. Scale bar: 1500μm **C)** Top view of the circular cell chamber: The cell chamber is composed from the inlets with two independent systems of 11 protuberances with juxtaposed rectangular pillars (20μmx40μm) with interval between pillars of 20μm; the inner of the chamber (with inner diameter of 3mm without filters) is completely supported by round pillars with 25μm and 50μm of diameter and spaced between them of 100μm; and the outer perimeter of the cell chamber composed by two levels of filters. Scale bar: 1000μm. **D)** Top view and disposition of 11 protuberances at the entry of cell chamber. Scale bar: 200μm. **E)** Top view of 2 types of filters: 1st level of filters with thin juxtaposed rectangular pillars in 4 concentric circular lines of filters (10 sets in all chamber; composed by individual pillars from 100μmx20μm (as maximum) to 40μmx20μm (as minimum) with interval between pillars respectively, 50μm and 20μm); 2nd level of filters with a large single circular line around the cell chamber (composed by individual pillars 150μmx50μm with interval between pillars of 50μm). Scale bar: 200μm. **F)** 3D cross section of the PDMS device with the same thickness in all pillars with 100μm. Scale bar: 400μm. **G&H)** Overlaid phase contrast and fluorescence image and only fluorescence image showing the rearrangement of FRC scaffold (stained in red and developed during 48h before the beginning of experiment), with trapped DC (green) and T cells (blue) interacting with each other. Scale bar: 1mm.

E. Simulation of velocity profile

COMSOL Multiphysics 4.4 software was used to simulate the velocity profile in the microfluidic structure used in this study

(**Figure 2**). This finite elements simulation solved the Navier–Stokes equation (assuming non-slipping walls) to calculate the velocity profile inside the cell chamber at XY plan at Z axis of 50µm (corresponding to the XY plane with maximum velocities achieved with parabolic velocity profile). Different flow rates, ranging from 50nL min^{-1} to 500nL min^{-1}, were applied at the inlet, and atmospheric pressure (1.01×10^6Dyn cm^{-2}) was imposed at the outlet.

In order to determine the maximum range of velocity for different flow rates, we have determined directly the ranges of shear stress at 5µm from a boundary, roughly corresponding to the expected position of a cell to a surface, modeled as a wall where the no-slip condition dictates that the velocity of the fluid at the boundary is zero. To determine the successive ranges of maximum velocities achieved at Z=50µm for different flow rates, from the Stokes equation and assuming the Poiseuille flow (39), we can solve the linear differential equation obtaining an expression of velocity in function of maximum velocity (1.1),

$$v_h = v_{max}\left(1-\left(\frac{h}{\left(\frac{H}{2}\right)}\right)^2\right) \quad (1.1)$$

where H is the height of the cell chamber, and h the Z position of DC or T cell on the glass or on the FRC network (where h=0 corresponds to the centre of the channel Z=50 µm). Then assuming as a constant the dynamic viscosity along the channel, the range of shear stress at Z=5µm from the wall can be calculated as function of the velocity derivate (1.1),

$$\tau(h) = \mu\frac{\partial v_h}{\partial h} = -\frac{2v_{max}h}{H^2}\mu \quad (1.2)$$

where τ is the shear stress in Dyn cm^{-2}, μ is the dynamic viscosity in Dyn s cm^{-2} (for cell medium at 37°C, 0.78×10^{-2} Dyn s cm^{-2} (40)), v is the velocity of the fluid along the boundary in cm s^{-1}, and h is height above the boundary in cm.

F. Antigen-presentation assays, cell staining, device's loading procedure and microfluidic setup:

Dendritic cells: *FRC+DC experiments:* Adherent DCs were matured (mDC) by preincubation with 100ng ml^{-1} LPS overnight before experiments.

FRC+DC+Tcell experiments: Adherent DCs were activated by preincubation with 10µg ml^{-1} Ovalbumin and 100ng ml^{-1} LPS for 4h before experiments.

Staining Cells: FRCs in suspension were stained in 0.5x solution CytoPainter Cell proliferation Staining Reagent - Deep Red Fluorescence ab176736 (Abcam) for 20min according to protocols. T cells in suspension were stained in 0.5x solution CytoPainter Live Cell Labelling Kit- Blue Fluorescence ab187966 (Abcam) for 45min according to protocols.

Microfluidic setup:

The cells were imaged using a Zeiss LSM 510 inverted confocal microscope, which was equipped with an on-stage incubator with controlled temperature, CO_2 pressure and humidity for long term cell tracking. The microscope and digital camera were controlled via Carl Zeiss Zen 2009 (Version 6.0 SP2). Syringe pumps (PHD 2000, Harvard Apparatus, Holliston, MA) were used to insert cells and fluids into the microfluidic structure (**Figure 1**). FRC:DC, FRC:T cell and FRC:DC:T cell interactions were visualized in 2D and 3D at different times, using a fully rendered multidimensional data set and a scheme of monochrome z-stacks, resulting in a "top view" projection. Time lapse fluorescence and differential interference contrast (DIC) images were captured with a 10×objective and 20×objective using a Zeiss LSM 510 inverted laser scanning confocal microscope while the devices were maintained at 37°C, 5% CO_2. The fluorescence micrographs were analysed using Matlab R2014, Bitplane Imaris 8.1 and ImageJ software. Cells were manually tracked over time from maximum intensity top-view image sequences. The instantaneous velocities of T cells and DCs were calculated from the distance moved between successive time points (~s each).

G. Preparation and characterization of FRC scaffold in 48 hours

All cultivation of cells in microdevices were performed using the culture medium described for MutuDC 1940. FRCs were stained red and subsequently pipetted into the device at a concentration of 10-20x10^6cells ml^{-1}, and let to adhere for 3-5h at 37°C, 5% CO_2 in static conditions (without perfusion) before perfusion was started at 100nl min^{-1}. After 2 days with continuous perfusion, mDCs were loaded by pipet into the device at 2x10^6cells ml^{-1} and were let to settle for ~1h in static conditions, before the device was analysed by confocal microscopy. The strength of FRC attachment and inter-cell connections was assessed by monitoring the cells at increasing flowrates. Flow rate was successively increased (50, 100, 200, 300, 400 and 500nl min^{-1}) every 20min.

H. Performance tests of cell interactions mimicking LN inflammatory stage on-a-chip

FRC+DC interaction: FRC scaffold was prepared as described in section G. At day 2, mDCs were loaded by pipet into the device at 2x10^6 cells ml^{-1}. mDCs were let to settle for ~1h in static conditions prior to analysis of flow rates at a confocal microscope. DCs were monitored with successive increment of flow rate (50, 100, 200, 300, 400 and 500nl min^{-1}) during intervals of 10min in 1h experiment.

FRC+T cell interaction: FRC scaffold was prepared as described in section G. At day 2, stained T cells resuspended at 4x10^6cells ml^{-1} in culture medium were loaded into syringes and introduced into the device by the syringe pump. T cells were monitored at a confocal microscope as the device was perfused with the solution of culture media and T cells, at a flow rate of 100nl min^{-1}. Three different locations within the device were monitored for 20min, in an 1h experiment.

FRC+DC+T cell interaction: FRC scaffold was prepared as described in section G. At day 2-3, DCs (with/without activation) were loaded by pipet into the device at 5x10^6cells ml^{-1} and let to settle for 1-2h in static conditions. Subsequently, the device was perfused with a solution of culture media and stained T cells (20x10^6cells ml^{-1}) using a syringe pump, in order to mimic the natural process of T cell

attachment during inflammatory stages inside the T cell zone. T cells and DCs were monitored with successive increment of flow rate (100, 200 and 300nl min^{-1}) during intervals of 20min in 1h experiment.

I. Statistical analysis

Measurements of the FRC, FRC:DC, FRC:T cell and FRC:DC:T cell interaction were obtained and quantified using time series (Zeiss LSM510) across 12 independent experiments, at the same position or in different positions inside the cell chamber along time according to the criteria/object of the experiment.

Bitplane Imaris 8.1 and XTensions (Matlab) were used for four dimensional image analyses and automated tracking of cells. As a criteria of cell counting, the accuracy of the automated tracking was manually controlled, and only tracks with durations of > 5 sec were included in the analysis (in order to minimize the noise of detection from other cells that were passing through the flow without adhesion or interaction). For statistical clustering treatment, multiple stack samples at the same time, average cell velocity, meandering index, histograms of instantaneous velocities and distributions of instantaneous velocity along time, tracks from the same origin (track length and duration) were calculated from Imaris and XTensions (Matlab). Statistical analysis of all collected data from Imaris was performed using GraphPad Prism software. All studies were performed in duplicates unless otherwise noted. All values are reported as Mean±SD.

Results and Discussion

Microfluidic chamber design and characterization of velocity profile

We developed the microfluidic cell chamber by adopting biodesign principles present on a 3D LN T cell zone stromal network. The device is characterized by thin inlets with a cross section area of 200µmx100µm, a main circular cell chamber with an outer diameter of 4mm, and two large outlets with a cross section area of 1000µmx100µm (**Figure 1**). To maximize the control of velocity profile inside the chamber, the same height 100µm was defined in the whole device (**Figure 1F**) (14). Considering that the interstitial flow of lymph is always present in draining LNs, we might assume the fluid direction and projection on the chip from the inlets, cell chamber and to the outlets, with the same direction from the afferent lymphatic vessel into the subcapsular sinus, through the conduits into the paracortex and medulla, to the via of efferent lymphatic vessel (10, 41-44).

The device contains a main circular cell chamber which is composed by inlets with two independents entries with 11 protuberances with juxtaposed rectangular pillars (20µmx40µm) with interval between pillars of 20µm; the inner of the chamber (with inner diameter of 3mm without filters) is completely supported by round pillars with 25µm and 50µm of diameter and spaced by 100µm; and the outer diameter of cell chamber composed by two levels of filters. We chose the largest possible spacing between round pillars (100µm) inside the main chamber to decrease the velocity among PDMS pillars when testing successive increment of fluid flow rates as found during inflammation, without compromising the viability and attachment of FRC filaments and 3D extracellular meshwork assembly around the PDMS pillars and filters, as well as to trap DC and T cells during the attachment tests. The purpose of the existence of 11 protuberances at the entries consisted to spread and dissipate the flow through all directions inside the cell chamber in order to guarantee the control and uniformity on the mechanical force and stimulation on FRC network, and to enhance nutrient delivery (**Figure 1**; **Figure 2**).

Furthermore, our strategy with uniform disposition of PDMS pillars pre-treated with dopamine in the central cell chamber, and also considering the height of the device limited to 100µm (in order to avoid becoming hypoxic in the absence of oxygen supply (14)), was to provide a mere artificial subtract/scaffold for FRC growth without the need to use polymeric hydrogels commonly used in tissue engineering.

To promote the FRC/RN trabecular network construction inside the cell chamber during 2-7days with continuous flow, as mechanical stimuli, force and gradient, and the progressive accumulation of lymphocytes on FRC network to induce the chemokine and integrin gradients production, we chose to apply two types of filters.

Considering the complexity of the tissue architecture of a LN, T cell zone is also characterized by a significant high dense number of T cells, on the order of 10^6 in a 2mm diameter LN, occupying roughly 60% of the total spherical volume (4.2 µL) (6, 45, 46). In this way, we decided to recreate a slice part with 100µm of thickness of this LN spherical volume on the chip, defining an inner diameter of main cell chamber with 3mm corresponding approximately 15% from the total spherical volume of LN (d=2mm), and defining as cell occupation rates for this reduced volume (0.6µL) to FRCs, DCs, and T cells in 29%, 3% and 7%, resulting an occupancy rate of 40% and with empty space of 60%, which served as our guide during experimentation.

Figure 2| Velocity profile determined from COMSOL Multiphysics 4.4 simulation. A) 2D graphic of half of the cell chamber at Z plane of 50µm with flow rate of 100nl min^{-1} on the inlet. For these conditions, the mean velocity range determined for the fluid passing through the chamber was 5-15 µm s^{-1}. **B)** 2D graphic of half of the cell chamber at Z plane of 50µm with a flow rate of 500nl min^{-1} on the inlet. For these conditions, the mean velocity range of fluid simulated was 25-75 µm s^{-1}.

Our objective with the simulation part was to understand and predict the flow behaviour, velocity and shear stress values inside the cell chamber and was useful in optimizing design. At a flow velocity similar to the reported *in vivo* (10-25µm min^{-1}, corresponding to 5-12x10^{-5}Dyn cm^{-2} (6, 46) proved to be too low for nutrient exchange and the survival of FRC (data not shown). However at 50 and 100nl min^{-1} (corresponding to shear stress at Z=5µm to 0.7-4x10^{-3} Dyn cm^{-2} and (0.001-0.004)Dyn cm^{-2}, and to analyse posteriorly the level of support of flow rates that this system can tolerate with successive increment of flow rates from 50nl min^{-1} to 500nl min^{-1}.

In this context, we decided to simulate and analyse the range of maximum velocity parabolic profiles inside the chamber from 50nl min^{-1} to 500nl min^{-1} in order to estimate from these maximum range of velocity the values of shear stress using the equation (1.2) with an h position corresponding to the localization of the DC or T cell on glass or on FRC scaffold (assuming a no-slip condition where the velocity of the fluid at the boundary is zero). From the simulations (**Figure 2**), the mean maximum velocity range determined for the fluid passing through the chamber at 100nl min^{-1} on a XY plan at Z=50µm was 5-15x10^{-6}m s^{-1} (or 300-900µm min^{-1}) with a correspondent range of shear stress at 5µm above the boundary of (0.001-0.004)Dyn cm^{-2} (**Figure 2A**). At 500nl min^{-1} on a XY plan at Z=50µm, the maximum velocity was 2.5-7.5x 10^{-5}m s^{-1} (or 1500-4500µm min^{-1}) with a correspondent range of shear stress at 5µm above the boundary of (0.007-0.02)Dyn cm^{-2} (**Figure 2B**).

With these results, we can identify a uniform distribution of fluid inside the cell chamber, with a laminar and predictable behaviour with a linear scaling of fluid flow, in this case 5 times more than at 100nl min^{-1} conditions.

One important aspect to be reflected is that the conception of this design allowed to achieve considerable low values of shear stress from 4.6X10^{-5}Dyn cm^{-2} to high values of 0.02Dyn cm^{-2}, giving to the operator a significant range of control on the mechanical forces to be exerted on FRC scaffold and on all cell interactions in study. It is important to mention that this range integrates the low range of shear stress corresponding to the physiological values for complex flow in the lymph node micro environment found and published until now in the literature, 0.005 to 0.05Dyn cm^{-2} (3, 30, 47, 48).

Characterization of FRC scaffold-on-a-chip

In the T cell zone high numbers of FRC form a fibrous reticular conduit network by wrapping around collagen strands (2, 49). In order to identify the influence of mechanical stimuli on the construction of FRC meshwork in our chip, we started with the development of a FRC scaffold-on-a-chip without and with perfusion at 50nl min^{-1} (with a corresponding range of shear stress at Z=5µm of 0.0007-0.002Dyn cm^{-2}) for 48h. At 3h after FRC loading, flow did not seem to affect FRC growth, both showing normal growth and scattering of the FRC filaments (data not shown). However, after 24h from initial loading, in the static system, a significant decrease and depletion of FRC filaments was evident, compared with the morphology 3h after the initial loading. On the other hand, in the system with perfusion, a highly dense level of FRC network was clearly visible, with cells crowding tightly around and between the pillars in the entire height of the chamber, 100µm (**Suplementary Figure 1**). The fibroblasts enwrapped the pillars of the entries (11 protuberances) and all filters, concentrating around columns, and producing a more uniform mesh-like distribution in the central inner chamber where shear stress was lower. This suggest that the increased shear stress experienced by the cells at constrictions was stimulating cells to form stronger fibrous networks. This is consistent with earlier findings showing that the application of a fluid flow can induce FRC to align with ECM (3, 50-52).

We further analysed by microscopy the level of the surface transmembrane protein podoplanin (PDPN, also called gp38, D240), widely used as a marker for FRCs of LN (3). The unperfused static system showed only low levels of podoplanin expression on the FRC, while the system with perfusion demonstrated higher expression of podoplanin (data not show) after 24h. The low expression of PDPN in static cultures could be due to lower shear stress and mechanical stimulation or also due to lower less favourable conditions related to oxygen, nutrients and waste. Nonetheless, FRC grown with perfusion showed many signs of being a stable and viable fibrous 3D network with functional potential.

To further explore the FRC 3D network, cell chambers with FRC perfused at a minimal flow rate at 50nl min^{-1} for 2 days, before subjecting the chips to increasing flow rates with successive increment every 20 min from 50-500nl min^{-1} (in steps of 100 nl min^{-1}). The results were very clear, at low flow rates 50nl min^{-1} (corresponding to shear stress range inside the chamber of 0.0007-0.002Dyn cm^{-2}), 100nl min^{-1} (0.0014-0.004Dyn cm^{-2}) and 200nl min^{-1} (0.003-0.008Dyn cm^{-2}), the network tolerated the flow well and seemed stable. For a flow rate of 300nl min^{-1} (0.004-0.01Dyn cm^{-2}), it was possible to identify some deflection of FRC filaments. At flow rates of 400nl min^{-1} (0.005-0.017Dyn cm^{-2}) and 500nl min^{-1} (0.007-0.021Dyn cm^{-2}) showed a high degree of deflection/disruption/destruction of the FRC filaments, sudden cell shrinkage and movement of the entire network inside the cell chamber (**Supplementary Video 1, 2, 3 and 4**). From the simulation data and considering the difficulty to determine microphysiologically relevant flow velocities in the LN (3, 30), we can assume that the range shear stress supported by this system with high cell density during initial loading (10-20x10^6cells ml^{-1}) is 0.0007 to 0.008Dyn cm^{-2}. In the device tested in this work, these shear stresses are attained for flows ranging from 50nl min^{-1} to 200nl min^{-1} corresponding to the fluid velocities between 150µm min^{-1} required for normal growth, and as maximum of 1800µm min^{-1}, still supporting the network. For shear stresses above 0.008Dyn cm^{-2}, cell detachment and structural destruction was dominating.

Having determined the suitable flow rate to apply to the FRC-network, we next investigated the effect of DC loading on the stability and integrity of the FRC network after 48h on chip pre-culture. We pre-stimulated DC with 100ng ml^{-1} LPS overnight and loaded DCs slowly by pipette 30-60min before experimentation with perfusion. As with FRCs alone, the FRC+DC network tolerated very well flow rates up to 200nl min^{-1} but started disrupting above 300nl min^{-1} and lost much of the integrity at 500nl/min. (**Figure 3; Supplementary Video 1, 2, 3 and 4**). However, even though the integrity of the mesh work was lost at high flow rates FRCs still remained attached to the solid structures in the device and seemed to survive the disruptions.

Our obtained network morphology, in that we can perfuse cells through the network, is in technical agreement with recent observations made by electron microscopy revealing

that FRC enwrap thin strands of ECM leaving much of the structure open to fluid flow. This is in contrast to connective tissues and *in vitro* 3D hydrogel cell cultures where cells are embedded in the ECM (2, 49). Thus our system, resembles LN in that the network forms a conduits system acting as corridors to provide direct and fast convection of soluble antigens, cytokines and chemokines into the deeper areas of the paracortex (1, 53-55). Another resemblance is that the there is direct contact between the FRC network with mechanical and chemical gradient, as well as with circulating resulting in rapid immobilization and massive parallel interaction of lymphocytes and DCs with the FRC network (12, 14, 41, 44). These FRC meshworks have also been shown to be an important source for chemokines (e.g., CCL19, CCL21, CCL2, CCL4, CCL5, CXCL12, CXCL16, CX3CL1) and other cytokines (e.g., IL-7, IL-6, TNF and LTα), pointing the active roles of these cells in adaptive response, as shown by the analysis of murine and human FRC lines derived from LN with many chemokines strongly induced upon TNFα and LTαβ stimulation (2, 43, 56, 57).

Figure 3|Flow rate dependent disruption of FRC networks. A) A chip with 48h FRC scaffold (stained in red) with immobilized dendritic cells (green), were submitted to a flow rate of 100nl min^{-1} for 20min. The image shows a uniform distribution of FRC filaments and confluence of the FRC meshwork in XY plane (with stained cells) and also in the Z plane (with bright field detection) around the PDMS pillars. **B)** The same system of FRCs (red) and immobilized DCs (green) in the same position as in A) but with 500nl min^{-1} flow rate for 20min showing an obvious partial disruption of network and mesh integrity, also around pillars. Scale bar: 100µm.

Together, these data suggest that our system allows construction and organization of a reticular meshwork of FRC sustained by flow and permissive of cellular traverse across the system leading to immobilization of antigen presenting cells. This is the first basic requirement for a LN construct. For this system in particular, the shear stress sustaining the FRC scaffold was found to be 0.008-0.01Dyn cm^{-2}, corresponding to fluid velocity of 150-1800µm min^{-1}. That roughly corresponds to 0.3-3 cell diameters per second, an intuitively correct speed for LN function.

DCs and T cells are motile on the FRC scaffold

In order for a LN to function by allowing many T cells to screen a few DCs for correct antigen, it is necessary for DCs to adhere to the scaffold and for T cells to interact with many antigen-irrelevant DCs along the scaffold in search of the DC with correct antigen. So cells should be able to move around the scaffold. Our next investigation was to study DC and T cell motility on the FRC scaffold under flow. This also served as a guide to integrate all three cell types in an experiment.

First we investigated the DC motility on the scaffold**.** After 48h FRC scaffold was loaded with LPS-activated DCs and subsequently subjected to increasing flow rates from 50nl min^{-1} to 500nl min^{-1}, every 10min in 1h of experiment. At each flow rate a movie was recorded in a thick confocal plane and single cell speed was calculated using imaging software and Matlab. **Figure 4B** represents the distribution of instantaneous DC velocities from 2 independent tests (1st test n=307 cells; 2nd test n=294 cells) with successive increment of flow rates. We found that the average DC velocity was almost constant, at approximately ~10µm min^{-1}, independent of flow rates from 50nl min^{-1} to 500nl min^{-1}. It should be noted that at 500nl min^{-1} much of the network is disrupted but that our data are from areas in the chip that could sustain the high flow rate. This is in line with previous studies showing that DCs can resist high levels of shear stress (3, 11, 47), even higher than what was tolerated by our on-chip FRC scaffold.

Figure 4| DCs and T cells interact and remain mobile on FRC scaffold.: A) Overlaid phase contrast and fluorescence image and only fluorescence image showing the FRC:DC interactions after 100nl/min perfusion for 10min. **B)** Distributions of DC velocities in two independent experiments (n=307 cells and n=294 cells) with successive increment of flow rate (50, 100, 200, 300, 400 and 500 nl/min) at 10min intervals. **C)** Fluorescence image showing the FRC (red): resting T cells (blue) interactions after 100nl/min for 20min. Scale bar: 100µm. **D)** Distributions of T cell velocities in three different positions (n=8 , n=22 cells, n=20 cells) with the same flow rate 100 nl/min for 20min each (total 1h). **E)** Histogram of spontaneous T cell velocities (mean=10.7 µm/min) derived from the tracking defined of all T cells of in (D).

Next we examined how T cells interacted with the native FRC scaffold, in the absence of DCs and activation. The loading of unactivated T cells was done by perfusing at constant velocity 2000cells/min (100nL/min) through the FRC for 1h. The accumulation of cells on the FRC scaffold was monitored continuously at three different locations for 20 min each, in a total of 1h. During the first 40min, it was a clear accumulation of T cells on the FRCs inside the chamber. However, after the first 40min the number of T cells started to decrease, and even detaching from FRC network. It should be noted that the T cells had no activation signal, that is no incentive, to be retained by the FRC. It should also be understood that an *in vitro* cell perfusion system is imperfect and will result in loss of cells over time.

Regarding the T cells that did attach to FRCs, they should move with the flow to allow new interaction of constantly fed naïve T cell repertoires to find the sparse antigen-specific T cells (with frequencies in blood ranging from 1 in 10^3 to 1 in 10^7). The distribution of T cell velocities was derived from the tracking of all the cells during the first 1h (**Figure 4E**). The mean velocity of the T cells was 10.7µm min^{-1} when subjected to shear stress ranging from 0.001 to 0.004Dyn cm^{-2} .This relatively high velocity of one cell diameter per minute is within the range (9-12µm min^{-1}) reported in several studies (6, 18, 58, 59) from intravital microscopy. From **Figure 4E**, large velocity fluctuations were also identified, reaching peak velocities of >20µm min^{-1}. We also observed that T cells crawl along the surface of FRC (**Supplementary Video 5 and 6**). This cell behaviour is very similar to what is found *in vivo* (41, 58, 60). In fact, these recent studies using two-photon intravital microscopy have revealed that naïve T cells crawl along the surface of the FRC network at an average two-dimensional velocity of ~10-12µm min^{-1} with an apparent random pattern

of motion. It is therefore possible that our system also harbours some of the hallmarks of LN resulting in T cell motility increasing the likelihood of LN function (10).

T cells interact with FRC:DCs in an antigen dependent manner

As a further step to investigate the potential of our system, we wanted to compare antigen specific *vs.* unspecific T cell interaction with FRC:DCs and also how DCs were affected by T cells. From insights obtained in this work, we generated a FRC scaffold by medium perfusion at 100nL/min, before loading DCs with or without pre-activation (100ng/mL LPS 24h, 10ug/mL Ovalbumin for 1h) for 1h, before perfusing T cells. The T cell perfusion was increased from 100nl min^{-1} to 300nl min^{-1} (corresponding to a shear stress at 5µm above the boundary between 0.001 to 0.01Dyn cm^{-2}), which is in accordance with *in vivo* data (3). The same position inside each chip was monitored for 1h in order to follow the nature cell encounters as well as the motility of DC and T cells. **Figure 5C** shows the difference between activated and non-activated DCs. There was a marked decrease in motility of DCs on FRC when the DCs were activated, compared to inactivated DCs being reduced from around 5µm min^{-1} to ~2.5µm min^{-1} (**Supplementary Video 5, 6, 7 and 8**). This makes sense since the correlative activation/antigenicity should promote DC adhesiveness to FRCs (30, 61-63).

These data were obtained as we simultaneously were pumping T cells through the system with successive increment of flow rate (100, 200, 300 $nl.min^{-1}$) every 20min. In contrast to DCs there was a less robust effect of activation of T cells to move differently from the non-activated, even the overall tendency was that activated cells were more stationary (**Supplementary Video 5, 6, 7 and 8**).

Figure 5| System with three types of cells – FRCs:DCs:T cells – without (as control) and with LPS+OVA II peptide activation. A) *System with activation*: Overlaid phase contrast and fluorescence image and only fluorescence image showing the FRC scaffold (stained with red; and completely developed inside the chip during 48h previously with continuous perfusion before the beginning of the experiment with DC loading), with DCs (green)- T cells (stained in blue) trapped and interacting with each other at 100nl/min. Scale bar: 100µm. **B)** *System without activation*: fluorescence image showing the FRC scaffold (stained with red; and completely developed inside the chip with 48h of continuous perfusion before the beginning of the experiment with DC loading), with DCs (green)-T cells (stained in blue) without activation, which are trapped and interacting with each other with a higher scan velocity than with specific activation. Scale bar: 100µm. **C)** Distributions of instantaneous DC velocities ($\mu m.min^{-1}$) without and with LPS+OVAII peptide activation in two independent experiments (1st test and 2nd test) per each conditions (with activation: 1st test n=67 and 2nd test n=23; without activation: 1st test n=78 and 2nd test n=98), by pumping in simultaneously "medium+T cells" solution in order to mimic the natural process of T cell attachment during inflammatory stages inside the T cell zone, with successive increment of flow rate (100, 200, 300 $nl.min^{-1}$) during intervals of 20min per each flow and an overall 1 hour of experiment. **D)** Distributions of instantaneous T cell velocities ($\mu m.min^{-1}$) without and with LPS+OVAII peptide activation in two independent experiments (1st test and 2nd test) per each conditions (with activation: 1st test n=48 and 2nd test n=20; without activation: 1st test n=55 and 2nd test n=5), by pumping in simultaneously "medium+T cells" solution in order to mimic the natural process of T cell attachment during inflammatory stages inside the T cell zone, with successive increment of flow rate (100, 200, 300 $nl.min^{-1}$) during intervals of 20min per each flow and an overall 1 hour of experiment.

Average velocities does not say anything about travelled path patterns or distribution. We therefore further compiled and analysed the data of the above experiments using BitPlane Imaris, XTensions functions (Matlab) and GraphPad Prism in order to obtain more information. First we found that DCs and T cells both were less motile after activation. Even if these cells where clones and we did not compare with other cells types, the results is both clear and intended. T cells and DCs are more likely to be retained in the LN when activated. The data also show a large variation in behaviour, even within clones. Secondly, neither speed over short distances or speed distribution says everything about migrational tendencies when individual cells were tracked. A central concept is track duration, meaning the time a cell was successfully tracked. A short track duration in a confocal slice may signify either movement in the Z-direction or a quick movement in the xy-plane. Inactivated DCs present an apparent random pattern of motion confined with their length duration approximately of 5µm in average, with track duration of 3.2±4.8min. For T cell without specific antigen activation, the track durations were 3.5±4.3 min. These results match findings in several studies (18, 19, 58, 59, 64-66), where the large velocity fluctuations and sudden directional changes give the impression that T cells once in every 1-3 min moves into a new direction. This "stop and go" behaviour suggests an intrinsic rhythmicity of the T cells as reported in (66). The same effect was observed by Miller *et al* (19), where T cells encountered DCs randomly, decelerating only slightly while in contact with DCs, and rapidly moving away after ~3min. This behaviour of the naïve T cell will be considered a baseline to which will be further compared the behaviour of the T cells activated with LPS+OVAII peptide.

From **Figure 6A and 6B**, we can investigated the effects of antigen stimulations on the OVA II:APC:FRC interactions on-a-chip. The proportion of stationary DCs and T cells increased since the average velocities decrease down to ~2µm min^{-1}. The motility of DCs was almost stationary (as average of 2µm per minute) with a track duration of 6.8±6.2min, while most T cells moved in characteristic looping patterns, making serial contacts as in scanner mode with the same or with neighbouring DCs with an average track duration of 7.3±6.8min. Furthermore, it was observed less T cells with large velocity and sharp directional changes reinforcing their motility change upon activation.

This significant decrease in DC and T cell motility can be explained considering that, in the system without activation, when the cognate pMHC is not detected, the T cell breaks contact with the DC and moves away allowing another T cell to interact with the DC. In the system with cognate interactions,

when the antigen is detected, the T cells enter into a stage characterized by the decrease of their velocity, promoting multiple interactions with both the original stimulating DC as well as other immature DC in the vicinity. According with Miller *et al.* (19), early antigen recognition involves multiple short-live signalling events, where the durations of these interactions involving T cells in serial contacts with multiple DCs are approximately 10min. The obtained interaction time with the microfluidic device are thus consistent with Millers findings.

These results demonstrate the viability of the developed microfluidic cell chamber to recreate similar microphysiological environment and conditions observed in the T cell zone of LN. This opens a vast field of possibilities of studies that can be performed using a T cell:DC:FRC interactions model that behaves as *in vivo*.

Figure 6| Representative case study of 1st test at 200 nl.min^{-1} without (control) and with activation of LPS+ OVA II peptide. A) Distributions of instantaneous velocities without and with activation for DCs and T cells (without activation DCs n=78 and T cells n=55; with activation DCs n=67 and T cells n=48) with a flow rate of 200nl.min^{-1} during 20min. **B)** Tracks from the same origin corresponding to the tracks defined in graphics (A) for without activation and with activation groups of dendritic cells and T cells.

Conclusion

In conclusion, this microfluidic cell chamber developed in this work presents a useful approach to mimic artificially microphysiological environment and conditions required to develop a T cell zone of LN on-the-chip. This allows the study of T cell:DC:FRC interactions with relevant importance in the adaptive immune response, and to promote the investigation of these principles as a tool *towards* immunological research and in development of novel immunotherapeutic approaches.

With the design and conception of this platform, it was possible to achieve and to have control on a high range of shear stress (from 5x10^{-5}Dyn cm^{-2} to 0.02Dyn cm^{-2}), which includes the normal microphysiological values reported in literature: 0.005 to 0.05Dyn cm^{-2}. Furthermore, it also allows the exploration of reduced values of shear stress necessary to study the mechanical and chemical stimuli. With this high range of shear stress, it was possible to determine the proper conditions of perfusion (100nl min^{-1}) to develop a FRC network on a chip. After 48h with continuous perfusion, the FRC meshwork were supported by PDMS pillars and filters, growing with a uniform distribution in XY plan and crossing Z axis (h=100µm). With mechanical and chemical stimuli induced by flow rates on FRC scaffold, it was possible to analyse several interactions configuration including 2 types of cells (FRC:DC and FRC:T cell) and 3 types of cells (FRC:DC:T cell).

In the system with 2 types of cells, the FRC:DC interactions with previous LPS activation and FRC:T cell interactions without antigen activation were studied, evidencing in general lines in both cases high motility with mean velocity around ~10µm min^{-1}, at a range of shear stress 0.001 to 0.004Dyn cm^{-2} corresponding to fluid velocities between 300-900µm min^{-1}.

In the system with 3 types of cell interactions, the system without and with cognate interactions using LPS+OVAII peptide activation was studied, where DCs were pre-loaded to interact with FRC scaffold during 1h. T cells were further perfused into the chamber with the DC:FRC scaffold in order to analyse a natural attachment by sucessive increment of flow rate (100 to 300nl min^{-1}) as an immediate response to inflammation. These results evidenced that without activation T cells and DC shown motility with 5µm min^{-1}, random movements and interactions during 3 min as an intrinsic rhythmicity program of "stop and go". With cognate interactions, it was visible a significant decrease of DC and T cell velocity to ~2.5µm min^{-1}, where T cells moved in characteristic looping patterns making serial contacts with the same or with neighbouring DCs, with interval of interactions around ~7min.

All these results were consistent to studies perform *in vivo* demonstrating that this microfluidics device mimics the cell behaviour in the T cells zone of LN being a LN-T cell zone-on-the-chip. It can be utilized as a research tool to better understand lymph node organogenesis, DC and T cell development and activation, contribution of different cell types in immunization protocols This a LN-T cell zone-on-the-chip can also be used as a clinical development tool towards *in vitro* immunization, personalized cancer vaccination, immunotherapeutic approaches for cancer and autoimmune diseases etc.

Acknowledgement

The Research Council of Norway is acknowledged for the support to the Norwegian Micro- and Nano-Fabrication Facility, NorFab, project number 245963/F50. Microfabrication process was performed at the NTNU NanoLab, Norwegian University of Science and Technology (NTNU).

Imaging was performed at the Cellular and Molecular Imaging Core Facility (CMIC), Norwegian University of Science and Technology (NTNU). CMIC is funded by the Faculty of Medicine at NTNU and Central Norway Regional Health Authority.

References

1. Graw F, Regoes RR. Influence of the fibroblastic reticular network on cell-cell interactions in lymphoid organs. PLoS computational biology. 2012;8(3):e1002436.

2. Katakai T, Hara T, Sugai M, Gonda H, Shimizu A. Lymph node fibroblastic reticular cells construct the stromal reticulum via contact with lymphocytes. The Journal of experimental medicine. 2004;200(6):783-95.

3. Tomei AA, Siegert S, Britschgi MR, Luther SA, Swartz MA. Fluid flow regulates stromal cell organization and CCL21 expression in a tissue-engineered lymph node microenvironment. Journal of immunology. 2009;183(7):4273-83.

4. Actor JK. Introductory Immunology Basic Concepts for Interdisciplinary Applications. London: Academic Press,; 2014. Available from: http://www.sciencedirect.com/science/book/9780124200302 MIT Access Only.

5. Giese C, Marx U. Human immunity in vitro - solving immunogenicity and more. Advanced drug delivery reviews. 2014;69-70:103-22.

6. Mirsky HP, Miller MJ, Linderman JJ, Kirschner DE. Systems biology approaches for understanding cellular mechanisms of immunity in lymph nodes during infection. Journal of theoretical biology. 2011;287:160-70.
7. Bousso P. T-cell activation by dendritic cells in the lymph node: lessons from the movies. Nature reviews Immunology. 2008;8(9):675-84.
8. von Andrian UH, Mempel TR. Homing and cellular traffic in lymph nodes. Nature reviews Immunology. 2003;3(11):867-78.
9. Giese C, Lubitz A, Demmler CD, Reuschel J, Bergner K, Marx U. Immunological substance testing on human lymphatic micro-organoids in vitro. Journal of biotechnology. 2010;148(1):38-45.
10. Girard JP, Moussion C, Forster R. HEVs, lymphatics and homeostatic immune cell trafficking in lymph nodes. Nature reviews Immunology. 2012;12(11):762-73.
11. Randolph GJ, Angeli V, Swartz MA. Dendritic-cell trafficking to lymph nodes through lymphatic vessels. Nature reviews Immunology. 2005;5(8):617-28.
12. Swartz MA. The physiology of the lymphatic system. Advanced drug delivery reviews. 2001;50(1-2):3-20.
13. Chen W, Zhu C. Mechanical regulation of T-cell functions. Immunological reviews. 2013;256(1):160-76.
14. Cupedo T, Stroock A, Coles M. Application of tissue engineering to the immune system: development of artificial lymph nodes. Frontiers in immunology. 2012;3:343.
15. Sixt M, Kanazawa N, Selg M, Samson T, Roos G, Reinhardt DP, et al. The conduit system transports soluble antigens from the afferent lymph to resident dendritic cells in the T cell area of the lymph node. Immunity. 2005;22(1):19-29.
16. van der Merwe PA, Dushek O. Mechanisms for T cell receptor triggering. Nature reviews Immunology. 2011;11(1):47-55.
17. Huppa JB, Davis MM. T-cell-antigen recognition and the immunological synapse. Nature reviews Immunology. 2003;3(12):973-83.
18. Mempel TR, Henrickson SE, Von Andrian UH. T-cell priming by dendritic cells in lymph nodes occurs in three distinct phases. Nature. 2004;427(6970):154-9.
19. Miller MJ, Safrina O, Parker I, Cahalan MD. Imaging the single cell dynamics of CD4+ T cell activation by dendritic cells in lymph nodes. The Journal of experimental medicine. 2004;200(7):847-56.
20. Ramadan Q, Gijs MA. In vitro micro-physiological models for translational immunology. Lab on a chip. 2015;15(3):614-36.
21. Webb DR. Animal models of human disease: inflammation. Biochemical pharmacology. 2014;87(1):121-30.
22. Vudattu NK, Waldron-Lynch F, Truman LA, Deng S, Preston-Hurlburt P, Torres R, et al. Humanized mice as a model for aberrant responses in human T cell immunotherapy. Journal of immunology. 2014;193(2):587-96.
23. Boussommier-Calleja A, Li R, Chen MB, Wong SC, Kamm RD. Microfluidics: A new tool for modeling cancer-immune interactions. Trends in cancer. 2016;2(1):6-19.
24. Esch MB, King TL, Shuler ML. The role of body-on-a-chip devices in drug and toxicity studies. Annual review of biomedical engineering. 2011;13:55-72.
25. Griffith LG, Swartz MA. Capturing complex 3D tissue physiology in vitro. Nature reviews Molecular cell biology. 2006;7(3):211-24.
26. Dura B, Dougan SK, Barisa M, Hoehl MM, Lo CT, Ploegh HL, et al. Profiling lymphocyte interactions at the single-cell level by microfluidic cell pairing. Nature communications. 2015;6:5940.
27. Faley S, Seale K, Hughey J, Schaffer DK, VanCompernolle S, McKinney B, et al. Microfluidic platform for real-time signaling analysis of multiple single T cells in parallel. Lab on a chip. 2008;8(10):1700-12.
28. Kim SK, Moon WK, Park JY, Jung H. Inflammatory mimetic microfluidic chip by immobilization of cell adhesion molecules for T cell adhesion. The Analyst. 2012;137(17):4062-8.
29. Wu J, Wu X, Lin F. Recent developments in microfluidics-based chemotaxis studies. Lab on a chip. 2013;13(13):2484-99.
30. Moura Rosa P, Gopalakrishnan N, Ibrahim H, Haug M, Halaas O. The intercell dynamics of T cells and dendritic cells in a lymph node-on-a-chip flow device. Lab on a chip. 2016;16(19):3728-40.
31. Gopalakrishnan N, Hannam R, Casoni GP, Barriet D, Ribe JM, Haug M, et al. Infection and immunity on a chip: a compartmentalised microfluidic platform to monitor immune cell behaviour in real time. Lab on a chip. 2015;15(6):1481-7.
32. Giese C, Demmler CD, Ammer R, Hartmann S, Lubitz A, Miller L, et al. A human lymph node in vitro--challenges and progress. Artificial organs. 2006;30(10):803-8.
33. Molteni R, Bianchi E, Patete P, Fabbri M, Baroni G, Dubini G, et al. A novel device to concurrently assess leukocyte extravasation and interstitial migration within a defined 3D environment. Lab on a chip. 2015;15(1):195-207.
34. Wong KH, Truslow JG, Khankhel AH, Chan KL, Tien J. Artificial lymphatic drainage systems for vascularized microfluidic scaffolds. Journal of biomedical materials research Part A. 2013;101(8):2181-90.
35. Bonvin C, Overney J, Shieh AC, Dixon JB, Swartz MA. A multichamber fluidic device for 3D cultures under interstitial flow with live imaging: development, characterization, and applications. Biotechnology and bioengineering. 2010;105(5):982-91.
36. Fuertes Marraco SA, Grosjean F, Duval A, Rosa M, Lavanchy C, Ashok D, et al. Novel murine dendritic cell lines: a powerful auxiliary tool for dendritic cell research. Frontiers in immunology. 2012;3:331.
37. McDonald JC, Duffy DC, Anderson JR, Chiu DT, Wu H, Schueller OJ, et al. Fabrication of microfluidic systems in poly(dimethylsiloxane). Electrophoresis. 2000;21(1):27-40.
38. Chuah YJ, Koh YT, Lim K, Menon NV, Wu Y, Kang Y. Simple surface engineering of polydimethylsiloxane with polydopamine for stabilized mesenchymal stem cell adhesion and multipotency. Scientific reports. 2015;5:18162.
39. Bruus H. Theoretical microfluidics. Oxford: Oxford University Press; 2008. xvi, 346 p p.
40. Young EW, Wheeler AR, Simmons CA. Matrix-dependent adhesion of vascular and valvular endothelial cells in microfluidic channels. Lab on a chip. 2007;7(12):1759-66.
41. Bajenoff M, Egen JG, Koo LY, Laugier JP, Brau F, Glaichenhaus N, et al. Stromal cell networks regulate lymphocyte entry, migration, and territoriality in lymph nodes. Immunity. 2006;25(6):989-1001.
42. Lammermann T, Sixt M. The microanatomy of T-cell responses. Immunological reviews. 2008;221:26-43.
43. Mueller SN, Germain RN. Stromal cell contributions to the homeostasis and functionality of the immune system. Nature reviews Immunology. 2009;9(9):618-29.
44. Swartz MA, Hubbell JA, Reddy ST. Lymphatic drainage function and its immunological implications: from dendritic cell homing to vaccine design. Seminars in immunology. 2008;20(2):147-56.
45. Catron DM, Itano AA, Pape KA, Mueller DL, Jenkins MK. Visualizing the first 50 hr of the primary immune response to a soluble antigen. Immunity. 2004;21(3):341-7.
46. Bogle G, Dunbar PR. Simulating T-cell motility in the lymph node paracortex with a packed lattice geometry. Immunology and cell biology. 2008;86(8):676-87.
47. Chary SR, Jain RK. Direct measurement of interstitial convection and diffusion of albumin in normal and neoplastic tissues by fluorescence photobleaching. Proceedings of the National

Academy of Sciences of the United States of America. 1989;86(14):5385-9.
48. Dafni H, Israely T, Bhujwalla ZM, Benjamin LE, Neeman M. Overexpression of vascular endothelial growth factor 165 drives peritumor interstitial convection and induces lymphatic drain: magnetic resonance imaging, confocal microscopy, and histological tracking of triple-labeled albumin. Cancer research. 2002;62(22):6731-9.
49. Cukierman E, Pankov R, Yamada KM. Cell interactions with three-dimensional matrices. Current opinion in cell biology. 2002;14(5):633-9.
50. Ng CP, Swartz MA. Mechanisms of interstitial flow-induced remodeling of fibroblast-collagen cultures. Annals of biomedical engineering. 2006;34(3):446-54.
51. Ng CP, Hinz B, Swartz MA. Interstitial fluid flow induces myofibroblast differentiation and collagen alignment in vitro. Journal of cell science. 2005;118(Pt 20):4731-9.
52. Ng CP, Swartz MA. Fibroblast alignment under interstitial fluid flow using a novel 3-D tissue culture model. American journal of physiology Heart and circulatory physiology. 2003;284(5):H1771-7.
53. Bajenoff M, Glaichenhaus N, Germain RN. Fibroblastic reticular cells guide T lymphocyte entry into and migration within the splenic T cell zone. Journal of immunology. 2008;181(6):3947-54.
54. Gretz JE, Anderson AO, Shaw S. Cords, channels, corridors and conduits: critical architectural elements facilitating cell interactions in the lymph node cortex. Immunological reviews. 1997;156:11-24.
55. Kaldjian EP, Gretz JE, Anderson AO, Shi Y, Shaw S. Spatial and molecular organization of lymph node T cell cortex: a labyrinthine cavity bounded by an epithelium-like monolayer of fibroblastic reticular cells anchored to basement membrane-like extracellular matrix. International immunology. 2001;13(10):1243-53.
56. Link A, Vogt TK, Favre S, Britschgi MR, Acha-Orbea H, Hinz B, et al. Fibroblastic reticular cells in lymph nodes regulate the homeostasis of naive T cells. Nature immunology. 2007;8(11):1255-65.
57. Luther SA, Vogt TK, Siegert S. Guiding blind T cells and dendritic cells: A closer look at fibroblastic reticular cells found within lymph node T zones. Immunology letters. 2011;138(1):9-11.
58. Miller MJ, Wei SH, Parker I, Cahalan MD. Two-photon imaging of lymphocyte motility and antigen response in intact lymph node. Science. 2002;296(5574):1869-73.
59. Miller MJ, Wei SH, Cahalan MD, Parker I. Autonomous T cell trafficking examined in vivo with intravital two-photon microscopy. Proceedings of the National Academy of Sciences of the United States of America. 2003;100(5):2604-9.
60. Cahalan MD, Parker I. Choreography of cell motility and interaction dynamics imaged by two-photon microscopy in lymphoid organs. Annual review of immunology. 2008;26:585-626.
61. Bianchi E, Molteni R, Pardi R, Dubini G. Microfluidics for in vitro biomimetic shear stress-dependent leukocyte adhesion assays. Journal of biomechanics. 2013;46(2):276-83.
62. Dong C, Lei XX. Biomechanics of cell rolling: shear flow, cell-surface adhesion, and cell deformability. Journal of biomechanics. 2000;33(1):35-43.
63. Alvarez D, Vollmann EH, von Andrian UH. Mechanisms and consequences of dendritic cell migration. Immunity. 2008;29(3):325-42.
64. Bousso P, Robey E. Dynamics of CD8+ T cell priming by dendritic cells in intact lymph nodes. Nature immunology. 2003;4(6):579-85.
65. Wei SH, Parker I, Miller MJ, Cahalan MD. A stochastic view of lymphocyte motility and trafficking within the lymph node. Immunological reviews. 2003;195:136-59.
66. Beltman JB, Maree AF, Lynch JN, Miller MJ, de Boer RJ. Lymph node topology dictates T cell migration behavior. The Journal of experimental medicine. 2007;204(4):771-80.

Figures

Lymph node-on-a-chip

Mimicking the microphysiology of the T cell zone

Patrícia Moura Rosa,[a,c] Cecilie Lund,[a] Markus Haug[b] and Øyvind Halaas*[a]

[a]Department of Clinical and Molecular Medicine, Norwegian University of Science and Technology, 7489 Trondheim, Norway

[b]Centre of Molecular Inflammation Research (SFF-CEMIR), Department of Clinical and Molecular Medicine, Norwegian University of Science and Technology, 7489 Trondheim, Norway

[c]NTNU NanoLab, Norwegian University of Science and Technology, 7489 Trondheim, Norway

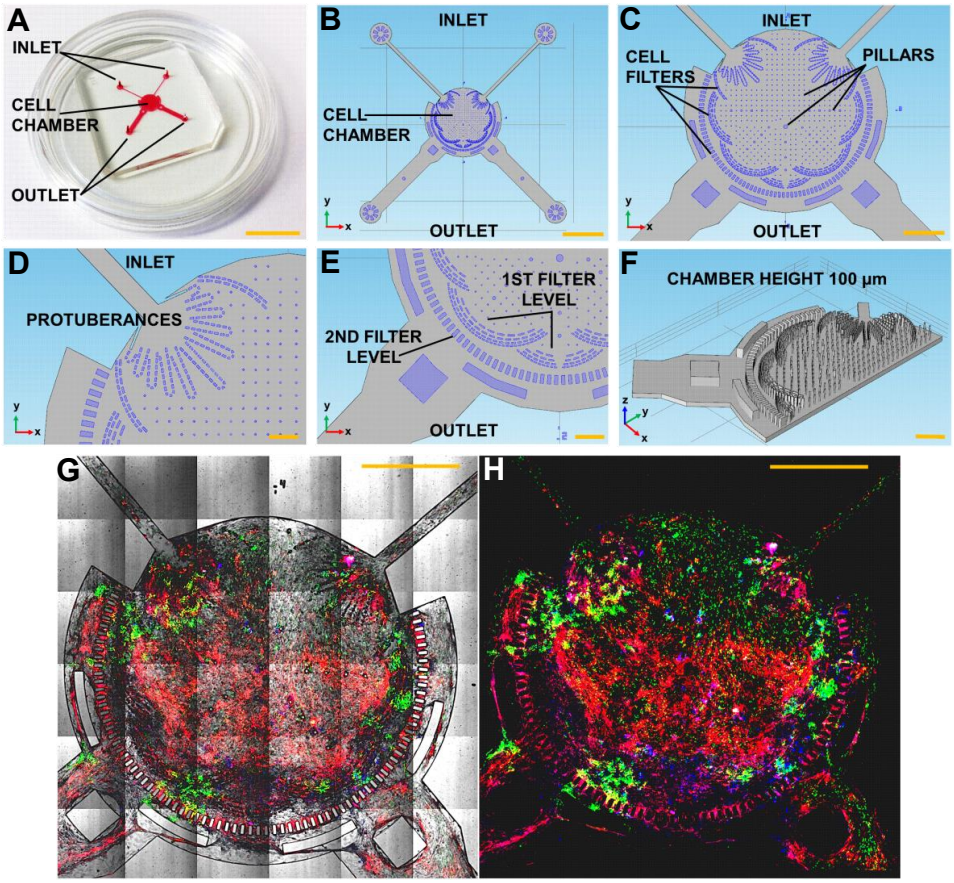

Figure 1| Lymph node on-a-chip. A) Photograph of the PDMS biochip bonded to a glass substrate. Inlets, cell chamber and outlets are in red. Scale bar: 1cm. **B)** Top view of whole biochip: The device is characterized by two thin inlets with a cross section area of 200µmx100µm, a main circular cell chamber with an outer diameter of 4mm and two large outlets with a cross section area of 1000µmx100µm. Scale bar: 1500µm **C)** Top view of the circular cell chamber: The cell chamber is composed from the inlets with two independent systems of 11 protuberances with juxtaposed rectangular pillars (20µmx40µm) with interval between pillars of 20µm; the inner of the chamber (with inner diameter of 3mm without filters) is completely supported by round pillars with 25µm and 50µm of diameter and spaced between them of 100µm; and the outer perimeter of the cell chamber composed by two levels of filters. Scale bar: 1000µm. **D)** Top view and disposition of 11 protuberances at the entry of cell chamber. Scale bar: 200µm. **E)** Top view of 2 types of filters: 1st level of filters with thin juxtaposed rectangular pillars in 4 concentric circular lines of filters (10 sets in all chamber; composed by individual pillars from 100µmx20µm (as maximum) to 40µmx20µm (as minimum) with interval between pillars respectively, 50µm and 20µm); 2nd level of filters with a large single circular line around the cell chamber (composed by individual pillars 150µmx50µm with interval between pillars of 50µm). Scale bar: 200µm. **F)** 3D cross section of the PDMS device with the same thickness in all pillars with 100µm. Scale bar: 400µm. **G&H)** Overlaid phase contrast and fluorescence image and only fluorescence image showing the rearrangement of FRC scaffold (stained in red and developed during 48h before the beginning of experiment), with trapped DC (green) and T cells (blue) interacting with each other. Scale bar: 1mm.

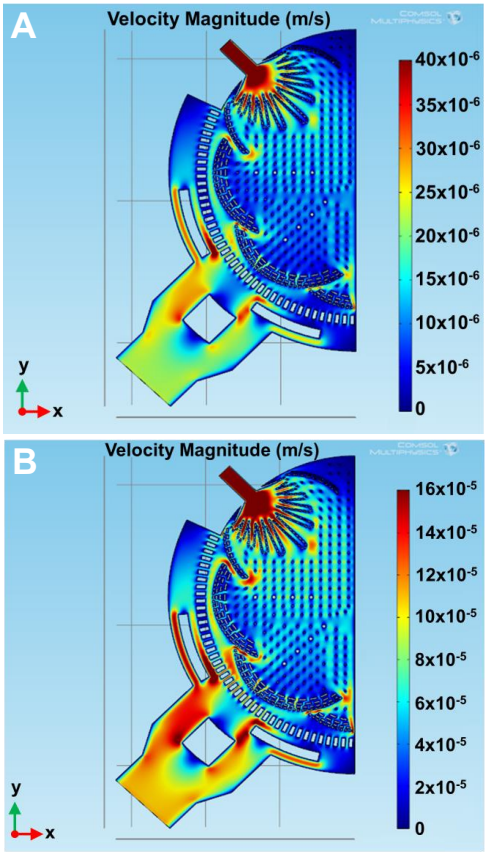

Figure 2| Velocity profile determined from COMSOL Multiphysics 4.4 simulation. A) 2D graphic of half of the cell chamber at Z plane of 50µm with flow rate of 100nl min^{-1} on the inlet. For these conditions, the mean velocity range determined for the fluid passing through the chamber was 5-15 µm s^{-1}. **B)** 2D graphic of half of the cell chamber at Z plane of 50µm with a flow rate of 500nl min^{-1} on the inlet. For these conditions, the mean velocity range of fluid simulated was 25-75 µm s^{-1}.

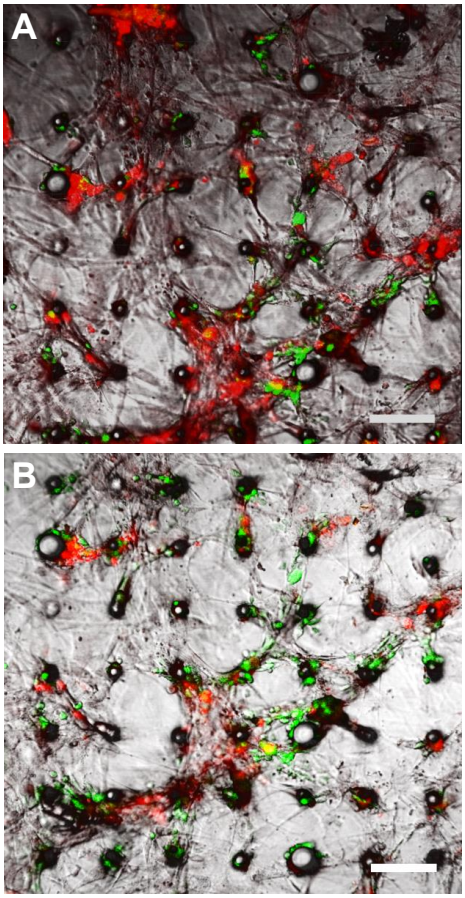

Figure 3|Flow rate dependent disruption of FRC networks. A) A chip with 48h FRC scaffold (stained in red) with immobilized dendritic cells (green), were submitted to a flow rate of 100nl min^{-1} for 20min. The image shows a uniform distribution of FRC filaments and confluence of the FRC meshwork in XY plane (with stained cells) and also in the Z plane (with bright field detection) around the PDMS pillars. **B)** The same system of FRCs (red) and immobilized DCs (green) in the same position as in A) but with 500nl min^{-1} flow rate for 20min showing an obvious partial disruption of network and mesh integrity, also around pillars. Scale bar: 100µm.

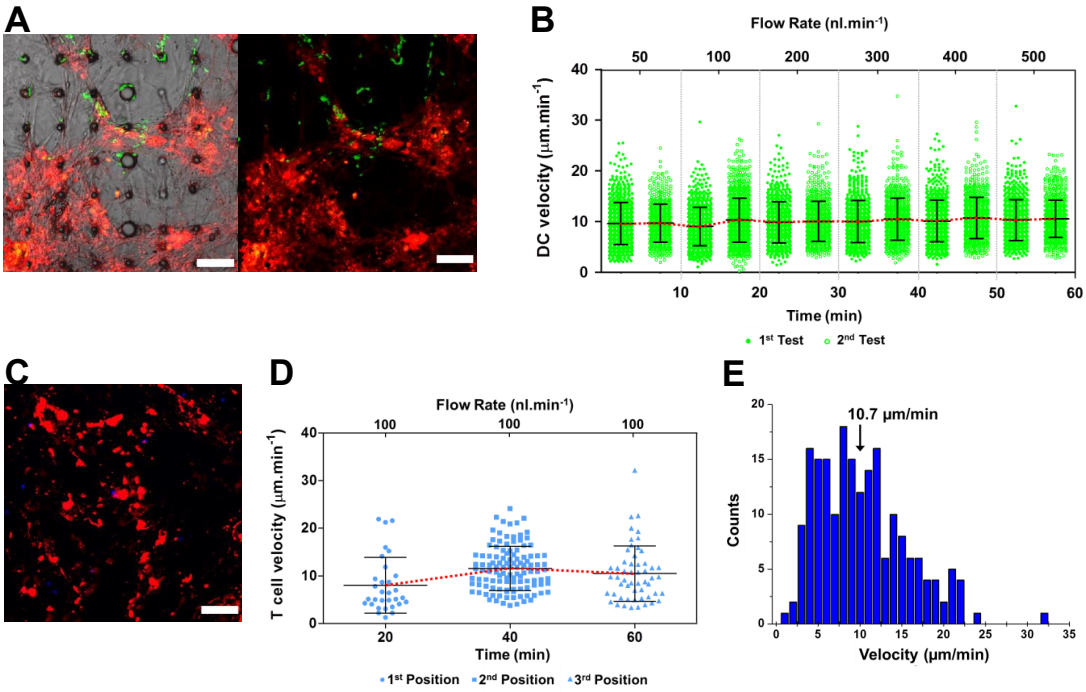

Figure 4| DCs and T cells interact and remain mobile on FRC scaffold.: A) Overlaid phase contrast and fluorescence image and only fluorescence image showing the FRC:DC interactions after 100nl/min perfusion for 10min. **B)** Distributions of DC velocities in two independent experiments (n=307 cells and n=294 cells) with successive increment of flow rate (50, 100, 200, 300, 400 and 500 nl/min) at 10min intervals. **C)** Fluorescence image showing the FRC (red): resting T cells (blue) interactions after 100nl/min for 20min. Scale bar: 100µm. **D)** Distributions of T cell velocities in three different positions (n=8 , n=22 cells, n=20 cells) with the same flow rate 100 nl/min for 20min each (total 1h). **E)** Histogram of spontaneous T cell velocities (mean=10.7 µm/min) derived from the tracking defined of all T cells of in (D).

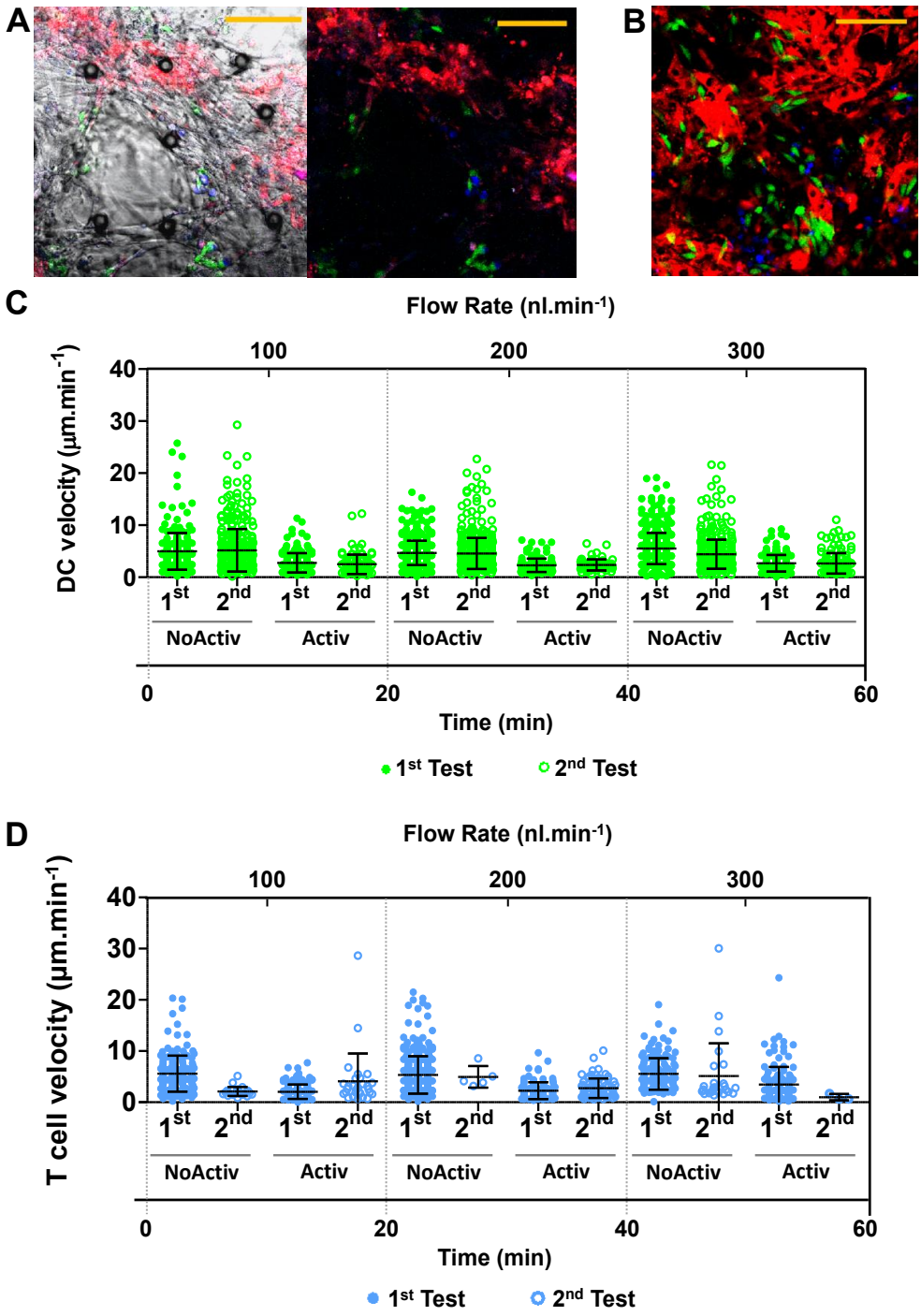

Figure 5| System with three types of cells – FRCs:DCs:T cells – without (as control) and with LPS+OVA II peptide activation. A) *System with activation*: Overlaid phase contrast and fluorescence image and only fluorescence image showing the FRC scaffold (stained with red; and completely developed inside the chip during 48h previously with

continuous perfusion before the beginning of the experiment with DC loading), with DCs (green)- T cells (stained in blue) trapped and interacting with each other at 100nl/min. Scale bar: 100µm. **B)** *System without activation*: fluorescence image showing the FRC scaffold (stained with red; and completely developed inside the chip with 48h of continuous perfusion before the beginning of the experiment with DC loading), with DCs (green)-T cells (stained in blue) without activation, which are trapped and interacting with each other with a higher scan velocity than with specific activation. Scale bar: 100µm. **C)** Distributions of instantaneous DC velocities ($\mu m.min^{-1}$) without and with LPS+OVAII peptide activation in two independent experiments (1^{st} test and 2^{nd} test) per each conditions (with activation: 1^{st} test n=67 and 2^{nd} test n=23; without activation: 1^{st} test n=78 and 2^{nd} test n=98), by pumping in simultaneously "medium+T cells" solution in order to mimic the natural process of T cell attachment during inflammatory stages inside the T cell zone, with successive increment of flow rate (100, 200, 300 $nl.min^{-1}$) during intervals of 20min per each flow and an overall 1 hour of experiment. **D)** Distributions of instantaneous T cell velocities ($\mu m.min^{-1}$) without and with LPS+OVAII peptide activation in two independent experiments (1^{st} test and 2^{nd} test) per each conditions (with activation: 1^{st} test n=48 and 2^{nd} test n=20; without activation: 1^{st} test n=55 and 2^{nd} test n=5), by pumping in simultaneously "medium+T cells" solution in order to mimic the natural process of T cell attachment during inflammatory stages inside the T cell zone, with successive increment of flow rate (100, 200, 300 $nl.min^{-1}$) during intervals of 20min per each flow and an overall 1 hour of experiment.

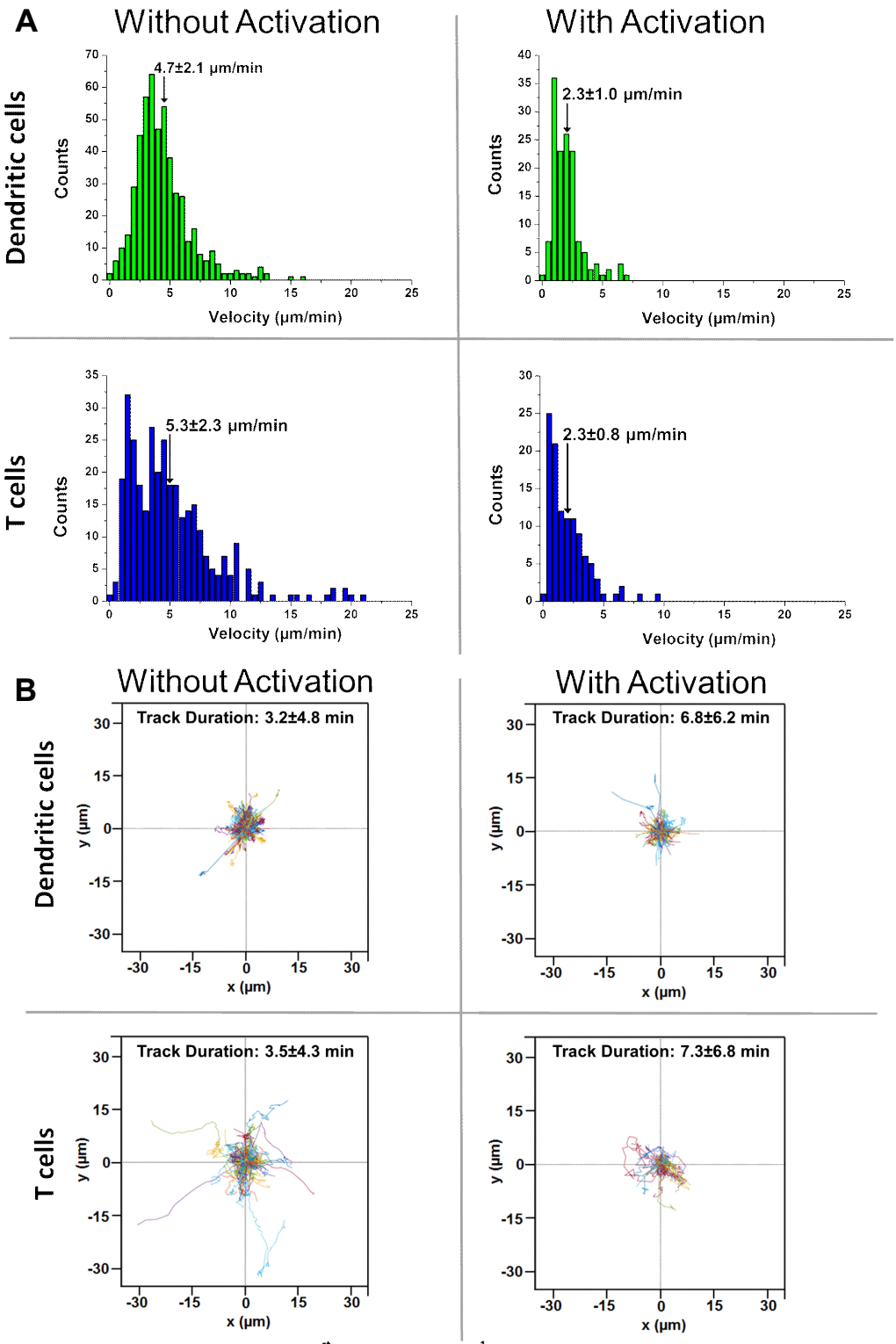

Figure 6| Representative case study of 1st test at 200 nl.min^{-1} without (control) and with activation of LPS+ OVA II peptide. A) Distributions of instantaneous velocities without and with activation for DCs and T cells (without activation DCs n=78 and T cells n=55; with activation DCs n=67 and T cells n=48) with a flow rate of 200nl.min^{-1} during 20min. **B)** Tracks

from the same origin corresponding to the tracks defined in graphics (A) for without activation and with activation groups of dendritic cells and T cells.

Supplemental Data

Lymph node-on-a-chip

Mimicking the microphysiology of the T cell zone

Patrícia Moura Rosa,[a,c] Cecilie Lund,[a] Markus Haug[b] and Øyvind Halaas*[a]

[a]Department of Clinical and Molecular Medicine, Norwegian University of Science and Technology, 7489 Trondheim, Norway

[b]Centre of Molecular Inflammation Research (SFF-CEMIR), Department of Clinical and Molecular Medicine, Norwegian University of Science and Technology, 7489 Trondheim, Norway

[c]NTNU NanoLab, Norwegian University of Science and Technology, 7489 Trondheim, Norway

Supplementary Video 1| FRC detachment test with successive increment of flow rate. Test 1.1 System of FRC scaffold (stained in red) with trapped dendritic cells (green), were submitted to a flow rate of 100nl/min during 20min, with left-to-right flow direction. In this video, it is visible an uniform distribution of FRC filaments and full construction of the FRC meshwork in XY plan (with stained cells) and also across the Z plan (with bright field detection) around the PDMS pillars.

Supplementary Video 2| FRC detachment test with successive increment of flow rate. Test 2.1 The same system of FRCs (stained in red) and trapped DCs (green) in the same initial position with 500nl/min during 20min, with left-to-right flow direction. In this video, it is visible a significant depletion and destruction of FRC scaffold and their irregular disposition among pillars, once the tentacles shrink in size and are disengaged from the pillars.

Supplementary Video 3| FRC detachment test with successive increment of flow rate. Test 2.1 Other system of FRCs (stained in red) and trapped DCs (green) in the specific position with 300nl/min during 20min, with left-to-right flow direction.

Supplementary Video 4| FRC detachment test with successive increment of flow rate. Test 2.2 The same system of FRCs (stained in red) and trapped DCs (green) in the specific position with 500nl/min during 20min, with left-to-right flow direction.

Supplementary Video 5| System with FRC-DC-T cell interactions without activation at 100nl min^{-1} during 20min, with left-to-right flow direction.

Supplementary Video 6| System with FRC-DC-T cell interactions without activation at 100nl min^{-1} during 20min, with left-to-right flow direction.

Supplementary Video 7| System with FRC-DC-T cell interactions with activation at 300nl min^{-1} during 20min, with left-to-right flow direction.

Supplementary Video 8| System with FRC-DC-T cell interactions with activation at 100nl min^{-1} during 20min, with left-to-right flow direction, and with representation of distribution of green spots (DCs) and blue spots(T cells), and areas determined by XTensions - Kiss and Run Analysis associated with interactions of 3 types of cells.

Supplementary Figure 1| FRC meshwork inside the cell chamber after ~48h of continuous perfusion with 100nl min^{-1}. A) FRCs (orange) organized extensively in XY plan crossing all height of chamber, 100µm, with left-to-right flow direction. Scale bar: 100µm .B) and C) Surface representation by Imaris from A). Scale bar: 100µm.

A)

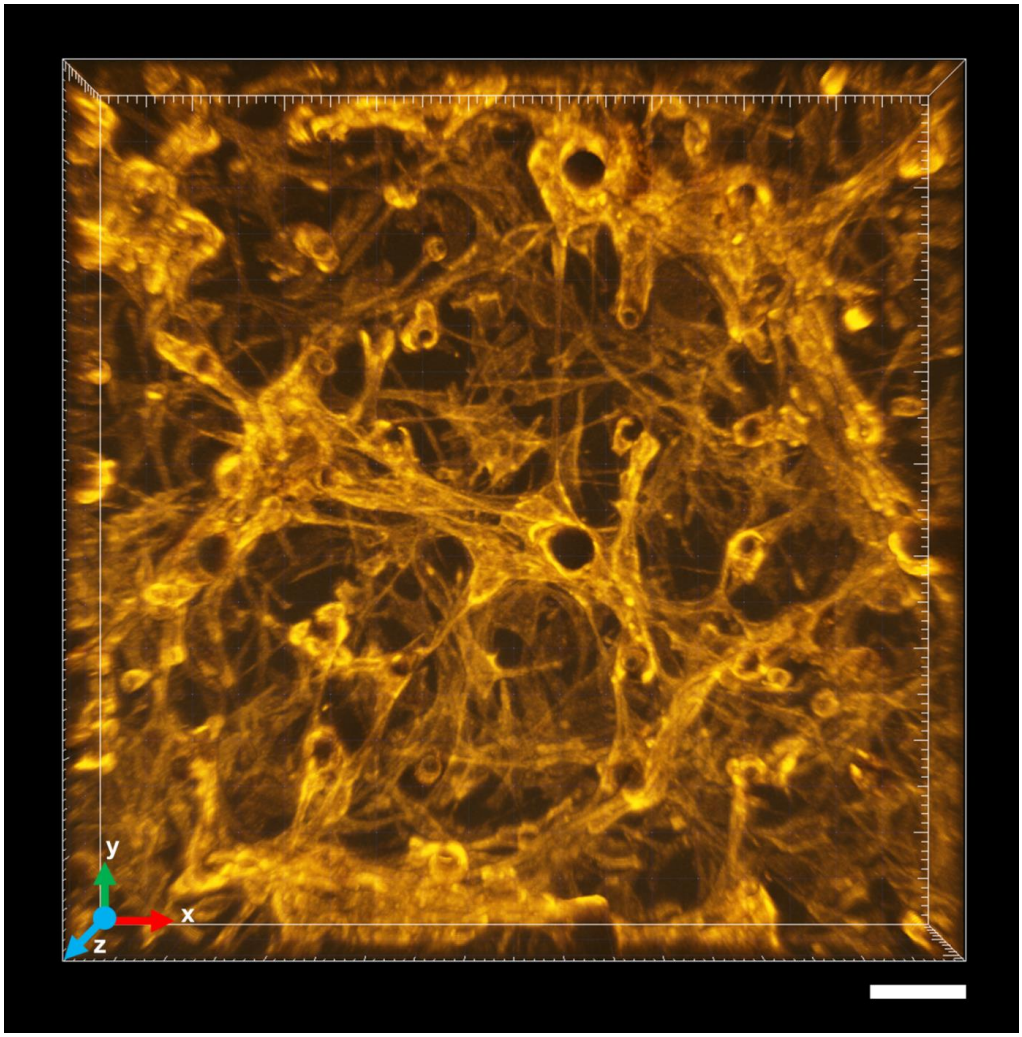

B)

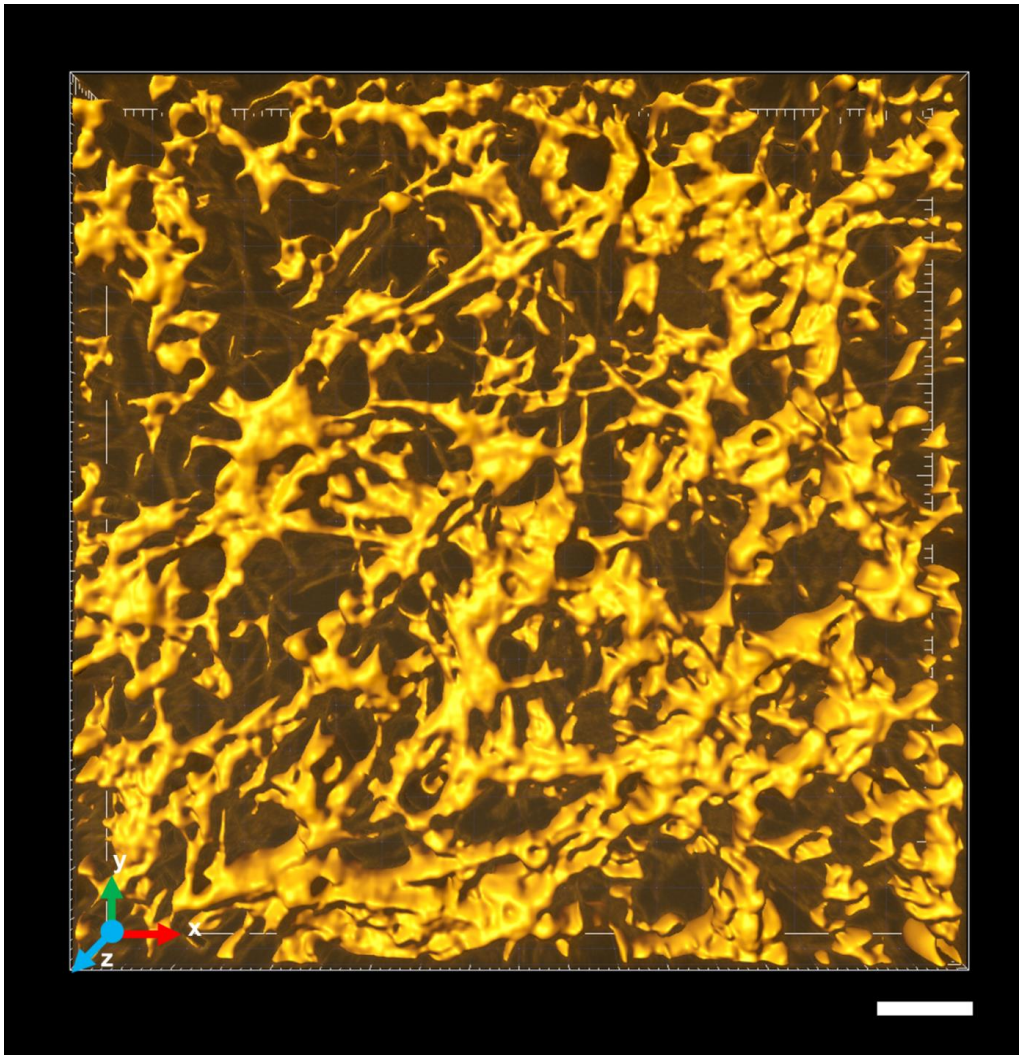

c)

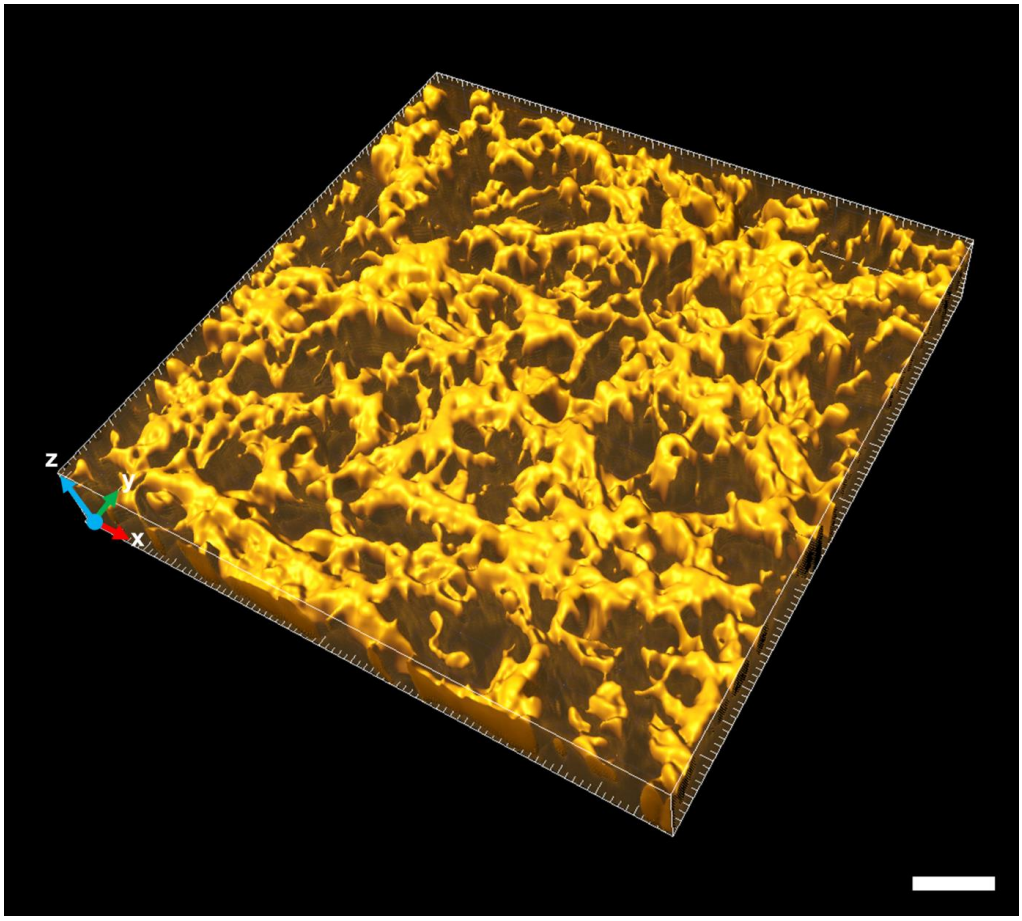

Supplementary Figure 2| 3D Visualization of the system with FRC-DC-T cell interactions without activation at 100nl min^{-1} during 20min, with left-to-right flow direction. A) Top view. Scale bar: 100μm. **B)** Lateral view. Scale bar: 100μm.

A)

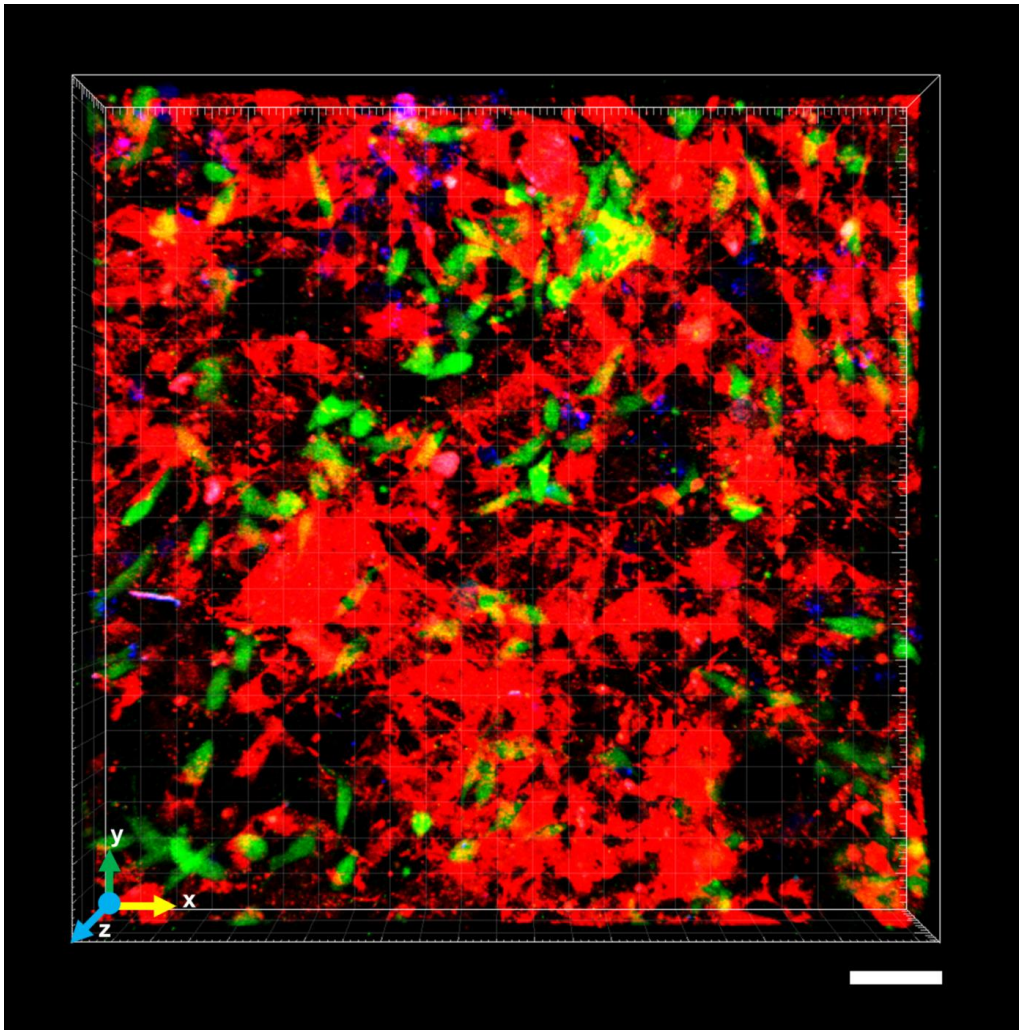

B)